

# Wave propagation on black hole spacetimes

David Dempsey

A thesis submitted for the degree of Doctor of Philosophy



School of Mathematics and Statistics

University of Sheffield

July 2017



# Acknowledgements

Firstly I would like to thank my supervisor Sam Dolan, without whom this work would not have been possible. He always found time to offer help and advice even if sometimes reading my work did send him to sleep. I could not have asked for a more encouraging, patient and supportive supervisor.

I must also thank Elizabeth Winstanley for her encouragement and helpful input over the last four years. Thanks must go to my other collaborator Sarp Akcay who was a pleasure to work with. I would also like to express my gratitude to Barry Wardell and Niels Warburton for their helpful input as well as discussions at various conferences.

My thanks also go to all the CRAG group members past and present, particularly my office mates over the last year, Jake, Tom, Tom, Jake, Luiz and before that Jack.

Outside of the PhD world I must thank the Tuesday track/carvery/quiz club, Tez, Steve and Will, for their friendship and support.

Thanks must go to my family for their support over the last 26 years, hopefully we can now end the discussion with granddad on whether this PhD is “just maths.”

Finally, to Bobbi, thanks for everything.

---

# Abstract

This thesis studies the propagation of fundamental fields on black hole and black hole analogue spacetimes. We consider the scalar, electromagnetic, gravitational and Dirac fields, and their governing equations, in various scenarios.

We initially consider an analogue gravity model, the draining bathtub vortex, that shares features with the Kerr black hole, such as a horizon and an ergoregion. We solve the wave equation approximately, via the eikonal approximation, and numerically, using the method of lines, and show that a point-like disturbance maps out the lightcone of the effective spacetime.

The Schwarzschild and Kerr black hole spacetimes are then introduced and we discuss their key features. We solve the scalar wave equation for the black hole spacetimes and compare with the analogue spacetime.

We then introduce the self force, the back reaction of a body's own field on its motion. The scalar self force on Kerr spacetime is calculated using the worldline integration method. This involves solving the scalar wave equation to find the Green function via the Kirchhoff representation and integrating over the entire past history of the worldline. The electromagnetic (EM) self force is calculated via the mode sum method. We use both analytical and numerical techniques to calculate EM self force for a particle held static outside of a Schwarzschild black hole.

The gauge freedom of the gravitational self force is also discussed. We construct for eccentric orbits on Schwarzschild the spin precession invariant, a gauge invariant quantity. We compare the spin precession invariant calculated

---

using numerical self force data with a post-Newtonian calculation.

Finally we investigate the Dirac (fermionic) field in searching for the existence of bound states. We find that the solutions which satisfy the boundary conditions, obey a three-term recurrence-relation. Using continued-fraction methods we find a spectrum of quasi-bound states of the Dirac field exists.

# Preface

The majority of the work of this thesis was carried out by the author under the supervision of Sam Dolan.

- Chapter 2 investigates an analogue black hole; the draining bathtub vortex. This work is based on work published in Ref. [1] in collaboration with Dolan.
- Chapter 3 reviews the Schwarzschild and Kerr black holes and investigates the behaviour of a scalar wave on the black hole spacetimes.
- Chapter 4 calculates scalar field self force using the worldline integration method. This is based on the method of Wardell *et.al.* [2]. We recreate their results for Schwarzschild spacetime and present new results for the Kerr spacetime.
- Chapter 5 calculates the electromagnetic self force acting on a particle sourcing its own electromagnetic field held static in Schwarzschild spacetime. We recover the result of Smith and Will [3] by applying the mode sum method.
- Chapter 6 presents a derivation of gauge invariant quantity, the spin precession invariant for gravitational self force. This work was carried out in collaboration with Akcay and Dolan in Ref. [4]. Numerical results were produced using a code developed by Akcay and compared with a

---

post-Newtonian calculation carried out by Akcay and Dolan. All plots presented in the chapter were created by the author.

- Chapter 7 presents a calculation of the bound states of the Dirac equation on Kerr spacetime. This is based on work done in collaboration with Dolan in Ref. [5].

Throughout this thesis we use geometrised units where  $G = c = 1$  and a metric signature  $(-, +, +, +)$ . Brackets  $()$  and  $[\ ]$  denote symmetrization and antisymmetrization of the indices respectively. We use Greek letters  $\mu, \nu \dots$  to denote spacetime indices, Latin letters  $a, b, c \dots$  denote tetrad indices and Roman letters  $i, j, k, \dots$  denote spatial indices 1, 2, 3.

# Contents

<b>1</b>	<b>Introduction</b>	<b>15</b>
1.1	Gravitational waves and two-body systems . . . . .	16
1.2	Wave propagation . . . . .	19
1.3	Self force . . . . .	21
1.4	Thesis outline . . . . .	24
<b>2</b>	<b>Wave propagation on analogue black holes</b>	<b>27</b>
2.1	Introduction . . . . .	27
2.2	Eikonal approximation . . . . .	29
2.2.1	Van Vleck determinant . . . . .	31
2.3	Draining bathtub model . . . . .	31
2.4	Null geodesic congruence . . . . .	35
2.4.1	Null geodesic equations . . . . .	35
2.4.2	Van Vleck determinant . . . . .	36
2.4.3	Eikonal-wavefront . . . . .	37
2.5	Wave propagation . . . . .	37
2.5.1	Mode decomposition . . . . .	37
2.6	Results . . . . .	40
2.6.1	Non-rotating vortex . . . . .	41
2.6.2	Slowly rotating vortex . . . . .	45
2.6.3	Rapidly rotating vortex . . . . .	48
2.7	Discussion . . . . .	48

<b>3</b>	<b>Wave propagation on astrophysical black holes</b>	<b>53</b>
3.1	Introduction . . . . .	53
3.2	Schwarzschild spacetime . . . . .	54
3.2.1	Spacetime symmetries and geodesics . . . . .	55
3.2.2	Wave evolution . . . . .	57
3.2.3	Numerical evolution . . . . .	58
3.2.4	Results . . . . .	61
3.3	Kerr spacetime . . . . .	62
3.3.1	Spacetime symmetries and geodesics . . . . .	64
3.3.2	Wave evolution . . . . .	67
3.3.3	Numerical evolution . . . . .	68
3.3.4	Results . . . . .	70
3.4	Comparisons and discussion . . . . .	71
 <b>4</b>	 <b>Scalar self force from worldline integrals</b>	 <b>75</b>
4.1	Introduction . . . . .	75
4.2	Scalar self force . . . . .	77
4.3	Green function construction . . . . .	80
4.3.1	Kirchhoff representation . . . . .	80
4.3.2	Hypersurfaces . . . . .	81
4.3.3	Initial data . . . . .	82
4.3.4	Gaussian approximation of delta function . . . . .	83
4.3.5	Quasi-local expansion . . . . .	84
4.3.6	Late time tail . . . . .	85
4.4	Worldline integration . . . . .	86
4.5	Schwarzschild method . . . . .	88
4.5.1	Kirchhoff representation for Schwarzschild spacetime . . . . .	89
4.5.2	Numerical method . . . . .	90
4.5.3	Worldline integration . . . . .	92
4.5.4	Fourfold structure . . . . .	94

## CONTENTS

---

4.5.5	Summary of errors . . . . .	95
4.6	Kerr method . . . . .	95
4.6.1	Initial conditions . . . . .	96
4.6.2	Worldline integration . . . . .	98
4.6.3	Numerical method . . . . .	99
4.6.4	Summary of errors . . . . .	101
4.7	Results . . . . .	102
4.7.1	Schwarzschild comparison . . . . .	102
4.7.2	Kerr results . . . . .	103
4.8	Conclusions and discussion . . . . .	103
<b>5</b>	<b>Electromagnetic self force via mode sum regularisation</b>	<b>107</b>
5.1	Introduction . . . . .	107
5.1.1	Electromagnetic self force . . . . .	109
5.2	Electromagnetic field equations . . . . .	111
5.2.1	Static equations . . . . .	112
5.2.2	Jump conditions . . . . .	115
5.3	Mode sum regularisation . . . . .	117
5.3.1	Mode sum calculation . . . . .	117
5.3.2	Regularisation parameters . . . . .	118
5.4	Monopole mode . . . . .	118
5.5	Analytical method . . . . .	119
5.5.1	Solution of radial equations . . . . .	120
5.6	Analytic self force calculation . . . . .	122
5.7	Numerical method . . . . .	123
5.7.1	Dealing with discontinuity . . . . .	125
5.7.2	Smooth initial conditions . . . . .	127
5.7.3	Implementation . . . . .	128
5.7.4	Comparison of numerical and analytical modes . . . . .	129
5.8	Results . . . . .	133

5.9	Discussion . . . . .	134
<b>6</b>	<b>Spin precession invariant for eccentric orbits</b>	<b>137</b>
6.1	Introduction . . . . .	137
6.2	Geodetic precession . . . . .	140
6.2.1	Historical background . . . . .	141
6.3	Tetrad basis . . . . .	143
6.3.1	Parallel transported tetrad . . . . .	145
6.3.2	Schwarzschild eccentric orbit . . . . .	147
6.4	Self force . . . . .	150
6.4.1	Gauge invariant spin precession . . . . .	150
6.4.2	Small $e$ expansions . . . . .	152
6.4.3	Circular orbit limit . . . . .	153
6.4.4	Perturbed tetrad . . . . .	155
6.4.5	Perturbed precession . . . . .	157
6.5	Results . . . . .	158
6.5.1	Numerical results . . . . .	158
6.5.2	Post-Newtonian expansion . . . . .	158
6.5.3	Comparison of self force and post-Newtonian results . . .	160
6.6	Discussion . . . . .	162
<b>7</b>	<b>Bound state solutions of the Dirac equation on Kerr spacetime</b>	<b>163</b>
7.1	Introduction . . . . .	163
7.2	Dirac equation on Kerr spacetime . . . . .	165
7.2.1	Spinors . . . . .	166
7.2.2	Tetrad basis . . . . .	167
7.2.3	Separability: Chandrasekhar-Page equations . . . . .	168
7.2.4	Mode frequency . . . . .	171
7.3	Recurrence relation method . . . . .	172
7.3.1	Formulation details . . . . .	173

## CONTENTS

---

7.3.2	Angular equations . . . . .	174
7.3.3	Radial equations . . . . .	176
7.4	Results . . . . .	182
7.4.1	Fine and hyperfine structure . . . . .	182
7.4.2	Decay rates . . . . .	183
7.4.3	Kerr spectrum . . . . .	186
7.5	Discussion . . . . .	190
<b>8</b>	<b>Conclusions</b>	<b>193</b>
	<b>Appendices</b>	<b>195</b>
<b>A</b>	<b>Dirac delta distribution</b>	<b>197</b>



# Chapter 1

## Introduction

The year 2015 will be marked as the year gravitational waves were finally detected directly, with the observation of GW150914 [6]. First predicted by Einstein in 1916, gravitational waves provide us with physical observations of curvature of spacetime. Gravitational waves are perturbations in the fabric of spacetime which travel at the speed of light, as opposed to Newtonian gravity's action at a distance.

Einstein's theory of general relativity is now over a hundred years old. Since general relativity (GR) was first introduced in 1915, it has passed a number of tests. For example, GR accounts for the anomalous perihelion precession of Mercury. Many of these early tests can be found as small relativistic corrections to Newtonian theory. To fully test GR we must look to areas of spacetime with much stronger gravitational interactions.

General relativity is described by Einstein's equations, a set of ten coupled second-order differential equations. The meaning of Einstein's equations are most succinctly described by Wheeler [7], who said, "Matter tells spacetime how to curve, and spacetime tells matter how to move." Einstein's equations describe the relation between the curvature of spacetime and the distribution of matter and energy.

Black holes are one of the more extreme predictions of Einstein's general

theory of relativity. They are regions of spacetime bounded by an event horizon beyond which not even light can escape. There is evidence for black holes with a range of masses. Black holes with masses from approximately 3 to 18 solar masses have been observed in X-ray binaries [8]. Larger mass black holes have been observed in the gravitational wave observations [6, 9, 10] with a maximum estimated final mass of approximately 62 solar masses. Supermassive black holes are believed to lie at the heart of galaxies. The Event Horizon Telescope (EHT) is aiming to directly observe the environment around Sagittarius A\*, the black hole at the centre of the Milky Way with an estimated mass of 4 million solar masses [11]. The EHT also hopes to observe the black hole at the centre of the M87 galaxy with an estimated mass of 6 billion solar masses [12].

Black holes also highlight the limits of general relativity. At their core, Einstein’s theory suggests that black holes harbour gravitational singularities where matter is collected with infinite densities. In isolation, a black hole, by its very nature, is difficult to distinguish from a massive dense body. Instead we must investigate a black hole’s unique interactions with other objects and physical fields.

Wheeler also coined the phrase “black holes have no hair” [13] in reference to the no-hair conjecture. The Israel-Carter uniqueness theorems [14, 15] imply that a stationary black hole in electrovacuum can be completely characterised by three parameters: mass  $M$ , charge  $Q$  and angular momentum  $J$ . The no-hair conjecture suggests that if a black hole interacts with some physical field, the field will rapidly decay onto the black hole or propagate to infinity. Any evidence that these fields can remain trapped around the black hole may impact on the no-hair conjecture.

## 1.1 Gravitational waves and two-body systems

A two body gravitational system creates perturbations in the fabric of spacetime which propagate as gravitational waves. The first direct detection of grav-

gravitational waves was announced in 2016 by the Laser Interferometer Gravitational-Wave Observatory (LIGO) experiment [6, 9, 10]. The gravitational wave signal of a black hole-black hole merger has a characteristic pattern. During the orbital phase, the gravitational wave signal has a frequency of twice the orbital frequency. The frequency and amplitude of the wave increases as the two bodies inspiral, up until the classic “chirp” as they merge. The final stage of the wave is driven by the quasinormal mode ringdown, as the merged black hole decays to a Kerr black hole.

Figure 1.1 (published in Ref. [6]) shows the estimated waveform from observed data of GW150914 (a binary black hole merger) by LIGO compared with numerical relativity predictions. The waveform is shown alongside estimated numerical relativity models for the inspiral and estimates for the relative separation distance and velocity. An observation of differences from these characteristic waveforms would provide evidence of deviations from GR. The current observations at LIGO have been shown to be consistent with predictions from GR [16].

The LIGO experiment seeks to identify physical signals by matching model waveforms from GR theory to infer the gravitational wave source. At present the creation of theoretical waveform models relies upon numerical relativity and post-Newtonian theory. Numerical relativity attempts to use numerical methods to fully solve the Einstein equations. This method is extremely computationally expensive. There are two important scales to consider: a length scale proportional to the size of the objects, and a time scale related to the ratio of rate of energy lost in gravitational waves compared with the orbital frequency. Both of these scales are proportional to the mass ratio of the two objects. When the two objects are of a similar mass, the two objects are in a highly relativistic regime for a small period of time before merger. Similar mass ratio systems can therefore be accurately modelled out to a regime in which the relativistic effects are suppressed and post-Newtonian theory can be used. Post-Newtonian theory expands Einstein’s equations in powers of  $(v/c)^2$  where

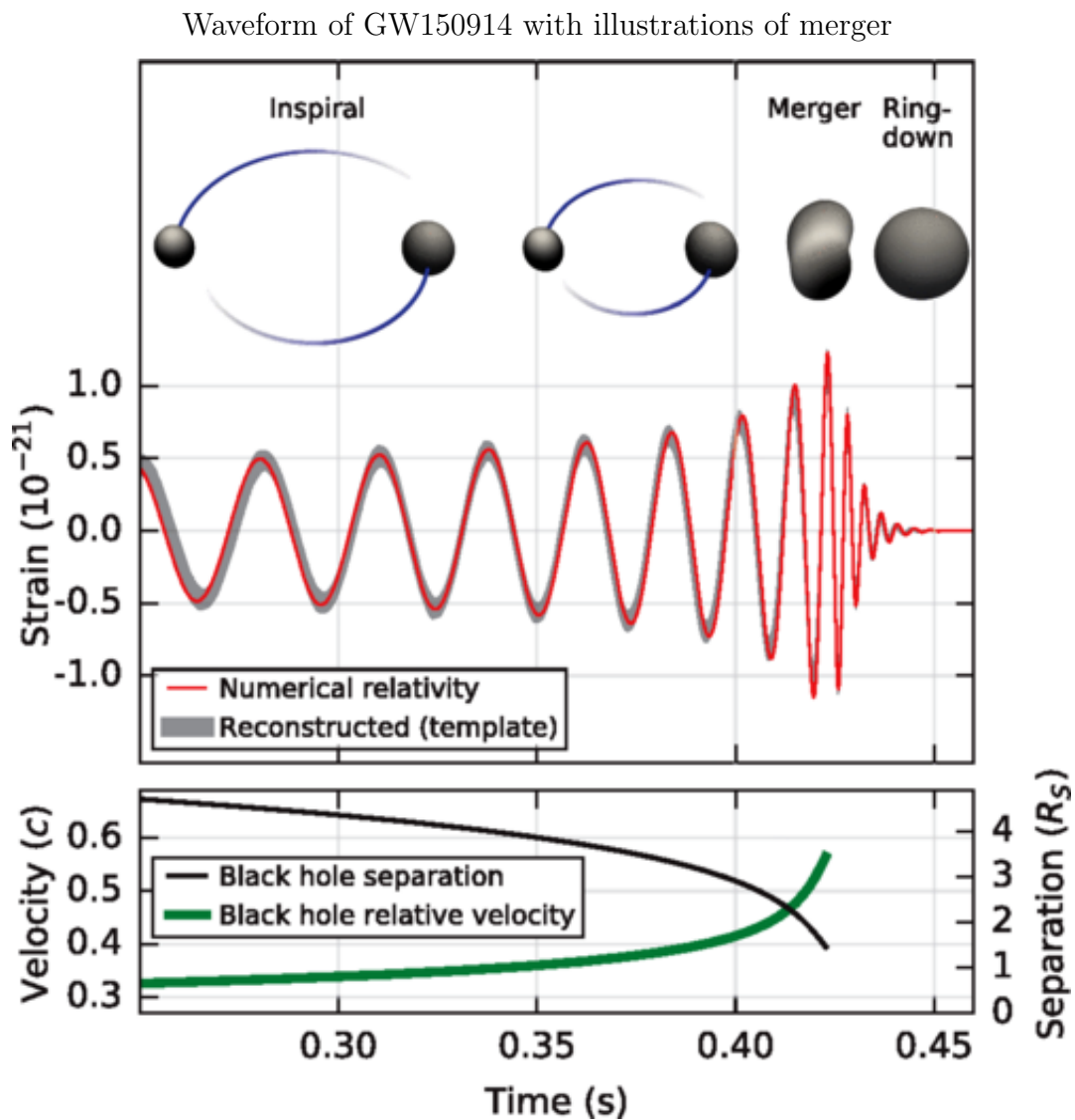


Figure 1.1: Estimated waveform of GW150914 projected onto numerical relativity models. Above, there are illustrations of the merger from numerical relativity models. Below, the plot shows the effective separation and relative velocity of the two black holes. This figure is reproduced from Ref. [6].

$v$  is the typical velocity of the objects. For the LIGO experiments, models of the gravitational waveforms are created by matching post-Newtonian solutions onto numerical relativity solutions.

The Laser Interferometer Space Antenna (LISA) [17] has recently been selected for development by the European Space Agency with an expected launch of 2034 [18]. The use of a space-based detector avoids seismic noise and uses much longer arms in the interferometer. LISA will be sensitive to a lower range of frequencies of gravitational waves. The LISA experiment will target some gravitational sources that are difficult to model using the numerical relativity and post-Newtonian theories, in particular extreme mass ratio inspirals (EMRIs).

EMRIs are systems where a compact body inspirals and merges with a supermassive black hole. For example, a ten solar mass black hole around a  $10^7$  supermassive black hole with a mass ratio of  $10^{-6}$ . The smaller body in these EMRI systems can orbit in a strong field regime over a large number of orbits; approximately  $10^5$  cycles over the final year of inspiral [19]. Thus neither numerical relativity nor post-Newtonian theory are naturally suited to constructing waveforms for LISA targets. This is, however, exactly the system in which the self force approach flourishes. Self force theory is a perturbation theory using the mass ratio of the two objects as a small parameter. The advantage is that self force can accurately model the highly relativistic regime whilst requiring less computational power than numerical relativity.

## 1.2 Wave propagation

In this thesis we consider how physical fundamental fields propagate on black hole spacetimes. We consider scalar, electromagnetic, gravitational and Dirac fields. Each of these fields has an associated wave equation which we solve for a variety of scenarios using a number of different methods. Results of such investigations highlight features of the black hole through their interactions.

By investigating the propagation of different physical fields we can probe different properties of the fields. High frequency perturbations to these fields can be modelled via an eikonal approximation. Under the eikonal approximation, perturbations to the field will propagate along geodesics.

Outside of the eikonal approximation the intrinsic properties, i.e. mass and spin, of the field have different impacts on the wave propagation. Hughes highlighted some key differences between electromagnetic EM and gravitational waves in Ref. [20]. One particularly interesting difference is that whilst EM waves interact strongly with matter, gravitational waves may pass through largely unaffected.

Many other physical systems obey wave equations. Unruh [21] found that the equations governing sound waves in a flowing fluid can be written in the same form as the equations governing the propagation of a scalar wave on a curved spacetime. The sound waves propagate on an effective spacetime created by the fluid. In this way one may observe features of wave propagation in curved spacetimes in a laboratory setting.

In the case of fermions, we have the additional differences associated with spin-half fields. One particularly interesting difference in fermionic and bosonic fields on black hole spacetimes is that bosonic fields experience superradiance whilst fermions do not. Superradiance is the effect that a bosonic field can be amplified by extracting rotational energy from the black hole.

We can consider the source of a physical field as some particle or body in spacetime. In this case the resulting field can scatter off the spacetime curvature on to the sourcing object and affect the body's motion. This highlights the link between wave propagation and our other main avenue of investigation in this thesis, self force.

### 1.3 Self force

The self force prescription addresses the two body problem by considering a compact object in orbit around a larger mass black hole. The mass ratio of the small mass to the larger mass acts as a small parameter for which we can use black hole perturbation theory. The full spacetime is described by a sum of the background spacetime of the large black hole and a perturbation due to the smaller object. Naively modelling the smaller object as a point mass, we can solve the linearised Einstein equations for the perturbed field. However the resulting field is singular at the position of the particle. We then require some physically well-motivated prescription to regularise the field. We henceforth describe the smaller object as a “particle” where it is understood that we can describe a small but extended body using some limiting procedure to describe its motion by a single worldline.

The self force is not an idea restricted to gravitational fields. A particle sourcing either a scalar or electromagnetic field will interact with its own field to experience some form of a self force. The self force in the electromagnetic context is often referred to as a radiation reaction. In fact the self force idea originated by considering an electrically charged particle and its interaction with its own field. It was shown by Abraham and Lorentz [22, 23] that an accelerating particle experiences a self force due to this interaction. All three cases describe a particle sourcing a field which is singular at the location of the particle and require similar methods to regularise these fields. We consider both the scalar and electromagnetic cases in this thesis as important crucibles to test methods and ideas to be used in the gravitational case.

The notion of a point mass was considered by Mino, Sasaki and Tanaka [24]. They used the method of Matched Asymptotic Expansions by exploiting the varying length scales associated with the two different masses to define near and far zones. In the near zone, they presumed the mass to be a Schwarzschild black hole whilst in the far zone, the spacetime is described by the perturbation of

the larger black hole spacetime by a point mass. Equations of motion resulting from the matched expansions method turn out to be equivalent to equations derived by pre-assuming a point mass at leading order in the mass ratio. The equations of motion for a point mass were derived by Mino, Sasaki and Tanaka [24] and independently by Quinn and Wald [25]. The set of equations were henceforth referred to as the MiSaTaQuWa equations. Gralla and Wald [26, 27] later extended this analysis to any suitably compact object, not just a Schwarzschild black hole.

The MiSaTaQuWa equations split the solution to the linearised Einstein equations into two parts, direct and tail fields. The direct part of the field is singular, yet has no effect on the self force. The self force is solely given by the derivative of the tail part of the field. This tail field can be formulated as an integral of the retarded Green function over the entire past history of the worldline of the particle excluding the point of coincidence. Calculating the self force by constructing the Green function is a relatively recent development perhaps due to the difficulty in constructing the global Green function. We consider this set-up in Chapter 4, where we calculate the scalar self force in Kerr spacetime.

Other calculations of the self force have relied on the mode-sum method developed by Barack and Ori [28]. The mode-sum method relies upon the fact that the perturbed field in the vicinity of the compact object diverges as  $1/r$ , where  $r$  is some appropriate measure of distance. This divergence can be decomposed into an infinite sum of angular modes. Each mode is finite and the divergence manifests itself in the failure of the sum to converge. To regularise we find an angular decomposition of the singular nature of the field and subtract this decomposition mode by mode such that the sum converges. The mode decomposition of the singular field gives rise to regularisation parameters. Once again we require a physically well-motivated way to construct the singular field.

Detweiler and Whiting [29, 30] proposed splitting the perturbed field into

regular radiative and singular symmetric parts. The Detweiler-Whiting regular field is a smooth vacuum solution to the linearised Einstein equations and its derivative fully accounts for the self force. The singular field encompasses all the singular nature of the full perturbed field, yet has no effect on the self force or the motion of the particle. For a full prescription of the Detweiler-Whiting split see Ref. [31]. The angular mode decomposition of the Detweiler-Whiting singular field now gives rise to the regularisation parameters for the mode-sum. We employ the mode sum method in chapter 5 to calculate the electromagnetic self force on a static particle.

Not all mode sum methods have depended on the Detweiler-Whiting decomposition. Other methods have simply investigated the singular nature of the perturbed field without physical justification.

A further interesting aspect of the self force is highlighted by the Detweiler-Whiting prescription. The particle experiencing the self force travels on a geodesic of the spacetime created by a sum of the background and regular fields. We can therefore take two alternative but equivalent viewpoints of the self force. One, a particle travels on an accelerated worldline in the background spacetime due to its self force or; two, a particle travels on a geodesic of the perturbed spacetime.

In formulating expressions for the self force we implicitly compare two trajectories; one on the perturbed spacetime and one on the background spacetime. A priori, there is no unique way to associate the two trajectories since they exist on different spacetimes. The ambiguity in relating trajectories is related to the freedom in the choice of coordinates for the perturbed spacetime. This freedom means that the self force and the metric perturbation are gauge dependent. To compare with other approaches to the two-body problem, we look for quantities which are invariant under gauge transformations which preserve the underlying symmetries of the system. Detweiler [32] was the first to suggest such a quantity, the red shift invariant. In chapter 6 we describe the construction of another such gauge invariant quantity: the spin

precession invariant for eccentric orbits on Schwarzschild spacetime.

We would like to be able to use the self force to construct waveforms which the community can observe using experiments such as LIGO and LISA. Due to the different mass scales self force is likely to be most useful for the planned LISA experiment although recent work [33] has shown that we may also obtain meaningful results for close to equal mass binaries which are targets for LIGO. Unfortunately we cannot yet accurately model waveforms using self force, since it requires a second-order in mass-ratio calculation for the dissipative part [34, 35, 36]. Recent progress on the second order formulation is given in Refs. [37, 38, 39, 40, 41]. Currently much of the focus of self force is in aiding calibration of unknown parameters in the effective one body (EOB) model. EOB combines the three main approaches to the two-body problem; numerical relativity, post-Newtonian and self force.

## 1.4 Thesis outline

We begin this thesis by investigating an analogue model of a black hole in Chapter 2. The analogy arises since one can show that a perturbation of a certain background flow obeys the same wave equation as a scalar field on a curved spacetime. The perturbation travels on an effective spacetime created by the background flow. We suggest a possible experiment by which a pulse disturbance maps out the lightcone of the effective spacetime. By investigating an analogue system it suggests the interesting possibility of observing black hole features in a laboratory setting.

We then consider, in Chapter 3, black hole spacetime solutions to Einstein's equations. Here we review the two black hole spacetimes investigated in this thesis, the Schwarzschild and Kerr black hole spacetimes. In this chapter we investigate the behaviour of a scalar field on these spacetimes. This highlights some of the interesting features of the spacetimes. We also compare the behaviour of the scalar field on the black hole spacetimes with the behaviour of

the perturbation on the analogue spacetime of the previous chapter.

In Chapter 4 we first investigate the self force. We calculate scalar field self force using the worldline integration method. The self force is calculated by integrating the Green function for the scalar wave equation over the entire past history of the worldline. The method relies upon techniques developed in the previous chapter to find solutions to the scalar wave equation.

Chapter 5 investigates electromagnetic self force. We consider a particle sourcing its own electromagnetic field held static at some fixed distance outside the black hole. The self force is calculated using the mode sum method with both analytical and numerical techniques.

We then consider gravitational self force in Chapter 6. A gauge independent quantity, the spin precession invariant is formulated. We compare numerically calculated values for the spin precession invariant with a post-Newtonian expansion.

In Chapter 7 we consider the Dirac field on Kerr spacetime. We consider the existence of quasi-bound states of fermions as described by the Dirac equation. Using a three-term recurrence relation and continued-fraction methods we find a spectrum of bound states for the Dirac field and their decay rates.

Finally in Chapter 8 we give some conclusions to the thesis. We discuss the work presented here and give some discussions on how it impacts on the wider scientific community.



# Chapter 2

## Wave propagation on analogue black holes

### 2.1 Introduction

This chapter investigates the intriguing possibility of observing general-relativistic effects in a lab setting. We examine a fluid-mechanical model which can be regarded as the analogue of a black hole. Analogue models for black holes were first proposed by Unruh [21]. In this 1981 paper it was shown that linearised equations governing sound waves in a fluid which is barotropic, inviscid and irrotational obey the same equations as a scalar field  $\psi$  in curved spacetime

$$\square\psi \equiv \frac{1}{\sqrt{|g|}}\partial_\mu(\sqrt{|g|}g^{\mu\nu}\partial_\nu\psi) = 0, \quad (2.1)$$

where  $g$  is the determinant of the metric  $g_{\mu\nu}$  and  $\square = \nabla_\mu\nabla^\mu$  is the d'Alembertian operator. In this case  $\psi$  is the velocity potential for the sound waves, whereas in general relativistic spacetimes  $\psi$  corresponds to the scalar field. In the fluid model the metric is no longer a spacetime metric satisfying the Einstein equations. It is instead an effective metric formed from the background fluid flow. A significant black-hole-like feature arises if one can arrange the speed of the background flow to exceed the wave propagation speed. This creates an

effective horizon, i.e., a surface beyond which no sound wave may propagate out.

Work has been ongoing, since 1981, to find experimental observations of general-relativistic processes. A first result was presented in Refs. [42, 43] where stimulated Hawking radiation was measured in an analogue system.

This chapter investigates a rotating model initially proposed by Visser [44]. This model, the draining bathtub vortex, is an imperfect analogue of the Kerr black hole. See Refs. [45, 46, 47] for further examples of analogue models. The draining bathtub vortex is described by a rotational flow which drains through a sink. We consider waves propagating on the surface of the draining bathtub. Schutzhold and Unruh [48] showed that surface waves also propagate according to Eq. (2.1). We present the derivation of the effective spacetime in Sec. 2.3.

Recently experimental results for the draining bathtub vortex were presented in Ref. [49]. Torres *et al.* report an observation of surface waves experiencing superradiance, the process by which incoming waves are amplified by extracting rotational energy from the system.

Here we propose another possible experiment motivated by the eikonal approximation, which we present in Sec. 2.2. The eikonal approximation was investigated for Schwarzschild spacetime in Ref. [50]. The eikonal approximation highlights the relation between a congruence of null geodesics and a propagating wavefront. A null geodesic congruence is a family of integral curves of the vector field  $u^\mu$ , where  $u^\mu$  are tangent vectors to null geodesics. If we consider a null geodesic congruence emanating from a single point in spacetime the congruence maps out the “lightcone” of that point. Taking constant-time slices of the lightcone allows us to construct an approximation to the solution of the wave equation (2.1), henceforth referred to as the *eikonal-wavefront*.

We investigate a pulse disturbance of the background flow, constructing a full numerical solution of the wave equation (2.1). We refer to this full numerical solution of the wave equation as the *full-wavefront* to differentiate

from the eikonal-wavefront which is an approximation. We show that the full-wavefront follows approximately the same path as the eikonal-wavefront. The resulting full-wavefront therefore essentially maps out the lightcone of the effective spacetime. As such an experimentalist may investigate the lightcone of their effective spacetime by creating a pulse disturbance and tracking the resulting wave. As the eikonal approximation is valid for any spacetime we conclude that any key insights in such an analogue system may carry over to spacetime solutions of the Einstein equations.

## 2.2 Eikonal approximation

Apart from very simple situations, the wave equation (2.1) does not have analytic solutions. Here we present an analytic approximation called the eikonal approximation which highlights the relation between individual light rays and wave propagation. We present the eikonal approximation here for the scalar wave equation (see [51] for eikonal method for Maxwell's equations).

Let us begin with the homogeneous scalar wave equation (2.1) in a general Lorentzian  $d$ -dimensional spacetime. The eikonal approximation considers a perturbation whose frequency varies over a much shorter lengthscale than the typical length scale of the curvature of the spacetime. We assume  $\psi$  takes form [51]

$$\psi(x) = A(x) \exp [i\omega\Theta(x)] \quad (2.2)$$

with  $\omega \gg \mathcal{R}^{-1}$  where  $\mathcal{R}$  is a typical lengthscale of the spacetime curvature.  $A(x)$  and  $\Theta(x)$  are the amplitude and phase functions, which depend on spacetime positions  $x$ . Here  $\omega$  is an order counting parameter for the frequency. We insert this ansatz into the wave equation (2.1) and expand in orders of  $1/\omega$ .

To leading order in  $1/\omega$  both derivatives act on the exponential so that

$$-g^{\mu\nu} A\omega^2 \Theta_{,\mu} \Theta_{,\nu} \exp [i\omega\Theta] = 0, \quad (2.3)$$

which reduces to

$$g^{\mu\nu}\Theta_{,\mu}\Theta_{,\nu} = 0, \quad (2.4)$$

which implies  $\Theta_{,\mu} = k_\mu$  is a null vector. We construct relations for covariant derivatives using  $k_{\mu,\nu} = k_{\nu,\mu}$  which implies  $k_{\mu;\nu} = k_{\nu;\mu}$  on replacing partial derivatives with covariant derivatives. Taking the covariant derivative of Eq. (2.4) and using the identity  $k_{\mu;\nu} = k_{\nu;\mu}$  we find  $\Theta_{,\mu} = k_\mu$  satisfies

$$k^\nu k^\mu_{;\nu} = 0, \quad (2.5)$$

which are the geodesic equations. We conclude that the eikonal-wavefront follows a null geodesic congruence. The full-wavefront should follow the eikonal wavefront to first order in  $1/\omega$ .

At second order in  $1/\omega$  only one of the derivatives acts on the exponential in Eq. (2.1), giving an equation for  $A$

$$\begin{aligned} \frac{i\omega}{\sqrt{|g|}}\partial_\mu(\sqrt{|g|}g^{\mu\nu}A\Theta_{,\nu})\exp[i\omega\Theta] + i\omega g^{\mu\nu}A_{,\nu}\Theta_{,\mu}\exp[i\omega\Theta] &= 0, \\ \frac{1}{\sqrt{|g|}}\partial_\mu(\sqrt{|g|}g^{\mu\nu}\Theta_{,\nu})A + 2g^{\mu\nu}A_{,\mu}\Theta_{,\nu} &= 0, \end{aligned} \quad (2.6)$$

which reduces to

$$k^\mu A_{,\mu} = -\frac{1}{2}k^\mu_{;\mu}A \quad (2.7)$$

since

$$\nabla_\mu V^\mu = \frac{1}{\sqrt{|g|}}\partial_\mu(\sqrt{|g|}V^\mu), \quad (2.8)$$

for any vector field  $V^\nu$ .

We observe that  $k^\mu_{;\mu} = \vartheta$  is the expansion scalar [52]. The transport equation for  $A$ , Eq. (2.7), may be written as

$$k^\mu A_{,\mu} = -\frac{1}{2}\vartheta A. \quad (2.9)$$

The expansion scalar  $\vartheta$  is governed by the Raychaudhuri equation which arises by considering the behaviour of a deviation vector in a null geodesic congruence

[52]

$$\frac{d\vartheta}{d\lambda} = -\frac{1}{d-2}\vartheta - \sigma_{\mu\nu}\sigma^{\mu\nu} + \omega_{\mu\nu}\omega^{\mu\nu} - R_{\mu\nu}k^\mu k^\nu \quad (2.10)$$

where  $\sigma_{\mu\nu}$  is the shear tensor and  $\omega_{\mu\nu}$  is the vorticity tensor. Here  $\lambda$  is an affine parameter which parametrises the null geodesics. We can therefore write  $k^\mu A_{,\mu} = \frac{dA}{d\lambda}$ .

### 2.2.1 Van Vleck determinant

The expansion scalar  $\vartheta$  has some drawbacks. In considering a congruence emanating from a single point the expansion scalar diverges in the limit  $\lambda \rightarrow 0$ . Instead we may consider the van Vleck determinant  $\Delta$  which measures the density of geodesics as a ratio between an expected flat space result and the actual density in the curved spacetime [53]. From Visser [53] we have an equation for the van Vleck determinant

$$\frac{d\Delta}{d\lambda} = \left( \frac{d-2}{\lambda} - \vartheta \right) \Delta. \quad (2.11)$$

Comparing Eq. (2.11) with Eq. (2.9) we see that the eikonal amplitude is related to the square root of the van Vleck determinant by

$$A = \frac{\sqrt{\Delta}}{\lambda^{\frac{d-2}{2}}}. \quad (2.12)$$

In conclusion, on analysing the scalar wave equation (2.1) we may construct a null congruence of geodesics to approximate the propagation of a wavefront. The amplitude of the wavefront is approximated by the square root of the van Vleck determinant through equation (2.11). This can be compared against full numerical solutions to the wave equation.

## 2.3 Draining bathtub model

The draining bathtub vortex initially proposed by Visser [44] considered sound waves in a fluid. Schutzhold and Unruh [48] noted the difficulties in creating

such an experimental set up due to the speed of flow required. Instead they proposed investigating surface waves which obey the same equation (2.1). In the experiment of Ref. [49] this surface wave model was used. Here we review the steps required to form the effective metric.

The draining bathtub is a tank of water with a central sink through which water drains. There is a background flow at a constant height  $h_b$  with waves travelling on the surface described by perturbations to this background flow. In the model the background flow is described by fluid velocity

$$\mathbf{v}_b = -\frac{D\hat{\mathbf{r}}}{r} + \frac{C\hat{\phi}}{r}, \quad (2.13)$$

where  $D$  and  $C$  are constants corresponding to the draining rate and the circulation respectively. This is given in cylindrical coordinates  $\{r, \phi, z\}$  which makes it clear that there is no vertical motion in the background flow. The flow is both irrotational  $\nabla \times \mathbf{v}_b = 0$  (except at the sink) and divergence free  $\nabla \cdot \mathbf{v}_b = 0$ . The effective spacetime is constructed by considering perturbations  $\delta\mathbf{v}$  to this flow such that the total flow takes the form  $\mathbf{v} = \mathbf{v}_b + \delta\mathbf{v}$ .

We assume that the total flow is also irrotational and divergence free and make the further assumption that the fluid is inviscid. The flow is governed by the Euler equation

$$\partial_t \mathbf{v} + (\mathbf{v} \cdot \nabla) \mathbf{v} = -\frac{\nabla p}{\rho} + \mathbf{g} + \frac{\mathbf{F}}{\rho} \quad (2.14)$$

where  $p = g(h - z)$  is the fluid pressure at height  $z$  with  $h$  the height of the surface of the fluid and  $\mathbf{g} = -g\hat{\mathbf{z}}$  is the gravitational acceleration. The force  $\mathbf{F} = -\rho\nabla f$  is a horizontal force ( $\partial_z f = 0$ ) driving the flow as described in Ref. [48]. Since the flow is irrotational we can form the velocity field as the gradient of a potential  $\psi$  via  $\mathbf{v} = \nabla\psi$ . The Euler equation (2.14) reduces to the Bernoulli equation

$$\partial_t \psi + \frac{1}{2}(\nabla\psi)^2 = -\frac{p}{\rho} - gz - f \quad (2.15)$$

CHAPTER 2. WAVE PROPAGATION ON ANALOGUE BLACK HOLES

---

where we have used the identity  $\nabla(\mathbf{v}^2)/2 = (\mathbf{v} \cdot \nabla)\mathbf{v}$ . The vertical velocity of the fluid is zero at the base of the tank ( $z = 0$ ) and equal to the change in height at the surface ( $z = h$ ) giving us two boundary conditions

$$\begin{aligned} v_z(z = 0) &= 0, \\ v_z(z = h) &= \partial_t h + (\mathbf{v} \cdot \nabla)h. \end{aligned} \quad (2.16)$$

Let us now consider perturbations to the background flow (2.13)  $\mathbf{v} = \mathbf{v}_b + \delta\mathbf{v}$ . Remember from Eq. (2.13) that the background flow is horizontal with constant height  $z = h_b$ . The Bernoulli equation for the background flow is

$$\frac{1}{2}(\mathbf{v}_b)^2 = \frac{1}{2}(\nabla\psi_b)^2 = -\frac{p_b}{\rho} - gz - f, \quad (2.17)$$

with  $p_b = g\rho(h_b - z)$ . The perturbations correspond to small vertical perturbations of the height, so that  $h = h_b + \delta h$ .

The Bernoulli equation for the perturbed potential  $\delta\psi$  is

$$\partial_t(\delta\psi) + (\mathbf{v}_b \cdot \nabla)\delta\psi = -\frac{\delta p}{\rho} = -g\delta h \quad (2.18)$$

with  $\delta p = g\rho\delta h$ . The vertical component of the perturbed velocity  $\delta v_z$  at the background height  $h_b$  is now given by the change in  $\delta h$  from Eq. (2.16)

$$\delta v_z = \partial_t(\delta h) + (\mathbf{v}_b \cdot \nabla)\delta h. \quad (2.19)$$

The perturbed potential is now decomposed into a Taylor series in  $z$

$$\delta\psi = \sum_{n=0}^{\infty} \frac{z^n}{n!} \delta\psi_n(r, \phi). \quad (2.20)$$

We will show by assuming that the wavelength  $\Lambda$  is much longer than the depth  $h_b$  that higher order terms in (2.20) are suppressed. We emphasise that this approximation is valid for long wavelength perturbations.

Considering the vertical velocity as the  $z$  derivative of Eq. (2.20)

$$\delta v_z = \partial_z(\delta\psi) = \delta\psi_1 + z\delta\psi_2 + \dots \quad (2.21)$$

the boundary condition (2.16) that the vertical velocity is zero at the base of the tank  $z = 0$  gives  $\delta\psi_1 = 0$ . Since the fluid is divergence free the equation  $\nabla^2\delta\psi = 0$  gives

$$\nabla_{\parallel}^2\delta\psi_n + \delta\psi_{n+2} = 0 \quad (2.22)$$

on matching powers of  $z$ , where

$$\nabla_{\parallel}^2 = \frac{1}{r} \frac{\partial}{\partial r} \left( r \frac{\partial}{\partial r} \right) + \frac{1}{r^2} \frac{\partial^2}{\partial \phi^2} \quad (2.23)$$

is the usual  $\nabla^2$  operator without terms containing derivatives with respect to  $z$ . Equation (2.22) shows that subsequent terms in the Taylor expansion are suppressed by  $O(h_b/\Lambda)$  as

$$z^{n+2}\delta\psi_{n+2} \sim z^{n+2}\nabla_{\parallel}^2\delta\psi_n \sim \frac{h_b^2}{\Lambda^2} z^n \delta\psi_n \quad (2.24)$$

since  $\nabla_{\parallel}^2 = O(1/\Lambda^2)$  and  $z = O(h_b)$ . We use the long wavelength assumption to consider the terms in Eq. (2.22) of leading order in  $h_b/\Lambda$ . The vertical velocity at the surface is given by combining the leading order terms in Eqs. (2.21-2.22) to give

$$\delta v_z(h_b) = h_b \delta\psi_2 = -h_b \nabla_{\parallel}^2 \delta\psi_0, \quad (2.25)$$

which with Eq. (2.19) gives

$$\partial_t(\delta h) + (\mathbf{v}_b \cdot \nabla)\delta h = -h_b \nabla_{\parallel}^2(\delta\psi_0). \quad (2.26)$$

We now obtain a wave equation by taking  $[\partial_t + (\mathbf{v}_b \cdot \nabla)]$  of the Bernoulli equation (2.18) and using Eq. (2.26) to replace the  $\delta h$

$$[\partial_t + (\mathbf{v}_b \cdot \nabla)]^2 \delta\psi_0 - g h_b \nabla_{\parallel}^2 \delta\psi_0 = 0, \quad (2.27)$$

where we can identify the wave speed as  $c_s = \sqrt{g h_b}$ .

We can see that Eq. (2.27) is a Klein-Gordon like equation in the same form as Eq. (2.1) (with  $\delta\psi_0 = \psi$  here). Thus we can find the components of the effective metric given by the line element

$$ds^2 = \left( -c_s^2 + \frac{C^2 + D^2}{r^2} \right) dt^2 + 2 \frac{D}{r} dr dt + dr^2 - 2C d\phi dt + r^2 d\phi^2, \quad (2.28)$$

where we have used Eq. (2.13) for  $\mathbf{v}_b$ . There exists an effective horizon at  $r = D/c_s$  where the radial background flow is faster than the wave speed such that all waves purely ingoing. There is also an effective ergosphere at  $D/c_s < r < \sqrt{C^2 + D^2}/c_s$  where all perturbations are corotating with the vortex. For the remainder of this chapter we set  $c_s = 1$ .

## 2.4 Null geodesic congruence

### 2.4.1 Null geodesic equations

We construct our null congruence by solving the null geodesic equations with initial conditions corresponding to starting at a single point and varying the initial angle of trajectories. The geodesic equations can be found from the metric given by the line element (2.28). We form a Lagrangian as  $\mathcal{L} = \frac{1}{2}g_{\mu\nu}u^\mu u^\nu$  with  $u^\mu = \dot{x}^\mu$  where the overdot corresponds to differentiation with respect to an affine parameter  $\lambda$  which parametrises the geodesic. The Euler-Lagrange equations now give the geodesic equations. Since the metric (2.28) is independent of  $t$  and  $\phi$  the temporal and angular geodesic equations give rise to constants of motion, energy  $E$  and angular momentum  $L$ ,

$$\begin{aligned} E = -u_t &= \dot{t} \left( 1 - \frac{C^2}{r^2} - \frac{D^2}{r^2} \right) + C\dot{\phi} - \frac{D\dot{r}}{r}, \\ L = u_\phi &= -C\dot{t} + r^2\dot{\phi}. \end{aligned} \quad (2.29)$$

We can rearrange to find,

$$\begin{aligned} \dot{t} &= \frac{r(D\dot{r} + Er) - CL}{r^2 - D^2}, \\ \dot{\phi} &= \frac{Cr(D\dot{r} + Er) - C^2L + L(r^2 - D^2)}{r^2(r^2 - D^2)}. \end{aligned} \quad (2.30)$$

Then, using the null condition  $\mathcal{L} = \frac{1}{2}g_{\mu\nu}\dot{x}^\mu\dot{x}^\nu = 0$ , we find an equation governing  $\dot{r}$ ,

$$\dot{r}^2 = \left( \frac{C^2}{r^2} + \frac{D^2}{r^2} - 1 \right) \frac{L^2}{r^2} + E \left( E - \frac{2CL}{r^2} \right). \quad (2.31)$$

We choose to set  $E = 1$  since any rescaling of  $E$  corresponds to a rescaling of  $\lambda$ . The angular momentum  $L$  may take positive or negative values. Null geodesics may pass by the vortex, fall into the sink or, for certain critical values of  $L$ , approach circular orbits. These critical values can be found from the conditions  $\dot{r} = 0$  and  $\ddot{r} = 0$  giving

$$L = L_c^\pm = 2 \left( -C \pm \sqrt{C^2 + D^2} \right), \quad (2.32)$$

which correspond to circular orbits at

$$r = r_c^\pm = \sqrt{2} \sqrt{C^2 + D^2 \pm C \sqrt{C^2 + D^2}}. \quad (2.33)$$

For  $C > 0$  the counterrotating circular orbit is at a larger radius than the corotating orbit.

### 2.4.2 Van Vleck determinant

The Raychaudhuri equation (2.10) for null geodesics in three dimensions ( $d = 3$ ) reduces to

$$\frac{d\vartheta}{d\lambda} = -\vartheta^2 - R_{\mu\nu} u^\mu u^\nu, \quad (2.34)$$

since we only have one degree of freedom and so the shear and vorticity are zero. The expansion scalar is divergent in the limit  $\lambda \rightarrow 0$ . This is because  $\vartheta$  approaches its flat space result  $\vartheta = \frac{1}{\lambda}$  (consider (2.34) with  $R_{\mu\nu} = 0$ ). For computational purposes we introduce the quantity  $\xi = \vartheta\lambda$  with  $\xi \rightarrow 1$  as  $\lambda \rightarrow 0$ . The transport equation for the van Vleck determinant (2.11) is then given by

$$\dot{\Delta} = (1 - \xi) \frac{\Delta}{\lambda}, \quad (2.35)$$

which approximates the amplitude of the wave according to the 3-dimensional version of Eq. (2.12)

$$A = \frac{\sqrt{\Delta}}{\lambda^{\frac{1}{2}}}. \quad (2.36)$$

We refer to this approximate wave amplitude as the eikonal-amplitude.

### 2.4.3 Eikonal-wavefront

We define the eikonal-wavefront to be the analytic approximate solution to the wave equation (2.1) according to the eikonal approximation. To construct our eikonal-wavefront we use the *Mathematica* `NDSolve` function to evolve the geodesic equations (2.30-2.31) and transport equations for the van Vleck determinant (2.35). As initial conditions we choose  $r(0) = r_0$  and  $\phi(0) = \phi_0$  whilst the van Vleck determinant is  $\Delta(0) = 1$ . We evolve the equations for a set of different  $L$  values to give us a range of geodesics. To construct the geodesic congruence at each  $t$  value we invert our solution for  $t(\lambda)$  and can then interpolate our set of geodesics to give the eikonal-wavefront. The eikonal-wavefront therefore maps out the lightcone of the effective spacetime (2.28). By comparing the eikonal-wavefront with a full solution to the wave equation (2.1) we investigate, in Sec. 2.6, the extent to which a real perturbation may map out the lightcone.

## 2.5 Wave propagation

We also analyse a full-wavefront by inputting the effective metric (2.28) into the wave equation (2.1). The resulting equations are  $2 + 1$  in space and time and we solve these using mode decomposition.

### 2.5.1 Mode decomposition

We can reduce the scalar wave equation (2.1) to a set of  $(1 + 1)D$  equations by decomposing  $\psi$  into angular modes using the ansatz

$$\psi(t, r, \phi) = \sum_{m=-\infty}^{\infty} \psi_m(t, r) \frac{e^{im\phi}}{\sqrt{r}}. \quad (2.37)$$

Since  $\psi$  is a real-valued field, negative  $m$ -modes are simply given by the complex conjugate  $\psi_{-m} = \psi_m^*$ . We therefore only need to solve for positive  $m$

values. If we input the decomposition (2.37) into the wave equation (2.1) using the metric (2.28) we obtain a set of 1 + 1 partial differential equations

$$\begin{aligned}
 0 = & -\frac{\partial^2 \psi_m}{\partial t^2} + \frac{2D}{r} \frac{\partial^2 \psi_m}{\partial t \partial r} + \left(1 - \frac{D^2}{r^2}\right) \frac{\partial^2 \psi_m}{\partial r^2} \\
 & - \frac{(D + 2imC)}{r^2} \frac{\partial \psi_m}{\partial t} + \frac{2D(D + imC)}{r^3} \frac{\partial \psi_m}{\partial r} \\
 & - \left( \frac{(m^2 - 1/4)}{r^2} + \frac{-m^2 C^2 + 3imCD + 5D^2/4}{r^4} \right) \psi_m.
 \end{aligned} \tag{2.38}$$

### Initial data

The eikonal-wavefront starts from a single initial point. This is not practical as numerical initial conditions for the field  $\psi$ . Instead we use a narrow Gaussian pulse centred at the same initial point as the geodesics. The Gaussian is symmetric around a central point with its peak at this central point. With a centre point given in Cartesian coordinates by  $(x_0, y_0) = (r_0 \cos \phi_0, r_0 \sin \phi_0)$  and Gaussian width  $\sigma$ , the initial Gaussian pulse takes the form

$$\psi(0, r, \phi) = \frac{1}{2\pi\sigma^2} \exp\left(-\frac{(r \cos \phi - r_0 \cos \phi_0)^2 + (r \sin \phi - r_0 \sin \phi_0)^2}{2\sigma^2}\right), \tag{2.39}$$

and  $\partial_t \psi(0, r, \phi) = 0$ . To decompose the initial data into  $m$ -modes we use,

$$\psi_m(0, r) = \frac{1}{2\pi} \int_0^{2\pi} e^{-im\phi} \psi(0, r, \phi) d\phi. \tag{2.40}$$

The narrower the Gaussian, the closer the initial conditions will match the eikonal-wavefront. However the narrower the Gaussian the greater the number of  $m$ -modes required for adequate resolution of the wavefront. There is therefore a trade off between numerical speed and accurate mapping to the null congruence.

### Method of lines and boundary conditions

To evolve Eq. (2.38) for  $\psi_m$  we used the *method of lines* [54]. The method of lines involves creating a uniformly spaced grid with spacing  $\bar{h}$  on  $r$  and setting

up a set of functions at each  $r$  coordinate  $\psi_{m,i}(t) = \psi_m(r_i, t)$ . Spatial derivatives were approximated using fourth-order finite difference derivatives [55]. We make use of *Mathematica's* function `NDSolve`FiniteDifferenceDerivative` to approximate spatial derivatives as

$$\begin{aligned}\psi'_{m,i}(t) &\sim \frac{1}{\bar{h}} \left[ \frac{1}{12}\psi_{m,i-2}(t) - \frac{2}{3}\psi_{m,i-1}(t) + \frac{2}{3}\psi_{m,i+1}(t) - \frac{1}{12}\psi_{m,i+2}(t) \right], \\ \psi''_{m,i}(t) &\sim \frac{1}{\bar{h}^2} \left[ -\frac{1}{12}\psi_{m,i-2}(t) + \frac{4}{3}\psi_{m,i-1}(t) \right. \\ &\quad \left. - \frac{5}{2}\psi_{m,i}(t) + \frac{4}{3}\psi_{m,i+1}(t) - \frac{1}{12}\psi_{m,i+2}(t) \right],\end{aligned}\quad (2.41)$$

where the prime  $\psi'_{m,i}(t)$  denotes a finite-difference approximation to the spatial derivative of  $\psi_m(r, t)$  at  $r_i$ . The expressions (2.41) are derived by Taylor expanding functions such as  $\psi_m(r + \bar{h}, t)$  around  $r$  up to fourth order in  $\bar{h}$ . This leaves an error of  $O(\bar{h}^5)$  in approximating derivatives by Eqs. (2.41). Equation (2.38) is now a set of coupled ordinary differential equations for each  $\psi_{m,i}(t)$ . These are then evolved numerically using *Mathematica's* `NDSolve` function for  $\psi_{m,i}(t)$ .

The grid was chosen large enough such that at  $r_{max}$  the propagating wave from the initial pulse does not come in contact with the boundary during the simulation, thus we can set  $\psi_m(r_{max}) = 0$ . We set the inner boundary inside the horizon at  $r = 0.8D$ , choosing free boundary conditions using one sided finite differencing in a similar way to Eqs. (2.41). At this point we find that, since all null geodesics are ingoing within the horizon, free perturbations naturally leave the domain without causing numerical disturbances due to the singularity at  $r = 0$ .

### Mode sum reconstruction

Formally the mode sum (2.37) is an infinite sum. In practice higher  $m$ -modes contribute to physical angular features on a scale proportional to  $2\pi/m$ . Thus we can truncate the sum at some sufficiently high cut-off  $m_{cut}$ .

We must use a smoothing mechanism to avoid any spurious features on small angular scales using a large- $m$  smoothing factor

$$F(m) = \frac{1}{2} \left( 1 - \tanh \left( \frac{m - m_{\text{cut}}}{2} \right) \right), \quad (2.42)$$

and take the finite sum

$$\psi(t, r) = \text{Re} \left[ \sum_{m=0}^{m_{\text{cut}}+N} a_m F(m) \frac{\psi_m(t, r)}{\sqrt{r}} e^{im\phi} \right], \quad a_m \equiv \begin{cases} 1, & m = 0, \\ 2, & m \neq 0. \end{cases} \quad (2.43)$$

We have adapted the mode sum of Eq. (2.37) to include only positive  $m$ -modes by summing over twice the  $m > 0$  modes and taking the real part. With the choice of initial data above (2.39) we use  $m_{\text{cut}} = 50$  and  $N = 5$ .

## 2.6 Results

In this section we now investigate the behaviour of both the eikonal-wavefront (given by constant time slices of a congruence of null geodesics) and the full-wavefront (the full numerical solution of the wave equation). We investigate three different scenarios: non-rotating ( $C = 0$ ) in Sec. 2.6.1, slowly rotating ( $C = 0.5$ ) in Sec. 2.6.2 and rapidly rotating ( $C = 2$ ) in Sec. 2.6.3. In all cases we set  $D = 1$  since only the relation of  $D$  with the Gaussian width  $\sigma$  or the circulation  $C$  affects the observed features. Essentially  $D$  sets a length scale on the draining bathtub.

By investigating these different scenarios, we build up our understanding of the associated effects of the effective spacetime on the wavefront propagation. The non-rotating case allows us to isolate features not associated with rotation. Examining two rotating cases with different  $C$  values allows us to investigate the effects of increasing rotation.

The eikonal-wavefront gives constant time slices of the lightcone. By investigating the eikonal-wavefront and full-wavefront simultaneously we observe to what extent a pulse disturbance maps out the lightcone of the effective spacetime described by the metric (2.28).

### 2.6.1 Non-rotating vortex

We begin our analysis by looking at the non-rotating  $C = 0$  case with  $D = 1$ . Fig. 2.1 shows the eikonal-wavefront formed from a congruence of geodesics emanating from the point  $x_0 = -10, y_0 = 0, (r_0 = 10, \phi_0 = \pi)$ . The effective horizon is at  $r_h = 1$ , and the null circular orbits are at  $r_c^\pm = \sqrt{2}$  (see Eq. (2.33)). The depth of colour corresponds to the value of the square root of the van Vleck determinant  $\Delta^{\frac{1}{2}}$ . We have plotted only the value of  $\Delta^{\frac{1}{2}}$  rather than the full eikonal-amplitude, related by (2.36), to emphasise effects due to the curvature of the effective spacetime over and above the usual damping one would expect on a flat spacetime. The lines show the eikonal-wavefront at successive values of  $t = \{3, 7, 12, 18\}$ . We observe a number of interesting features.

As the set of geodesics approaches the vortex, the centre of the eikonal-wavefront is accelerated and dragged in towards the centre of the vortex. Following this, the eikonal-wavefront is dragged around the vortex and crosses over itself opposite the initial pulse. This crossing occurs where two geodesics having  $L$  values of opposite sign meet, having travelled around either side of the vortex. We expect this crossing to correspond to a doubling of the amplitude in the full-wavefront due to a superposition of the waves from opposite sides of the vortex. There is also a reduction in the magnitude of the van Vleck determinant as the eikonal-wavefront is wrapped and stretched around the vortex which will correspond to a damping of the wavefront.

Fig. 2.2 shows the full-wavefront simulation with initial conditions corresponding to a Gaussian of width  $\sigma = 1$  at  $x_0 = -10, y_0 = 0$ , the same initial point as the geodesics. We can see the wavefront contains many of the same features as the geodesics. The wavefront propagates symmetrically on either side of the vortex before being dragged around the vortex and meeting on the opposite side. There is a doubling in the height of the wavefront where the wavefront meets itself having travelled around each side of the vortex.

We plot in Fig. 2.3 the full-wavefront evolution and the eikonal-wavefront together. It can be seen that they follow the same paths around the vortex

Eikonal-wavefront on non-rotating draining bathtub with draining rate

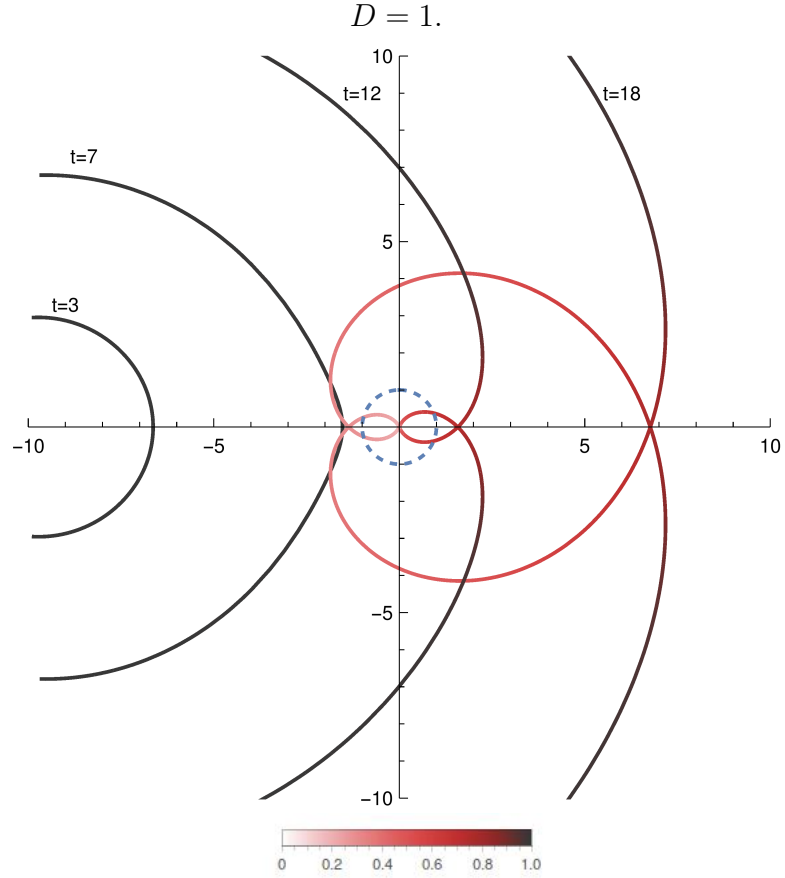


Figure 2.1: Eikonal-wavefront formed from a congruence of null geodesics emanating from  $(-10, 0)$  at successive  $t$  values  $t = \{3, 7, 12, 18\}$  on the draining bathtub with  $D = 1$ ,  $C = 0$ . The van Vleck determinant is given by the depth of colour along the eikonal wavefront. The effective horizon is shown by a dashed line at  $r_h = 1$ . The eikonal-wavefront initially propagates as in flat spacetime before being dragged in towards the vortex. The eikonal-wavefront then wraps around the vortex. The van Vleck determinant decreases as it wraps around showing a decrease in the density of geodesics which we expect to correspond to a decrease in wave-height.

Full-wavefront evolution on non-rotating bathtub with draining rate  $D = 1$ .

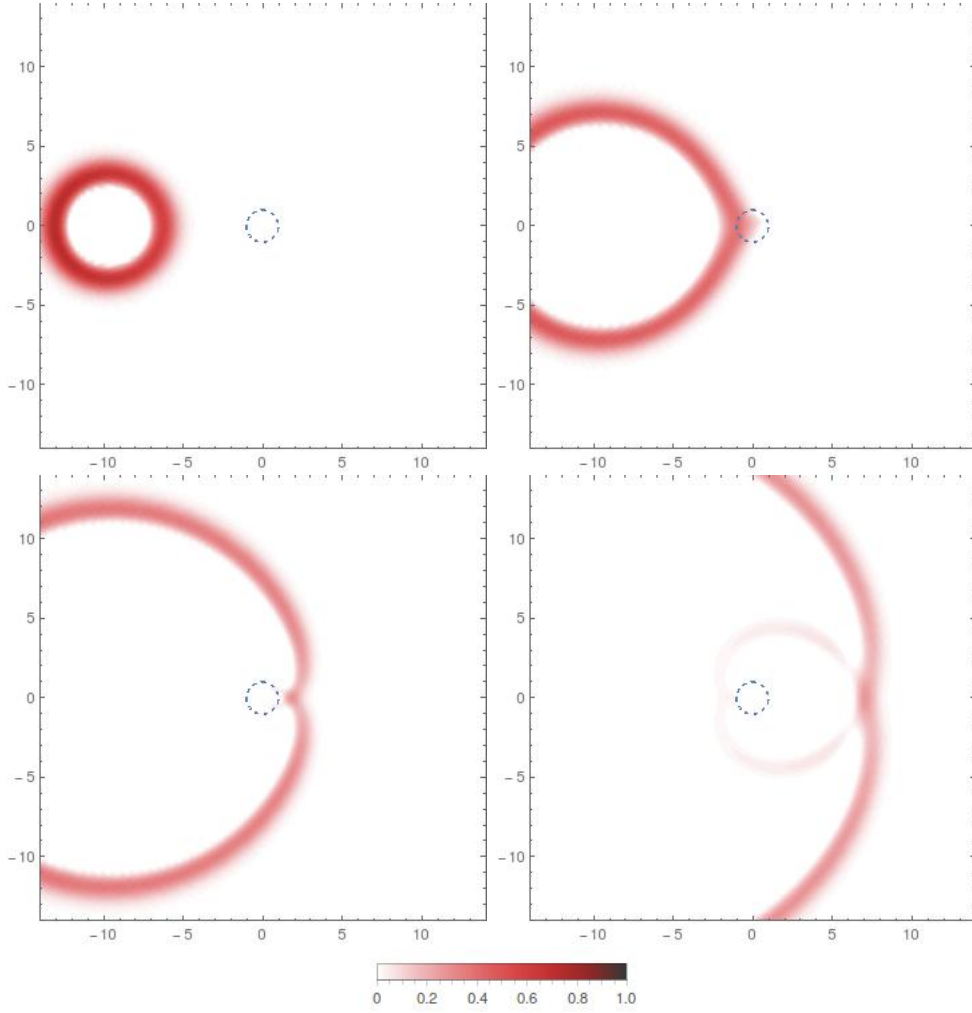


Figure 2.2: The evolution of a full-wavefront from a Gaussian of width  $\sigma = 1$  at  $(-10, 0)$  at successive  $t$  values  $t = \{3, 7, 12, 18\}$ . Initially the wave propagates as a circle as in flat space, before the leading front is dragged in towards the vortex. Once the wave has crossed the vortex it is now dragged back towards and wraps around the vortex. At the point where the waves cross there is a doubling of the wave amplitude.

Full-wavefront and eikonal-wavefront on non-rotating bathtub with draining rate  $D = 1$ .

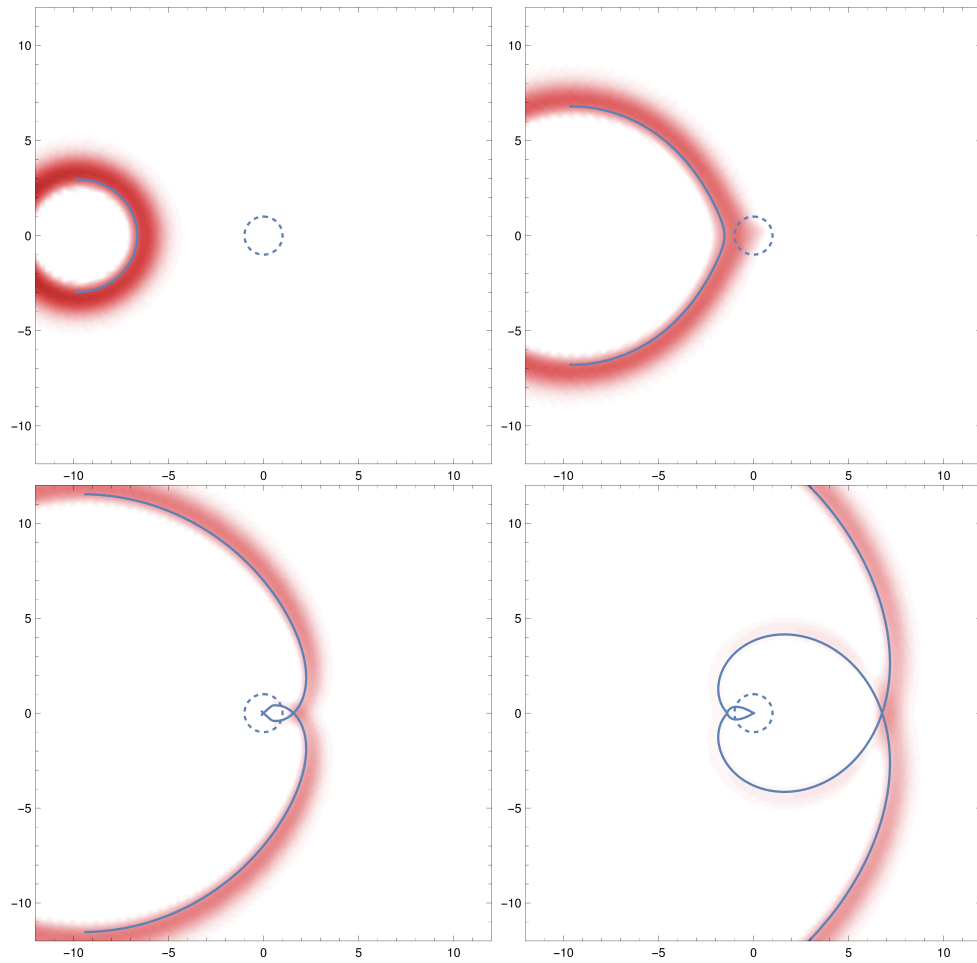


Figure 2.3: The evolution of the full wavefront (red shading) from a Gaussian of width  $\sigma = 1$  and the eikonal-wavefront (blue solid line) from initial point  $(-10, 0)$  at successive  $t$  values  $t = \{3, 7, 12, 18\}$ . The geodesics and wavefront follow closely related paths in the effective spacetime.

to a good approximation. The finite size of the initial Gaussian means that the full-wavefront leads the eikonal-wavefront (which emanates from a single point). This close conformity suggests that a real lab experiment could be envisaged to map out the light-cone of the effective spacetime.

### 2.6.2 Slowly rotating vortex

We now consider the rotating case. Initially we look at relatively slow rotation with  $C = 0.5$  and keep  $D = 1$ . Fig. 2.4 shows the eikonal-wavefront: a congruence of geodesics emanating from the point  $x_0 = -10, y_0 = 0$ . The effective horizon is at  $r_h = 1$ , and the ergosphere is at  $r_e = 1.11803$ . The null circular orbits are at  $r_c^+ = 1.17557$  and  $r_c^- = 1.90211$  (see Eq. (2.33)).

We observe many of the same features, as in Fig. 2.1, such as wrapping of the eikonal-wavefront around the vortex and crossing of geodesics. In this case the corotating part of the eikonal-wavefront is dragged much further around the vortex. This is because corotating geodesics (below the vortex) pass much closer to the vortex and are accelerated by the rotation whilst counterrotating geodesics are impacted in the opposite sense. This leads to a stretching of the eikonal-wavefront of corotating geodesics and therefore a reduction in the van Vleck determinant. The point of crossing of geodesics is pushed to an angle in the direction of rotation of the vortex.

Fig. 2.5 shows the wavefront simulation of this case. The wavefront once again follows the behaviour of the geodesics, further confirming the accuracy of the eikonal approximation. It is clear that the wavefront corotating with the vortex is dragged much further and faster. The increase in wave height at the point the two waves meet is clearly seen at an angle to the horizontal. A further feature becomes apparent in this case. As the waves cross there is a reduction in the trailing wavefront due to the fact that the initial Gaussian data creates a wave with leading positive amplitude and a trailing negative amplitude.

Eikonal-wavefront on rotating bathtub with rotation  $C = 0.5$  and draining rate  $D = 1$ .

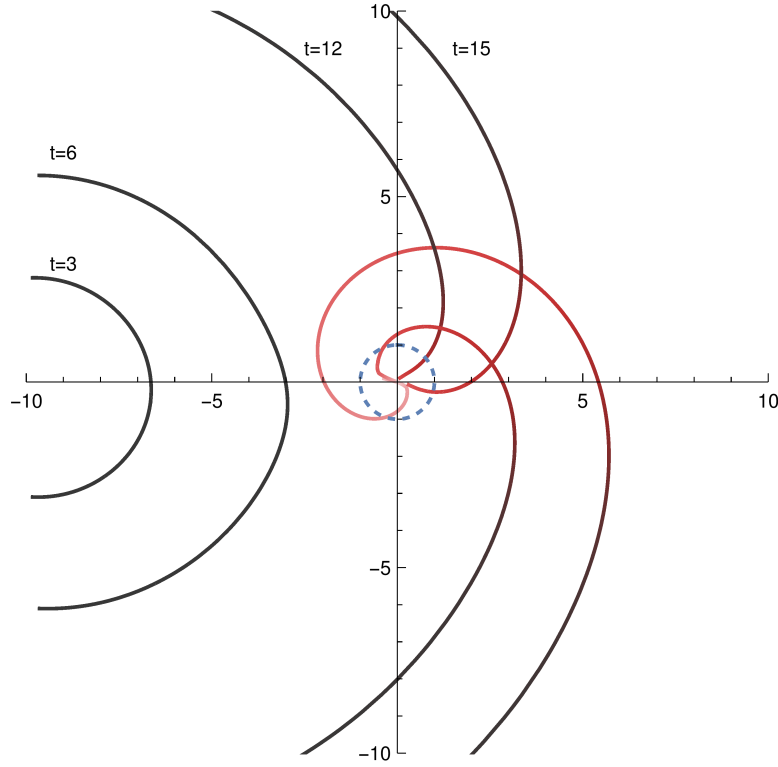


Figure 2.4: Eikonal-wavefront formed from a congruence of null geodesics emanating from  $(-10, 0)$  at successive  $t$  values  $t = \{3, 6, 12, 15\}$ . The vortex is rotating anticlockwise. The eikonal-wavefront initially propagates as in flat spacetime, before being dragged in towards the vortex. In this rotating case the corotating geodesics are dragged around the vortex faster than counterrotating geodesics. The eikonal-wavefront wraps around the vortex asymmetrically meaning the point of crossing occurs above the  $x$  axis. The van Vleck determinant decreases more on the corotating arm of the eikonal-wavefront since it is stretched much further around the vortex.

Full-wavefront evolution on rotating bathtub with rotation  $C = 0.5$  and draining rate  $D = 1$ .

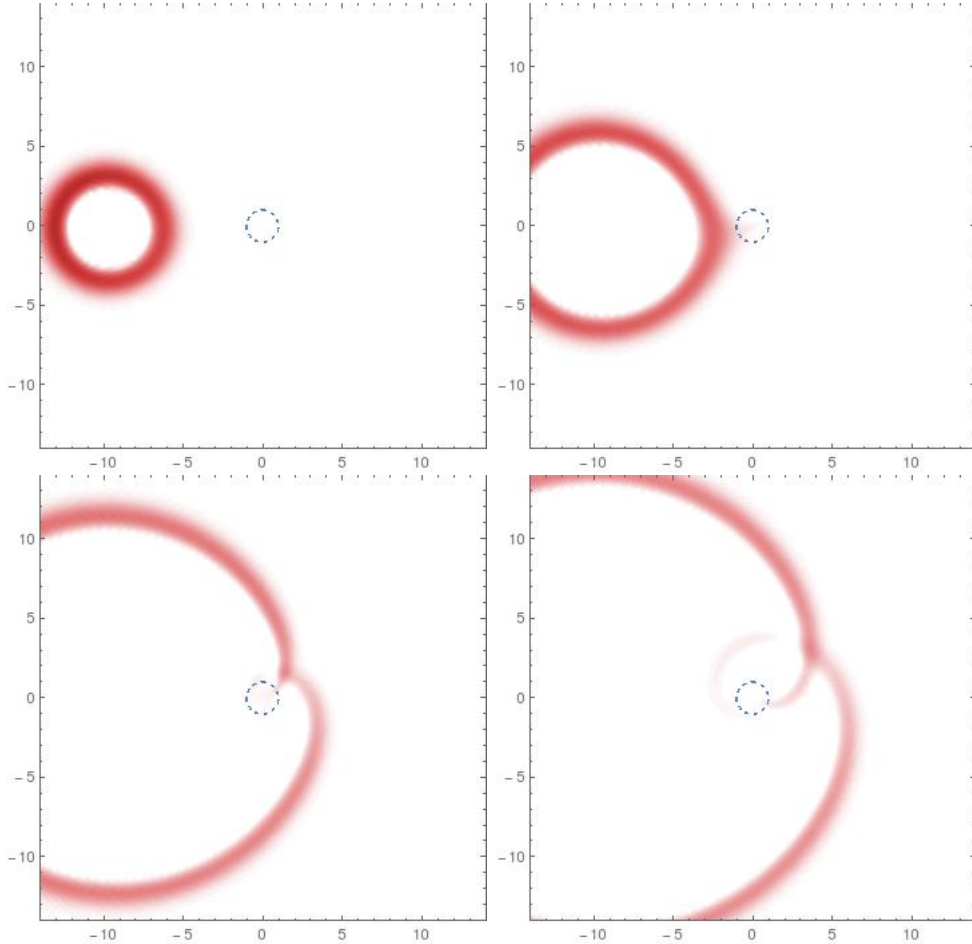


Figure 2.5: The evolution of a full-wavefront from a Gaussian of width  $\sigma = 1$  at  $(-10, 0)$  at successive  $t$  values  $t = \{3, 6, 12, 15\}$ . Initially the wave propagates as in flat space again, before the leading front is dragged in towards the vortex with the corotating front dragged faster and further around the vortex. The waves cross on the opposite side of the vortex at an angle to the  $x$  axis. The corotating wave is stretched over a longer span meaning the height is reduced.

### 2.6.3 Rapidly rotating vortex

If we now allow the rate of rotation to increase to  $C = 2$  we see additional interesting features. Here the effective horizon is at  $r_h = 1$ , and the ergosphere is at  $r_e = 2.23607$ . The null circular orbits are at  $r_c^+ = 1.02749$  and  $r_c^- = 4.3525$  (see Eq. (2.33)).

Many of the same features persist from the slower rotating case, such as the dragging of the corotating geodesics and the wavefront. Fig. 2.6 shows the eikonal-wavefront. We can see that the corotating geodesics can wrap completely around the vortex before the counterrotating geodesics reach the vortex. A further feature at late times shows the congruence wrapping around the vortex multiple times.

The full-wavefront shown in Fig. 2.7 again matches up well with the eikonal-wavefront. We can see the wavefront being dragged rapidly around the vortex and stretched very thin. The wave amplitude is only increased slightly at crossing due to this. However the following wave is damped completely behind the counterrotating wavefront due to the following negative wave created by initial Gaussian data.

## 2.7 Discussion

In this work we have investigated the behaviour of null geodesics and the flow of a wavefront in an effective analogue spacetime. We have shown that a wavefront follows the same path as the geodesics, as expected from the eikonal approximation. This means that the wavefront maps out the lightcone of the effective spacetime. Interesting features observed from the geodesic analysis, such as the wrapping around the vortex and the crossing of geodesics transferred over to the wavefront analysis. We have shown also the qualitative relationship between the van Vleck determinant and the height of a wavefront.

The model describes the behaviour of surface waves with long wavelengths

Eikonal-wavefront on rotating bathtub with rotation  $C = 2$  and draining rate

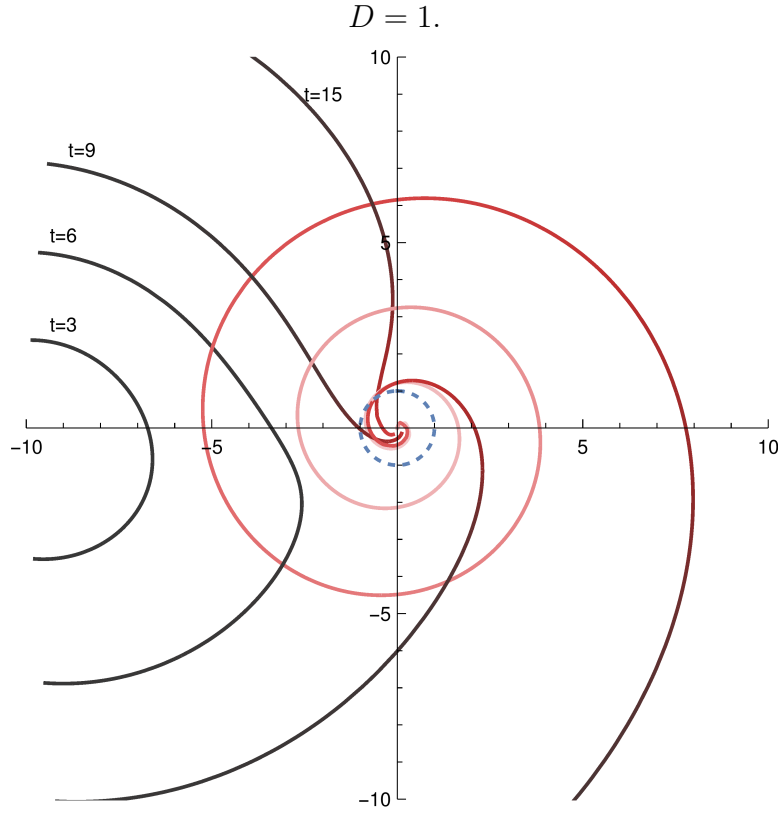


Figure 2.6: Eikonal-wavefront formed from a congruence of null geodesics emanating from  $(-10, 0)$  with van Vleck determinant at successive  $t$  values  $t = \{3, 7, 12, 18\}$ . As before, the corotating part of the eikonal-wavefront is dragged much faster around the vortex. Observe now that the corotating arm of the eikonal-wavefront wraps completely around the vortex before the counterrotating arm reaches the vortex.

Wavefront evolution on rotating bathtub with rotation  $C = 2$  and draining rate  $D = 1$ .

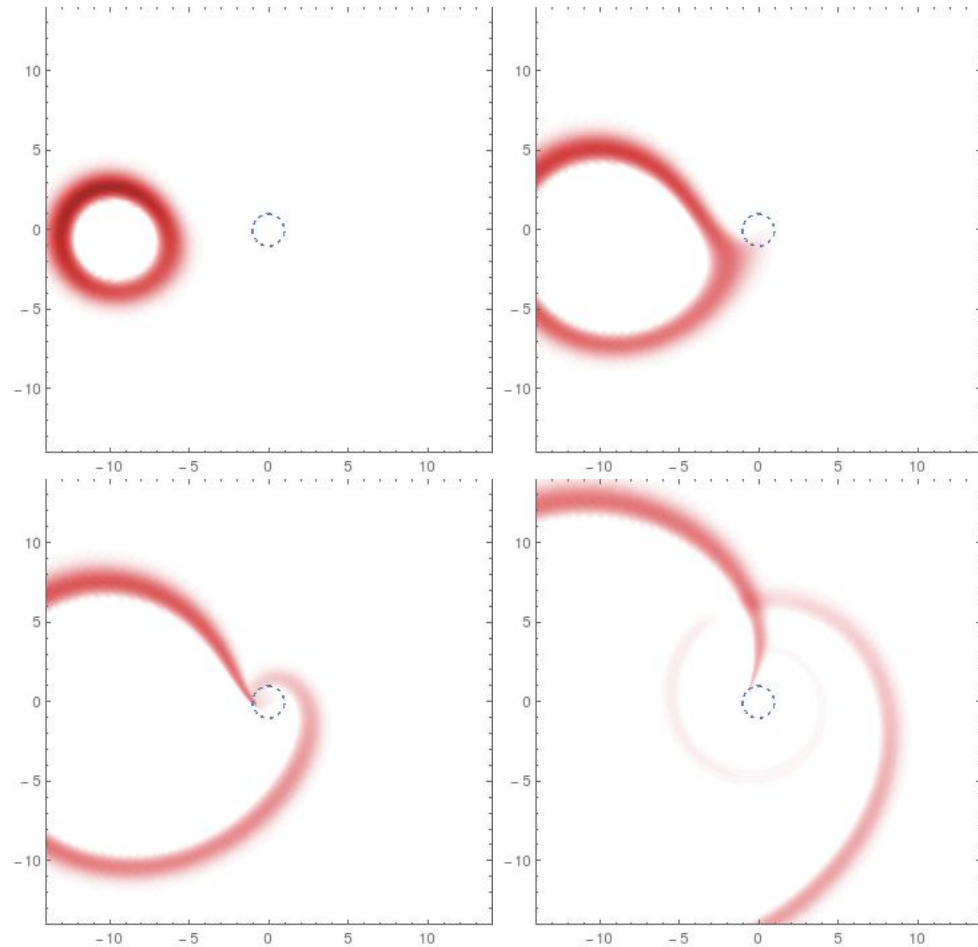


Figure 2.7: The evolution of a full-wavefront from a Gaussian at  $(-10, 0)$  at successive  $t$  values  $\{t = 3, 7, 12, 18\}$ . The initial wave evolves in a circle as in flat space before being dragged by the vortex. The corotating wave is dragged rapidly around the vortex and stretches twice around the vortex. The counterrotating wavefront however is held back by the background flow. Note in the final plot the increase in wave-height where the waves cross followed by a damping due to the following negative amplitude wave.

relative to the depth of the fluid, as described in Sec. 2.3. Our numerical wavefronts model a pulse-like disturbance, which creates a wavefront of approximately the same wavelength as the Gaussian width  $\sigma$ . Thus for a narrower Gaussian one must reduce the height of the background flow accordingly. However, as we have shown in Fig. 2.3, a Gaussian of width  $\sigma = 1$  is sufficient to match the full-wavefront to the lightcone.

The recent experimental results from the draining bathtub experiment reported in Ref. [49] did not attempt to relate their physical experiment to an effective spacetime. One possible future project would be to develop an experiment to relate observations of the evolution of a physical pulse-like disturbance in the draining bathtub, to the underlying effective spacetime. As we have shown, such a pulse-like disturbance maps out the lightcone of the effective spacetime. A real experiment must obey two key conditions if we are to extract the experiment's effective spacetime. Firstly the flow must be barotropic, inviscid and irrotational so that perturbations are governed by an equation in the form of Eq. (2.1). Secondly we must be in a regime where the eikonal approximation of Sec. 2.2 is valid.

A key consequence of the assumptions in forming the effective metric Eq. (2.28) was that all waves propagate at the same speed  $c_s$ . This means that there is a linear dispersion relation  $\omega = c_s k$  where  $\omega$  is the frequency,  $k = 2\pi/\Lambda$  is the wavenumber and  $\Lambda$  is the wavelength. For surface waves in water [48]

$$\omega^2 = \left( gk + \frac{s}{\rho} k^3 \right) \tanh(kh), \quad (2.44)$$

where  $g$  is the gravitational field and  $s$  is the surface tension. For  $\Lambda \gg h$  the relation is approximately linear  $\omega = \sqrt{gh}k$  with wave speed as  $c_s = \sqrt{gh}$  as expected. The next to leading order term is  $\frac{s}{2\rho} \sqrt{\frac{h}{g}} k^3$  therefore we would expect our model to fail as the background height approaches  $h \sim \frac{\Lambda}{2\pi}$ .

In the eikonal approximation of Sec. 2.2, we require perturbations to propagate with width much smaller than the typical lengthscale of the spacetime curvature. In the draining bathtub, an appropriate lengthscale is given by the

effective horizon  $\frac{D}{c_s}$ . Thus we assume  $\omega \gg \frac{c_s}{D}$ . With  $\omega$  given by the leading order term of Eq. (2.44) the eikonal condition becomes  $\Lambda \ll \frac{2\pi D}{c_s}$ . We may conclude that for a real fluid mechanical system to reflect our results we require perturbations to propagate with a wavelength in the region

$$h \ll \Lambda \ll \frac{2\pi D}{c_s}. \quad (2.45)$$

The eikonal expansion described in Sec. 2.2 is valid for any spacetime. In Chapter 3 we consider black hole spacetimes whose metrics satisfy the Einstein equations. We solve the scalar wave equation (2.1) on the real black hole spacetimes and compare with the analogue model presented in this chapter.

# Chapter 3

## Wave propagation on astrophysical black holes

### 3.1 Introduction

The previous chapter, Chap. 2, investigated the behaviour of a scalar wave on an analogue black hole. We highlighted the connection between a wavefront created by an initial pulse and the lightcone of the effective geometry.

In this chapter we introduce two important black hole spacetimes. We investigate the behaviour of scalar fields on these spacetimes with initial pulse disturbances. In Chap. 4 we will see that scalar wave propagation is related to the self force experienced by a particle sourcing a scalar field.

Section 3.2 introduces the Schwarzschild spacetime, which describes an uncharged non-rotating black hole. Section 3.3 introduces the Kerr spacetime, which describes an uncharged rotating black hole. For both spacetimes we give a review of their key features. We then investigate scalar wave evolution on these spacetimes and compare the rotating and non-rotating cases and the analogue case of Chap. 2.

Investigation of the Schwarzschild spacetime allows us to build up our knowledge of black hole spacetimes. By focussing on the non-rotating case

initially we highlight many of the interesting features of black hole spacetimes which are unrelated to rotation. From a computational perspective, the simplifications due to spherical symmetry allow correspondingly simpler methods to be developed for calculations. The results of such calculations can then be used as initial checks on the more sophisticated methods required in the rotating case.

## 3.2 Schwarzschild spacetime

The Schwarzschild solution was one of the first exact solutions to Einstein's equations. Discovered by Karl Schwarzschild in 1916 [56], it describes the spacetime in the exterior vacuum region of a spherically symmetric gravitational source.

The Schwarzschild solution is described by the metric

$$ds^2 = -f dt^2 + f^{-1} dr^2 + r^2 d\theta^2 + r^2 \sin^2 \theta d\phi^2, \quad (3.1)$$

where

$$f = 1 - \frac{2M}{r}, \quad (3.2)$$

and  $M$  is the mass of the spherically symmetric gravitational source. If the matter source lies within  $r = 2M = \frac{2GM}{c^2}$  we have a black hole. Birkhoff's theorem [57] established that the Schwarzschild solution is the unique spherically symmetric solution to Einstein's field equations in vacuum.

The metric in the form (3.1) has two singularities. At  $r = 2M$  we have the event horizon, beyond which particles would have to travel faster than light to escape. This is a coordinate singularity which can be removed from the metric by a coordinate transformation. At  $r = 0$  we have a curvature singularity which cannot be removed by a coordinate transformation. At a curvature singularity spacetime curvature scalars diverge. For example, the Kretschmann scalar  $K = R^{\alpha\beta\gamma\delta} R_{\alpha\beta\gamma\delta}$ , formed from the Riemann tensor, diverges as  $r \rightarrow 0$ . All timelike and null trajectories which pass through the event horizon

encounter the singularity in finite (proper or affine) time. See Ref. [58] for further discussions about the Schwarzschild solution.

### 3.2.1 Spacetime symmetries and geodesics

From the form of the metric Eq. (3.1), we can see that it is independent of both time  $t$  and rotation in the azimuthal coordinate  $\phi$ . This gives rise to two Killing vectors,  $k^\mu$  and  $h^\mu$ , given by

$$k^\mu \partial_\mu = \partial_t, \quad h^\mu \partial_\mu = \partial_\phi, \quad (3.3)$$

which satisfy the Killing equation [52]

$$k_{(\mu;\nu)} = 0, \quad h_{(\mu;\nu)} = 0. \quad (3.4)$$

Now consider a geodesic with tangent vector  $u^\mu = \dot{x}^\mu = \frac{dx^\mu}{d\lambda}$ , where  $\lambda$  is an affine parameter. The two Killing vectors (3.3) give rise to two conserved quantities

$$-k^\mu u_\mu = E, \quad h^\mu u_\mu = L, \quad (3.5)$$

where  $E$  is the particle's energy and  $L$  is the angular momentum. Geodesics are governed by the equations

$$u^\nu u^\mu{}_{;\nu} = \frac{du^\mu}{d\lambda} + \Gamma^\mu_{\lambda\nu} u^\lambda \frac{dx^\nu}{d\lambda} = 0, \quad (3.6)$$

where  $\Gamma^\mu_{\lambda\nu}$  is the affine connection. It is easy to show that the quantity

$$g_{\mu\nu} u^\mu u^\nu = \alpha \quad (3.7)$$

is conserved along geodesics, as

$$u^\beta \alpha_{;\beta} = u^\beta (g_{\mu\nu} u^\mu u^\nu)_{;\beta} = 0, \quad (3.8)$$

since  $u^\beta u^\mu{}_{;\beta} = 0$  by the geodesic equations and  $u^\beta g_{\mu\nu;\beta} = 0$  because we choose the affine connection  $\Gamma^\mu_{\lambda\nu}$  by enforcing metric compatibility  $g_{\mu\nu;\beta} = 0$ . The

quantity  $\alpha$  (3.7) takes the value of  $\{-1, +1, 0\}$  for timelike, spacelike and null geodesics respectively. The affine parameter  $\lambda$  is the proper time (distance) for timelike (spacelike) geodesics.

Geodesics in Schwarzschild spacetime are always planar due to the spherical symmetry. We can always make a coordinate transformation such that an orbiting particle lies in the equatorial plane. Thus we can set  $\theta = \pi/2$ , without loss of generality, in the geodesic equations. Knowledge of the three constants  $\{E, L, \alpha\}$  along with the condition  $\theta = \pi/2$  allows us to parametrise the geodesics and write the geodesic equations in integrable form as

$$\begin{aligned} \dot{t} &= \frac{E}{f}, \\ \dot{r}^2 &= \alpha f + E^2 - \frac{f}{r^2} L^2, \\ \theta &= \frac{\pi}{2}, \\ \dot{\phi} &= \frac{L}{r^2}. \end{aligned} \tag{3.9}$$

We could alternatively have found these equations by forming the Lagrangian  $\mathcal{L} = \frac{1}{2}g_{\mu\nu}u^\mu u^\nu$ , and using the principle of least action. The Euler-Lagrange equations give rise to an equivalent set of equations to Eqs. (3.9) for the geodesics.

### Timelike circular orbits

As an example, let us consider circular orbits for timelike geodesics. We set  $\alpha = -1$  and identify the affine parameter as the proper time  $\lambda = \tau$ . We find equations for circular orbits by imposing the conditions  $\dot{r} = \ddot{r} = 0$ . Taking the radial derivative of the radial equation from Eqs. (3.9) gives

$$2\dot{r}\ddot{r} = 0 = -\frac{2M}{r^2} + \frac{2L^2 f}{r^3} - \frac{2ML^2}{r^4}, \tag{3.10}$$

and solving for  $L$  we have

$$L = \pm \frac{\sqrt{Mr}}{\sqrt{1 - \frac{3M}{r}}}, \tag{3.11}$$

where the  $\pm$  corresponds to orbiting in opposite directions, which are equivalent by symmetry. Choosing the positive sign and using this value of  $L$  (3.11) with  $\dot{r} = 0$  we can find from the second equation of (3.9)

$$E = \frac{f}{\sqrt{1 - \frac{3M}{r}}}. \quad (3.12)$$

From Eqs. (3.9) with the values of  $E$  and  $L$  from Eqs. (3.11-3.12) we find

$$\dot{t} = \frac{1}{\sqrt{1 - \frac{3M}{r}}}, \quad \dot{\phi} = \dot{t} \sqrt{\frac{M}{r^3}}. \quad (3.13)$$

Finally we can identify the orbital frequency

$$\Omega = \frac{d\phi}{dt} = \frac{\dot{\phi}}{\dot{t}} = \sqrt{\frac{M}{r^3}}, \quad (3.14)$$

which will be used later in the thesis.

### 3.2.2 Wave evolution

We now consider scalar wave evolution on the Schwarzschild spacetime by solving the scalar wave Eq. (2.1),  $\square\Psi = 0$ . The eikonal approximation of Sec. 2.2 highlighted the relation between null geodesics and scalar wave propagation. Investigating the behaviour of a scalar wave on the Schwarzschild spacetime allows us to probe the features of the spacetime.

#### Separable equation

We initially decompose the field into spherical harmonics  $Y_{lm}(\theta, \phi)$  using

$$\Psi(t, r, \theta, \phi) = \sum_{l=0}^{\infty} \sum_{m=-l}^l \frac{1}{r} \Psi_{lm}(t, r) Y_{lm}(\theta, \phi). \quad (3.15)$$

If we set up axisymmetric initial data for  $\Psi$  we can rewrite the decomposition (3.15) in terms of  $m = 0$  modes only, due to the spherical symmetry of the

Schwarzschild spacetime, namely

$$\Psi(t, r, \theta, \phi) = \sum_{l=0}^{\infty} \frac{1}{r} (2l+1) \Psi_l(t, r) P_l(\cos \gamma), \quad (3.16)$$

where

$$\cos \gamma = \sin \theta_0 \sin \theta \cos(\phi_0 - \phi) + \cos \theta_0 \cos \theta, \quad (3.17)$$

and  $(\theta_0, \phi_0)$  is the axis of symmetry. Using Eq. (3.16) in the scalar wave equation  $\square \Psi = 0$ , Eq. (2.1), allows us to separate the equations for each  $l$ -mode

$$-\frac{\partial^2 \Psi_l}{\partial t^2} + \frac{\partial^2 \Psi_l}{\partial r^{*2}} - V(r) \Psi_l = 0, \quad (3.18)$$

where  $V(r)$  is the potential

$$V(r) = \left(1 - \frac{2M}{r}\right) \left(\frac{l(l+1)}{r^2} + \frac{2M}{r^3}\right). \quad (3.19)$$

The tortoise coordinate  $r^*$  is governed by the relation

$$dr^*/dr = 1/f \quad (3.20)$$

with the solution

$$r^* = r + 2M \ln \left( \frac{r}{2M} - 1 \right). \quad (3.21)$$

For large  $r \gg 2M$  the tortoise coordinate approaches the radial coordinate  $r^* \sim r$ . As we approach the horizon  $r \rightarrow 2M$  the tortoise coordinate tends to negative infinity  $r^* \rightarrow -\infty$ .

### 3.2.3 Numerical evolution

#### Initial conditions

In this section we investigate the evolution of an initial Gaussian pulse centred on the point  $(x_0, y_0, z_0)$  in Cartesian coordinates. We can write a Gaussian of width  $\sigma$  in three spatial dimensions as

$$\Psi(t_0, x, y, z) = \frac{1}{(2\pi\sigma^2)^{3/2}} \exp \left( -\frac{(x-x_0)^2 + (y-y_0)^2 + (z-z_0)^2}{2\sigma^2} \right), \quad (3.22)$$

where  $t_0$  is the initial time. We can convert to Schwarzschild coordinates  $\Psi(t_0, r, \theta, \phi)$  via the definitions

$$\begin{aligned}x &= r \sin \theta \cos \phi, \\y &= r \sin \theta \sin \phi, \\z &= r \cos \theta.\end{aligned}\tag{3.23}$$

To solve the wave equation (3.18) for each  $l$  mode we must decompose the initial conditions into  $l$  modes. We do this by using the ansatz (3.16), multiplying both sides by  $rP_l(\cos \gamma)$  and integrating over the angular coordinates. This gives

$$\Psi_l(t_0, r^*) = \frac{r}{4\pi} \int_0^\pi \int_0^{2\pi} \Psi(t_0, r, \theta, \phi) P_l(\cos \gamma) \sin \theta d\theta d\phi,\tag{3.24}$$

since [59]

$$\int_0^\pi \int_0^{2\pi} P_l(\cos \gamma) P_l(\cos \gamma) \sin \theta d\theta d\phi = \delta_{ll} \frac{4\pi}{2l+1}.\tag{3.25}$$

### Matrix method

In Sec. 2.5.1 we evolved the scalar wave equation using Mathematica's `NDSolve` inbuilt function. Whilst this is also possible here on the Schwarzschild space-time, we find that due to the additional complexities involved, the `NDSolve` function is heavily time and memory constrained. Instead we have developed a matrix method that relies upon Mathematica's `SparseArray` function. We outline this here.

Since the equations (3.18) are fully decoupled for each  $l$  mode we can solve them independently for each value of  $l$ . We drop the  $l$  subscript here for clarity. First we set up a grid of  $n$  points  $x_i$  in the spatial coordinates  $r_i^* = x_i$  and define a function at each point  $\Psi_i(t) = \Psi(t, x_i)$ . The function  $\Psi$  at time  $t$  is now represented by a vector of length  $n$ . To approximate the spatial derivatives we use finite differencing [55]. We make use of Mathematica's function `NDSolve`FiniteDifferenceDerivative` which, given an input of a grid of  $n$  points,

outputs an  $(n \times n)$  matrix  $\mathbf{D}^{(m)}$  of the finite difference derivatives at desired difference order and derivative order  $m$ . The matrix produced by this function allows spatial derivatives to be converted into matrix multiplications applied to the vector  $\Psi$ . Since the finite difference matrix  $\mathbf{D}^{(m)}$  is sparse we apply Mathematica's `SparseArray` function to  $\mathbf{D}^{(m)}$ . This has the effect of speeding up matrix operations and reducing memory usage.

To evolve in time we use the fourth-order Runge-Kutta method (see Sec. 16.1 of Ref. [55]). To make use of the Runge-Kutta algorithm we write the equations (3.18) in first order form by defining  $\partial_t \Psi(t) = \Pi(t)$ . The Runge-Kutta method takes as its input the two vectors  $\Psi(t_i)$  and  $\Pi(t_i)$  at a certain time  $t_i$ , a time step  $\delta t$ , and a vector-valued function  $F[\Psi(t_i), \Pi(t_i)]$ . The function  $F[\Psi(t_i), \Pi(t_i)]$  gives the time derivatives at time  $t_i$ ,

$$\begin{aligned} F[\Psi(t_i), \Pi(t_i)] &= [\partial_t \Psi(t_i), \partial_t \Pi(t_i)], \\ &= [\Pi(t_i), \mathbf{D}^{(2)} \cdot \Psi(t_i) - \tilde{V} \cdot \Psi(t_i)], \end{aligned} \quad (3.26)$$

where  $\tilde{V}$  is a vector of values of the potential (3.19) at each spatial point with components  $\tilde{V}_i = V(x_i)$ . The Runge-Kutta algorithm outputs two new vectors corresponding to  $\Psi(t_i + \delta t)$  and  $\partial_t \Psi(t_i + \delta t) = \Pi(t_i + \delta t)$  via

$$\begin{aligned} \Psi(t_i + \delta t) &= \Psi(t_i) + \frac{\delta t}{6} (k_{1\Psi} + 2k_{2\Psi} + 2k_{3\Psi} + k_{4\Psi}), \\ \Pi(t_i + \delta t) &= \Pi(t_i) + \frac{\delta t}{6} (k_{1\Pi} + 2k_{2\Pi} + 2k_{3\Pi} + k_{4\Pi}), \end{aligned} \quad (3.27)$$

where

$$\begin{aligned} (k_{1\Psi}, k_{1\Pi}) &= F(\Psi, \Pi), \\ (k_{2\Psi}, k_{2\Pi}) &= F\left(\Psi + \frac{\delta t}{2} k_{1\Psi}, \Pi + \frac{\delta t}{2} k_{1\Pi}\right), \\ (k_{3\Psi}, k_{3\Pi}) &= F\left(\Psi + \frac{\delta t}{2} k_{2\Psi}, \Pi + \frac{\delta t}{2} k_{2\Pi}\right), \\ (k_{4\Psi}, k_{4\Pi}) &= F\left(\Psi + \delta t k_{3\Psi}, \Pi + \delta t k_{3\Pi}\right). \end{aligned} \quad (3.28)$$

The Runge-Kutta algorithm is derived by Taylor expanding a function  $\Psi(t_i + \delta t)$  around  $t_i$  to fourth order in  $\delta t$ . There is therefore an error of  $O(\delta t^5)$  at

each time step. In effect the algorithm is simply a series of matrix operations of  $(n \times n)$  matrices on vectors of length  $n$ .

### Large $l$ cut off

We can solve for only a limited number of  $l$  modes  $l_{max}$ . Higher  $l$ -modes oscillate more rapidly at a scale  $\theta \sim \frac{2\pi}{l}$ . Naively one may assume that we can truncate the mode-sum (3.16) at  $l_{max} \gg \frac{2\pi}{\theta_{min}}$  where  $\theta_{min}$  is the minimum angular scale in the initial data (3.22). However if we were to employ a sharp cut-off this could introduce unphysical oscillatory features in solutions of the wave equation. We therefore employ a smooth cut off around  $l = l_{cut}$  in the summation via

$$\Psi(t, r, \theta, \phi) = \sum_{l=0}^{l_{max}} e^{-l^2/2l_{cut}^2} \frac{1}{r} \Psi_l(t, r) P_l(\cos \gamma), \quad (3.29)$$

as suggested in Ref. [60]. The effect of this smooth cut off is to smear out features of the full solution at an angular scale of  $\theta \sim \frac{2\pi}{l_{cut}}$  by the convolution theorem [60]. We typically use a value  $l_{cut} = l_{max}/5$  as suggested by Ref. [2].

## 3.2.4 Results

In Fig. 3.1 we plot the evolution of a scalar wave with initial conditions described by a Gaussian of width  $\sigma = 1$  centred at  $(x_0, y_0, z_0) = (6, 0, 0)$ , Eq. (3.22). We plot in the plane  $\theta = \pi/2$ , equivalently  $z = 0$ . Due to the symmetry of the Schwarzschild spacetime the wave propagates symmetrically in all directions around the black hole. This means that our solutions are axisymmetric around the  $x$  axis. The wavefront propagates with a leading positive (red) sign front followed by a trailing negative (blue) sign front. We see this same feature in flat space. There is a build-up of the wavefront on the horizon due to the use of the Schwarzschild coordinate time; this is because the wavefront takes an infinite coordinate time to reach the horizon. Using ingoing coordinates we would expect the wavefront to pass through the horizon.

We see that the wavefront wraps around the black hole and meets itself on the opposite side. Here there is a caustic, a point where an infinite number of null geodesics emanating from the initial point converge. This means that there is a significant increase in the wave magnitude. After crossing, a part of the wavefront changes sign and continues to wrap around the black hole. We see “secondary” caustics where null geodesics, which have already met once, have orbited right around the black hole to converge again.

The sign change in the wavefront is related to the four-fold structure of the Green function for the scalar wave equation (2.1) [61] as discussed in Ref. [62]. We will highlight the importance of the relation between scalar wave propagation and the Green function in the next chapter, Chap. 4.

### 3.3 Kerr spacetime

A rotating black hole is described by the Kerr metric, discovered by Kerr in 1963 [63]. In Boyer-Lindquist coordinates the Kerr metric is

$$ds^2 = - \left( 1 - \frac{2Mr}{\rho^2} \right) dt^2 - \frac{4aMr \sin^2 \theta}{\rho^2} dt d\phi + \frac{\rho^2}{\Delta} dr^2 + \rho^2 d\theta^2 + \left( r^2 + a^2 + \frac{2Mra^2 \sin^2 \theta}{\rho^2} \right) \sin^2 \theta d\phi^2, \quad (3.30)$$

where

$$\rho^2 = r^2 + a^2 \cos^2 \theta, \quad \Delta = r^2 - 2Mr + a^2. \quad (3.31)$$

The mass is given by  $M$  and  $a$  is the spin parameter related to the angular momentum  $J$  by  $a = J/M$ . There is a curvature singularity located on a ring where

$$\rho^2 = 0 = r^2 + a^2 \cos^2 \theta, \quad (3.32)$$

and the coordinates take the values  $r = 0$  and  $\theta = \pi/2$ .

The Kerr spacetime has two horizons, where the metric component  $g_{rr} \rightarrow \infty$  and thus  $\Delta = 0$ . The horizons are given by the radial coordinates

$$r = r_{\pm} = M \pm \sqrt{M^2 - a^2}, \quad (3.33)$$

Wavefront evolution of a scalar wave in the equatorial plane of a Schwarzschild black hole

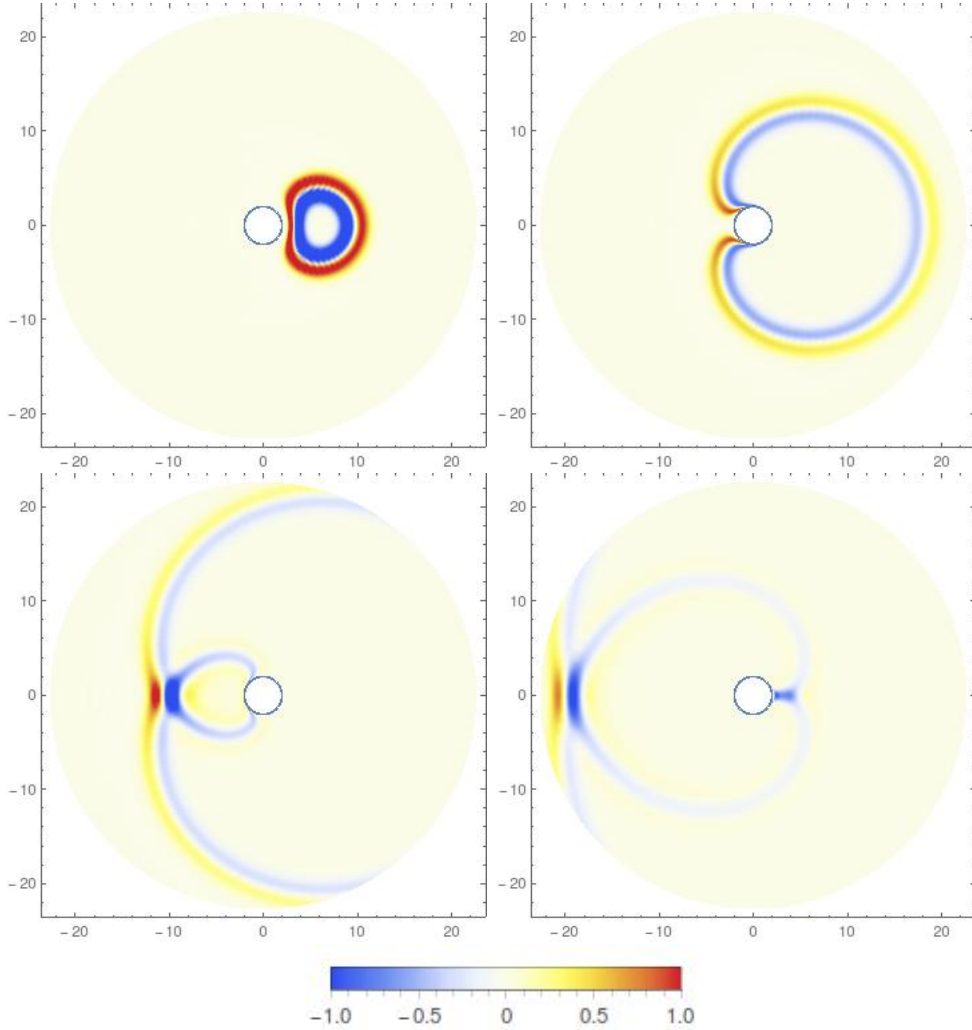


Figure 3.1: The evolution of a wavefront, at successive  $t$  values  $t = \{5, 15, 25, 35\}$ , starting from a Gaussian (3.22) of width  $\sigma = 1$  centred at  $(6, 0, 0)$  and plotted in the equatorial plane. The Gaussian creates a wavefront with a leading front of positive sign and a trailing front with negative sign. We observe wrapping of the wavefront around the black hole with an increase in the amplitude at the caustics on the opposite side of the black hole. There is then a secondary wave with opposite sign which wraps around and again increases in magnitude at the secondary caustics.

with  $r_+$  corresponding to the event horizon of the Kerr black hole. For  $a \geq M$  an event horizon does not form and there is a naked singularity. The case  $a = M$  is known as extremal Kerr spacetime [64]. In this thesis we only consider the case where  $a < M$ .

There is a further interesting hypersurface at

$$r = r_e = M + \sqrt{M^2 - a^2 \cos^2 \theta}, \quad (3.34)$$

inside which all observers must be corotating with the black hole. The region  $r_+ < r < r_e$  is referred to as the ergoregion [45, 65].

### 3.3.1 Spacetime symmetries and geodesics

As in the Schwarzschild case, the Kerr metric (3.30) is both stationary and axisymmetric. This means that the Killing vectors  $k^\mu$  and  $h^\mu$  defined in Eq. (3.3) also exist for the Kerr spacetime. Once again we can form the conserved quantities, energy  $E = -k^\mu u_\mu$  and angular momentum  $L = h^\mu u_\mu$ . Geodesics in Kerr are no longer always planar and therefore we cannot now restrict geodesic motion to the equatorial plane in general. There is however a third constant of motion arising from the existence of a Killing tensor, namely the Carter constant discovered by Carter [66]. This “hidden” symmetry was investigated by Penrose [67] who showed that the Killing tensor is given by the square of a Killing-Yano tensor. Note that this Killing tensor also exists for Schwarzschild.

#### Killing-Yano tensor

A Killing-Yano tensor  $f_{\mu\nu}$  is antisymmetric  $f_{(\mu\nu)} = 0$ , and satisfies the the Killing-Yano equation

$$f_{[\mu\nu;\lambda]} = f_{\mu\nu;\lambda}. \quad (3.35)$$

One can see that the “square” of the Killing-Yano tensor

$$K_{\mu\nu} = f_{\mu\lambda} f_\nu{}^\lambda, \quad (3.36)$$

is symmetric and satisfies the Killing equation

$$K_{(\mu\nu;\lambda)} = 0. \quad (3.37)$$

The tensor  $K_{\mu\nu}$  is therefore a Killing tensor which gives rise to the Carter constant  $\mathcal{K}$

$$\mathcal{K} = K_{\mu\nu}u^\mu u^\nu. \quad (3.38)$$

The Carter constant  $\mathcal{K}$  is a conserved quantity since

$$u^\alpha \mathcal{K}_{;\alpha} = u^\alpha K_{\mu\nu;\alpha} u^\mu u^\nu + u^\alpha K_{\mu\nu} u^\mu_{;\alpha} u^\nu + u^\alpha K_{\mu\nu} u^\mu u^\nu_{;\alpha} = 0, \quad (3.39)$$

because  $u^\alpha K_{\mu\nu;\alpha} u^\mu u^\nu = 0$  by Eq. (3.37) and  $u^\alpha u^\mu_{;\alpha} = 0$  from the geodesic Eqs. (3.6).

One can form a vector from the Killing-Yano tensor

$$J_\mu = f_{\mu\nu}u^\nu, \quad (3.40)$$

whose “square” is the Carter constant, and which is parallel transported along geodesics

$$J_\mu J^\mu = \mathcal{K}, \quad u^\mu J_{\nu;\mu} = 0. \quad (3.41)$$

### Geodesics

The three constants of motion  $E$ ,  $L$  and  $\mathcal{K}$  along with the condition Eq. (3.7) allow us to find the geodesic equations. The geodesic equations in first order form are given in Ref. [58],

$$\begin{aligned} \rho^2 \dot{t} &= E \left[ \frac{(r^2 + a^2)^2}{\Delta} - a^2 \sin^2 \theta \right] - L \frac{2Mar}{\Delta}, \\ \rho^4 \dot{r}^2 &= [E(r^2 + a^2) - aL]^2 - \Delta [\mathcal{K} - \alpha r^2], \\ \rho^4 \dot{\theta}^2 &= \mathcal{K} - \alpha a^2 \cos^2 \theta - \frac{1}{\sin^2 \theta} (Ea \sin^2 \theta - L)^2, \\ \rho^2 \dot{\phi} &= E \frac{2Mar}{\Delta} - L \left( \frac{a^2}{\Delta} - \frac{1}{\sin^2 \theta} \right). \end{aligned} \quad (3.42)$$

### Timelike equatorial circular orbits

As an example, consider circular timelike orbits in the equatorial plane. We set  $\theta = \pi/2$ ,  $\alpha = -1$  and  $\dot{r} = \ddot{r} = 0$ . The  $\dot{\theta} = 0$  equation (3.42) reduces to a condition on the Carter constant

$$\mathcal{K} = (Ea - L)^2. \quad (3.43)$$

The equations for  $\dot{r} = \ddot{r} = 0$  give

$$\begin{aligned} 0 &= [E(r^2 + a^2) - aL]^2 - \Delta [r^2 + (Ea - L)^2], \\ 0 &= 4Er [E(a^2 + r^2) - aL] - 2r\Delta - (2r - 2M) [(aE - L)^2 + r^2]. \end{aligned} \quad (3.44)$$

Solving for  $E$  and  $L$  simultaneously we have,

$$\begin{aligned} E &= \frac{1 - \frac{2M}{r} \pm \frac{aM^{1/2}}{r^{3/2}}}{\sqrt{1 - \frac{3M}{r} \pm \frac{2aM^{1/2}}{r^{3/2}}}}, \\ L &= \pm \sqrt{rM} \frac{\left(1 + \frac{a^2}{r^2} \mp \frac{2aM^{1/2}}{r^{3/2}}\right)}{\sqrt{1 - \frac{3M}{r} \pm \frac{2aM^{1/2}}{r^{3/2}}}}, \end{aligned} \quad (3.45)$$

where the alternate signs correspond to co(+) and counter(-) rotating orbits. The equations for  $\dot{t}$  and  $\dot{\phi}$  (3.42) are then

$$\begin{aligned} \dot{t} &= \frac{r^{3/2} \pm aM^{1/2}}{M^{1/2}r^{3/2} \sqrt{1 - \frac{3M}{r} \pm \frac{2aM^{1/2}}{r^{3/2}}}}, \\ \dot{\phi} &= \pm \dot{t} \frac{M^{1/2}}{r^{3/2} \pm aM^{1/2}}, \end{aligned} \quad (3.46)$$

and we can identify an azimuthal frequency  $\Omega$  via  $\frac{d\phi}{dt} = \dot{\phi}/\dot{t}$ ,

$$\Omega = \pm \frac{M^{1/2}}{r^{3/2} \pm aM^{1/2}}. \quad (3.47)$$

### 3.3.2 Wave evolution

#### Separable equation

In Ref. [68] a method is proposed to solve the scalar field wave equation (2.1) in the time domain by reducing the equation to a coupled set of  $(1 + 1)D$  equations using spherical harmonics. We outline the steps taken here.

Firstly we introduce an alternative azimuthal coordinate  $\varphi$  via

$$d\varphi = d\phi + \frac{a}{\Delta} dr. \quad (3.48)$$

We then decompose the full field into spherical harmonic modes,

$$\Psi(t, r, \theta, \varphi) = \frac{1}{r} \sum_{l=0}^{\infty} \sum_{m=-l}^l \psi_{lm}(t, r) Y_{lm}(\theta, \varphi), \quad (3.49)$$

which is then used to decompose the scalar wave equation, Eq. (2.1), into  $(1 + 1)D$  equations for the  $\psi_{lm}(t, r)$ . To find equations for  $\psi_{lm}(t, r)$  we input the ansatz (3.49) into the scalar wave equation (2.1), multiply by  $Y_{l'm'}^*(\theta, \varphi)$  and integrate over the angular coordinates. For terms with no  $\theta$  dependence the decomposition is straightforward using the identity [59]

$$\int_0^\pi \int_0^{2\pi} Y_{l'm'}^*(\theta, \phi) Y_{lm}(\theta, \phi) \sin \theta d\theta d\phi = 4\pi \delta_{ll'} \delta_{mm'}. \quad (3.50)$$

Due to the dependence of the Kerr metric on  $\theta$  we also find terms involving  $\cos^2 \theta$ , which lead to coupling between  $l$  modes. To deal with this, we introduce the coupling coefficient

$$c_{jl}^m = \langle lm | \cos^2 \theta | jm \rangle \quad (3.51)$$

where

$$\langle lm | f(\theta) | jm \rangle = 2\pi \int Y_{lm}^*(\theta, \phi) f(\theta) Y_{jm}(\theta, \phi) d(\cos \theta). \quad (3.52)$$

We can make use of identities, presented in Ref. [69], for the coupling coefficient (3.51)

$$c_{jl}^m = \frac{1}{3} \delta_{jl} + \frac{2}{3} \sqrt{\frac{2j+1}{2l+1}} \langle j, 2, m, 0 | l, m \rangle \langle j, 2, 0, 0 | l, 0 \rangle \quad (3.53)$$

to highlight some useful properties. In Eq. (3.53) the  $\langle j, i, m, 0 | l, n \rangle$  are Clebsch-Gordan coefficients [70]. The only non-zero values of  $c_{jl}^m$  (3.51) are for  $j = l$  and  $j = l \pm 2$ . Thus only modes with even or odd values of  $l$  interact and each  $l$ -mode is coupled only to its nearest odd or even neighbours.

Using the identities (3.50, 3.53) we can now write down the equations for each mode

$$\begin{aligned} & [\Sigma_0^2 + a^2 \Delta c_{ll}^m] \ddot{\psi}_{lm} + a^2 \Delta \left( c_{l,l+2}^m \ddot{\psi}_{l+2,m} + c_{l,l-2}^m \ddot{\psi}_{l-2,m} \right) = \\ & (r^2 + a^2)^2 \psi_{lm}'' + \left( 2iam(r^2 + a^2) - 2a^2 \frac{\Delta}{r} \right) \psi_{lm}' - 4iamMr \dot{\psi}_{lm} - V_{lm} \psi_{lm}, \end{aligned} \quad (3.54)$$

where

$$\Sigma_0^2 = (r^2 + a^2)^2 - a^2 \Delta, \quad (3.55)$$

and

$$V_{lm} = \Delta \left[ l(l+1) + \frac{2M}{r} \left( 1 - \frac{a^2}{Mr} \right) + \frac{2iam}{r} \right]. \quad (3.56)$$

The overdot denotes a partial derivative with respect to time, whilst the primes denote partial derivatives with respect to the Kerr tortoise coordinate, defined by

$$\frac{dr^*}{dr} = \frac{r^2 + a^2}{\Delta}. \quad (3.57)$$

Integrating Eq. (3.57) we find, up to a constant of integration,

$$r^* = r + \frac{2M}{r_+ - r_-} \left( r_+ \ln \left| \frac{r - r_+}{2M} \right| - r_- \ln \left| \frac{r - r_-}{2M} \right| \right). \quad (3.58)$$

### 3.3.3 Numerical evolution

The wave equation Eq. (3.54) is a set of coupled  $(1+1)D$  equations for the  $lm$  modes. Whilst each  $m$  mode can be solved independently, the  $l$  modes only decouple into even and odd sectors for  $l$ , with each sector solved simultaneously.

### Initial conditions

As initial conditions, we use the same 3-dimensional Gaussian as for the Schwarzschild spacetime, Eq. (3.22). Now we choose to relate the Boyer-Lindquist coordinates to Cartesian coordinates by

$$\begin{aligned}x &= \sqrt{r^2 + a^2} \sin \theta \cos \phi, \\y &= \sqrt{r^2 + a^2} \sin \theta \sin \phi, \\z &= r \cos \theta.\end{aligned}\tag{3.59}$$

To decompose Eq. (3.22) into spherical harmonics we multiply the Gaussian by the complex conjugate of the spherical harmonics and by  $r$  to give the initial conditions in  $lm$  modes

$$\psi_{lm}(t_0, r) = \frac{r}{4\pi} \int_0^\pi \int_0^{2\pi} Y_{lm}^*(\theta, \phi) \Psi(t_0, r, \theta, \phi) \sin \theta \, d\theta \, d\phi,\tag{3.60}$$

using the identity of Eq. (3.50).

Finally, due to the coupling between  $l$  modes in the wave equation Eq. (3.54), a cut off in  $l$  modes at  $l_{max}$  may create some numerical noise. To counteract this we apply our smoothing function  $e^{-l^2/2l_{cut}^2}$ , from Eq. (3.29), to our initial conditions

$$\psi_{lm}(t_0, r) \rightarrow e^{-l^2/2l_{cut}^2} \psi_{lm}(t_0, r).\tag{3.61}$$

### Matrix evolution

To use the Runge-Kutta method, described in Sec. 3.2.3, for time evolution we must formulate our equations in first order form for each  $l$  mode. Each mode  $\psi_l$  (dropping  $m$  subscripts) is only coupled to the nearest  $\psi_{l\pm 2}$  modes and the even and odd mode equations can be decoupled. We set  $\pi_l = \dot{\psi}_l$  so that the equations for  $\boldsymbol{\pi}$ , a vector of the  $\pi_l$  even or odd modes, can be written in matrix form

$$\mathbf{A}\dot{\boldsymbol{\pi}} = \mathbf{B}\boldsymbol{\pi} + \mathbf{C}\boldsymbol{\psi},\tag{3.62}$$

where  $\mathbf{A}$  is now a tridiagonal matrix, since in Eq. (3.54) each mode only depends on its nearest two neighbours. The matrices  $\mathbf{B}$  and  $\mathbf{C}$  are found from the right hand side of Eq. (3.54) for each  $l$  mode. We invert the matrix  $\mathbf{A}$  to write the equations decoupled in  $\dot{\pi}_l$ .

Now we discretise on a spatial grid in  $r^*$  of  $n$  points so that the vector  $\boldsymbol{\pi}$  is now a vector of length  $n\tilde{l}$  where  $\tilde{l}$  is total number of  $l$  modes being considered. For example for  $l_{max} = 100$ , even modes have  $\tilde{l} = 51$  and odd modes  $\tilde{l} = 50$ . Thus the matrices  $\mathbf{A}$ ,  $\mathbf{B}$  and  $\mathbf{C}$  are  $n\tilde{l} \times n\tilde{l}$  matrices. We calculate the inverse of  $\mathbf{A}$  and the multiplications  $\mathbf{A}^{-1}\mathbf{B}$  and  $\mathbf{A}^{-1}\mathbf{C}$  prior to beginning the time evolution. The Runge-Kutta method described in Sec. 3.2.3 is then a series of matrix operations. As in the Schwarzschild case, we make use of the `SparseArray` commands to greatly increase speed of numerical calculations since the matrices have mainly zero entries.

### 3.3.4 Results

We now investigate the evolution of a scalar wave with initial conditions of a Gaussian of width  $\sigma = 1$  centred at  $(x_0, y_0, z_0) = (6, 0, 0)$  on the Kerr spacetime (the same initial conditions investigated in Schwarzschild spacetime). We again plot in the equatorial plane ( $\theta = \pi/2$ ). However, we cannot expect the same behaviour as in Schwarzschild spacetime due to the lack of spherical symmetry. The wavefront will propagate in all directions around the black hole, however we focus on the equatorial plane where the features due to rotation are enhanced.

Fig. 3.2 shows the evolution of the Gaussian on Kerr spacetime with  $a = 0.5M$ . The black hole is rotating in a clockwise direction. Many of the same features from the Schwarzschild spacetime persist, yet are deformed by rotation. The wavefront is dragged around the black hole with the corotating arm (lower) dragged at a faster rate. This accelerated dragging of the wavefront means that the wavefront meets itself at an angle above the horizontal. Once

again we see the increase in the waveheight at this caustic. A part of the wavefront continues to orbit the black hole with a change of sign. A particular feature of the rotating case is that the counterrotating arm, near to the black hole, has a greater magnitude than the corotating arm. This difference is due to the stretching of the corotating arm as it is accelerated around the black hole. In the later plots we see essentially a repetition of these features with the meeting of the wavefronts at a caustic below the horizontal axis.

We also investigate a near-extremal Kerr space time with  $a = 0.999M$  in Fig. 3.3. We show the evolution of the same Gaussian and see many of the same features as in the  $a = 0.5M$  case. The higher rate of rotation emphasises the disparity between the corotating and counterrotating arms. The corotating arm is carried further around the black hole. This stretches the wavefront, causing it to have a much lower waveheight. The two arms meet at a greater angle to the horizontal than in the  $a = 0.5M$  case.

### 3.4 Comparisons and discussion

We now compare our analysis of the Kerr black hole spacetime with the analogue bathtub described in Chap. 2 with an effective metric Eq. (2.28). Fig. 3.4 compares the evolution of an initial Gaussian on a draining bathtub with  $D = 1$  and  $C = 0.5$  and the Kerr spacetime with  $a = 0.7M$ . We have reflected the plot for evolution on Kerr spacetime by  $180^\circ$  to aid comparison. The key difference between the two spacetimes is that the draining bathtub is 3-dimensional whilst the Kerr spacetime is 4-dimensional. This means that the wave plotted in Fig. 3.4 for the draining bathtub encompasses all of the features of the effective spacetime, whereas in the Kerr spacetime we show only a planar slice of the spacetime. The main effect of this is that in the analogue spacetime when the two wavefront arms, travelling either side of the vortex, meet there is simply a superposition of the two. The waveheight in the analogue case is therefore given by the sum of the two arm heights. In the Kerr spacetime,

Wavefront evolution of a scalar wave in the equatorial plane of a Kerr black hole with  $a = 0.5M$

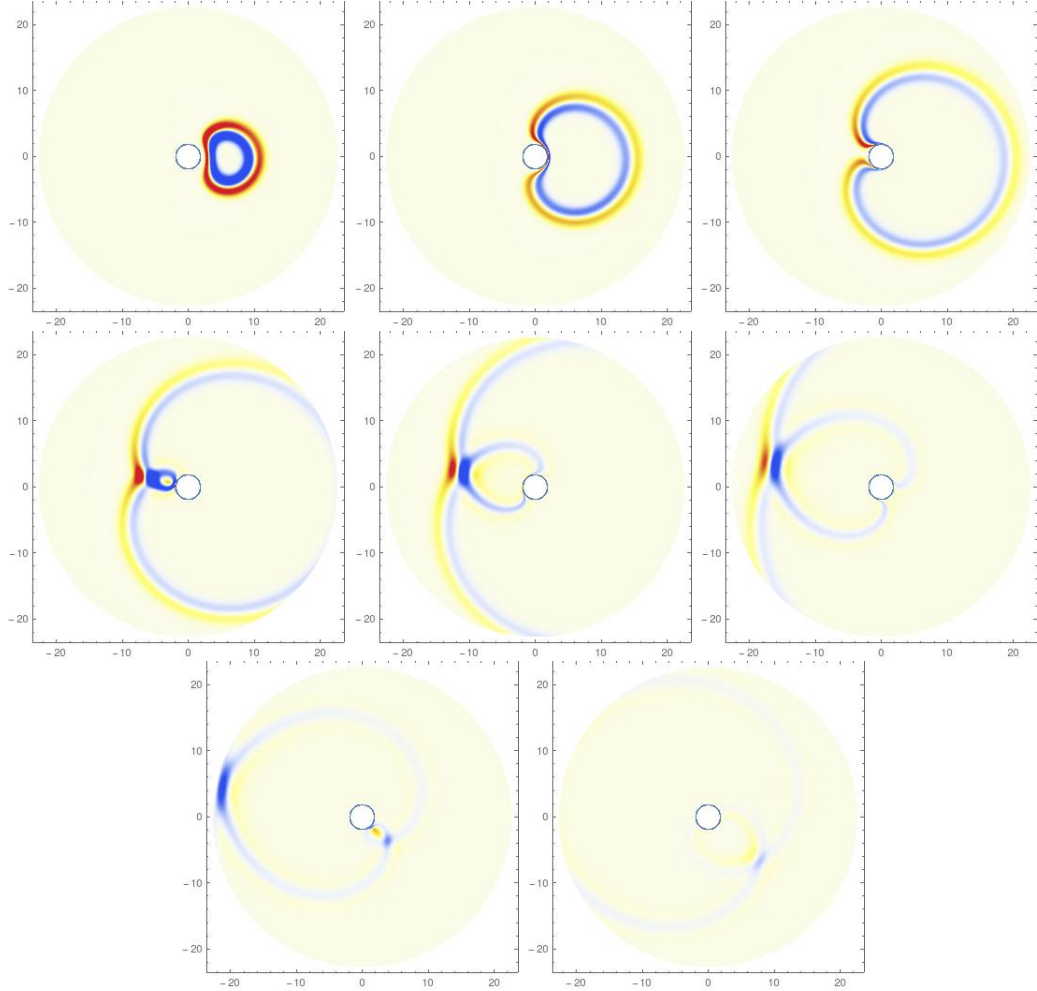


Figure 3.2: The evolution of a wavefront starting from a Gaussian centred at  $(6, 0, 0)$  at successive  $t$  values  $t = \{5, 10, 15, 20, 25, 30, 35, 40\}$ . The black hole is rotating clockwise in this picture. We observe that the wavefront is dragged around the black hole with the corotating arm (lower) being dragged around at a greater rate. This creates a greater amplitude in the counterrotating arm. The wavefront increases in amplitude where the two arms meet at the caustic which is dragged above the horizontal axis due to rotation. In the later plots we see the trailing wavefronts which have switched sign meet again below the axis.

Wavefront evolution of a scalar wave in the equatorial plane of a Kerr black hole  $a = 0.999$

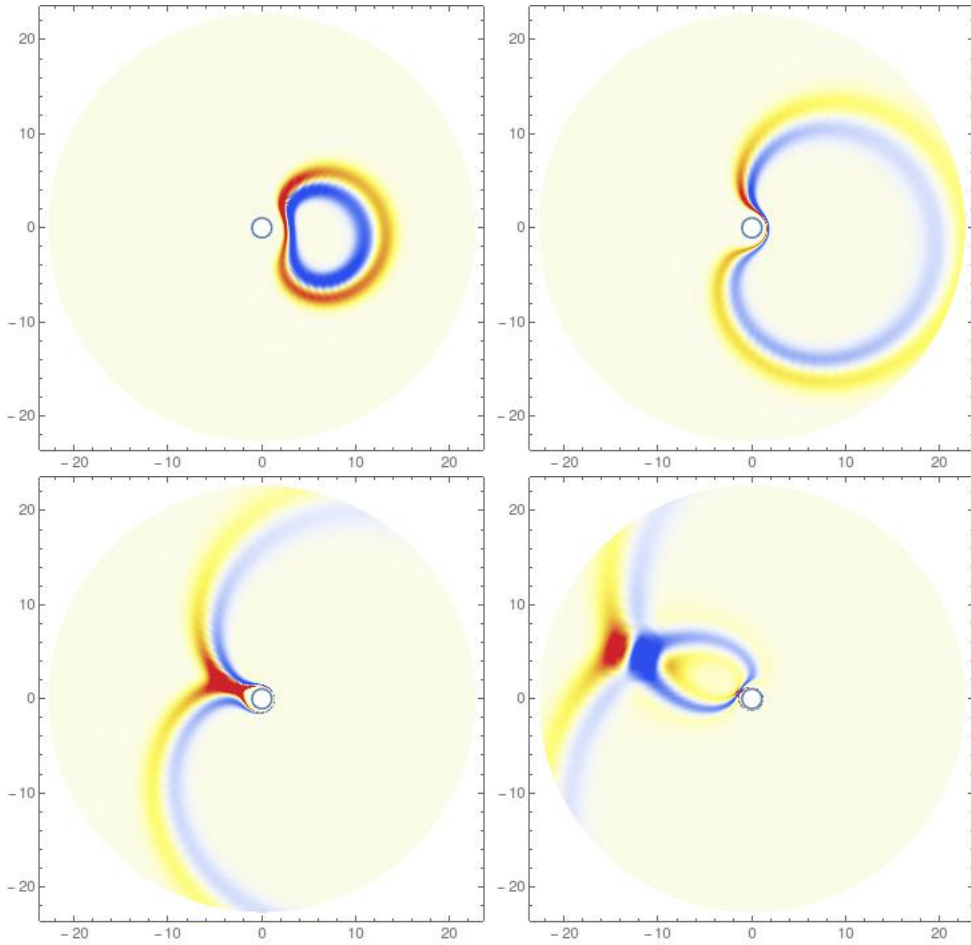


Figure 3.3: The evolution of a wavefront from a Gaussian centred at  $(6,0,0)$  at successive  $t$  values  $t = \{5, 10, 15, 20\}$ . We observe the greater dragging of the corotating arm of the wavefront. This stretching of the corotating arm causes it to have a lower magnitude than the counter rotating arm. The two arms meet at an angle to the horizontal greater than that in the  $a = 0.5M$  case.

Comparisons of the evolution of a scalar field on the draining bathtub versus a Kerr black hole spacetime

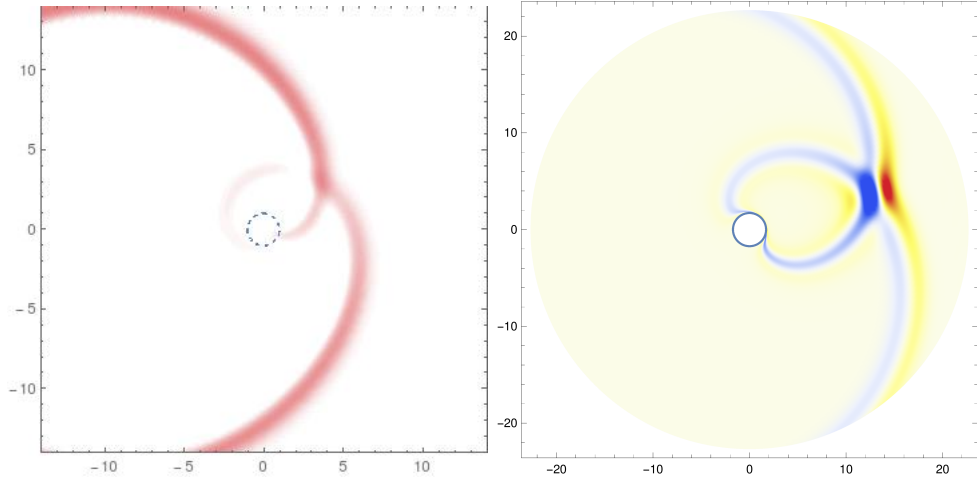


Figure 3.4: Comparison of the evolution of a wavefront from a Gaussian of width  $\sigma = 1$  on the draining bathtub ( $D = 1, C = 0.5$ ) and Kerr spacetime with  $a = 0.7M$ . We observe that the corotating arms of the wavefront are dragged faster around the vortex/black hole before meeting at an angle to the horizontal. The wavefront increases in amplitude where the two arms meet on the opposite side of the vortex/black hole. In the draining bathtub case, this is simply a superposition of the two arms, whilst the increase in the Kerr spacetime is due to the waves travelling in all directions around the black hole.

we have the contribution from the waves travelling around all directions of the black hole which creates a significant increase in the wave height at the intersection. A further difference is the swapping of the sign of the wavefront in the Kerr spacetime which does not occur in the draining bathtub.

# Chapter 4

## Scalar self force from worldline integrals

### 4.1 Introduction

In this chapter we consider the scalar field self force as an important first step into developing methods for calculating the gravitational self-force. First we review the gravitational problem in terms of worldline integrals, before introducing the scalar equations considered later in the chapter. As we discussed in the introduction, Chap. 1, the self force programme considers the two-body problem in terms of a small body with mass  $\mu$  perturbing the “background spacetime” of a much larger body of mass  $M$  with  $\mu \ll M$ . The small object can be seen to travel on an accelerated worldline in the background spacetime, perturbed away from geodesic motion by the self force. The MiSaTaQuWa equations [24, 25] give an expression for the self force at leading order in the mass ratio.

We write the full perturbed spacetime  $\tilde{g}_{\alpha\beta}$  as a sum of the spacetime of the large black hole  $g_{\alpha\beta}$  and a perturbation  $h_{\alpha\beta}$  at  $O(\mu)$ ,

$$\tilde{g}_{\alpha\beta} = g_{\alpha\beta} + h_{\alpha\beta}. \quad (4.1)$$

Using this expression in the Einstein equations, applying the Lorenz gauge condition  $\bar{h}^{\mu\nu}{}_{;\nu} = 0$  and retaining terms of  $O(\mu)$ , i.e. linear in  $h_{\alpha\beta}$ , gives the linearised Einstein equations [31]

$$\square \bar{h}_{\mu\nu} + 2R^{\alpha\beta}{}_{\mu\nu} \bar{h}_{\alpha\beta} = -16\pi T_{\mu\nu}, \quad (4.2)$$

where  $\square = g_{\mu\nu} \nabla^\mu \nabla^\nu$ ,  $R_{\alpha\mu\beta\nu}$  is the Riemann tensor of the background spacetime and  $T_{\mu\nu}$  is the perturbing energy momentum tensor. We have also defined the trace reversed metric perturbation

$$\bar{h}_{\mu\nu} = h_{\mu\nu} - \frac{1}{2} g_{\mu\nu} g^{\alpha\beta} h_{\alpha\beta}. \quad (4.3)$$

If we model the object as a point particle, the linearised Einstein equations (4.2) have a delta-function source. Consequently the solution is singular at the particle. Furthermore distributional sources are not well defined in full (non-linear) general relativity. The question is how to use this solution to construct a meaningful description of motion of a small but extended body. We require some physically motivated way of regularising  $h_{\alpha\beta}$  to give a well defined self force.

The idea of the MiSaTaQuWa formalism is to split the solution  $h_{\mu\nu}$  of the linearised Einstein field equations into two parts [24, 25]

$$h_{\mu\nu} = h_{\mu\nu}^{dir} + h_{\mu\nu}^{tail}, \quad (4.4)$$

where the direct field  $h_{\mu\nu}^{dir}$  contains contributions only from the local geometry of the object and contributes to the self force at next-to-leading-order in the mass-ratio. At leading order the self force  $F^\alpha$  depends only on the tail part of the metric  $h_{\mu\nu}^{tail}$  via [19]

$$F^\alpha = \frac{\mu}{2} (g^{\alpha\beta} + u^\alpha u^\beta) (2\bar{h}_{\beta\gamma;\lambda}^{tail} - \bar{h}_{\gamma\lambda;\beta}^{tail}) u^\gamma u^\lambda + O(\mu^2), \quad (4.5)$$

where covariant derivatives are taken with respect to the background metric.

The derivative of the tail field is constructed from integrating the derivative of the retarded Green function for Eqs. (4.2) with appropriate boundary

conditions over the entire past history of the particle's worldline

$$\nabla_\lambda \bar{h}_{\alpha\beta}^{tail} = \mu \lim_{\epsilon \rightarrow 0} \int_{-\infty}^{\tau-\epsilon} \nabla_\lambda G_{\alpha\beta\alpha'\beta'}^{ret}(z(\tau), z(\tau')) u^{\alpha'} u^{\beta'} d\tau', \quad (4.6)$$

where  $z(\tau)$  is the worldline of the particle. The derivative within the integral of Eq. (4.6) is taken with respect to the first argument of the Green function. The regularisation is carried out by excluding the point of coincidence. The scalar self force is also constructed in terms of a worldline integral as we outline below.

## 4.2 Scalar self force

The case of a particle sourcing a scalar field moving on a curved spacetime background interacting with its own self field was considered by Quinn [71]. A particle with scalar charge  $q$  sources a self field which is defined as the solution to the inhomogeneous wave equation

$$\square\Phi(x) = -4\pi\rho(x), \quad (4.7)$$

with

$$\rho(x) = q \int_{-\infty}^{\infty} \delta_4(x, z(\tau)) d\tau. \quad (4.8)$$

Here  $\delta_4(x, x') = \frac{1}{\sqrt{-g}} \delta^4(x - x')$  is the 4-dimensional delta function. Solutions of (4.7) for  $\Phi(x)$  can be found via the retarded Green function as

$$\Phi(x) = \int \sqrt{-g} G_{ret}(x; x') \rho(x') d^4x', \quad (4.9)$$

which gives

$$\Phi(x) = q \int_{-\infty}^{\infty} G_{ret}(x; z(\tau)) d\tau. \quad (4.10)$$

The retarded Green function is defined as a solution of the equation

$$\square G_{ret}(x; x') = -4\pi\delta_4(x, x'), \quad (4.11)$$

with appropriate boundary conditions. The field calculated through Eq. (4.10) is singular at the particle  $x = z(\tau)$ .

The field creates a self force acting on the particle. Quinn [71] showed that the particle experiences the self force as a sum of a history-dependent “tail” force  $F_\alpha^{\text{tail}}$  and an instantaneous “direct” force  $F_\alpha^{\text{dir}}$  which vanishes for geodesic motion in vacuum spacetimes. For non-geodesic motion the instantaneous self force depends on interactions of the scalar field with the local spacetime geometry and contributes to the self force at second order in the scalar charge  $q$ . In the same way, the gravitational self force is fully determined, to leading order in the mass ratio, by the tail force. The history-dependent force is related to the derivative of the history-dependent part of the self field. We only consider the history-dependent “tail” force in this chapter.

Quinn [71] showed that the history-dependent self-field is given by

$$\Phi^{\text{tail}}(z(\tau)) = q \lim_{\epsilon \rightarrow 0^+} \int_{-\infty}^{\tau-\epsilon} G_{\text{ret}}(z(\tau); z(\tau')) d\tau'. \quad (4.12)$$

This is an integral of the retarded Green function over the entire past history of the particle’s worldline up until just before coincidence. The regularisation of the force is carried out by cutting off our integral before coincidence. This cut-off has the effect of removing singular features of the field which do not contribute to the self force. The exclusion of the coincidence point is analogous to the regularisation done in the gravitational case in Eq. (4.6).

The retarded Green function can be used similarly to calculate the field’s self force. The history-dependent self force depends on the derivative of the Green function [71]

$$F_\alpha^{\text{tail}}(z(\tau)) = q^2 \lim_{\epsilon \rightarrow 0} \int_{-\infty}^{\tau-\epsilon} \nabla_\alpha G_{\text{ret}}(z(\tau); z(\tau')) d\tau', \quad (4.13)$$

where the derivative acts on the first argument of the Green function. If the retarded Green function is known globally this would allow us to calculate the self-field along any worldline. Unfortunately constructing the retarded Green

function is not straightforward. The retarded Green function has support both on and within the past lightcone on curved spacetimes.

Certain features of the retarded Green function have been derived analytically. In the near field, the retarded Green function has the form of the Hadamard parametrix [72]. The Hadamard form of the retarded Green function  $G_{ret}(x, x')$  is only valid for  $x'$  in a causal domain of  $x$ , where  $x$  is connected to  $x'$  by a unique geodesic (the normal neighbourhood). A near field form of the retarded Green function is insufficient for calculating the self field (or force) since the field at a point depends on the entire past history of the particle through Eqs. (4.12-4.13).

Outside of a normal neighbourhood, caustics can form. Caustics occur when a congruence of null geodesics emanating from the worldline point  $z(\tau)$  in Eq. (4.13) has a focal point at which the expansion scalar diverges ( $\vartheta \rightarrow \infty$ ). Caustics create singular features in the retarded Green function. In Ref. [61] Ori discovered that, in 4-dimensional spacetime, each time the Green function encounters a caustic it cycles through a fourfold structure. We discuss this fourfold structure in Sec. 4.5.4.

In Ref. [73], Zenginoglu and Galley used a Gaussian approximation for the source in Eq. (4.11) to calculate the retarded Green function. Wardell *et al.* [2] developed a similar method using the Kirchhoff representation. They approximated the initial delta function conditions by a narrow Gaussian. The method outlined in Ref. [2] used a combination of numeric and analytic methods to globally construct the Green function for the Schwarzschild spacetime and consequently the self-force.

The purpose of this chapter is to extend the method of Ref. [2] from Schwarzschild to Kerr. Preliminary results were presented in a conference talk by Casals and Wardell [74] though the calculations presented here were produced independently. Secs. 4.3-4.4 outline the general method for any spacetime as described in Ref. [2]. In Sec. 4.5 we recreate the results of [2] for circular geodesics in Schwarzschild. We describe our method for Kerr in Sec. 4.6 and

first compare with our Schwarzschild results. In Sec. 4.7 we present calculations of the self field  $\Phi$  for circular geodesics and compare with results provided by Warburton [75] calculated using the mode sum method of Ref. [76]. Though we only present circular orbit results here, the key advantage of the method presented in this chapter is that it can be used to calculate the self force for any worldline. We set  $q = 1$  and  $M = 1$  for the remainder of this chapter.

### 4.3 Green function construction

Wardell *et al.* [2] outlined a method for constructing the retarded Green function using the Kirchhoff representation. By choosing appropriate initial conditions, the Kirchhoff representation allows the Green function to be constructed from solutions of the homogeneous wave equation. This method constructs the Green function backwards in time along the worldline.

To construct the retarded Green function we combine three methods:

- In the near field region we make use of a quasilocal expansion. This was defined for Schwarzschild in Ref. [77].
- For intermediate times we use a numerical method using the Kirchhoff representation proposed by Ref. [2].
- At late times we use knowledge of the late time tail given in Ref. [78].

#### 4.3.1 Kirchhoff representation

The Kirchhoff representation [79] gives solutions of the homogeneous wave equation

$$\square\Psi(x) = 0 \tag{4.14}$$

in terms of integrals of the Green function. By specifying initial data on a Cauchy hypersurface  $\Sigma$ , we find solutions at any point  $x'$  in the past history

of  $\Sigma$  by [79]

$$\Psi(x') = -\frac{1}{4\pi} \int_{\Sigma} [G_{ret}(x; x') \nabla^{\mu} \Psi(x) - \Psi(x) \nabla^{\mu} G_{ret}(x; x')] d\Sigma_{\mu}. \quad (4.15)$$

The integral is evaluated with respect to  $d\Sigma_{\mu} = n_{\mu} \sqrt{k} d^3x$ , the surface element on the hypersurface  $\Sigma$ . Here  $n^{\mu}$  is the unit normal and  $k$  is the determinant of the induced metric on the hypersurface  $\Sigma$ .

### 4.3.2 Hypersurfaces

We define a Cauchy hypersurface  $\Sigma$  of constant time by restricting coordinates via

$$\xi(x^{\mu}) = t - t_0 = 0, \quad (4.16)$$

where  $t$  is a time coordinate and  $t_0$  is a constant (see [52] for details). A Cauchy hypersurface is defined such that all causal curves (non-spacelike) passing through the surface  $\Sigma$  pass through only once and map out the entire spacetime. This means that given initial data for a field and its derivative on the hypersurface  $\Sigma$ , with a governing hyperbolic wave equation, solutions of the wave equation uniquely specify the values of the field in both the future and the past. The spatial hypersurface may equivalently be defined by specifying parametric equations  $x^{\mu} = x^{\mu}(y^i)$ , where  $y^i$  are coordinates intrinsic to the hypersurface and  $i = \{1, 2, 3\}$ . Since we have a hypersurface of constant time we have

$$t = t_0, \quad x^i = y^i. \quad (4.17)$$

The unit normal vector  $n_{\mu}$  is defined by [52]

$$n_{\mu} = -\frac{\xi_{,\mu}}{|g^{\alpha\beta} \xi_{,\alpha} \xi_{,\beta}|^{\frac{1}{2}}}. \quad (4.18)$$

This satisfies  $n_{\mu} n^{\mu} = -1$  since the hypersurface is spacelike and therefore the normal vector is timelike. We have  $\xi_{,\mu} = \delta_{\mu}^t$ , thus

$$n_{\mu} = \frac{-\delta_{\mu}^t}{\sqrt{-g^{tt}}}. \quad (4.19)$$

The induced metric on  $\Sigma$  is given by

$$k_{ij} = \frac{\partial x^\mu}{\partial y^i} \frac{\partial x^\nu}{\partial y^j} g_{\mu\nu} = g_{ij}, \quad (4.20)$$

since  $\frac{\partial x^\mu}{\partial y^i} = \delta_i^\mu$ . The induced metric  $k_{ij}$  therefore reduces to the spatial part of the full spacetime metric. Alternatively this can be seen by setting  $dt = 0$  in the line element which reduces to the line element on the hypersurface  $\Sigma$ .

### 4.3.3 Initial data

To construct the self field and self force we require the retarded Green function and its derivatives in Eqs. (4.12-4.13). By choosing initial data for  $\Psi$  at  $t = t_0$  on  $\Sigma$  using delta functions we can construct the Green function and its derivatives from solutions of the homogeneous wave equation (4.14). By choosing different appropriate initial data for  $\Psi$ , different solutions of the wave equation (4.14) give the retarded Green function and its derivatives.

Suitable initial data to find the retarded Green function are

$$\begin{aligned} \Psi(t_0, \mathbf{x}) &= 0, \\ n_\mu \nabla^\mu \Psi(t_0, \mathbf{x}) &= -4\pi \delta_3(\mathbf{x}, \mathbf{x}_0), \end{aligned} \quad (4.21)$$

where  $\delta_3(\mathbf{x}, \mathbf{x}_0) = \frac{1}{\sqrt{k}} \delta_3(\mathbf{x} - \mathbf{x}_0)$  is now the 3-dimensional delta function on the hypersurface  $\Sigma$  and  $k$  is the determinant of the induced metric  $k_{ij}$ . We also use the bold  $\mathbf{x}$  to denote the three spatial coordinates. With these initial conditions we have from Eq. (4.15)

$$\begin{aligned} \Psi(x') &= \int_\Sigma G_{ret}(x; x') \delta_3(\mathbf{x}, \mathbf{x}_0) \sqrt{k} d^3x, \\ &= G_{ret}(x_0; x'). \end{aligned} \quad (4.22)$$

Thus by solving the wave equation (4.14) with initial data (4.21) *backwards* in time we can formulate the retarded Green function globally.

The self force, defined in equation (4.13), depends upon the derivative acting on the first argument of the retarded Green function. We can find such

derivatives by modifying the initial conditions. To find the spatial derivatives of the retarded Green function we use the initial conditions

$$\begin{aligned}\Psi^{(i)}(t_0, \mathbf{x}) &= 0, \\ n_\mu \nabla^\mu \Psi^{(i)}(t_0, \mathbf{x}) &= 4\pi \partial_i \delta_3(\mathbf{x}, \mathbf{x}_0),\end{aligned}\tag{4.23}$$

to give, using integration by parts on Eq. (4.15),

$$\Psi^{(i)}(x') = \partial_i G_{ret}(x_0, x').\tag{4.24}$$

Similarly choosing initial data as

$$\begin{aligned}\Psi^{(t)}(t_0, \mathbf{x}) &= 4\pi \delta_3(\mathbf{x}, \mathbf{x}_0), \\ n_\mu \nabla^\mu \Psi^{(t)}(t_0, \mathbf{x}) &= 0,\end{aligned}\tag{4.25}$$

gives the time derivative of the retarded Green function

$$\Psi^{(t)}(x') = n_\mu \nabla^\mu G_{ret}(x_0, x').\tag{4.26}$$

#### 4.3.4 Gaussian approximation of delta function

A delta function is impractical for numerical calculations and therefore we must find a suitable approximation. In solving the wave equation we decompose the solutions  $\Psi$  into spherical harmonics. To perform a similar decomposition of our initial conditions we make use of an identity for spherical harmonics, given in Eq. (1.17.25) of DLMF [59],

$$\frac{1}{\sin \theta} \delta(\theta - \theta_0) \delta(\phi - \phi_0) = \sum_{l=0}^{\infty} \sum_{m=-l}^{m=l} Y_{lm}(\theta, \phi) Y_{lm}^*(\theta_0, \phi_0).\tag{4.27}$$

Applying this identity to the 3-dimensional delta function gives

$$\delta_3(\mathbf{x} - \mathbf{x}_0) = \sin \theta \delta(r - r_0) \sum_{l=0}^{\infty} \sum_{m=-l}^{m=l} Y_{lm}(\theta, \phi) Y_{lm}^*(\theta_0, \phi_0).\tag{4.28}$$

We now are left with a delta function in only one variable. To allow for numerical initial data we use a Gaussian of finite width  $\sigma$  to approximate the delta function

$$\delta^\sigma(r - r_0) = \frac{1}{(2\pi\sigma^2)^{1/2}} \exp\left[-\frac{(r - r_0)^2}{2\sigma^2}\right], \quad (4.29)$$

such that in the limit as  $\sigma \rightarrow 0$  we recover the delta function. We have used a value of  $\sigma = 0.1M$  throughout this chapter as in Ref. [2].

We use the Gaussian approximation (4.29) in the initial conditions for the field  $\Psi$  given in Eqs. (4.21, 4.23, 4.25). We can use the method presented in Chapter 3 to solve the wave equation (4.14) for both Schwarzschild and Kerr. This Kirchhoff method constructs an approximation to the full solution of the retarded Green function  $G_{ret}^\sigma(x_0, x')$ . This means that  $G_{ret}^\sigma(x_0, x')$  contains the singular nature of the field at coincidence.

The initial Gaussian means that the singular features are spread to some finite  $t > t_0$  and therefore the numerical solution is only valid after some  $t_{min} \sim \sigma$ . We are also limited to some maximum value in time  $t_{max}$  since we cannot integrate indefinitely. Use of this Kirchhoff method therefore constructs an approximation to the retarded Green function  $G^{num}$  for times  $t_{min} < t < t_{max}$ . To calculate the self force through equation (4.13) we require knowledge of the Green function from past infinity all the way up to coincidence. We make use of analytical methods to find both near and far field expansions and amalgamate the three approaches to find the retarded Green function for all past times.

### 4.3.5 Quasi-local expansion

In the region where the points  $x$  and  $x'$  are connected by a unique geodesic, the Green function is uniquely given by the Hadamard parametrix [72]

$$G_{ret}(x, x') = \Theta(x - x')[U(x, x')\delta(\varsigma) - V(x, x')\Theta(-\varsigma)], \quad (4.30)$$

where  $\varsigma = \varsigma(x, x')$  is the Synge world function,  $\Theta$  is the Heaviside step function (given in Eq. (A.8)) and  $U$  and  $V$  are smooth biscalars. Within the normal

neighbourhood  $U(x, x')$  does not contribute to the integrals (4.12-4.13). This is because it is multiplied by  $\delta(\varsigma)$  which only has support when  $x = x'$  and is therefore excluded by the integrals (4.12-4.13). Thus by excluding  $U(x, x')$  in our near field approximation we remove the singular feature at coincidence and can integrate our remaining expressions in Eqs. (4.12-4.13) up to  $t = 0$ .

Attempts to use the Hadamard parametrix to calculate the self-force can be found in [80, 81, 82] using expansions for  $V(x, x')$ . Other authors present expansions in general spacetimes for both geodesic [83] and non-geodesic [84] motion.

In Schwarzschild spacetime a quasi-local expansion is given in Ref. [77]. The coordinate expansion of  $V(x, x')$  which gives the quasi-local expansion, denoted  $G_{ret}^{QL}$ , takes the form

$$G_{ret}^{QL} = -V(x, x') = - \sum_{i,j,k=0}^{\infty} v_{ijk}(r)(t-t')^{2i}(1-\cos\gamma)^j(r-r')^k, \quad (4.31)$$

where  $\cos\gamma$  was given in Eq. (3.17). The  $v_{ijk}(r)$  are analytic functions of  $r$ . To find a quasi-local expansion for the derivatives we directly take derivatives of Eq. (4.31). In Ref. [77] they also propose a Padé resummation which increases the accuracy and region of validity.

For the Kerr calculation we make use of as yet unpublished results for the near field expansion courtesy of Wardell [85]. The Kerr quasi-local expansion is calculated from Ref. [83] as an application of their Eqs. (B4) and (3.9b) adapted to the Kerr spacetime. Unfortunately we currently only have up to fourth order terms in powers of  $(t-t')^n$  in the expansion for Kerr spacetime compared with  $n = 26$  for Schwarzschild spacetime.

### 4.3.6 Late time tail

It is known [78] that at late times the Green function for Schwarzschild has the same functional form in time as perturbations to the black hole. Initial work on scalar perturbations of the Schwarzschild metric by Price [86, 87] showed that

at late times the perturbation decays with a power law behaviour with leading order of  $t^{-2l-3}$  for each spherical harmonic  $l$  mode. The late time behaviour is related to the form of the potential in the radial perturbation equation at large radius. Recent work [78] has expanded to higher orders. A new non-power-law term  $t^{-2l-5} \ln(t/M)$  was found in Ref. [78] using the method detailed in Ref. [88]. The late time tail in Kerr was shown to have the same power law and log behaviour in Ref. [89].

We use knowledge of this late time behaviour to fit our numerical data at late times so that we can integrate to infinity. We first find the retarded Green function along a worldline as a function of time. We use *Mathematica's* `Fit` function to fit numerical data for  $G_{ret}$  at late times to the expansion

$$G_{ret}^{late} = at^{-3} + bt^{-4} + ct^{-5} + d \ln(t)t^{-5} + O(t^{-6}) \quad (4.32)$$

to find the coefficients  $\{a, b, c, d\}$ . The series (4.32) is in principle infinite in negative powers of  $t$ . We choose to cut off at  $t^{-5} \ln(t)$  since higher order terms are smaller than the magnitude of numerical errors. The late time behaviour for the spatial derivatives of the retarded Green function takes the same form as Eq. (4.32). For the time derivative we can just take the time derivative of Eq. (4.32).

## 4.4 Worldline integration

The preceding sections have outlined how to calculate the Green function and its derivatives globally as a function of time  $G(t_0, \mathbf{x}_0; t, \mathbf{x})$ , given an initial fixed point  $x_0$ . Given  $G(t_0, \mathbf{x}_0; t, \mathbf{x})$  we can then construct the Green function along a specific worldline. We can in principle choose any worldline which ends at  $x_0$  by specifying functions for the coordinates backwards in time  $\mathbf{x}(t)$ . For example we can choose to calculate along geodesics by solving the geodesic equations.

To calculate the self-field at the initial point  $x_0$  we then integrate over the

past worldline of the particle and Eq. (4.12) becomes

$$\Phi^{tail}(t_0, \mathbf{x}_0) = \int_{-\infty}^{t_0} G_{ret}(t_0, \mathbf{x}_0; t, \mathbf{x}(t)) \frac{dt}{u^t}, \quad (4.33)$$

where  $u^t = \frac{dt}{d\tau}$  along the geodesic. We no longer have a limit, as in Eq. (4.12), since we have excluded the singular part at coincidence by ignoring  $U(x, x')$  in the near field expansion Eq. (4.31). Similarly we can construct the self-force using the derivative of the Green function from Eq. (4.13) giving

$$F_{\alpha}^{tail}(t_0, \mathbf{x}_0) = \int_{-\infty}^{t_0} \partial_{\alpha} G_{ret}(t_0, \mathbf{x}_0; t, \mathbf{x}(t)) \frac{dt}{u^t}. \quad (4.34)$$

We summarise the key steps of the method here. We begin with a numerical method to solve the homogeneous wave equation (4.14). Making use of the Kirchhoff formula (4.15) we use this solution to construct the Green function  $G^{num}$  for a set of intermediate times  $t_{min} < t < t_{max}$ . We then construct a near field quasi-local analytic expansion  $G_{ret}^{QL}$  Eq. (4.31) using the Hadamard parametrix from Eq.(4.30) valid in the region  $t_0 < t < t_{min}$ . For the late times  $t > t_{max}$  we fit our numerical Green function data to the power law behaviour including the log terms  $G_{ret}^{late}$  via Eq. (4.32). We find each of these functions along a specific worldline and can then find the self field via Eq. (4.12) written schematically as

$$\Phi^{tail} = \int_{-t_{min}}^{t_0} G_{ret}^{QL} + \int_{-t_{max}}^{-t_{min}} G_{ret}^{num} + \int_{-\infty}^{-t_{max}} G_{ret}^{late}. \quad (4.35)$$

The steps to calculate the self force are equivalent where the relevant derivatives of the Green function are used in Eq. (4.13) in place of the Green function. In practice we choose our  $t_{min}$  by finding the value of  $t$  for which the difference between the numerical and quasi-local expansions is smallest. The value  $t_{max}$  is chosen so that the the late time tail (4.32) is an accurate description of the Green function up to some error.

## 4.5 Schwarzschild method

In this section we calculate the self field and force on Schwarzschild spacetime and compare our results with those presented in Wardell *et.al.* [2]. In Sec. 4.6 we will present a method to calculate the self field and force on Kerr spacetime. By developing an independent method for Schwarzschild spacetime we are able to compare with the Kerr method when  $a = 0$ . This allows us to highlight the additional sources of error due to the additional complexities which arise because of rotation.

In Chapter 3 we solved the scalar wave equation on Schwarzschild spacetime. We use the method outlined there with different initial conditions that we give below in Sec. 4.5.1. Since Schwarzschild spacetime is spherically symmetric and the initial conditions are axisymmetric, we can decompose the field in terms of Legendre polynomials as we did in Eq. (3.16):

$$\Psi(t, r, \theta, \phi) = \sum_{l=0}^{\infty} \frac{1}{r} (2l+1) \Psi_l(t, r) P_l(\cos \gamma), \quad (4.36)$$

where  $\cos \gamma$  was given in Eq. (3.17). We only solved for a certain maximum number of  $l$  modes  $l_{max}$ . To prevent any high frequency numerical errors we used a smooth cut-off via a prefactor  $e^{-l^2/2l_{cut}^2}$  in the summation of Eq. (3.29) and we do this again in Eq. (4.36). In Ref. [60] the cut-off was shown to be related to the smoothing of the delta function via a Gaussian of width  $\sigma$  Eq. (4.29). The smallest angular resolution from the  $l$ -mode sum (4.36) is approximately  $2\pi/l_{cut}$  whilst the resolution of the Gaussian is approximately  $\sigma/r_0$ . For values of  $l_{cut}$  for which  $2\pi/l_{cut} \ll \sigma/r_0$  we obtain diminishing returns from the higher  $l$ -modes.

### 4.5.1 Kirchhoff representation for Schwarzschild space-time

We decompose the Green function by

$$G(t_0, \mathbf{x}_0; x') = \sum_{l=0}^{\infty} \frac{1}{r_0} \frac{1}{r'} G_l(t_0, r_0; t', r') P_l(\cos \gamma'), \quad (4.37)$$

where  $(t_0, \mathbf{x}_0)$  is some initial point at which we calculate the self field.

The Kirchhoff formula Eq. (4.15) then reduces to

$$\Psi_l(t', r') = \int_{-\infty}^{\infty} [G_l(t_0, r_0; t', r') \partial_t \Psi_l(t, r) - \Psi_l(t, r) \partial_t G_l(t_0, r_0; t', r')] dr^*, \quad (4.38)$$

where  $r^*$  is the Schwarzschild tortoise coordinate defined in Eq. (3.20).

The Kirchhoff formula given in the form of Eq. (4.38) allows us to choose initial conditions for each  $l$  mode of the field  $\Psi_l$ . These will be different from the initial conditions given in Sec. 4.3.3 due to the different decompositions of the field (4.36) and the Green function (4.37).

To find the  $l$  modes of the Green function we use the initial conditions

$$\begin{aligned} \Psi_l(t_0, r_0) &= 0, \\ \partial_t \Psi_l(t_0, r_0) &= \delta(r^* - r_0^*), \end{aligned} \quad (4.39)$$

so that  $\Psi_l(t', r') = G_l(t_0, r_0, t', r')$ . Angular derivatives of the Green function can be found by using solutions for  $\Psi_l(t', r')$  from the initial conditions of Eq. (4.39) and taking derivatives of the Legendre polynomials in Eq. (4.37).

We can find similar simplifications for radial and time derivatives of the Green function. Using the initial conditions

$$\begin{aligned} \Psi_l^{(r)}(t_0, r_0) &= 0, \\ \partial_t \Psi_l^{(r)}(t_0, r_0) &= -\frac{f}{r} \partial_r \left[ \frac{1}{f} \delta(r^* - r_0^*) \right], \end{aligned} \quad (4.40)$$

where  $f$  is given in Eq. (3.2), gives the radial derivatives of the  $l$  modes of the Green function

$$\Psi_l^{(r)}(t', r') = \partial_{r_0} \left[ \frac{1}{r_0} G_l(t_0, r_0, t', r') \right], \quad (4.41)$$

using integration by parts.

For the time derivative of the Green function we use the initial conditions

$$\begin{aligned} \Psi_l^{(t)}(t_0, r_0) &= \delta(r^* - r_0^*), \\ \partial_t \Psi_l^{(t)}(t_0, r_0) &= 0, \end{aligned} \quad (4.42)$$

which give

$$\Psi_l^{(t)}(t', r') = \partial_{t_0} G_l(t_0, r_0, t', r'). \quad (4.43)$$

We use a Gaussian approximation to the delta function in  $r^*$  given by Eq. (4.29) with  $r$  replaced by  $r^*$ .

## 4.5.2 Numerical method

We use the method of Chapter 3 to solve the homogeneous wave equation. We solve for 200  $l$  modes with a step size in  $r^*$  of 0.02 and a maximum time  $t_{max} = 300$ . This yields an approximation to the retarded Green function. We can then choose a worldline and construct the retarded Green function as a function in time along that worldline.

For early times we make use of the quasi-local expansion presented in Ref. [77] and given in Eq. (4.31). The expansions presented there are available from Wardell's website [90] in the form of Mathematica notebooks. We then evaluate in Eq. (4.31) as a function of time along the worldline. Padé resummation is proposed in Ref. [77] as a way to increase accuracy and expand the region of validity. The Padé resummation method to the series expansion is done by using *Mathematica's* `PadeApproximant` function by Wardell [90].

In Fig. 4.1 we plot the quasi-local expansion for the retarded Green function  $G_{ret}^{QL}$  and the numeric calculation  $G_{ret}^{num}$ . The Green functions plotted in

Matching the quasi-local and numeric Green functions for Schwarzschild spacetime

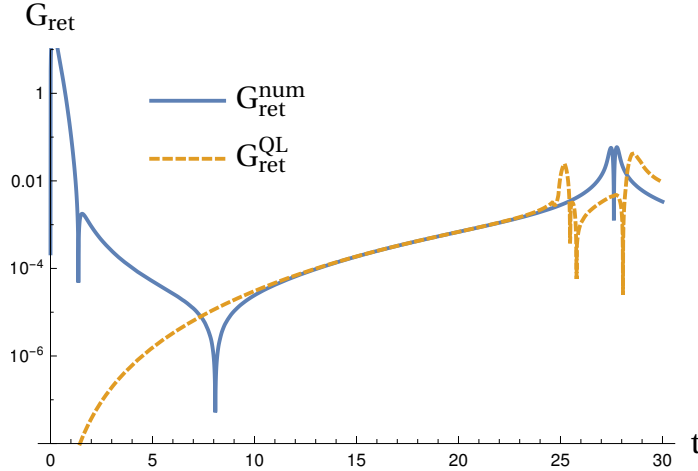


Figure 4.1: The numeric Green function  $G_{ret}^{num}$  and quasi-local Green function  $G_{ret}^{QL}$ . We can clearly see the effect of using the Gaussian approximation to the delta function in the initial conditions. The quasi-local expansion breaks down at late times. There is some intermediate region  $15 \lesssim t \lesssim 20$  for which the two solutions coincide.

Fig. 4.1 are for circular orbits at  $r_0 = 6$  as outlined in the following section, Sec. 4.5.3. At early times we observe the effect of using the finite-width Gaussian approximation to delta functions in the initial conditions. The quasi-local expansion  $G_{ret}^{QL}$  breaks down for larger values of  $t$ . There is some intermediate region  $15 \lesssim t \lesssim 20$  in which we can match the two solutions.

The late time tail is straightforward to calculate once the numeric Green function is given as a function of time along the worldline. We use *Mathematica's* `Fit` function to fit numerical data at late times, in the region  $150 < t < 250$ , to find the coefficients  $\{a, b, c, d\}$  in the series defined in Eq. (4.32).

### 4.5.3 Worldline integration

We calculate the self force and self field for circular geodesic orbits on Schwarzschild. In Sec. 3.2.1 we discussed geodesics on Schwarzschild. For circular orbits at constant radius  $r_0$  we have the tangent vector from Eqs. (3.13)

$$u^t = \frac{1}{\sqrt{1 - \frac{3}{r_0}}}, \quad u^\phi = u^t \Omega, \quad (4.44)$$

with orbital frequency given by Eq. (3.14) as  $\Omega = \sqrt{\frac{1}{r_0^3}}$  and  $u^r = u^\theta = 0$ . The radial  $r = r_0$  and angular  $\theta = \frac{\pi}{2}$  coordinates are constant. The azimuthal coordinate is given by

$$\frac{d\phi}{dt} = \frac{u^\phi}{u^t} = \Omega, \quad \phi = \Omega t + \phi_0. \quad (4.45)$$

In Table 4.1 we compare our results with those presented in Table I of Ref. [2] which is a previous implementation of the worldline integration method. We also compute the relative difference with results from the frequency domain method of Ref. [91] which is claimed to be highly accurate. We have not attempted to push our numerical code to match that of Ref. [2] since our goal is not to match their results but to allow for us to compare with our Kerr spacetime results. Our results are not as accurate as those presented in Ref. [2] due to our choices of step size and  $t_{max}$ . Our numerical code uses a greater step size of 0.02 versus 0.01 in discretising the numerical grid. We integrate to  $t_{max} = 300$  rather than  $t_{max} = 400$ .

In Fig. 4.2 we plot the Green function and its derivatives. We observe that the magnitude of the retarded Green function is generally much greater than its derivatives. This means that the spreading of the singular features, due to using a narrow Gaussian may contribute more to the integrals (4.13) for the self force than the self field (4.12). We suggest that this accounts for the greater errors found for the self force shown in Table 4.1. Figure 4.2 also highlights the singular features for the Green function and its derivatives occur at the same times as they cycle through the fourfold structure.

Numerical Schwarzschild results		
$r_0 = 6$	Calculated value	Relative difference
$\Phi$	<b><math>-5.45452 \times 10^{-3}</math></b>	<b><math>6 \times 10^{-5}</math></b>
	$-5.45517 \times 10^{-3}$	$6 \times 10^{-5}$
$F_t$	<b><math>3.60685 \times 10^{-4}</math></b>	<b><math>6 \times 10^{-4}</math></b>
	$3.60779 \times 10^{-4}$	$4 \times 10^{-4}$
$F_r$	<b><math>1.68588 \times 10^{-4}</math></b>	<b><math>5 \times 10^{-3}</math></b>
	$1.67861 \times 10^{-4}$	$8 \times 10^{-4}$
$F_\phi$	<b><math>-5.30559 \times 10^{-3}</math></b>	<b><math>2 \times 10^{-4}</math></b>
	$-5.30452 \times 10^{-3}$	$5 \times 10^{-5}$

Table 4.1: Numerical results for the self field and self force for Schwarzschild spacetime for a particle in a circular orbit at  $r_0 = 6$ . We present our results in **bold**. For reference results taken from Table. I in Ref. [2] are quoted below. We compute the relative error by comparing with results from the frequency domain mode sum method of Ref. [91].

Schwarzschild Green functions

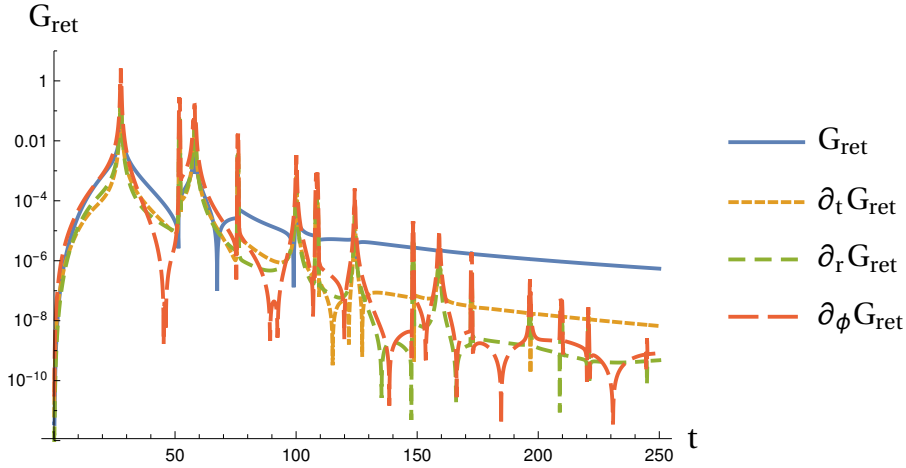


Figure 4.2: Green function and derivatives along a circular geodesic worldline with  $r_0 = 6$ . The log scale highlights the power-law decay of the Green function and its derivatives according to Eq. (4.32).

Fourfold structure of Green function

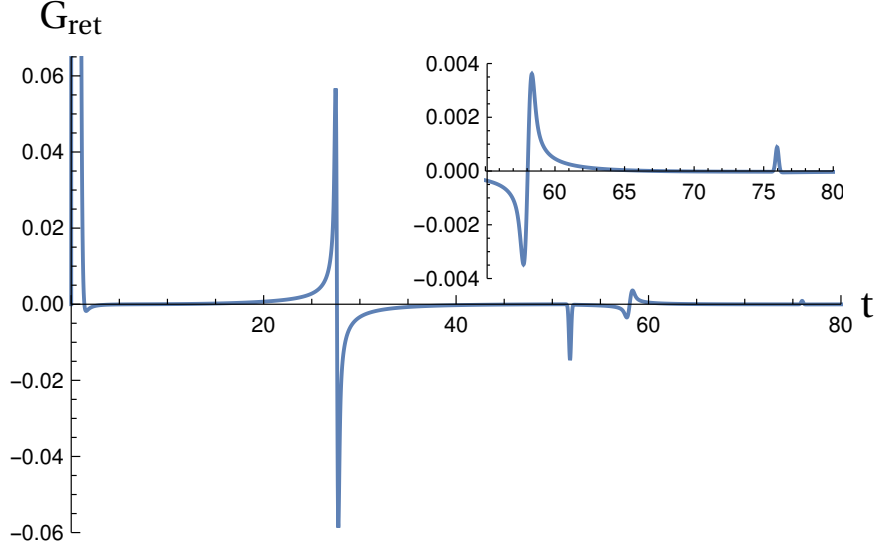


Figure 4.3: Green function along a circular geodesic worldline with  $r_0 = 6$ . The Green function cycles through a fourfold sequence in agreement with Eq. (4.46).

#### 4.5.4 Fourfold structure

In Ref. [61] Ori discovered that, in 4-dimensional spacetime, each time the Green function encounters a caustic it has a singular feature which cycles through a fourfold structure. The fourfold structure was further investigated in Ref. [62] where they showed the singular features of the Green function on Schwarzschild spacetime cycles through the fourfold structure

$$\delta(\varsigma) \rightarrow \frac{1}{\pi\varsigma} \rightarrow -\delta(\varsigma) \rightarrow -\frac{1}{\pi\varsigma} \rightarrow \dots \quad (4.46)$$

where  $\varsigma$  is the Synge world function. In Fig. 4.3 we plot the Green function along the worldline of a circular geodesic. We can clearly see the cycling through of the fourfold structure with the singular nature of Eq. (4.46) is smeared due to our use of Gaussian initial conditions (4.29).

### 4.5.5 Summary of errors

The method has a number of sources of error. Ref. [2] goes into further detail on the qualitative nature of these sources of error. We emphasise that the purpose of this chapter is to extend the worldline integration method to the Kerr spacetime. To this end we summarise the sources of error here with the expectation that they carry forward to Kerr spacetime.

For our numerical method we replace delta function initial data with a narrow Gaussian using Eq. (4.29). This has the effect of smoothing out sharp singular features in the Green function. The error arising from Gaussian initial data is related to the error from cutting off the infinite sum of  $l$  modes as described in Ref. [60]. The numerical method also has the usual numerical errors arising from discretising the spatial grid and taking finite time steps.

At early times we use a series expansion for the Green function using Eq. (4.31). This series decreases in accuracy the later in time it is used. Errors arising from the series expansion are also related to the cut-off in  $l$  modes in the summation of Eq. (4.36). This is because using higher  $l$  modes allows the numerical method to more accurately construct the Green function for early times. We exploit this in our Kerr method, where we only have access to lower order terms in the Taylor expansion.

Finally we use numerical fitting at late times. This has the effect of ignoring any non-tail-like (e.g. singular) features past  $t = t_{max}$ . On calculating the integral of the late time tail we find that it contributes only a small amount to the self field and even less to the self force calculations.

## 4.6 Kerr method

In extending to Kerr spacetime, we have a number of additional challenges. Our numerical method relies on Sec. 3.3, where we solved the homogeneous wave equation by solving a set of coupled radial equations. We made a coor-

dinate transformation to the azimuthal coordinate  $\varphi$  in Eq. (3.48). We also decomposed the field in terms of spherical harmonic modes using Eq. (3.49). The initial conditions must therefore also be decomposed into spherical harmonics.

### 4.6.1 Initial conditions

We begin with initial conditions for the self field given in Eq. (4.21). The condition on the field is trivial,  $\Psi(t_0, \mathbf{x}) = 0$  implies that  $\psi_{lm}(t_0, r_0) = 0$ . However, in considering the derivative, we find couplings between  $l$ -modes similar to the couplings in the equations for the  $lm$  modes (3.54). We convert the delta function in the initial conditions (4.21) to a function of  $r^*$ , given in Eq. (3.57), via

$$\delta(r - r_0) = \frac{dr^*}{dr} \delta(r^* - r_0^*) = \frac{r^2 + a^2}{\Delta} \delta(r^* - r_0^*). \quad (4.47)$$

The induced metric on the hypersurface of constant  $t_0$ ,  $\Sigma$  is given by  $k_{ij} = g_{ij}$ , from Eq. (4.20), with determinant

$$k = \rho^4 \sin^2 \theta (-g^{tt}). \quad (4.48)$$

We substitute (4.47,4.48) into the initial conditions, given in Eq. (4.21), to obtain

$$\frac{-g^{t\mu} \partial_\mu \Psi(t_0, \mathbf{x})}{|g^{tt}|^{1/2}} = -4\pi \frac{(r^2 + a^2)}{\rho^2 \Delta |g^{tt}|^{1/2}} \delta(r^* - r_0^*) \sum_{l=0}^{\infty} \sum_{m=-l}^l Y_{lm}(\theta, \varphi) Y_{lm}^*(\theta_0, \varphi_0). \quad (4.49)$$

Noting that  $g^{t\mu} \partial_\mu \Psi(t_0, \mathbf{x}) = (g^{tt} \partial_t + g^{t\varphi} \partial_\varphi) \Psi(t_0, \mathbf{x})$  and  $\partial_\varphi \Psi(t_0, \mathbf{x}) = 0$  since  $\Psi(t_0, \mathbf{x}) = 0$ , gives

$$-g^{tt} \partial_t \Psi(t_0, \mathbf{x}) = 4\pi \frac{(r^2 + a^2)}{\rho^2 \Delta} \delta(r^* - r_0^*) \sum_{l=0}^{\infty} \sum_{m=-l}^l Y_{lm}(\theta, \varphi) Y_{lm}^*(\theta_0, \varphi_0). \quad (4.50)$$

We then substitute the decomposition of the field (3.49) into the initial conditions (4.50). Multiplying Eq. (4.50) by  $\sin\theta Y_{lm}(\theta, \varphi)$  and integrating over angular coordinates, we find initial conditions for the time derivative of the  $lm$  modes  $\dot{\psi}_{lm}(t_0, r_0)$  satisfy

$$\begin{aligned} & [\Sigma_0^2 + a^2 \Delta c_{ll}^m] \dot{\psi}_{lm}(t_0, r_0) + a^2 \Delta \left( c_{l,l+2}^m \dot{\psi}_{l+2,m}(t_0, r_0) + c_{l,l-2}^m \dot{\psi}_{l-2,m}(t_0, r_0) \right) \\ & = -4\pi r(r^2 + a^2) Y_{lm}^*(\theta_0, \varphi_0) \delta(r^* - r_0^*), \end{aligned} \quad (4.51)$$

where  $\Sigma_0$  was defined in Eq. (3.55). Here we have used the identities for  $c_{l,j}$ , given in Eq. (3.53), from Ref. [69] to decompose into  $lm$  modes through coupling coefficients  $c_{l,j}$ . The left hand side of Eq. (4.51) is the same left hand side as the wave equation (3.54). Thus we can use the methods in Sec. 3.3 (using the inverse matrix  $\mathbf{A}^{-1}$  of Eq. (3.62)) to find initial conditions for each  $lm$  mode.

To find the angular derivatives of the Green function, we can simply use the numerical results for  $G_{ret}$  and take derivatives of the spherical harmonics in the summation of Eq. (3.49).

The initial conditions required to find the radial derivative of the Green function (4.23) follows. We use the radial derivative of the delta function related to the derivative of the delta function with respect to  $r^*$ , using the definitions in Appendix A, as

$$\delta'(r - r_0) = \frac{r^2 + a^2 r_0^2 + a^2}{\Delta} \frac{r_0^2 + a^2}{\Delta_0} \delta'(r^* - r_0^*), \quad (4.52)$$

where  $\Delta_0$  is the value of  $\Delta$  at  $r_0$ . Using this in the initial conditions (4.23) and decomposing into  $lm$  modes gives an equation equivalent to Eq. (4.51) with the replacement

$$\delta(r^* - r_0^*) \rightarrow \frac{r_0^2 + a^2}{\Delta_0} \delta'(r^* - r_0^*). \quad (4.53)$$

The initial conditions to find the time derivative of the Green function (4.25) is much simpler since the initial time derivative of the field is zero. The

initial conditions in  $lm$  modes are given by

$$\psi_{lm}(t_0, r_0) = 4\pi \frac{r(r^2 + a^2)}{\Delta} Y_{lm}^*(\theta_0, \varphi_0) \delta(r^* - r_0^*). \quad (4.54)$$

Finally we can use the Gaussian approximation to the delta function from Eq. (4.29) in all of the above initial conditions.

### 4.6.2 Worldline integration

We need to choose a specific worldline along which to integrate. In principle we can use the same numerical data for  $G_{ret}(x_0, x)$  to calculate the self field (or force) for a family of worldlines that go through the base point  $x_0$ . In practice we would like to calculate values that we can compare with other methods as an initial check on the accuracy and validity of our method. Following this we can then calculate the self-field for other physically relevant worldlines. Mode-sum methods have succeeded in calculating the self force on various geodesic orbits; circular [76], eccentric [92] and inclined circular [93].

We construct the worldline by solving the geodesic equations. In Sec. 3.3.1 we discussed geodesics for Kerr spacetime. For circular orbits at radius  $r = r_0$  in the equatorial plane  $\theta = \frac{\pi}{2}$  we have  $u^r = u^\theta = 0$  and

$$\begin{aligned} u^t &= \frac{r^{3/2} + a}{r^{3/2} \sqrt{1 - \frac{3}{r} + \frac{2a}{r^{3/2}}}}, \\ u^\phi &= u^t \Omega, \end{aligned} \quad (4.55)$$

with  $\Omega = \frac{1}{r_0^{3/2} + a}$  from Eqs. (3.46-3.47). The expressions (4.55) reduce to the Schwarzschild values (4.44) on setting  $a = 0$ . We have also changed our azimuthal coordinate through Eq. (3.48), however since  $dr/dt = 0$ ,

$$\frac{d\varphi}{dt} = \frac{d\phi}{dt} = \Omega \quad (4.56)$$

giving  $\varphi = \Omega t + \varphi_0$ .

Quasi-local Green function comparison of Schwarzschild and Kerr expansions

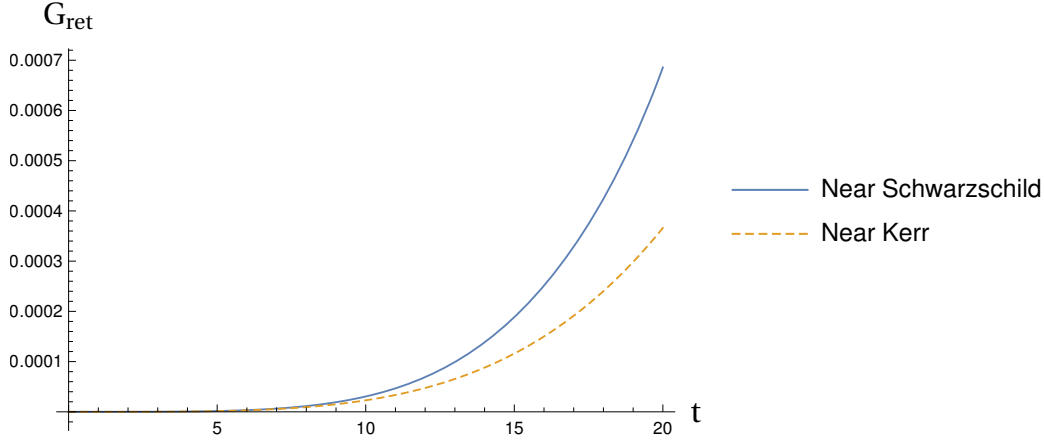


Figure 4.4: Comparisons of the quasi-local expansion of the Green function of Eq. (4.31) for the Kerr (with  $a = 0$ ) and Schwarzschild spacetime. We observe that the two expansions disagree at  $t \approx 10$ .

### 4.6.3 Numerical method

For late times we know [89] that the retarded Green function takes the same form as that for Schwarzschild, given in Eq. (4.32). We therefore can use the same fitting algorithm as described in Sec. 4.3.6. At early times we do not have as accurate expansions in Eq. (4.31) of the retarded Green function compared with the Schwarzschild case. We only have terms up to fourth order in  $(t - t_0)$  from, Wardell [85], compared with 26 orders for Schwarzschild. Figure 4.4 compares quasi-local expansions for both Kerr (with  $a = 0$ ) and Schwarzschild spacetimes for a circular orbit at  $r_0 = 6$ . We can see that the quasi-local expansions for Kerr and Schwarzschild spacetimes disagree at  $t \approx 10$ . In the Schwarzschild case we matched this expansion in the region  $15 \lesssim t \lesssim 20$ . Due to the lack of higher order terms in the quasi-local expansion for Kerr we require highly accurate numerical data at early times up to  $t \approx 10$  for matching purposes.

We also need to solve out to the region dominated by the late time tail. To

## Quasi-local expansions compared with numerical data

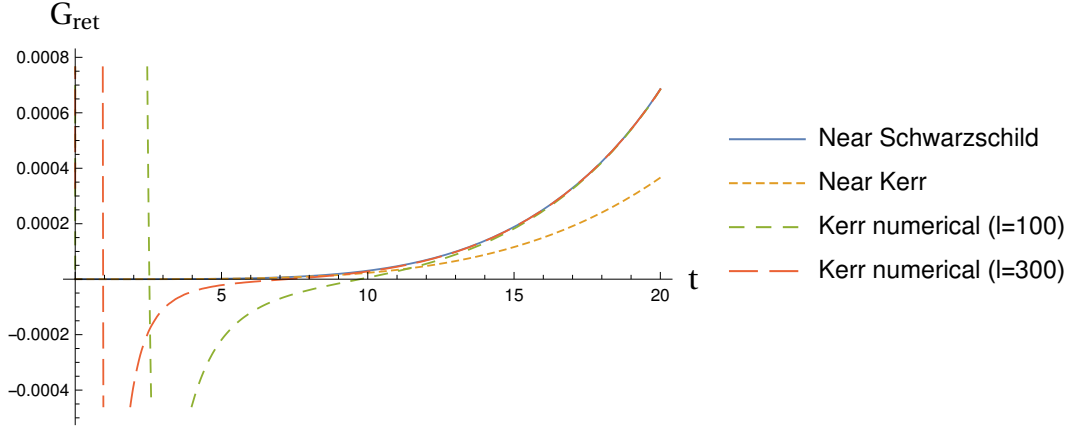


Figure 4.5: Comparisons of numerical methods using  $l = 100$  (green) and  $l = 300$  (red) modes with quasi-local expansions on Schwarzschild (blue) and Kerr (with  $a = 0$ ) (yellow) spacetimes. We observe that there is a region  $10 \lesssim t \lesssim 15$  in which the neither the Kerr near field expansion nor the  $l = 100$  data match the Schwarzschild result. The  $l = 300$  data is used in this region to provide an accurate result for the retarded Green function.

overcome this we employ two versions of our numerical method. We use the method outlined in Sec. 3.3.2 to solve the wave equation (4.14). This method involved solving  $\Psi$  in terms of  $l$ -modes. Since at late times the Green function is dominated by its low  $l$ -modes we solve for high  $l_{max}$  for early times and lower  $l_{max}$  for late times. For early times we typically solve for  $l_{max} = 300$  up to a  $t_{max} = 25$ . This is sufficient to match to the quasi-local expansion around  $t \approx 10$ . We then solve for  $l_{max} = 100$  out to a  $t_{max} = 250$  and match the two numerical methods at  $t = 25$ . We illustrate this in Fig. 4.5, where we plot the two numerical calculations for the retarded Green function with the near field approximations. As we know the form of the late time tail from Eq. (4.32) we can numerically fit the coefficients in Eq. (4.32) over the region  $t = [150, 250]$ .

#### 4.6.4 Summary of errors

The method presented in this section to calculate the self field and self force for Kerr spacetime contains all of the same sources of error discussed in Sec. 4.5.5. The late time tail follows the same fitting algorithm and therefore contributes errors of a similar magnitude.

The quasi-local expansion is much less accurate since we only have access to four orders in  $(t - t_0)$  compared with 26 in the Schwarzschild case. We go some way to mitigating this by using a more accurate numerical construction of the Green function calculating 300  $l$ -modes, as illustrated in Fig. 4.5.

Our numerical method involves decomposing the field into  $lm$  modes via Eq. (3.49). We then find solutions by solving the scalar wave equation (4.14) as a set of coupled  $(1 + 1)D$  equations (3.54). Whilst Eqs. (3.54) decouple for  $m$  modes, the  $l$  modes only decouple into two sets of coupled equations for even and odd values of  $l$ . This means that for each  $m$  mode we must solve the sets of odd and even  $l$  mode equations simultaneously. Therefore the Kerr method involves evolving a set of  $(l_{max} - m) \times n$  functions for each  $m$  mode, where  $n$  is the size of the spatial grid. Compare this with the Schwarzschild method, which involves a set of  $l$  modes evolving independently on a spatial grid of  $n$  points. This increased numerical challenge impacts upon accuracy since we cannot solve for the same  $l_{max}$  due to time and memory constraints.

There is an additional source of error in the Kerr spacetime case. Since the equations for Kerr spacetime (3.54) are coupled, the cut-off at  $l_{max}$  creates a boundary in the equations which could cause numerical error. We mitigate this by multiplying our initial conditions (4.52) by the smoothing factor  $e^{-l^2/2l_{cut}^2}$ .

Numerical results for  $\Phi$  on circular orbits at  $r_0 = 6$  with  $a = 0$ 

	$\Phi$	Relative Error
Schwarzschild	$-5.45452 \times 10^{-3}$	$6 \times 10^{-5}$
Kerr ( $l = 100$ ) with Schwarz QL	$-5.46003 \times 10^{-3}$	$9 \times 10^{-4}$
Kerr ( $l = 100$ ) with Kerr QL	$-5.51612 \times 10^{-3}$	$1 \times 10^{-2}$
Kerr QL+Kerr ( $l = 300$ ) +Kerr ( $l = 100$ )	$-5.48185 \times 10^{-3}$	$5 \times 10^{-3}$

Table 4.2: Calculations of the self field for a particle on a circular orbit at  $r_0 = 6$  using different methods for  $a = 0$ . In all cases we use the same late-time tail. The first two lines present  $\Phi$  using the same Schwarzschild quasi-local expansion SchwarzQL with the numerical Green function given by Schwarzschild code and Kerr code. The third line uses the quasi-local expansion for Kerr with the Kerr code. The fourth line adds to this the higher accuracy Kerr code.

## 4.7 Results

### 4.7.1 Schwarzschild comparison

As a first check, we used the Kerr method with  $a = 0$  to allow us to compare with our Schwarzschild method. This enables us to estimate errors over and above that of the Schwarzschild method. In Table 4.2 we present results using both methods. Comparison of the first two lines, for which the same Schwarzschild quasi-local (QL) expansion was used, make it clear that there is a loss of accuracy from the numerical method of approximately one order of magnitude. When we use the Kerr QL expansion we lose accuracy by a further  $O(10^{-2})$ , as shown in the third line. Finally when we include the higher accuracy numerical data with  $l = 300$  modes we find that we meet in the middle with an relative error of  $O(10^{-3})$ . We infer from this that the best results from our Kerr code can be expected to be accurate up to a relative error of  $O(10^{-3})$ .

Field value comparisons for circular orbits on Kerr

$\Phi$				
$r_0$	$a$	Computed Value	Quoted Result	Relative Error
6	0.5	-0.00392534	-0.00389824	$7 \times 10^{-3}$
	0.7	-0.00335124	-0.00333783	$4 \times 10^{-3}$
	0.9	-0.00279115	-0.00280434	$5 \times 10^{-3}$
10	0.7	-0.000753777	-0.00075792	$5 \times 10^{-3}$
	0.9	-0.000638622	-0.00067883	$6 \times 10^{-2}$

Table 4.3: Comparisons of our results for the self field  $\Phi$  for a particle on a circular orbit on the Kerr spacetime with results from the mode sum method of Ref. [76] provided by Warburton [75].

### 4.7.2 Kerr results

In Table 4.3 we present results for the self field of a particle on a circular orbit for a number of different values of  $a$ . We compare with results provided by Warburton [75] using the frequency domain mode-sum method of Ref. [76]. We see agreement up to a relative error of  $O(10^{-3})$  which is as much as can be expected given the estimated accuracy from Sec. 4.7.1.

## 4.8 Conclusions and discussion

In this chapter we have extended the worldline integration method for calculating the self field or force of Ref. [2] from the Schwarzschild spacetime to Kerr spacetime. Our method involves a combination of analytic expansions at early and late times with a numerical calculation for intermediate times. We have shown in Table 4.3 that our results for the self field agree with results from the mode sum method of Ref. [76].

In Table. 4.2 we calculated the self field for  $a = 0$  in order to compare with the Schwarzschild method. There is some loss of accuracy due to additional numerical challenges in Kerr above those of Schwarzschild as discussed

in Sec. 4.6.4. We can in principle reduce these errors by increasing the number of  $lm$  modes calculated and increasing the maximum time. Due to the finite width Gaussian in the initial conditions, we are always in need of the quasi-local expansion. We conclude that the accuracy of the quasi-local expansion is a limiting factor in the accuracy of our results.

We used the method in this chapter to calculate the self force. In principle the method may calculate the self force. However, we found the results to lack enough accuracy to be presented here. We again conclude that the low order quasi-local expansion is the limiting factor.

Having shown that the methods presented in this chapter can calculate the self field by comparing with the mode sum method of Ref. [76], we could move on to calculate self force for worldlines not yet considered in the literature. The fruitfulness of such investigations is perhaps questionable since we would not expect the results to be very accurate. Instead, an interesting consequence of this method is that it allows us to investigate how a particle's worldline interacts with the global Green function. In Fig. 4.6 we plot the Green function "globally" in the equatorial plane and we plot the worldline from  $t_0$ . Below this we plot the Green function against time along the worldline. We observe the fourfold structure of the Green function first discussed in Sec. 4.5.4. By investigating the Green function in this way we can clearly see how the fourfold structure in the Green function [61] arises from crossing of the wavefront.

One particular interesting investigation would be to examine the highly eccentric orbits around a Kerr black hole recently considered in Ref. [94]. They observe "wiggles" in the self force calculated on the outward leg of an eccentric orbit and postulate that these "wiggles" are created by the the excitation of quasinormal modes as the particle travels close to the black hole. A possible further project could be to investigate the behaviour of the Green function in the scenarios given by Ref. [94].

Comparison of global Green function with Green function along worldline

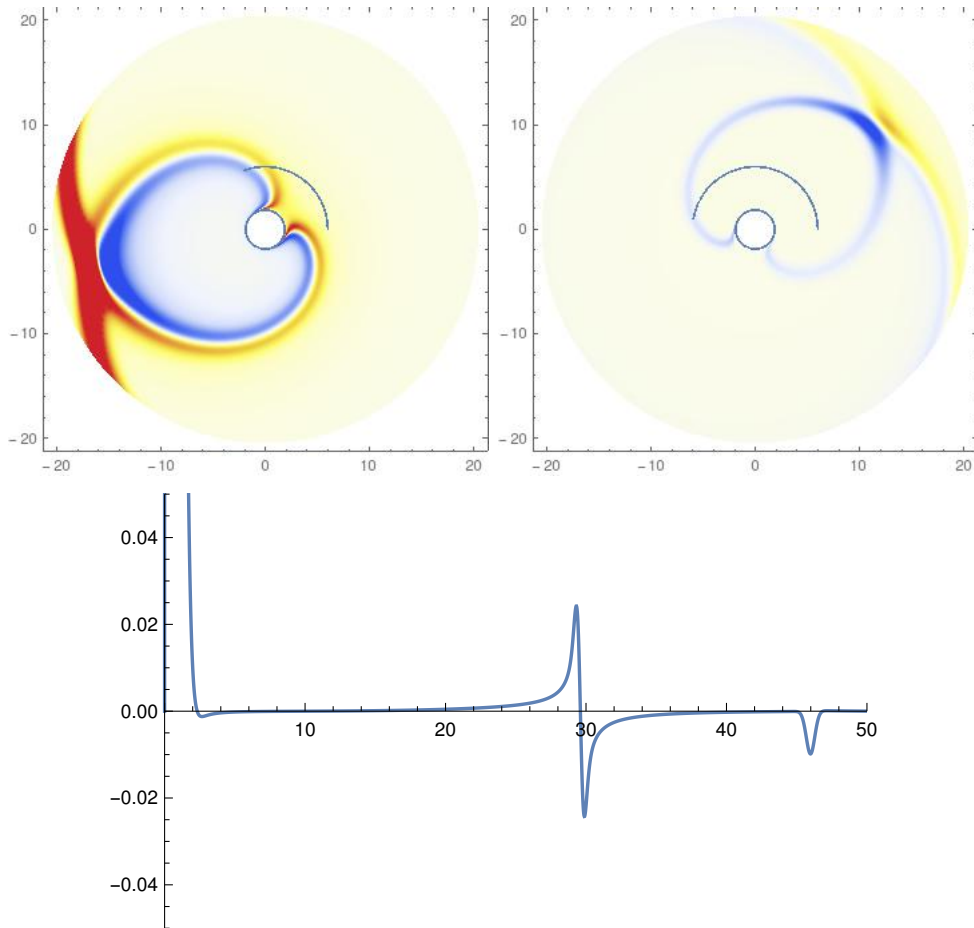


Figure 4.6: The above plots show the Green function with base point  $r_0 = 6, \phi = 0$  at  $t = 30$  and  $t = 46$  plotted in the equatorial plane. The worldline from the initial base point to the times  $t = 30$  and  $t = 46$  is also plotted. The below plot shows the value of the Green function along the worldline as a function of time. By investigating the Green function in this way highlights how features in the worldline Green function occur. We can observe how the Green function cycles through the fourfold structure [61].

## 4.8. CONCLUSIONS AND DISCUSSION

---

# Chapter 5

## Electromagnetic self force via mode sum regularisation

### 5.1 Introduction

The mode sum method developed by Barack and Ori [28] provides an alternative approach to calculating the self force, in addition to the worldline integration method of Chap. 4. We apply the mode sum method in this chapter to calculate the electromagnetic self force. First we review how the mode sum method works in the gravitational case.

The mode sum method solves the linearised Einstein equations for the metric perturbation  $h_{\mu\nu}$  by splitting it into angular  $l$  modes. Each of these modes are finite at the particle, yet their sum is divergent. The regularisation is carried out by calculating the angular decomposition of the singular nature of the field and subtracting mode by mode so that the sum is finite. The terms arising from the angular decomposition of the singular nature of the field are known as the regularisation parameters.

Though regularisation parameters can be found by identifying the divergent nature of the sum, their physical significance may be dubious if we have no physical motivation for subtracting a particular singular field. Instead, we

make use of the Detweiler-Whiting decomposition [29, 30]

$$h_{\alpha\beta} = h_{\alpha\beta}^R + h_{\alpha\beta}^S, \quad (5.1)$$

where  $h_{\alpha\beta}^S$  is called the singular field and contains all the divergent features of the field. The singular field is defined in terms of a sum of advanced and retarded Green functions so that the singular field is symmetric about the particle. The singular field is constructed so that it has the same singular nature as the metric perturbation, whilst having no effect on the motion of the particle and therefore has no contribution to the self force [31]. The angular decomposition of the singular field gives the required regularisation parameters. The regular field  $h_{\mu\nu}^R$  is smooth and finite at the particle as well as being a homogeneous solution to the Einstein equations. In the Detweiler-Whiting set-up the particle freely moves on a geodesic of the spacetime  $g_{\mu\nu} + h_{\mu\nu}^R$ .

The regular field is related to the tail field defined in Eq. (4.4) by [31]

$$h_{\alpha\beta;\lambda}^R = h_{\alpha\beta;\lambda}^{tail} - 4\mu (u_{(\alpha} R_{\beta)\nu\lambda\xi} + R_{\alpha\nu\beta\xi} u_{\lambda}) u^{\nu} u^{\xi}. \quad (5.2)$$

Though the regular and tail fields are not equivalent, they do give equivalent values for the self force through Eq. (4.5). This is because the terms involving the Riemann tensor cancel out.

We now illustrate how the mode-sum regularisation arises. We can write the regular field  $h_{\alpha\beta}^R(x_0)$  (5.1) at the position of the particle  $x_0$  in terms of the difference between the full field and the singular field [29, 30]

$$h_{\alpha\beta}^R(x_0) = \lim_{x \rightarrow x_0} [h_{\alpha\beta}(x) - h_{\alpha\beta}^S(x)], \quad (5.3)$$

where the limit is taken after the singular nature of the full field is subtracted by the singular field. We now decompose  $h_{\alpha\beta}$  and  $h_{\alpha\beta}^S$  into spherical harmonic modes

$$h_{\alpha\beta}^R(x_0) = \lim_{x \rightarrow x_0} \sum_{l=0}^{\infty} [h_{\alpha\beta}^l(x) - h_{\alpha\beta}^{lS}(x)], \quad (5.4)$$

where

$$h_{\alpha\beta}^l(x) = \sum_{m=-l}^{m=l} h_{\alpha\beta}^{lm}(t, r) Y_{lm}(\theta, \phi). \quad (5.5)$$

The singular field's angular modes can be found analytically by expanding the Detweiler-Whiting singular field [29] in powers of  $r$  where  $r$  is an appropriate measure of distance from the particle. The expansion of  $h_{\alpha\beta}^{lS}(x)$  has a multipole decomposition of the form [31]

$$h_{\alpha\beta}^{lS}(x) = B(x) + \frac{C(x)}{l + \frac{1}{2}} + \frac{D(x)}{(l - \frac{1}{2})(l + \frac{3}{2})} + O(l^{-3}). \quad (5.6)$$

The sum of the  $D$  term from  $l = 0$  to  $l = \infty$  gives zero, as do higher order terms at  $O(l^{-n})$ . This is because the  $D$  term arises from an expansion in the singular field to  $O(r)$ , which disappears at location the particle. In contrast the  $B$  and  $C$  terms in Eq. (5.6) arise at  $O(r^0)$  in the expansion of  $h_{\alpha\beta}^{lS}(x)$ .

We therefore replace  $h_{\alpha\beta}^{lS}(x)$  in Eq. (5.4) by its decomposition (5.6) to give the mode sum formula of Barack and Ori [28]

$$h_{\alpha\beta}^R(x_0) = \lim_{x \rightarrow x_0} \sum_{l=0}^{\infty} \left[ h_{\alpha\beta}^{lS}(x) - B(x) - \frac{C(x)}{l + \frac{1}{2}} - \frac{D(x)}{(l - \frac{1}{2})(l + \frac{3}{2})} - O(l^{-3}) \right], \quad (5.7)$$

where the sum (5.7) is now uniformly convergent since the singular nature of the full field  $h_{\alpha\beta}(x)$  is the same as that of the singular field  $h_{\alpha\beta}^S(x)$ . We note that since the self force involves a derivative of the field, regularisation of the self force requires an additional parameter of the form  $A(l + \frac{1}{2})$ . As the  $D$  term (and higher order terms at  $O(l^{-n})$ ) sum to zero these are not necessarily needed in the mode sum (5.7). In practice however we only calculate a finite number of modes and use the  $D$  term to increase the rate of convergence.

We apply the mode sum method to calculate the electromagnetic self force below.

### 5.1.1 Electromagnetic self force

In this chapter we return to the original consideration of a self force. The idea of a self force did not originate in only a gravitational sense. Abraham and Lorentz [22, 23] discussed the radiation reaction on an accelerating charged

particle created by its own electromagnetic field. They calculated the resulting electromagnetic (EM) self force to be

$$F = \frac{q^2}{6\pi\epsilon_0 c^3} \dot{a} \quad (5.8)$$

where  $\epsilon_0$  is the electric constant,  $q$  is the electric charge of the particle, and  $\dot{a}$  is the rate of change of acceleration. Dirac [95] extended the formula to encompass the effects of special relativity. Later DeWitt and Brehme [96] extended the work to curved spacetime.

When a particle is travelling on a curved spacetime, we have an additional consideration coming from the scattering of the EM field by the curvature of spacetime. Smith and Will [3] considered this problem for a particle with electric charge  $q$  at some fixed distance  $r_0$  from a Schwarzschild black hole sourcing an electromagnetic field. They calculated the external force required to hold the particle static. The electromagnetic self force is identified as the difference between the full external force and the gravitational force exerted by the black hole. It was shown that the EM self force is given by

$$F = \frac{q^2 GM}{4\pi\epsilon_0 c^2 r_0^3}, \quad (5.9)$$

where  $r_0$  is the Schwarzschild coordinate of the particle. Throughout this chapter we set  $\{q, M, 4\pi\epsilon_0\} = 1$ , and as throughout the rest of the thesis  $\{G, c\} = 1$ , so that  $F = 1/r_0^3$ .

In this chapter we use a different method to recreate the result of Smith and Will [3] by assuming that the particle is held static and calculating the EM self force directly from the electromagnetic field sourced by the particle. The method presented here calculates the electromagnetic self force from the Faraday tensor. Gralla *et al.* [97] provide a rigorous description of the electromagnetic self force in terms of the regularised Faraday tensor. The static self force acts only in the radial direction and is formed by combining the Faraday tensor  $\mathcal{F}_{\mu\nu}^R$  with the particle's tangent vector  $u^\mu$  via

$$F_r = \mathcal{F}_{r\mu}^R u^\mu, \quad (5.10)$$

where the Faraday tensor is regularised according to the Detweiler-Whiting prescription [30]. Since for static particles  $u^t$  is the only non-zero component of the tangent vector, we have only to consider

$$F_r = \mathcal{F}_{rt}^R u^t = -\mathcal{F}_{tr}^R u^t. \quad (5.11)$$

The Smith and Will result (5.9) is a coordinate invariant quantity, related to the radial force (5.10), via

$$F = \sqrt{g_{\mu\nu} F^\mu F^\nu} = f^{1/2} F_r \quad (5.12)$$

as described in Ref. [98]. Here  $f$  is the usual function from the Schwarzschild metric Eq. (3.2).

Others have investigated the situation of a static self force. Wiseman [99] showed that for a particle sourcing a scalar field, the self force is zero. This difference between electromagnetic self force and scalar self force has been discussed by many authors [100, 101, 102].

Here we confirm the result of Smith and Will [3] by using the mode-sum regularisation scheme formulated by Barack and Ori [28]. By considering a particle in this idealised static scenario we reduce much of the complexity, whilst maintaining many of the key features of the self force, including the need for regularisation. We find that we are able to solve the problem using both analytical and numerical methods. The numerical method we develop involves solving the field equations in the time domain. By confirming the validity of this method when compared to analytic methods, we lay the foundation for future work on, for example, the EM self force on a radially in-falling particle.

## 5.2 Electromagnetic field equations

An electromagnetic field is described by the Faraday tensor  $\mathcal{F}_{\mu\nu}$ . In the static case we consider,  $F_r$  is the only non-vanishing component of the self force (see Eq. (5.11)). Thus we only consider the  $\mathcal{F}_{tr}$  component of the Faraday tensor.

Although in the static case the field does not vary in time, we may find the static solution numerically by allowing the field to vary, using trivial initial conditions and allowing the solution to settle to a static, time-independent solution. We construct the equations describing the Faraday tensor, allowing variations in time. This sets up extensions to non-static solutions in potential future work. In [103] the equations governing  $\mathcal{F}_{\mu\nu}$  were derived for each component. We present a re-derivation of the equations here, focussing on  $\mathcal{F}_{tr}$ .

### 5.2.1 Static equations

The Maxwell equations governing  $\mathcal{F}_{\mu\nu}$  are [103]

$$\nabla_\nu \mathcal{F}^{\mu\nu} = 4\pi j^\mu, \quad (5.13)$$

where

$$j^\mu = q \int_\Gamma u^\mu \delta_4(x, z(\tau)) d\tau, \quad (5.14)$$

with the world line  $\Gamma$  given by  $z(\tau)$  specifying the position of the particle at proper time  $\tau$  and  $x$  a position in spacetime at which the field is evaluated. Here  $\delta_4(x, z(\tau))$  is the Dirac delta function adapted to the spacetime  $\delta_4(x, z(\tau)) = \frac{1}{\sqrt{-g}} \delta_4(x - z(\tau))$ . In Schwarzschild spacetime the square root of the metric determinant is  $\sqrt{-g} = r^2 \sin \theta$ . The Faraday tensor is written in terms of a four vector potential  $A_\mu$  as

$$\mathcal{F}_{\mu\nu} = A_{\nu,\mu} - A_{\mu,\nu}. \quad (5.15)$$

Using the identity of Eq. (2.8) we can write Maxwell's equations in terms of partial derivatives of  $A_\mu$ ,

$$\frac{1}{\sqrt{-g}} (\sqrt{-g} g^{\alpha\nu} g^{\beta\mu} A_{\alpha,\beta})_{,\nu} - \frac{1}{\sqrt{-g}} (\sqrt{-g} g^{\alpha\nu} g^{\beta\mu} A_{\beta,\alpha})_{,\nu} = 4\pi j^\mu. \quad (5.16)$$

To find a governing equation for  $\mathcal{F}_{tr}$  we consider the equations for  $j^t$  and

$j^r$ , which are

$$\begin{aligned}
4\pi j^t &= \frac{1}{r^2}(r^2 A_{t,r})_{,r} - \frac{1}{r^2}(r^2 A_{r,t})_{,r} \\
&\quad + \frac{1}{r^2 f} \left[ \frac{1}{\sin \theta} (\sin \theta A_{t,\theta})_{,\theta} + \frac{1}{\sin^2 \theta} A_{t,\phi\phi} \right] \\
&\quad - \frac{1}{r^2 f} \left[ \frac{1}{\sin \theta} (\sin \theta A_{\theta})_{,\theta} + \frac{1}{\sin^2 \theta} A_{\phi,\phi} \right]_{,t}, \tag{5.17}
\end{aligned}$$

$$\begin{aligned}
4\pi j^r &= A_{r,tt} - A_{t,rt} \\
&\quad - \frac{f}{r^2} \left[ \frac{1}{\sin \theta} (\sin \theta A_{r,\theta})_{,\theta} + \frac{1}{\sin^2 \theta} A_{r,\phi\phi} \right] \\
&\quad + \frac{f}{r^2} \left[ \frac{1}{\sin \theta} (\sin \theta A_{\theta})_{,\theta} + \frac{1}{\sin^2 \theta} A_{\phi,\phi} \right]_{,r}. \tag{5.18}
\end{aligned}$$

Now cancelling the terms involving  $A_{\theta}$ ,  $A_{\phi}$  by summing  $(\partial_r[r^2 f(5.17)])$  and  $\partial_t[r^2 f^{-1}(5.18)]$ , we can obtain an equation for  $\mathcal{F}_{tr} = A_{r,t} - A_{t,r}$ , namely

$$\begin{aligned}
4\pi \left( (r^2 f j^t)_{,r} + \frac{r^2}{f} j^r_{,t} \right) &= - [f(r^2 \mathcal{F}_{tr})_{,r}]_{,r} + \frac{r^2}{f} \mathcal{F}_{tr,tt} \\
&\quad - \left[ \frac{1}{\sin \theta} (\sin \theta \mathcal{F}_{tr,\theta})_{,\theta} + \frac{1}{\sin^2 \theta} \mathcal{F}_{tr,\phi\phi} \right] \tag{5.19}
\end{aligned}$$

For static solutions, the tangent vector has only one component  $u^t$ , which is found by normalisation of the tangent vector

$$g_{\mu\nu} u^\mu u^\nu = -1 \tag{5.20}$$

for timelike geodesics, giving  $u^t = 1/f^{1/2}$  and  $u_t = -f^{1/2} = -1/u^t$ . The only non-zero contribution to the current is then

$$j^t = \int_{\Gamma} u^t \delta_4(x, z(\tau)) d\tau. \tag{5.21}$$

This is converted to an integral over time using  $d\tau = dt/u^t$ . We also decompose  $j^t$  into spherical harmonics

$$j^t = \sum_{l=0}^{\infty} \sum_{m=-l}^{m=l} j_{lm}^t Y_{lm}(\theta, \phi). \tag{5.22}$$

---

## 5.2. ELECTROMAGNETIC FIELD EQUATIONS

Using the identity Eq. (4.27) to convert the delta functions of the angular coordinates to spherical harmonics we can write the modes as

$$j_{lm}^t = \frac{1}{r_0^2} \delta(r - r_0) Y_{lm}^*(\theta_0, \phi_0), \quad (5.23)$$

where  $\{r_0, \theta_0, \phi_0\}$  are the coordinates of the particle. We choose to put the particle at the pole  $(\theta_0, \phi_0) = (0, 0)$  so that all  $m \neq 0$  modes are zero, by axisymmetry, reducing our sum to only  $l$  modes. The modes of the current reduce to

$$j_{l(m=0)}^t = j_l^t = \frac{1}{r_0^2} \delta(r - r_0) \sqrt{\frac{2l+1}{4\pi}}. \quad (5.24)$$

The left hand side of Eq. (5.19) now becomes

$$\begin{aligned} 4\pi \left( (r^2 f j^t)_{,r} + \frac{r^2}{f} j^r_{,t} \right) &= 4\pi \partial_r \left( r_0^2 f_0 \sum_{l=0}^{\infty} \frac{1}{r_0^2} \delta(r - r_0) \sqrt{\frac{2l+1}{4\pi}} Y_{l,0}(\theta, \phi) \right) \\ &= \sum_{l=0}^{\infty} f_0 \delta'(r - r_0) \sqrt{4\pi(2l+1)} Y_{l,0}(\theta, \phi) \end{aligned} \quad (5.25)$$

where  $f_0 = f(r_0)$ . The derivative of the Dirac delta distribution is discussed in Appendix A.

We now decompose  $\mathcal{F}_{tr}$  into spherical harmonic modes, including the factor  $\sqrt{4\pi(2l+1)}$  in our ansatz,

$$\mathcal{F}_{tr} = \sum_{l=0}^{\infty} \frac{\psi_l(t, r)}{r^2} Y_{l,0}(\theta, \phi) \sqrt{4\pi(2l+1)}. \quad (5.26)$$

The equation governing each  $\psi_l$  mode is, dropping the subscripts  $l$  since there is no coupling between modes,

$$-\frac{\partial^2 \psi}{\partial t^2} + f \frac{\partial}{\partial r} \left( f \frac{\partial \psi}{\partial r} \right) - \mathcal{V}(r) \psi = S(r, r_0) \quad (5.27)$$

where the effective potential is

$$\mathcal{V}(r) = \frac{l(l+1)f}{r^2} \quad (5.28)$$

and the source function is

$$S(r, r_0) = -f f_0 \delta'(r - r_0). \quad (5.29)$$

The radial form of the equations (5.27) is useful for an analytic solution as we will see in Sec. 5.5. The boundary at the horizon needs to be considered carefully. To find numerical solutions, we transform to the tortoise coordinate  $r^*$  where the horizon lies at  $r^* = -\infty$ . The tortoise coordinate was first introduced in Eq. (3.20). The particle lies at the position  $r^*(r_0) = r_0^*$ . To transform Eqs. (5.27) to the tortoise coordinate we need transform the Dirac delta distribution and its derivative

$$\begin{aligned} f \delta(r - r_0) &= \delta(r^* - r_0^*), \\ f f_0 \delta'(r - r_0) &= \delta'(r^* - r_0^*), \end{aligned} \quad (5.30)$$

using the definitions of Appendix A, where the prime denotes differentiation with respect to the argument of the delta function. The equations governing  $\psi_l$  in terms of the tortoise coordinate are

$$-\frac{\partial^2 \psi}{\partial t^2} + \frac{\partial^2 \psi}{\partial r^{*2}} - \mathcal{V}(r) \psi = -\delta'(r^* - r_0^*). \quad (5.31)$$

To solve Eq. (5.31) numerically we can input trivial initial conditions and evolve in time until the solution settles down to a time independent solution (see Sec. 5.7). A difficulty here is the  $\delta'(r^* - r_0^*)$  which means that the  $l$ -mode of the field at the particle will be discontinuous. By considering the field near the particle we can formulate conditions which match solutions across the particle. These we refer to as jump conditions.

## 5.2.2 Jump conditions

Since we know that the field is discontinuous at the position of the particle  $r_0^*$  we may write the full solution in the form

$$\psi(r^*) = \psi^+(r^*) \Theta(r^* - r_0^*) + \psi^-(r^*) \Theta(r_0^* - r^*), \quad (5.32)$$

where  $\Theta(r^* - r_0^*)$  is the Heaviside step function discussed in Appendix A, whose derivative is the delta function. By substituting (5.32) into Eqs. (5.31) we are able to match the singular structure of the equations. This amounts to matching coefficients of the delta function and its derivatives.

Following the notation of Haas [103] we define

$$[G(r^*)] = \lim_{r^* \rightarrow r_0^{*+}} G(r^*) - \lim_{r^* \rightarrow r_0^{*-}} G(r^*), \quad (5.33)$$

for a general function  $G(r^*)$ . The jump conditions are defined as

$$J_n = \left[ \frac{\partial^n \psi}{\partial r^{*n}} \right]. \quad (5.34)$$

Substituting (5.32) into Eq. (5.31) gives

$$\begin{aligned} & \frac{\partial^2 \psi^+}{\partial r^{*2}} \Theta(r^* - r_0^*) + \frac{\partial^2 \psi^-}{\partial r^{*2}} \Theta(r_0^* - r^*) \\ & + \left[ \frac{\partial \psi}{\partial r^*} \right] \delta(r^* - r_0^*) + [\psi] \delta'(r^* - r_0^*) - \mathcal{V}(r) \psi = -\delta'(r^* - r_0^*). \end{aligned} \quad (5.35)$$

Comparing coefficients of the delta function and its derivative gives the jump conditions

$$J_0 = -1, \quad J_1 = 0. \quad (5.36)$$

Jump conditions of higher order are found by taking derivatives of Eq. (5.35). We will require up to fourth order in derivative jump conditions, which take the form

$$\begin{aligned} J_2 &= -\mathcal{V}(r), \\ J_3 &= -f \frac{\partial \mathcal{V}(r)}{\partial r}, \\ J_4 &= -f \frac{\partial (f \mathcal{V}(r))}{\partial r} - f \mathcal{V}(r) \frac{\partial \mathcal{V}(r)}{\partial r}. \end{aligned} \quad (5.37)$$

## 5.3 Mode sum regularisation

### 5.3.1 Mode sum calculation

Due to the delta function in the source terms (5.29), the field that we calculate, though finite in each  $l$  mode, will diverge when summed over  $l$ . To find a regular and physically well-defined field we use the mode sum regularisation method of Ref. [28]. The self force can be calculated from our  $\psi_l$  modes and Eqs. (5.11-5.12) with suitable regularisation parameters using the formula [28] to regularise  $\mathcal{F}_{tr}$ ,

$$\begin{aligned}
 F &= -f^{1/2} \mathcal{F}_{tr}^R u^t \\
 &= -\lim_{r \rightarrow r_0^\pm} \sum_{l=0}^{\infty} \left( \frac{\psi_l(r)}{r^2} (2l+1) \mp A \left( l + \frac{1}{2} \right) + B \right. \\
 &\quad \left. + \frac{C}{l + \frac{1}{2}} + \frac{D}{(l - 1/2)(l + 3/2)} \right), \quad (5.38)
 \end{aligned}$$

where the  $\{A, B, C, D\}$  are regularisation parameters which depend on  $r_0$ . The  $\pm$  on the limit denotes taking the limit from right (+) or left (-). To obtain a convergent sum only the  $A, B$  and  $C$  parameters are necessary. The  $D$  term sums to 0 when the sum is taken to infinity (this can be easily shown by splitting into partial fractions and considering the infinite limit of partial sums). In using only the  $A, B$  and  $C$  terms there is a power law decay in the sum at  $O(l^{-2})$  whilst using the  $D$  term increases this drop off to  $O(l^{-3})$ . Since we can only calculate a finite number of modes, we must employ some cut off in  $l$  modes, use of the  $D$  term greatly reduces the total number of modes required in the sum (5.38) for a given accuracy.

We can also remove the necessity for the  $A$  parameter by taking the average of the field found by taking the limit from either side of  $r_0$ . Alternatively, this idea can be viewed as the  $A$  term specifying the difference in the field  $\psi_l(r)$  given by taking the limit from either side of the particle

$$A = - \left[ \frac{\psi_l(r)}{r^2} \right]. \quad (5.39)$$

### 5.3.2 Regularisation parameters

Regularisation parameters for static self forces were calculated by Casals *et al.* [104]. They were constructed using the Detweiler-Whiting singular Green function [30]. This is a singular field with the same singular structure as the unregularised field given by solutions to Maxwell's equations (5.13). The singular field was shown [30] to exert no force on the particle. By subtracting the singular field from the full field, the regular field is calculated, which is solely responsible for the self force. To subtract the singular field, we decompose the singular field into  $l$  modes, thereby giving the regularisation parameters. The regularisation parameters for the static EM self force are given in Ref. [104] as

$$\begin{aligned}
 A &= \frac{1}{r_0^2}, \\
 B &= \frac{r_0 - 3}{2f_0^{1/2}r_0^3}, \\
 C &= 0, \\
 D &= \frac{3}{16} \frac{5 - 3r_0}{f_0^{3/2}r_0^5}.
 \end{aligned} \tag{5.40}$$

## 5.4 Monopole mode

For the monopole mode, the case when  $l = 0$ , we can find solutions of Eq. (5.31) completely analytically as shown in [103]. Equation (5.31) in the static case reduces to

$$\frac{d^2\psi}{dr^{*2}} = -\delta'(r^* - r_0^*), \tag{5.41}$$

which has the solution

$$\psi = -\Theta(r^* - r_0^*), \tag{5.42}$$

when the first jump condition from Eqs. (5.36) is taken into account. For the higher  $l$  values we seek solutions both analytically and numerically.

It is interesting to look at the contribution of the monopole mode to the final mode sum (5.38). To find the regularized mode  $F^{(l=0)}$  we substitute our

monopole mode into the mode sum formula Eq. (5.38) with  $l = 0$ . We are able to write the result as a series in  $1/r_0$

$$F^{(l=0)} = \frac{1}{r_0^3} - \frac{5}{16r_0^6} + O\left(\frac{1}{r_0^7}\right). \quad (5.43)$$

The EM self force is, from Eq. (5.9),  $1/r_0^3$  according to Ref. [3]. We can see that the monopole mode Eq. (5.43) is a large contribution to the final result especially for large values of  $r_0$ . Interestingly if we omit the  $D$  term the monopole contribution is

$$F^{(l=0)} = \frac{1}{r_0^3} + \frac{3}{4r_0^4} + \frac{1}{r_0^5} - \frac{25}{16r_0^6} + O\left(\frac{1}{r_0^7}\right). \quad (5.44)$$

It is clear that the  $D$  regularisation parameter significantly increases the accuracy of the monopole mode compared to the Smith and Will result [3]. We will see in Sec. 5.8 that use of the  $D$  parameter also decreases the number of  $l$  modes required to calculate the self force to a given numerical accuracy.

## 5.5 Analytical method

In the static case, Eq. (5.27) reduces, from a partial differential equation, to an ordinary second order differential equation. The solution must be regular at the horizon and at infinity. We therefore have a boundary value problem. Away from the particle at  $r = r_0$ , solutions satisfy the homogeneous form of Eq. (5.27), that is, with the source term (5.29) set to  $S(r, r_0) = 0$ . We can find two linearly independent solutions; one is regular at the horizon, and the other regular at infinity. Then by matching at the particle using the jump conditions (5.36-5.37) we can find the solution of the inhomogeneous Eq. (5.27).

### 5.5.1 Solution of radial equations

Consider the static form of the radial equations (5.27), where the time derivative vanishes. Setting  $r/2 = z$  and multiplying by  $-r^2/f$ , Eq. (5.27) becomes

$$z(1-z)\frac{d^2\psi}{dz^2} - \frac{d\psi}{dz} + l(l+1)\psi = 0. \quad (5.45)$$

We find this equation is in the same form as the hypergeometric differential equation [70]

$$z(1-z)\frac{d^2\psi}{dz^2} + [c - (a+b+1)z]\frac{d\psi}{dz} - ab\psi = 0, \quad (5.46)$$

which has two linearly independent solutions when  $|z| > 1$ ,

$$\begin{aligned} r^{-a} {}_2F_1[a, 1+a-c; 1+a-b; 1/z] \\ r^{-b} {}_2F_1[b, 1+b-c; 1+b-a; 1/z], \end{aligned} \quad (5.47)$$

where  ${}_2F_1[p, q; r; x]$  are Gauss hypergeometric functions [59].

Comparing Eqs. (5.45-5.46) we see that  $c = -1, a = l, b = -l - 1$  giving solutions

$$\begin{aligned} \psi_1(r) &= r^{-l} {}_2F_1[l, l+2; 2l+2; 2/r] \\ \psi_2(r) &= r^{l+1} {}_2F_1[-l-1, -l+1; -2l; 2/r]. \end{aligned} \quad (5.48)$$

Note that the hypergeometric function  ${}_2F_1[p, q; s; x]$  is not in general defined when  $s$  takes negative integer arguments. For the function  $\psi_2(r)$  from Eq. (5.48) however, as all the parameters in  $\psi_2$  are negative integers, and  $2l > l+1 > l-1$ , the solution is valid. It is understood that we take the limit  $l+\epsilon \rightarrow l$  such that all arguments approach the negative integers at the same rate. See Eq. (15.2.6) of DLMF [59] and Eq. (15.4.1) of Abramowitz and Stegun [70] for further details.

Let us now examine the solutions (5.48) at both the horizon and infinity. At infinity  $r \rightarrow \infty$  and  $2/r \rightarrow 0$ . Since in general  ${}_2F_1[p, q; s; 0] = 1$  we find

$$\begin{aligned} \lim_{r \rightarrow \infty} \psi_1(r) &\sim r^{-l} \rightarrow 0, \\ \lim_{r \rightarrow \infty} \psi_2(r) &\sim r^{l+1} \rightarrow \infty. \end{aligned} \quad (5.49)$$

Therefore at infinity we can write  $\psi = \alpha\psi_1$ , where  $\alpha$  is a constant.

At the horizon  $r = 2$  ( $r = 2M$  if  $M$  is not set equal to unity) and  $2/r = 1$ . The function  $\psi_1$  is undefined at  $r = 2$  since the hypergeometric series does not converge. If we have a negative integer for  $p$  or  $q$  of  ${}_2F_1[p, q; s; x]$  (as we do for  $\psi_2$ ),

If either  $p$  or  $q$  is a negative integer in  ${}_2F_1[p, q; s; x]$ , (as we do for  $\psi_2$ ), the hypergeometric function is defined from Eq. (15.4.20) of DLMF [59] as

$${}_2F_1[-n, b; c; 1] = \frac{(c-b)_n}{(c)_n} \quad (5.50)$$

where  $(c)_n$  is the Pochhammer symbol which is defined for negative integers  $c$  as

$$(c)_n = \frac{(-1)^n (-c)!}{(-c+n)!}. \quad (5.51)$$

Using these definitions for  $\psi_2$  at the horizon ( $r = 2$ ) we have

$$\psi_2(2) = 2^{l+1} \frac{(l-1)!(l+1)!}{(2l)!}, \quad (5.52)$$

which is clearly finite at the horizon for all  $l$ . We can now set  $\psi = \beta\psi_2$  at the horizon. The full inhomogeneous solution can be written as

$$\psi = \alpha\psi_1\theta(r^* - r_0^*) + \beta\psi_2\theta(r_0^* - r^*), \quad (5.53)$$

with  $\alpha$  and  $\beta$  to be determined by the jump conditions.

Using the first two jump conditions from Eqs. (5.36) we have simultaneous equations for  $\alpha, \beta$

$$\begin{aligned} \alpha\psi_1(r_0) - \beta\psi_2(r_0) &= -1, \\ \alpha\psi_1'(r_0) - \beta\psi_2'(r_0) &= 0 \end{aligned} \quad (5.54)$$

where  $\psi' = \frac{\partial\psi}{\partial r}$ . Solutions of Eq. (5.54) are given by

$$\alpha = -\frac{\psi_2'(r_0)}{W}, \quad \beta = -\frac{\psi_1'(r_0)}{W} \quad (5.55)$$

where  $W$  is the Wronskian defined by

$$W = \psi_1(r_0)\psi_2'(r_0) - \psi_1'(r_0)\psi_2(r_0) \quad (5.56)$$

which, using the identity from Eq. (15.10.7) of DLMF [59], is

$$W = (a - b)z^{-c}(z - 1)^{c-a-b-1} = \frac{(2l + 1)}{f}. \quad (5.57)$$

Eq. (5.53) gives a full solution for each  $l$  mode which we can put in to our mode sum formula (5.38) to calculate the EM self force.

## 5.6 Analytic self force calculation

We are now in a position to calculate the self force using our analytical solution (5.53) in the mode sum formula (5.38).

As described in Eq. (5.39), the  $A$  regularisation parameter can be found from the difference in the field calculated by taking the limit from either side of the particle

$$A = - \left[ \frac{\psi_l(r)}{r^2} \right] = - \frac{(\alpha\psi_1(r_0) - \beta\psi_2(r_0))}{r_0^2} = \frac{1}{r_0^2}, \quad (5.58)$$

which is equal to the  $A$  regularisation parameter at the particle given in Ref. [104] and presented in Eqs. (5.40). The fact that the  $A$  parameter found in Eq. (5.58) matches that calculated by Ref. [104] provides an additional check on our analytic solutions (5.48).

We now compute the self force using the mode sum formula of Eq. (5.38) using our analytic solutions for the  $l$ -modes (5.53) and the regularisation parameters of Eqs. (5.40). Though this sum is analytic in principle we cannot in practice calculate infinite sum of  $l$ -modes. We instead calculate a finite number of 500  $l$ -modes since, for the values of  $r_0$  we consider, the value of hypergeometric functions of (5.48) at  $l = 500$  is approximately machine precision. We use *Mathematica* to numerically calculate the values of the hypergeometric functions of (5.48) and the sum (5.38).

Table 5.1 gives the self force for a range of different values of  $r_0$ . There is a good agreement between our mode sum and the known result of Smith and Will (5.9) [3]. We are limited from higher accuracy by machine limits on the small values of the high  $l$ -modes. We further note that the relative error appears to scale with  $r_0^3$ .

This agreement suggests that there is an identity for an infinite sum of hypergeometric functions. Let us investigate what form this might take. We can remove any need to use the  $A$  regularisation parameter completely by taking the average of our mode solutions from either side of the particle

$$\begin{aligned}\psi_l(r_0) &= \frac{1}{2} (\alpha\psi_1(r_0) + \beta\psi_2(r_0)), \\ &= -\frac{f_0}{2(2l+1)} (\psi_1(r_0)\psi_2'(r_0) + \psi_1'(r_0)\psi_2(r_0)), \\ &= -\frac{f_0}{2(2l+1)} \frac{d}{dr_0} (\psi_1(r_0)\psi_2(r_0)).\end{aligned}\tag{5.59}$$

We now use this in our mode sum formula Eq. (5.38)

$$\begin{aligned}F &= -\sum_{l=0}^{\infty} \left[ \frac{\psi_l(r_0)}{r_0^2} (2l+1) + B \right], \\ &= \frac{1}{2r_0^2} - B + \frac{f_0}{2r_0^2} \frac{d}{dr_0} \sum_{l=1}^{\infty} \left[ \psi_1(r_0)\psi_2(r_0) - \hat{B} \right],\end{aligned}\tag{5.60}$$

where we have defined  $\frac{f_0}{2r_0^2} \frac{d}{dr_0} \hat{B} = B$  and  $B$  is given in Eqs. (5.40). We are only able to reverse the order of the derivative and sum since we have already assumed the sum is uniformly convergent. As we expect  $F = 1/r_0^3$  we expect the sum of hypergeometric functions in Eq. (5.60), with  $\psi_1$  and  $\psi_2$  given in Eq. (5.48), to converge.

## 5.7 Numerical method

In this section we solve Eq. (5.31) in the time domain. There are two key challenges which we outline here.

## Analytic results

$r_0$	Mode Sum $F$	Relative Error	$r_0^3$ Relative Error
5	$8.0000 \times 10^{-3}$	$5. \times 10^{-11}$	$6. \times 10^{-9}$
6	$4.6296 \times 10^{-3}$	$3. \times 10^{-11}$	$7. \times 10^{-9}$
7	$2.9155 \times 10^{-3}$	$1. \times 10^{-11}$	$4. \times 10^{-9}$
8	$1.9531 \times 10^{-3}$	$8. \times 10^{-12}$	$4. \times 10^{-9}$
9	$1.3717 \times 10^{-3}$	$5. \times 10^{-12}$	$4. \times 10^{-9}$
10	$1.0000 \times 10^{-3}$	$4. \times 10^{-12}$	$4. \times 10^{-9}$
11	$7.5131 \times 10^{-4}$	$3. \times 10^{-12}$	$3. \times 10^{-9}$
12	$5.7870 \times 10^{-4}$	$2. \times 10^{-12}$	$3. \times 10^{-9}$
13	$4.5517 \times 10^{-4}$	$1. \times 10^{-12}$	$3. \times 10^{-9}$
14	$3.6443 \times 10^{-4}$	$1. \times 10^{-12}$	$3. \times 10^{-9}$
15	$2.9630 \times 10^{-4}$	$9. \times 10^{-13}$	$3. \times 10^{-9}$
16	$2.4414 \times 10^{-4}$	$7. \times 10^{-13}$	$3. \times 10^{-9}$
17	$2.0354 \times 10^{-4}$	$6. \times 10^{-13}$	$3. \times 10^{-9}$
18	$1.7147 \times 10^{-4}$	$5. \times 10^{-13}$	$3. \times 10^{-9}$
19	$1.4579 \times 10^{-4}$	$6. \times 10^{-13}$	$4. \times 10^{-9}$
20	$1.2500 \times 10^{-4}$	$5. \times 10^{-13}$	$4. \times 10^{-9}$

Table 5.1: Values of analytic mode sum compared with known result of Smith and Will [3]. Here we have used a maximum number of 500  $l$ -modes in all cases.

First, we know from the jump conditions (5.36-5.37) that the  $l$ -modes of the field are discontinuous at the particle. Commonly, field discontinuities are dealt with by decomposing the domain either side of the particle and then matching solutions. This method may be relatively simple to implement in the static case; however, with a move to non-static scenarios in mind, difficulties may arise since the domain walls will need to move along with the particle. Instead we use the method introduced by Markakis and Barack in Ref. [105]. The method due to Markakis and Barack allows a piecewise continuous function to be constructed as an interpolating polynomial by generalising the Lagrange interpolation formula, allowing dependence on points across the discontinuity via knowledge of the jump conditions.

Second we do not know what initial data is appropriate; if we did we would already have the desired solution in the static case. Usually, trivial initial data is chosen with the field and its derivative set to zero. In certain situations more realistic initial data has been constructed [106, 107, 108, 109]. A choice of trivial initial data is clearly incompatible with the jump conditions (5.36-5.37) and subsequently creates some high frequency unphysical noise in the numerical solution. Some of this propagates away from the particle and running the simulation for sufficient time allows this “noise” to propagate off the computational domain. Unfortunately there is also the possibility of some persistent unphysical noise at the particle position. This situation was studied in Ref. [110] where it was proposed that the jump conditions are smoothly turned on.

### 5.7.1 Dealing with discontinuity

We consider here the method outlined in [105] to discretise our function across the discontinuity, so that we can evolve our equations numerically on a single domain. In general, to find numerical solutions of equations we discretise our function  $f(x)$  on a set of  $N$  points  $f_i = f(x_i)$ . If the function is continuous we

can recover the full function  $f(x)$  from the set  $f_i$  (with some numerical error) using Lagrange interpolation

$$f(x) = \sum_{j=0}^N f_j \pi_j(x) \quad (5.61)$$

where

$$\pi_j(x) = \prod_{\substack{k=0 \\ k \neq j}}^N \frac{x - x_k}{x_j - x_k}. \quad (5.62)$$

Spatial differentiation is done using finite differencing which can be written in matrix form as

$$f^{(n)}(x_i) = \sum_{j=0}^N D_{ij}^{(n)} f_j, \quad (5.63)$$

where  $D_{ij}^{(n)}$  is a matrix containing finite difference operations as described in Sec. 3.2.3. These methods give the function's value and its derivatives at a single point, defined via its values at neighbouring points. To extend these methods to piecewise-continuous functions, Markakis and Barack [105] propose adding an additional term  $s_j(x_0)$  to Eqs. (5.61,5.63), namely

$$f(x) = \sum_{j=0}^N (f_j + s_j(x_0)) \pi_j(x), \quad (5.64)$$

$$f^{(n)}(x_i) = \sum_{j=0}^N D_{ij}^{(n)} (f_j + s_j(x_0)). \quad (5.65)$$

This term allows a function's value or its derivative to depend on neighbouring points beyond the discontinuity at  $x = x_0$ . The  $s_j(x_0)$  term is defined using knowledge of the jump conditions, as follows.

Consider the piecewise continuous function written as

$$f(x) = f_+(x) \Theta(x - x_0) + f_-(x) \Theta(x_0 - x), \quad (5.66)$$

where  $f_+$  and  $f_-$  are continuous functions. The difference in  $f_+$  and  $f_-$ , and their derivatives, at the discontinuity are given by the jump conditions

$$f_+^{(n)}(x_0) - f_-^{(n)}(x_0) = J_n, \quad (5.67)$$

where  $J_n = \left[ \frac{\partial^n f(x)}{\partial x^n} \right]$  are the  $n^{\text{th}}$  order jump conditions. At points  $x_i < x_0$  it is clear  $f_-(x_i) = f(x_i)$ . We define  $f_-(x_i)$  past the point of the discontinuity  $x_i > x_0$  to be  $f_-(x_i) = f(x_i) - g_i(x_0)$  where

$$g_i(x_0) = \sum_{n=0}^{\infty} \frac{J_n}{n!} (x_i - x_0)^n, \quad (5.68)$$

and similarly define  $f_+(x_i) = f(x_i) + g_i(x_0)$  in the region  $x_i < x_0$ . The  $g_i(x_0)$  function is defined in this way so that  $f_+$  and  $f_-$  are continuous functions. This can be seen by taking derivatives of  $g_i(x_0)$  at the discontinuity and observing that they match the jump conditions

$$\lim_{x_i \rightarrow x_0} \frac{d^n g_i(x_0)}{dx_i^n} = J_n. \quad (5.69)$$

With functions  $f_+$  and  $f_-$  defined at the grid points we can find their values over the whole domain via Lagrange interpolation

$$f_{\pm}(x) = \sum_{j=0}^N (f_j \pm g_j(x_0) \Theta[\pm(x_0 - x_i)]) \pi_j(x), \quad (5.70)$$

which when substituted back into (5.66) gives the full interpolation function (5.64) with

$$s_j(x_0) = [\Theta(x - x_0)\Theta(x_0 - x_j) - \Theta(x_0 - x)\Theta(x_j - x_0)] g_j(x_0). \quad (5.71)$$

We can now approximate the derivatives of the “full” function (5.66) across the whole domain using (5.65). In principle there are an infinite number of jump conditions but we choose to cut off at some value  $N$  so that  $J_{n>N} = 0$ , noting that this may be a source of numerical error.

## 5.7.2 Smooth initial conditions

In Ref. [110] Field *et al.* investigated how the presence of delta functions and delta function derivatives in the source terms of wave equations may create

persistent junk radiation in solutions where trivial initial data is used. They propose smoothly “turning on” the source terms by multiplying the jump conditions by a smoothing function. In practice we apply this idea by turning on  $J_n$  via

$$J_n \rightarrow J_n \begin{cases} \frac{1}{2} [\operatorname{erf}(\sqrt{\delta}(t - \tau/2)) + 1] & t < \tau, \\ 1 & t > \tau. \end{cases} \quad (5.72)$$

where  $\operatorname{erf}(t)$  is the error function. The values of  $\delta$  and  $\tau$  are chosen so that at initial time  $t = 0$  the magnitude of the jump conditions is less than machine precision. The value of  $\tau$  must also be chosen so that the jump conditions are fully turned on before the end of the numerical evaluation. The transition at  $t = \tau$  in Eq. (5.72) must also be of machine precision. We use values of  $\tau = 150$  and  $\delta = .0058$  as suggested in [110].

Alternatively, we may construct initial data more compatible with the jump conditions. However, one would need to find some function compatible with all jump conditions (5.36-5.37). We did attempt the numerical solution of Eqs. (5.31) with initial data compatible with the first two jump conditions and found errors of a similar magnitude to smoothly turning on the conditions. The more complicated jump conditions in the non-static case, increase the complexity in finding compatible initial data. Smoothly turning these on however is straightforward for any given jump conditions.

### 5.7.3 Implementation

We are now in a position to find the solution of Eq. (5.31) for each value of  $l$ . Our method uses the numerical method of lines [54], outlined in Sec. 2.5.1 with the time evolution handled using the *Mathematica* `NDSolve` function. We outline how we apply the method to Eqs. (5.31) here.

Firstly we set up a grid of points in  $r^*$ . We vary the step size depending on the requirements of the mode. Higher values of  $l$  require greater resolution which necessitates higher grid precision; we set the step size as 0.25. The

lower  $l$  modes require less precision yet wider grids since we have more noise propagating to the boundaries; here we set the step size as 0.7.

At each point  $x_i$  we define a function  $u_i(t)$  which depends on time. Using the jump conditions found in Eqs. (5.36-5.37) and the smooth turn on function Eq. (5.72) we formulate the  $s_j$  functions Eq. (5.71). For the spatial derivatives we use the inbuilt *Mathematica* function `NDSolve`FiniteDifferenceDerivative` to find a finite difference differentiation matrix for second derivatives. We then use this matrix in our formula (5.65) to give the second derivatives of the functions at each point. We set the boundaries sufficiently far away from the particle so that at late times there is no reflected radiation at the particle. **For initial conditions we set all  $u_i(0)$  to 0.** `NDSolve` is then used to integrate Eqs. (5.31) out to  $t_{max} = 300$ . This ensures that the full jump conditions have been switched on and any unphysical junk has radiated far enough away from the particle that it does not affect the field at the particle.

Once we have a numerical solution for the field we can use the interpolation formula (5.64) to find the value of the field at the particle. This data can then be used in the regularisation formula (5.38).

#### 5.7.4 Comparison of numerical and analytical modes

Before we implement the mode sum method and calculate the self force, we check the accuracy of our individual modes. In Fig. 5.1 we show the evolution of the numerically calculated field mode  $\psi_l$  over time as it approaches the analytical results from Eq. (5.53). We can see that by  $t = 300$  the numerical solution has approached the analytic solution and much of the noise has propagated away. In Table 5.2 we compare a number of unregularised modes and show errors of  $O(10^{-6})$  or  $O(10^{-7})$  between numerically calculated modes and analytical modes.

In Fig. 5.2 we plot numerically calculated modes on a log-log plot. We plot the same set of numerical data points for  $\psi_l$  with successive use of regularisation

Time domain evolution of field versus analytical solution

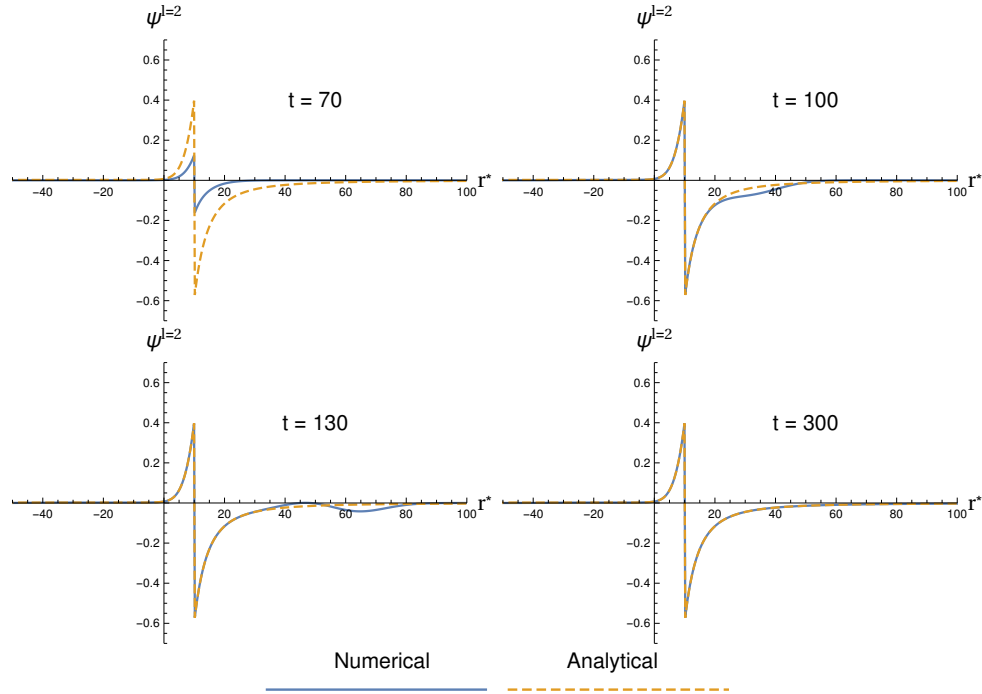


Figure 5.1: Plot of the numerically calculated field (blue solid curve) approaching the analytically calculated field (yellow dashed curved) for  $\psi^{l=2}$  at  $t = 70, 100, 130, 300$  for a particle at  $r_0^* = 10$ . We can see the numerical solution approaching the analytical solution over time. See Tab. 5.2 for errors at  $t = 300$ . Note that we found qualitatively similar results for other values of  $r_0$  and  $l$ .

Table comparing numerically and analytically calculated modes

$r_0$	$l$	Analytical $\psi_l$	Numerical $\psi_l$	Absolute Error
5	1	-0.577980	-0.577985	$4.8 \times 10^{-6}$
	5	-0.523371	-0.523375	$3.8 \times 10^{-6}$
	10	-0.512281	-0.512282	$7.1 \times 10^{-7}$
10	1	-0.628710	-0.628708	$1.9 \times 10^{-6}$
	5	-0.535553	-0.535554	$7.3 \times 10^{-7}$
	10	-0.518631	-0.518636	$4.6 \times 10^{-6}$
15	1	-0.642492	-0.642486	$6.1 \times 10^{-6}$
	5	-0.539052	-0.539052	$1.9 \times 10^{-7}$
	10	-0.520459	-0.520461	$1.2 \times 10^{-6}$

Table 5.2: Comparison table of numerically calculated  $l$  modes versus analytically calculated modes. We compare  $\psi_l$  modes for a range of  $r_0 = \{5, 10, 15\}$  and  $l = \{1, 5, 10\}$ .

terms from the mode sum formula Eq. (5.38) to give regularised modes of the self force, denoted  $F^{(l)}$ . The points marked “unreg” correspond to the numerical output with no regularisation terms. The A points refer to numerical modes using only the  $A$  term from Eq. (5.38). The B points then correspond to using  $A$  and  $B$  terms whilst the D points use the full mode sum formula from Eq. (5.38). As expected the unregularised terms increase approximately linearly with  $l$ , whilst the terms using the  $A$  regularisation parameter are constant. The  $B$  and  $D$  regularised terms initially drop off with  $O(l^{-2})$  and  $O(l^{-4})$  behaviour before hitting numerical errors at around  $10^{-5}$  for  $r_0 = 5$  and  $10^{-6}$  for  $r_0 = 10$  and  $15$ . This means we can only use approximately the first three  $l$  modes in the regularisation formula if using the  $D$  term or 10 modes if omitting the  $D$  term.

Log-log plot of numerically calculated  $l$  modes

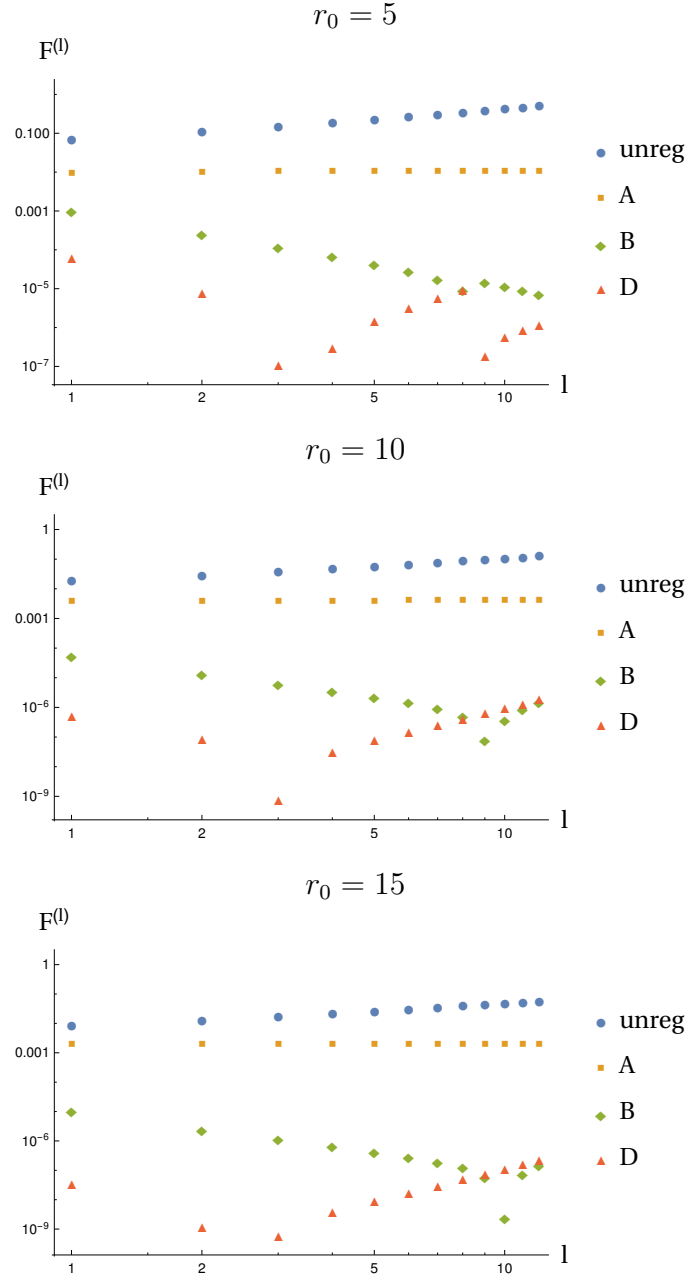


Figure 5.2: Regularisation plot of  $l$  modes for  $r_0 = \{5, 10, 15\}$  after subtracting terms from the mode sum formula (5.38), unregularised (unreg) and with  $A$  term,  $B$  term and  $D$  term. Numerical errors occur at around  $10^{-5}$  for  $r_0 = 5$  and  $10^{-6}$  for  $r_0 = 10$  and  $15$ .

$r_0$	$F$	Absolute Error	Relative Error	$F^{(l=0)} - 1/r_0^3$
5	$8.00589 \times 10^{-3}$	$5.9 \times 10^{-6}$	$7.3 \times 10^{-4}$	$4.92815 \times 10^{-5}$
	$8.00000 \times 10^{-3}$			
10	$9.99986 \times 10^{-4}$	$1.4 \times 10^{-8}$	$1.4 \times 10^{-5}$	$4.65366 \times 10^{-7}$
	$1.00000 \times 10^{-3}$			
15	$2.96227 \times 10^{-4}$	$6.9 \times 10^{-8}$	$2.3 \times 10^{-4}$	$3.54447 \times 10^{-8}$
	$2.96296 \times 10^{-4}$			

Table 5.3: Numerical results regularised using the  $D$  regularisation parameter. We give the numerical result for the self force  $F$  above the known Smith and Will result [3]  $F = 1/r_0^3$  for comparison.

$r_0$	$F$	Absolute Error	Relative Error	$F^{(l=0)} - 1/r_0^3$
5	$8.14427 \times 10^{-3}$	$1.4 \times 10^{-4}$	$1.8 \times 10^{-2}$	$-1.67204 \times 10^{-3}$
	$8.00000 \times 10^{-3}$			
10	$1.00853 \times 10^{-3}$	$8.2 \times 10^{-6}$	$8.5 \times 10^{-3}$	$-8.6881 \times 10^{-5}$
	$1.00000 \times 10^{-3}$			
15	$2.97646 \times 10^{-4}$	$1.3 \times 10^{-6}$	$4.6 \times 10^{-3}$	$-1.62863 \times 10^{-5}$
	$2.96296 \times 10^{-4}$			

Table 5.4: Numerical results regularised omitting the  $D$  regularisation parameter.

## 5.8 Results

Using the numerical data plotted in Fig. 5.2, we now calculate the self force using the mode sum regularisation formula (5.38). As the  $D$  regularisation parameter is optional, we calculate the self force both with and without this term. We used only the first 3 modes when using the  $D$  term and 10 modes when neglecting the  $D$  term, since we observed numerical errors above these values of  $l$  in Fig. 5.2. The results are presented in Tables 5.3 and 5.4.

An interesting observation is that use of the  $D$  regularisation parameter,

whilst unnecessary for a convergent sum, not only decreases the number of modes required in the mode sum, but also provides us with a much more accurate result by  $O(10^{-2})$  despite using the same numerical data.

We also state the monopole ( $l = 0$ ) error; that is the difference between the analytically calculated  $F^{(l=0)}$  and  $F = 1/r_0^3$ . This highlights the effect that using the numerically calculated modes increases the accuracy of our results above the monopole mode by a factor of  $10^{-1}$ . This also makes clear that although the  $r_0 = 5$  results appear to be less accurate, the relative error from our numerical analysis compared with the monopole is roughly the same magnitude.

## 5.9 Discussion

In this chapter we have investigated the electromagnetic self force experienced by a particle sourcing an electromagnetic field, with the particle held static outside a Schwarzschild black hole. We have used both analytical and numerical techniques, with the mode sum method developed by Barack and Ori [28], to recreate the result of Smith and Will [3]. Analytically we have shown the mode sum of hypergeometric functions agrees with the Smith and Will result to high accuracy. The numerical results are in agreement with the analytical results though numerical errors remain at around  $O(10^{-6})$  in each mode (see Table 5.2).

In extending our numerical analysis to calculate the EM self force in a non-static radially-infalling case some challenges remain though the method should follow from the method described in this chapter. We summarise these challenges here. A radially-infalling particle travelling on a geodesic has a tangent vector of the form

$$u^t = \frac{E}{f(r_0)}, \quad u^r = \dot{r}_0 = -\sqrt{E^2 - f(r_0)}, \quad (5.73)$$

where the overdot corresponds to differentiation with respect to proper time.

$E$  parametrises the geodesics and corresponds to energy,  $u_t = -E$ . The radial coordinate  $r_0 = r_0(t)$  is now a function of time (implicitly a function of proper time through  $t = t(\tau)$ ), which means that the source terms on the right hand side of Eq. (5.27) are no longer static. The source now has a radial component  $j^r$  given by

$$j^r = \int_{\Gamma} u^r \delta_4(x, z(\tau)) d\tau, \quad (5.74)$$

which we decompose into spherical harmonics in the same form as  $j^t$  (see Eq. (5.22)) giving

$$j_l^r = \frac{1}{r_0^2} \frac{u^r}{u^t} \delta(r - r_0(t)) \sqrt{\frac{2l+1}{4\pi}}. \quad (5.75)$$

The left hand side of the  $\mathcal{F}_{tr}$  equation (5.19) contains the expression,

$$4\pi \frac{r^2}{f} j_{,t}^r = 4\pi \partial_t \left( \frac{r^2}{f} \sum_{l=0}^{\infty} \frac{1}{r_0(t)^2} \frac{u^r}{u^t} \delta(r - r_0(t)) \sqrt{\frac{2l+1}{4\pi}} \right) \quad (5.76)$$

$$= \sum_{l=0}^{\infty} H(r, r_0(t)) \sqrt{4\pi(2l+1)} Y_{l0}(\theta, \phi), \quad (5.77)$$

with

$$H(r, r_0(t)) = \frac{f_0 \ddot{r}_0}{E^2} \delta(r - r_0(t)) - f_0 \frac{\dot{r}_0^2}{E^2} \delta'(r - r_0(t)), \quad (5.78)$$

where we have used the relation  $\partial_t \delta(r - r_0(t)) = -[\partial_t r_0(t)] \delta'(r - r_0(t)) = -\frac{u^r}{u^t} \delta'(r - r_0)$ . The source term in Eq. (5.27) is now given by

$$S(r, r_0(t)) = -f_0^2 \frac{\ddot{r}_0}{E^2} \delta(r - r_0(t)) - f f_0 \left( 1 - \frac{\dot{r}_0^2}{E^2} \right) \delta'(r - r_0(t)). \quad (5.79)$$

Using the tortoise coordinate Eq. (3.20) we have

$$S(r^*, r_0^*(t)) = G(t) \delta(r^* - r_0^*(t)) + K(t) \delta'(r^* - r_0^*(t)), \quad (5.80)$$

with

$$G(t) = -f_0 \frac{\ddot{r}_0}{E^2}, \quad K(t) = - \left( 1 - \frac{\dot{r}_0^2}{E^2} \right). \quad (5.81)$$

Jump conditions can be similarly derived, allowing now for time dependence. Here we give the first three conditions

$$\begin{aligned}
[\psi] &= \frac{K(t)}{1 - (\partial_t r_0^*)^2}, \\
\left[ \frac{\partial \psi}{\partial r^*} \right] &= \frac{G(t)}{1 - (\partial_t r_0^*)^2} - \frac{K(t)(1 + 3(\partial_t r_0^*)^2)\partial_t^2 r_0^*}{(1 - (\partial_t r_0^*)^2)^3} - \frac{2K'(t)(\partial_t r_0^*)}{(1 - (\partial_t r_0^*)^2)^2}, \\
\left[ \frac{\partial \psi}{\partial t} \right] &= -\frac{G(t)\partial_t r_0^*}{1 - (\partial_t r_0^*)^2} + \frac{K(t)(3 + (\partial_t r_0^*)^2)\partial_t r_0^*\partial_t^2 r_0^*}{(1 - (\partial_t r_0^*)^2)^3} + \frac{K'(t)(1 + (\partial_t r_0^*)^2)}{(1 - (\partial_t r_0^*)^2)^2}.
\end{aligned} \tag{5.82}$$

Jump conditions were presented in Appendix D of Ref. [103]. However, we find a sign error in their Eq. (D3) and in the final two terms of Eq. (D4). These jumps in the time derivatives mean that use of *Mathematica's* `NDSolve` function may no longer be possible. Instead, time evolution would need to be implemented via matrix multiplication methods to allow use of the formula presented in Eq. (5.63), such as the method presented in Sec. 3.2.3 using Runge Kutta time evolution. Finally, regularisation parameters are not the same for the non-static case and will need to be replaced by those given in Ref. [103]. Though these challenges remain, numerical results presented in Tab. 5.3 provide hope that such an analysis in the future could provide accurate results.

# Chapter 6

## Spin precession invariant for eccentric orbits

### 6.1 Introduction

Previous chapters 4,5 have dealt with the calculation of the scalar and electromagnetic self force. Here we consider the gravitational self force acting on a small object of mass  $\mu$  in orbit around a larger mass black hole of mass  $M$ , with  $\mu/M \ll 1$ . We set  $M = 1$  throughout the rest of this chapter. We do not present a calculation of the self force in this chapter, instead we consider what meaningful quantities we can construct, given the self force and metric perturbation. The gravitational self force arises from the perturbation to the “background” spacetime (that of the larger black hole) created by the smaller mass at  $O(\mu)$ . It is well known that the gravitational self force is gauge dependent [111]. We can see this if we consider a gauge transformation

$$x^\mu \rightarrow x^\mu - \xi^\mu, \quad (6.1)$$

then the metric perturbation transforms as

$$h_{\mu\nu} \rightarrow h_{\mu\nu} + \xi_{\mu;\nu} + \xi_{\nu;\mu}. \quad (6.2)$$

The self force  $F^\mu$  then transforms as  $F^\mu \rightarrow F^\mu + \tilde{F}^\mu$  with [31]

$$\tilde{F}^\mu = (\delta_\nu^\mu + u^\mu u_\nu) (u^\beta [u^\alpha \xi^\nu]_{;\alpha};\beta + R^\nu_{\alpha\beta\gamma} u^\alpha \xi^\beta u^\gamma). \quad (6.3)$$

To compare with other approaches to the two-body problem, such as the post-Newtonian expansion and numerical relativity, we would like to consider “physical” quantities that can be computed independently via all three methods. We must consider quantities which are gauge invariant under gauge transformations which preserve the underlying symmetry of the perturbed spacetime and the orbital motion.

A useful and interesting feature of the self force is that it can be split into a conservative piece and a dissipative piece whose features can be considered separately. The dissipative part can be related to Teukolsky fluxes [112, 113, 114, 115]. Restricting our attention to only the conservative part of the self force allows us to consider  $O(\mu)$  perturbations to geodesic quantities. Detweiler and Whiting [30] have shown that, under the self force, the smaller mass travels on a geodesic of a regularly-perturbed spacetime  $\tilde{g}_{\mu\nu} = g_{\mu\nu} + h_{\mu\nu}^R$ . Here  $g_{\mu\nu}$  is the background spacetime and  $h_{\mu\nu}^R$  is a regular smooth vacuum solution of the Einstein equations. The regular perturbed metric  $h_{\mu\nu}^R$  is obtained by subtracting a singular field from the full metric solution of the linearised Einstein equations (4.2).

The first gauge invariant quantity, the redshift invariant  $z$ , was introduced by Detweiler [32]. Detweiler’s derivation depended on the underlying helical symmetry of circular orbits. For perturbations by a particle on circular orbits with tangent vector

$$u^\mu = u^t [1, 0, 0, \Omega], \quad (6.4)$$

with orbital frequency  $\Omega = u^\phi/u^t$ , there exists a helical Killing vector field

$$k^\mu \partial_\mu = \partial_t + \Omega \partial_\phi \quad (6.5)$$

in the perturbed spacetime. The metric perturbation respects this helical symmetry (6.5) through  $k^\lambda h_{\mu\nu;\lambda}^R = 0$ . The background spacetime must also

respect this helical symmetry (6.5) (which is the case for both Schwarzschild and Kerr spacetimes). The redshift invariant  $z$  is given by [32]

$$z = -k^\mu u_\mu = E - \Omega L = \frac{1}{u^t}, \quad (6.6)$$

where we have the energy  $E = -u_t$  and angular momentum  $L = u_\phi$ . The orbital frequency  $\Omega$  may in principle be measured from the gravitational wave.

The spin precession invariant  $\psi$  was introduced in [116]. The formulation of the spin precession invariant  $\psi$  built upon the work of Harte [117], who emphasised that a spin vector is parallel transported in a regularly perturbed spacetime to  $O(\mu)$ . The spin vector experiences geodetic precession along the orbit due to the curvature of the spacetime. The spin precession scalar is defined as the average angle of precession per radian of orbital motion. The spin precession invariant  $\psi$  has been further investigated in Refs. [118, 119, 120].

Various other invariant quantities have been proposed such as shifts in the ISCO [121], periapsis advance [121, 122, 123, 124, 125] and tidal invariants [126, 127, 128, 129].

For eccentric orbits there is no helical Killing vector for the perturbed spacetime. There is however a discrete symmetry in passing between points of closest approach (the periapsides). In passing from one periapsis to the next we essentially undergo a coordinate transformation,  $r' = r$ ,  $\theta' = \theta$ ,  $\phi' = \phi + \Phi$ ,  $t' = t + T$  and  $\tau' = \tau + \mathcal{T}$ , where  $\Phi, T, \mathcal{T}$  are the accumulated  $\phi, t$  and  $\tau$  over one periapsidal period. From this we can define two frequencies

$$\Omega_r = \frac{2\pi}{T}, \quad \Omega_\phi = \frac{\Phi}{T}, \quad (6.7)$$

the radial and azimuthal frequencies respectively. These are physical quantities and may be measured from the gravitational wave flux received by an observer at infinity. The frequencies  $\Omega_r, \Omega_\phi$  define each orbit gauge independently within the class of gauges that respect the symmetry between periapsides.

Barack and Sago [122] used the symmetry of passing between periapsides to construct the averaged red shift invariant. They restricted the metric perturbation to a class of gauges so that (in polar-type coordinates)

$$h_{\mu\nu}(\tau + \mathcal{T}) = h_{\mu\nu}(\tau), \quad (6.8)$$

and thus the perturbed spacetime respects the periodicity of radial motion of the orbit. Essentially this restricts us to periodic gauges which do not produce any spurious growth in the metric perturbation. Barack and Sago [122] compared eccentric orbit geodesics in the background and perturbed spacetimes with the same frequencies. They then construct the quantity

$$z = \frac{\mathcal{T}}{\mathcal{T}}, \quad (6.9)$$

as the average of the redshift invariant which reduces to the circular orbit result of Eq. (6.6) in the circular orbit limit. In this chapter we use the ideas of [122], further developed in [130], to construct the eccentric version of the spin precession invariant for the Schwarzschild spacetime. The spin precession invariant is given by [116]

$$\psi = \frac{\Phi - \Psi}{\Phi}, \quad (6.10)$$

where  $\Psi$  is the accumulated spin precession angle over one radial period, with respect to a polar type basis.

In collaboration with Akcay and Dolan [4] we used the implementation presented here to numerically calculate the  $O(\mu)$  perturbation to the spin precession invariant, which we denote as  $\Delta\psi$ . Numerical results were produced by Akcay using the code developed in Ref. [130]. We compare with post Newtonian calculations, carried out by Akcay and Dolan [4], and show agreement with our results.

## 6.2 Geodetic precession

Before presenting the spin precession invariant, we first present a discussion of geodetic precession. The spin precession invariant, defined in [116] for circular

orbits, is essentially the self force effect on geodetic precession.

### 6.2.1 Historical background

Geodetic precession was first discovered by de Sitter in 1916 [131], who predicted a precession of the axis of rotation of the Earth-Moon system of approximately 1.9 arcsec/century different from the Newtonian prediction. This, one of the key tests of General Relativity, was confirmed in 1988 using lunar laser ranging [132]. Gravity Probe B used gyroscopes to measure the rate of geodetic precession from a polar Earth orbit [133]. The experiment reported a precession frequency of  $6.602 \pm .018$  arcsec/year which agreed with predictions. Other systems outside of our Solar System have also been studied, such as the double pulsar system PSR J0737-3039, where a precession rate of  $4.77 \pm 0.66$  deg/yr was measured [134]. The dynamics of all these systems can still be described by weak field approximations with  $GM/rc^2 \ll 1$ , where  $M$  and  $r$  are typical mass and length scales of the system. In this weak field approximation the spin vector of a test body in orbit around a non spinning body experiences a precession effect of its spin vector  $\mathbf{s}$  through

$$\frac{d\mathbf{s}}{dt} = \boldsymbol{\Omega}_s \times \mathbf{s} \quad (6.11)$$

with a precession frequency  $\boldsymbol{\Omega}_s = \mathbf{v} \times \nabla \Phi_s$ , where  $\mathbf{v}$  is the orbital velocity and  $\Phi_s$  is Newton's gravitational potential.

Geodetic precession describes how the curvature of spacetime causes the precession of a parallel transported vector. As a vector is parallel transported along a path in curved spacetime it will be rotated due to the geodetic effect. See Fig. 6.1 for an illustration. If the central body is spinning there is an additional precession effect, the Lense-Thirring precession [135] caused by frame dragging. We may ignore this in our scenario as the Schwarzschild black hole is non-spinning. However the Lense-Thirring effect would need to be taken in to account if we were to extend the analysis to the Kerr spacetime.

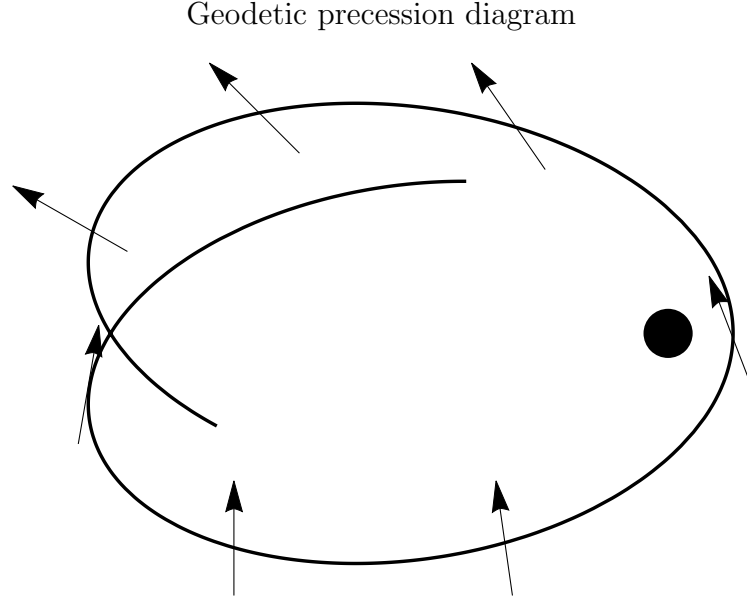


Figure 6.1: Diagram showing how a vector transported around a precessing elliptical orbit precesses.

Typically a spinning body travels on a different orbit to a non-spinning object since it experiences a spin-force governed by the Mathisson-Papapetrou equations for a particle of mass  $\mu$  [136, 137]

$$\begin{aligned}
 p^\gamma{}_{;\alpha} u^\alpha &= -\frac{1}{2} u^\lambda R^\gamma{}_{\lambda\alpha\beta} S^{\alpha\beta}, \\
 S^{\gamma\nu}{}_{;\alpha} u^\alpha + u^\gamma u_\lambda S^{\nu\lambda}{}_{;\alpha} u^\alpha - u^\nu u_\lambda S^{\gamma\lambda}{}_{;\alpha} u^\alpha &= 0,
 \end{aligned} \tag{6.12}$$

with the momentum defined as

$$p^\gamma = \mu u^\gamma + u_\lambda S^{\gamma\lambda}{}_{;\alpha} u^\alpha, \tag{6.13}$$

and  $S^{\alpha\beta}$  the spin tensor. One must impose a supplementary condition on the spin to fix a worldline. We use centre of mass conditions

$$p_\alpha S^{\alpha\beta} = 0, \tag{6.14}$$

in agreement with Harte, see Eq. (69) in [117]. We define a spin vector

$$s_\lambda = \frac{1}{2} \sqrt{-g} \epsilon_{\lambda\alpha\beta\gamma} u^\alpha S^{\beta\gamma}, \tag{6.15}$$

with magnitude  $s$ , where  $s_\alpha s^\alpha = s^2$ . The change in momentum  $p^\gamma$  occurs at  $p^\gamma{}_{;\alpha} u^\alpha = O(s)$ . Taking the derivative of (6.14) we can see that the change in the spin occurs with magnitude  $O(s^2)$

$$p_\alpha S^{\alpha\beta}{}_{;\gamma} u^\gamma = -p_{\alpha;\gamma} u^\gamma S^{\alpha\beta} \sim O(s^2), \quad (6.16)$$

since  $S^{\alpha\beta} \sim O(s)$ . If we consider a particle with spin  $s$  sufficiently small  $s \ll \frac{G\mu^2}{c}$ , we can neglect the effects of spin on the motion. The particle travels on a geodesic with the the spin vector  $s^\mu$  parallel transported and orthogonal to the tangent vector  $u^\mu$

$$s^\mu{}_{;\alpha} u^\alpha = 0, \quad s^\mu u_\mu = 0. \quad (6.17)$$

Harte [117] showed that Eqs. (6.17) are also valid for a compact body in the regularly perturbed spacetime described by Detweiler and Whiting [30].

### 6.3 Tetrad basis

We now choose to work in a tetrad basis by defining a set of four linearly independent vectors at each spacetime point. These vectors are written as  $e_a^\mu(x)$  where  $a = \{0, 1, 2, 3\}$ . The inverse of the tetrad vectors  $e_\mu^a$  are defined so that

$$e_a^\mu e_\nu^a = \delta^\mu{}_\nu, \quad e_a^\mu e_\mu^b = \delta_a{}^b. \quad (6.18)$$

Vectors are decomposed in the tetrad basis as

$$V^\mu = V^a e_a^\mu, \quad V^a = V^\mu e_\mu^a, \quad (6.19)$$

and tensors of any order follow in the same way. We have found it useful to impose the additional condition that the tetrad be orthonormal,

$$g_{\mu\nu} e_a^\mu e_b^\nu = \eta_{ab}, \quad \eta_{ab} e_\mu^a e_\nu^b = g_{\mu\nu}. \quad (6.20)$$

The tetrad can be defined along a worldline, with tangent vector  $u^\alpha$ , by setting the  $0^{th}$  tetrad leg to be equal to the tangent vector  $u^\alpha = e_0^\alpha$ . The remaining three spatial vectors  $e_i^\alpha$  define a spatial reference basis carried along the geodesic.

If we now write  $s^\mu$  in terms of an orthonormal tetrad basis with  $e_0^\mu = u^\mu$ , we find from (6.17) that  $s^0 = 0$ . We can write the parallel transport equation for  $s^\mu$  (6.17) as a three-dimensional equation

$$\frac{ds^i}{d\tau} = -\Gamma_{\alpha\beta}^\mu u^\alpha e_j^\beta e_\mu^i s^j = (\boldsymbol{\omega} \times \mathbf{s})^i, \quad (6.21)$$

where  $\boldsymbol{\omega}_i = \frac{1}{2}\epsilon_{ijk}\omega^{jk}$  and

$$\omega_{ij} = g_{\alpha\beta} e_i^\alpha e_{j;\gamma}^\beta u^\gamma. \quad (6.22)$$

Equation (6.22) describes how a reference basis  $e_a^\alpha$  fails to be parallel transported. We consider a parallel transported basis  $\tilde{e}_a^\mu$  and compare with the reference basis  $e_a^\alpha$  to find precession. In considering planar orbits, if we choose the reference basis such that  $e_2^\mu = \tilde{e}_2^\mu$ , and is therefore also parallel transported, we can restrict the rotation to the plane constructed from the two tetrad legs  $e_1, e_3$ . There is now an angle  $\Psi$  between the reference tetrad legs  $e_a^\mu$  and the parallel transported  $\tilde{e}_a^\mu$  with  $a = 1, 3$ . We can relate the two tetrads via

$$\begin{aligned} \tilde{e}_1 &= e_1 \cos \Psi - e_3 \sin \Psi, \\ \tilde{e}_3 &= e_1 \sin \Psi + e_3 \cos \Psi. \end{aligned} \quad (6.23)$$

Enforcing the parallel transport equation on  $\tilde{e}_a^\mu$  gives an equation for the rate of change of the angle

$$\dot{\Psi} = e_{3\mu} e_{1;\alpha}^\mu u^\alpha = -e_{1\mu} e_{3;\alpha}^\mu u^\alpha \quad (6.24)$$

We integrate over one orbit to find  $\Psi$ , which we use in our formula Eq. (6.10) to construct  $\psi$  which is the the average accumulated spin precession per radian.

We have complete freedom to choose a reference frame. Unfortunately this also means the  $\psi$  formula Eq. (6.10) is free from physical content unless we

have some physical motivation to fix the reference basis. For example, we could choose the reference basis to be parallel transported, which would give zero precession, with  $\Psi = 0$ . We must restrict our reference tetrad using physically well-motivated ideas related to the spacetime and orbit under consideration.

In the circular case there is a continuous isometry due to the helical Killing vector (6.5). In the eccentric case, we use the symmetry associated with passing from one periapsis to the next to restrict our attention to tetrads which respect the symmetry

$$e_a^\mu(\tau + \mathcal{T}) = e_a^\mu(\tau), \quad (6.25)$$

so that at each periapsis the tetrad's components are unchanged in a polar basis. To construct the spin precession invariant we must seek such a tetrad.

### 6.3.1 Parallel transported tetrad

In Ref. [138] Marck presented a method for constructing a parallel transported tetrad for generic geodesic orbits in Kerr. Marck first sets the the  $0^{th}$  tetrad leg equal to the tangent vector  $u^\alpha = e_0^\alpha$ . Marck then used the vector  $J^\mu = f^{\mu\nu}u_\nu$  formed using the Killing-Yano tensor  $f^{\mu\nu}$  (discussed in Sec. 3.3.1) to define a second tetrad leg. The tetrad leg is chosen as  $e_2^\mu = J^\mu/\mathcal{K}^{1/2}$ , where  $\mathcal{K}$  is the Carter constant [66], so that  $g_{\mu\nu}e_2^\mu e_2^\nu = 1$ . The vector  $J^\mu$  (and therefore  $e_2^\mu$ ) is parallel transported along  $u^\mu$ , as

$$u^\lambda J^\mu{}_{;\lambda} = u^\lambda f^{\mu\nu}{}_{;\lambda} u_\nu + f^{\mu\nu} u^\lambda u_{\nu;\lambda} = 0, \quad (6.26)$$

where the first term vanishes due to antisymmetry in  $f^{\mu\nu;\lambda} = -f^{\mu\lambda;\nu}$  and the second term vanishes since  $u^\nu$  is tangent to a geodesic.

If we restrict motion to the equatorial plane in Schwarzschild by setting  $\theta = \pi/2$ ,  $e_2^\mu$  reduces to the unit vector in the  $\theta$  direction. We now have the

two parallel transported tetrad legs given by

$$\begin{aligned} e_0^\mu &= u^\mu = \left\{ \dot{t}, \dot{r}, \dot{\theta}, \dot{\phi} \right\} = \left\{ \frac{E}{f}, \dot{r}, 0, \frac{L}{r^2} \right\}, \\ e_2^\mu &= \left\{ 0, 0, \frac{1}{r}, 0 \right\}. \end{aligned} \quad (6.27)$$

Here  $E = -u_t$  and  $L = u_\phi$ . The value of  $\dot{r}$  is given by the energy equation  $g_{\mu\nu}u^\mu u^\nu = -1$ , that is,

$$\dot{r}^2 = E^2 - f \left( 1 + \frac{L^2}{r^2} \right). \quad (6.28)$$

The two additional legs are also given by Marck [138]

$$\begin{aligned} e_1^\mu &= \left( \frac{r\dot{r}}{f(r^2 + L^2)^{\frac{1}{2}}}, \frac{Er}{(r^2 + L^2)^{\frac{1}{2}}}, 0, 0 \right), \\ e_3^\mu &= \left( \frac{EL}{f(r^2 + L^2)^{\frac{1}{2}}}, \frac{\dot{r}L}{(r^2 + L^2)^{\frac{1}{2}}}, 0, \frac{(r^2 + L^2)^{\frac{1}{2}}}{r^2} \right), \end{aligned} \quad (6.29)$$

These vectors (6.29) satisfy the orthonormality conditions  $g_{\mu\nu}e_a^\mu e_b^\nu = \eta_{ab}$ . The tetrad (6.27, 6.29) only depends upon  $r$  and  $\dot{r} = \frac{dr}{dt}$ , and therefore respects the symmetry condition of Eq. (6.25). The tetrad legs (6.29) are not unique since we are always free to rotate in the 1-3 plane as long as they still respect the symmetry of Eq. (6.25).

We can now use the tetrad, (6.27, 6.29), to calculate  $\dot{\Psi}$ , the rate of change of the angle between the reference tetrad and the parallel transported tetrad, using Eq. (6.24), to give

$$\dot{\Psi} = \frac{EL}{r^2 + L}. \quad (6.30)$$

To calculate the spin precession invariant  $\psi$ , the average change in the angle  $\Psi$  over one orbit, we require some prescription to parametrise the orbit so that we can integrate over one radial period.

### 6.3.2 Schwarzschild eccentric orbit

An eccentric geodesic in the equator ( $\theta = \frac{\pi}{2}$ ) of Schwarzschild spacetime may be parametrised by

$$r(\chi) = \frac{p}{1 + e \cos \chi}, \quad (6.31)$$

where  $p$  is the semi-latus rectum,  $e$  is the eccentricity. The value  $\chi$  is known as the “relativistic anomaly,” defined by Eq. (6.31) whose values of  $\chi = 0$  and  $\chi = \pi$  correspond to periapsis and apapsis respectively. Eccentric geodesics exist for  $p > 6 + 2e$ , where  $p = 6 + 2e$  is called the separatrix [139]. Along the separatrix  $\Phi$  and  $T$  diverge whilst  $\Omega_\phi$ , as defined in Eq. (6.7), remains finite. The divergence in  $\Phi$  and  $T$  is associated with the zoom-whirl behaviour discussed in Ref. [140].

The particle is at periapsis for  $\chi = 2\pi n$ , where  $n$  is an integer. If we construct all our quantities with respect to  $\chi$ , we can integrate over one period to find the total accumulated values. For example,

$$\Phi = \int_0^{2\pi} \frac{d\phi}{d\chi} d\chi. \quad (6.32)$$

The energy and angular momentum are given in terms of  $p$  and  $e$  in [122]

$$E = \left[ \frac{(p - 2 - 2e)(p - 2 + 2e)}{p(p - 3 - e^2)} \right]^{1/2},$$

$$L = \frac{p}{\sqrt{p - 3 - e^2}}. \quad (6.33)$$

The rate of change of  $\chi$  with respect to proper time  $\tau$  may be found from the relation  $\dot{r} \frac{d\tau}{d\chi} = \frac{dr}{d\chi}$  which gives

$$\frac{d\tau}{d\chi} = \frac{p^{\frac{3}{2}}}{(1 + e \cos \chi)^2} \sqrt{\frac{p - 3 - e^2}{p - 6 - 2e \cos \chi}}. \quad (6.34)$$

Other quantities can be found via the chain rule,  $\frac{dt}{d\chi} = \dot{t} \frac{d\tau}{d\chi}$  and  $\frac{d\phi}{d\chi} = \dot{\phi} \frac{d\tau}{d\chi}$ . These are given in terms of  $p$  and  $e$  in Eqs. (4) and (5) of Ref. [122]. We find,

as in Ref. [122], that  $\Phi$  can be given as an elliptic integral

$$\Phi = 4\sqrt{\frac{p}{p-6+2e}} \text{ellipK}\left(\frac{4e}{p-6+2e}\right), \quad (6.35)$$

where  $\text{ellipK}$  is the complete elliptic integral of the first kind [122].

Finally we can calculate the spin precession via

$$\Psi = \int_0^{2\pi} \dot{\Psi} \frac{d\tau}{d\chi} d\chi, \quad (6.36)$$

and subsequently  $\psi$  using Eq. (6.10). Combining Eq. (6.30) for  $\dot{\Psi}$ , Eq. (6.33) for  $E$  and  $L$  and Eq. (6.34) for  $\frac{d\tau}{d\chi}$ , we can construct the integrand of Eq. (6.36) as

$$\dot{\Psi} \frac{d\tau}{d\chi} = \sqrt{\frac{p-3-e^2}{p-6-2e\cos\chi}} \frac{\sqrt{(p-2-2e)(p-2+2e)}}{(p-2+2e\cos\chi - e^2\sin^2\chi)}. \quad (6.37)$$

We cannot evaluate the integral Eq. (6.36) for  $\Psi$  in closed form.

Instead we present here a series expansion in powers of  $\frac{1}{p}$  for  $\Psi$

$$\begin{aligned} \frac{\Psi}{2\pi} = & 1 + \frac{3}{2}p^{-1} + \left(\frac{63}{8} - \frac{3}{4}e^2\right)p^{-2} + \left(\frac{675}{16} - \frac{21}{8}e^2 - \frac{3}{16}e^4\right)p^{-3} \\ & + \left(\frac{29403}{128} + \frac{363}{32}e^2 - \frac{249}{64}e^4 - \frac{3}{32}e^6\right)p^{-4} + O(p^{-5}), \end{aligned} \quad (6.38)$$

and using Eqs. (6.10, 6.35), we find a series expansion for  $\psi$

$$\begin{aligned} \psi = & \frac{3}{2}p^{-1} + \left(\frac{9}{8} + \frac{3}{2}e^2\right)p^{-2} + \left(\frac{27}{16} + \frac{33}{4}e^2 + \frac{3}{16}e^4\right)p^{-3} + \\ & + \left(\frac{405}{128} + \frac{705}{16}e^2 + \frac{123}{32}e^4 + \frac{3}{32}e^6\right)p^{-4} + O(p^{-5}). \end{aligned} \quad (6.39)$$

In the circular orbit case  $e = 0$  we have an exact expression for the spin precession angle

$$\psi_{circ} = 1 - \sqrt{1 - 3/p}. \quad (6.40)$$

In Fig. 6.2 we plot a graph of geodetic precession on eccentric orbits.

Unfortunately  $p$  and  $e$  are not gauge invariant quantities [122] in the perturbed spacetime. Instead in constructing gauge invariant quantities Barack

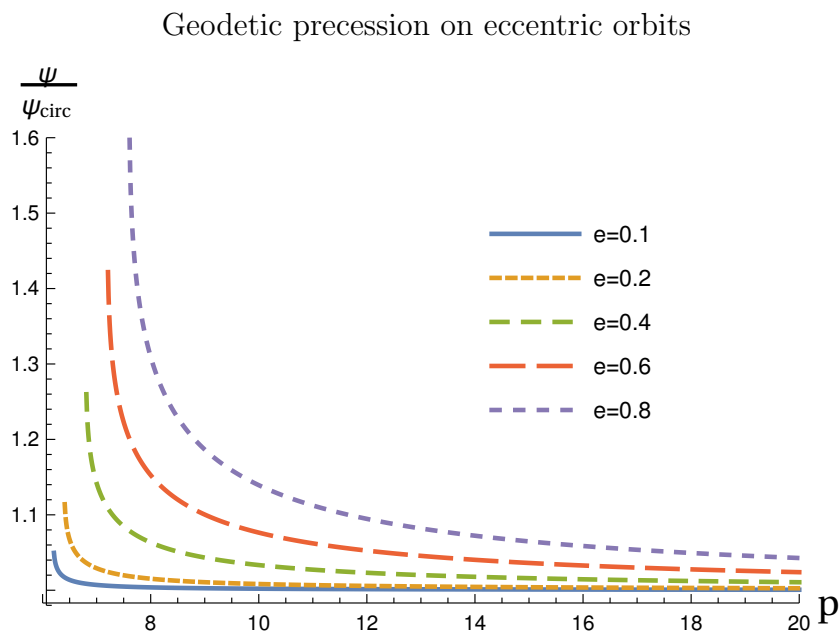


Figure 6.2: Graph of geodetic precession on eccentric orbits in Schwarzschild. Note the divergence of  $\psi$  at the separatrix  $p = 6 + 2e$ .

and Sago [122] define the redshift invariant by comparing orbits with the same frequencies  $(\Omega_r, \Omega_\phi)$  in both the background and perturbed spacetimes. Calculations of gauge invariant quantities then reduce to finding perturbed quantities with respect to  $p$  and  $e$  and adding correction terms proportional to changes in frequencies due to  $p$  and  $e$ .

## 6.4 Self force

In this section we consider the effects of self force on spin precession. We consider a body of mass  $\mu$  in an eccentric orbit around a Schwarzschild black hole of mass  $M$  with  $\mu \ll M$ .

### 6.4.1 Gauge invariant spin precession

To define our gauge invariant measure of spin precession we introduce the operator  $\Delta$  which compares orbits on background and perturbed spacetimes with the *same frequencies*  $\Omega_r$  and  $\Omega_\phi$ . Our gauge invariant measure of spin precession is defined as

$$\Delta\psi = [\psi(\Omega_r, \Omega_\phi, \mu) - \psi(\Omega_r, \Omega_\phi, 0)]_{O(\mu)}, \quad (6.41)$$

where  $[ ]_{O(\mu)}$  denotes the  $O(\mu)$  part. The quantity  $\Delta\psi$  (6.41) is the  $O(\mu)$  difference between precession of a test body and precession by a massive body travelling on worldlines with the same radial and angular frequencies. We also define an operator  $\delta$  which compares quantities on background and perturbed spacetimes with the same  $p$  and  $e$  values. We construct  $\delta\psi$  as

$$\delta\psi = [\psi(p, e, \mu) - \psi(p, e, 0)]_{O(\mu)}. \quad (6.42)$$

An orbit in the perturbed spacetime with the same  $p$  and  $e$  values has perturbed frequencies  $\Omega_r + \delta\Omega_r$  and  $\Omega_\phi + \delta\Omega_\phi$ , or equivalently perturbed values of  $T, \Phi$  through Eq. (6.7). The quantities  $\delta\Omega_r$  and  $\delta\Omega_\phi$  are of  $O(\mu)$ . We therefore

relate  $\Delta\psi$  and  $\delta\psi$  via

$$\Delta\psi = \delta\psi - \frac{\partial\bar{\psi}}{\partial\bar{T}}\delta T - \frac{\partial\bar{\psi}}{\partial\bar{\Phi}}\delta\Phi, \quad (6.43)$$

where the bar denotes background quantities. Equivalently one can use Eq. (6.43) to relate any perturbed quantities, e.g.  $\Delta\Psi$  and  $\delta\Psi$ , by substituting for  $\psi$ .

One may expect, on starting with a geodesic orbit parametrised by  $p, e$ , that a self force perturbation would also shift the values of  $p, e$ , thus requiring us to use different values  $p_0, e_0$  for our reference geodesic. Whilst this is one perspective, this shift contributes at  $O(\mu)$  to the coordinates of the trajectory in the perturbed spacetime. To first order in  $\mu$  the computed self force using either reference geodesic is equivalent.

By comparing background and perturbed spacetimes with fixed  $p$  and  $e$ , the operator  $\delta$  implicitly compares points with the same coordinate radius in both spacetimes and subsequently the same  $\chi$ . The  $\delta$  operator amounts to a perturbation of geodesic quantities on Schwarzschild spacetime whilst holding  $(p, e)$  fixed, for example

$$u^\mu = \bar{u}^\mu + \delta u^\mu. \quad (6.44)$$

Using this we can construct quantities such as  $\Psi = \bar{\Psi} + \delta\Psi$ , where  $\bar{\Psi}$  is given in Eq. (6.36). The quantity  $\delta\Psi$  is found by applying  $\delta$  to the integrand of Eq. (6.36) and integrating over  $\chi$

$$\delta\Psi = \int_0^{2\pi} \delta \left( \dot{\Psi} \frac{d\tau}{d\chi} \right) d\chi = \int_0^{2\pi} \left( \frac{\delta\dot{\Psi}}{\dot{\Psi}} - \frac{\delta u^r}{\bar{u}^r} \right) \dot{\Psi} \frac{d\bar{\tau}}{d\chi} d\chi. \quad (6.45)$$

The second term in the integrand in Eq. (6.45) arises by applying the  $\delta$  operator to  $\frac{d\tau}{d\chi}$

$$\delta \left( \frac{d\tau}{d\chi} \right) = \delta \left( \frac{1}{u^r} \frac{dr}{d\chi} \right) = -\frac{\delta u^r}{(\bar{u}^r)^2} \frac{d\bar{\tau}}{d\chi} = -\frac{\delta u^r}{\bar{u}^r} \frac{d\bar{\tau}}{d\chi}, \quad (6.46)$$

since  $\delta \left( \frac{dr}{d\chi} \right) = 0$  as the  $\delta$  operator compares quantities with the same coordinate radius.

The calculations of  $\delta T$  and  $\delta\Phi$  in Eq. (6.43) were developed by Barack and Sago [122] and we follow their approach below to find  $\delta\Psi$ . Derivative terms  $\{\frac{\partial\bar{\Psi}}{\partial\bar{T}}, \frac{\partial\bar{\Psi}}{\partial\bar{\Phi}}\}$  may be found by inverting the Jacobian for relations  $\{\frac{\partial\bar{T}}{\partial p}, \dots\}$  and using the chain rule

$$\frac{\partial\bar{\Psi}}{\partial\bar{T}} = \frac{\partial\bar{\Psi}}{\partial p} \frac{\partial p}{\partial\bar{T}} + \frac{\partial\bar{\Psi}}{\partial e} \frac{\partial e}{\partial\bar{T}}. \quad (6.47)$$

The  $\bar{\Psi}$  and  $\bar{T}$  are defined in terms of integrals (6.36). We therefore find  $\{\frac{\partial\bar{\Psi}}{\partial\bar{T}}, \frac{\partial\bar{\Psi}}{\partial\bar{\Phi}}\}$  by taking derivatives of the integral expressions and integrating numerically for arbitrary  $p, e$ .

We find  $\Delta\Psi$  by substituting  $\Psi$  for  $\psi$  in Eq. (6.43). By definition at fixed frequencies  $\Delta T = \Delta\Phi = 0$ . Thus applying  $\Delta$  to Eq. (6.10) for  $\psi$

$$\Delta\psi = \Delta \left( \frac{\Phi - \Psi}{\Phi} \right) = - \left( \frac{\Delta\Psi}{\bar{\Phi}} - \frac{\bar{\Psi}\Delta\Phi}{\bar{\Phi}^2} \right) = - \frac{\Delta\Psi}{\bar{\Phi}}. \quad (6.48)$$

### 6.4.2 Small $e$ expansions

For small  $e$  we can make use of series expansions in powers of  $e$  for the partial derivatives  $\{\frac{\partial\bar{T}}{\partial p}, \dots\}$  in Eq. (6.47). We first take derivatives of the integrand, then expand as a series in  $e$  and integrate each term. For example to find  $\frac{\partial\bar{T}}{\partial p}$  to  $O(e^n)$  we take

$$\frac{\partial\bar{T}}{\partial p} = \int_0^{2\pi} \frac{\partial}{\partial p} \left( \frac{dt}{d\tau} \frac{d\tau}{d\chi} \right) d\chi, \quad (6.49)$$

then expand the integrand as a series in  $e$

$$\frac{\partial}{\partial p} \left( \frac{dt}{d\tau} \frac{d\tau}{d\chi} \right) = t_0(p) + t_1(p)e + t_2(p)e^2 + \dots \quad (6.50)$$

and integrate each term separately. This provides an analytical check on numerical values for small  $e$  whilst also allowing us to find expressions for the  $e \rightarrow 0$  limit considered in the next subsection 6.4.3. One needs to ensure that in finding the circular orbit limit enough orders of  $e^n$  are retained to allow for cancellations. Since there are two operations in Eq. (6.47), first inverting the Jacobian and second combining partial derivatives, e.g.  $\frac{\partial\bar{\Psi}}{\partial p} \frac{\partial p}{\partial\bar{T}}$ , we must retain at least the first two terms that depend upon  $e$ .

### 6.4.3 Circular orbit limit

In the background case, the spin precession invariant calculated by taking the  $e \rightarrow 0$  limit of eccentric orbit quantities is equal to the circular orbit result, i.e.  $\lim_{e \rightarrow 0} \bar{\psi} = \bar{\psi}_{\text{circ}}$ . In the perturbed case however,  $\lim_{e \rightarrow 0} \Delta\psi$  does not in general give the circular orbit result  $\Delta_c\psi$  defined in [116]. This is due to the fundamental difference in our method for constructing  $\Delta\psi$  compared with the circular orbit  $\Delta_c\psi$ . In the circular case, the spin precession invariant  $\Delta_c\psi$  is constructed by comparing circular orbits in both background and perturbed spacetimes with the same angular frequency  $\Omega_\phi$ . In the eccentric case we compare orbits with the same azimuthal  $\Omega_\phi$  and radial frequencies  $\Omega_r$ . In the  $e \rightarrow 0$  limit the perturbed eccentric orbit does not necessarily reduce to a circular orbit, when  $\Omega_r$  and  $\Omega_\phi$  are held fixed, even when the background orbit does. We show here that the difference in  $\lim_{e \rightarrow 0} \Delta\psi - \Delta_c\psi$  is related to  $\Delta_c\Phi/(2\pi)$ , the  $O(\mu)$  part of the periapsis advance per unit angle considered in Refs. [122, 124, 125].

If  $\alpha = \{\psi, \Phi, T, \dots\}$  is the quantity of interest, the definition for  $\Delta_c\alpha$  is [116]

$$\Delta_c\alpha = \delta_c\alpha - \left( \frac{d\bar{\alpha}}{d\bar{\Omega}_\phi} \delta_c\Omega_\phi \right), \quad (6.51)$$

where  $\delta_c$  compares quantities with the same  $p$  values on background and perturbed spacetimes. The quantity  $\Delta\alpha$  in the  $e \rightarrow 0$  limit is, from Eq. (6.43)

$$\lim_{e \rightarrow 0} \Delta\alpha = \lim_{e \rightarrow 0} \delta\alpha - \lim_{e \rightarrow 0} \left( \frac{\partial\bar{\alpha}}{\partial\bar{\Omega}_r} \delta\Omega_r + \frac{\partial\bar{\alpha}}{\partial\bar{\Omega}_\phi} \delta\Omega_\phi \right). \quad (6.52)$$

We can obtain expressions such as  $\delta_c\alpha$  by setting  $e = 0$  in our expressions for eccentric orbits; in this case  $\lim_{e \rightarrow 0} \delta\alpha = \delta_c\alpha$ . We have written  $\Delta\alpha$  in terms of perturbations of frequencies, rather than  $\delta T$  and  $\delta\Phi$  as in Eq. (6.43) to aid comparison with the circular orbit.

We know that  $\lim_{e \rightarrow 0} \Delta\Phi = 0$ , since in the eccentric case holding both frequencies fixed is equivalent to holding  $T$  and  $\Phi$  fixed. On the other hand,

for  $\Delta_c \Phi$  we have

$$\Delta_c \Phi = \lim_{e \rightarrow 0} \delta \Phi - \lim_{e \rightarrow 0} \left( \frac{d\bar{\Phi}}{d\bar{\Omega}_\phi} \delta \Omega_\phi \right). \quad (6.53)$$

Using the definition  $\Phi = 2\pi\bar{\Omega}_\phi/\Omega_r$  from Eq. (6.7) and dividing by  $2\pi$  gives

$$\begin{aligned} \frac{\Delta_c \Phi}{2\pi} &= \lim_{e \rightarrow 0} \left[ \frac{\delta \Omega_\phi}{\bar{\Omega}_r} - \frac{\delta \Omega_r \bar{\Omega}_\phi}{\bar{\Omega}_r^2} - \left( \frac{\partial \bar{\Phi}}{\partial \bar{\Omega}_\phi} + \frac{\partial \bar{\Phi}}{\partial \bar{\Omega}_r} \frac{d\bar{\Omega}_r}{d\bar{\Omega}_\phi} \right) \delta \Omega_\phi \right], \\ &= \lim_{e \rightarrow 0} \left[ \frac{\delta \Omega_\phi}{\bar{\Omega}_r} - \frac{\delta \Omega_r \bar{\Omega}_\phi}{\bar{\Omega}_r^2} - \left( \frac{1}{\bar{\Omega}_r} - \frac{\bar{\Omega}_\phi}{\bar{\Omega}_r^2} \frac{d\bar{\Omega}_r}{d\bar{\Omega}_\phi} \right) \delta \Omega_\phi \right], \\ &= \lim_{e \rightarrow 0} \left[ -\frac{\bar{\Omega}_\phi}{\bar{\Omega}_r^2} \left( \delta \Omega_r - \frac{d\bar{\Omega}_r}{d\bar{\Omega}_\phi} \delta \Omega_\phi \right) \right]. \end{aligned} \quad (6.54)$$

Now consider the difference

$$\begin{aligned} \lim_{e \rightarrow 0} \Delta \psi - \Delta_c \psi &= -\lim_{e \rightarrow 0} \left( \frac{\partial \bar{\psi}}{\partial \bar{\Omega}_r} \delta \Omega_r + \frac{\partial \bar{\psi}}{\partial \bar{\Omega}_\phi} \delta \Omega_\phi \right) + \lim_{e \rightarrow 0} \left( \frac{d\bar{\psi}}{d\bar{\Omega}_\phi} \delta \Omega_\phi \right), \\ &= -\lim_{e \rightarrow 0} \left[ \frac{\partial \bar{\psi}}{\partial \bar{\Omega}_r} \delta \Omega_r - \frac{\partial \bar{\psi}}{\partial \bar{\Omega}_r} \frac{d\bar{\Omega}_r}{d\bar{\Omega}_\phi} \delta \Omega_\phi \right], \\ &= \lim_{e \rightarrow 0} \left[ \frac{\Omega_r^2}{\Omega_\phi} \frac{\partial \bar{\psi}}{\partial \bar{\Omega}_r} \right] \frac{\Delta_c \Phi}{2\pi}. \end{aligned} \quad (6.55)$$

The limit as  $e \rightarrow 0$  for the background quantities is simply given by taking the  $e = 0$  values and the partial derivative term is given by

$$\lim_{e \rightarrow 0} \frac{\partial \bar{\psi}}{\partial \bar{\Omega}_r} = -\frac{2p^{3/2} \sqrt{p-3} (p-6)^{3/2}}{4p^2 - 39p + 86}, \quad (6.56)$$

which gives

$$\lim_{e \rightarrow 0} \Delta \psi - \Delta_c \psi = -\frac{2\sqrt{p-3} (p-6)^{5/2} \Delta_c \Phi}{p(4p^2 - 39p + 86) 2\pi}, \quad (6.57)$$

in terms of  $p$  and the periapsis advance on an infinitesimally eccentric orbit  $\Delta_c \Phi$  considered in Refs. [122, 124, 125]. This is a well understood gauge invariant quantity. The importance of the periapsis advance  $\Delta_c \Phi$  for self force, post-Newtonian and numerical relativity was discussed in Ref. [123].

### 6.4.4 Perturbed tetrad

To calculate the perturbed quantities, such as  $\delta\dot{\Psi}$  of Eq. (6.45), we first calculate the perturbed tetrad. As we are still considering equatorial motion, the vector  $e_2^\mu$  remains orthogonal to the plane. The tangent vector may be written as

$$u^\mu = \left[ \frac{\bar{E} + \delta E}{f}, \dot{r} + \delta\dot{r}, 0, \frac{\bar{L} + \delta L}{r^2} \right] \quad (6.58)$$

which is normalised by the full perturbed metric

$$g_{\mu\nu}u^\mu u^\nu = (\bar{g}_{\mu\nu} + h_{\mu\nu})u^\mu u^\nu = -1. \quad (6.59)$$

Since  $\bar{g}_{\mu\nu}\bar{u}^\mu\bar{u}^\nu = -1$ , Eq. (6.59) leads to

$$h_{00} + 2\bar{g}_{\mu\nu}\bar{u}^\mu\delta u^\nu = 0, \quad (6.60)$$

where  $h_{ab} = h_{\mu\nu}e_a^\mu e_b^\nu$ .

While  $\bar{E}$  and  $\bar{L}$  are constants, given in Eq. (6.33),  $\delta E$  and  $\delta L$  are functions of  $\chi$  which vary around the orbit. We construct  $\delta E$  and  $\delta L$  using the method outlined in Ref. [122]. The quantities  $\delta E$  and  $\delta L$  are given by

$$\begin{aligned} \delta E &= \frac{1}{2}h_{00}\bar{E} + \hat{\delta}E(\chi), \\ \delta L &= \frac{1}{2}h_{00}\bar{L} + \hat{\delta}L(\chi), \end{aligned} \quad (6.61)$$

where  $\hat{\delta}E$  and  $\hat{\delta}L$  involve the conservative self force  $F_t^{\text{cons}}$  through [122]

$$\begin{aligned} \hat{\delta}E(\chi) &= \hat{\delta}E(0) - \int_0^\chi d\chi' F_t^{\text{cons}}(\chi') \frac{d\tau}{d\chi'}, \\ \hat{\delta}L(\chi) &= \hat{\delta}L(0) + \int_0^\chi d\chi' F_\phi^{\text{cons}}(\chi') \frac{d\tau}{d\chi'}. \end{aligned} \quad (6.62)$$

The quantity  $\delta\dot{r}$  is constructed from the normalisation of the tangent vector, using Eq. (6.60), which gives

$$\delta\dot{r} = \frac{1}{2}h_{00}\dot{r} + \frac{1}{\dot{r}} \left( \bar{E}\hat{\delta}E - \frac{f}{r^2}\bar{L}\hat{\delta}L \right). \quad (6.63)$$

To find the perturbed tetrad legs, we write the tangent vector and the tetrad legs in terms of perturbations of the background tetrad. The perturbation of the  $e_2^\mu$  tetrad leg is simply given by a rescaling of  $e_2^\mu = (1 + c_{22})\bar{e}_2^\mu$  since it is orthogonal to the plane of motion. The other tetrad legs are given by perturbations in the  $\bar{u}^\mu$ ,  $\bar{e}_1^\mu$  and  $\bar{e}_3^\mu$  directions

$$\begin{aligned}\delta u^\mu &= \delta e_0^\mu = c_{00}\bar{u}^\mu + c_{01}\bar{e}_1^\mu + c_{03}\bar{e}_3^\mu, \\ \delta e_1^\mu &= c_{10}\bar{u}^\mu + c_{11}\bar{e}_1^\mu + c_{13}\bar{e}_3^\mu, \\ \delta e_3^\mu &= c_{30}\bar{u}^\mu + c_{31}\bar{e}_1^\mu + c_{33}\bar{e}_3^\mu.\end{aligned}\tag{6.64}$$

The coefficients  $c_{ab}$  are of  $O(\mu)$  and the background tetrad legs are given in Eq. (6.29).

The orthonormality conditions (6.20) are then used to calculate the  $c_{ab}$  coefficients

$$\begin{aligned}c_{00} &= \frac{1}{2}h_{00}, & c_{11} &= -\frac{1}{2}h_{11}, \\ c_{33} &= -\frac{1}{2}h_{33}, & c_{10} &= h_{01} + c_{01}, \\ c_{30} &= h_{03} + c_{03}, & c_{13} + c_{31} &= -h_{13}.\end{aligned}\tag{6.65}$$

Comparing Eqs. (6.64) with Eqs. (6.29,6.58) we find

$$\begin{aligned}c_{01} &= \frac{\bar{E}\dot{r}}{f\sqrt{1 + \bar{L}^2/r^2}} \left( \frac{\hat{\delta}r}{\dot{r}} - \frac{\hat{\delta}E}{\bar{E}} \right), \\ c_{03} &= \frac{\hat{\delta}L}{r\sqrt{1 + \bar{L}^2/r^2}}.\end{aligned}\tag{6.66}$$

There is still some ambiguity in the  $c_{13}$  and  $c_{31}$  coefficients due to the freedom to rotate the tetrad vectors in the 13 plane. By integrating over one orbit and imposing the symmetry condition (6.25) this ambiguity is removed.

### 6.4.5 Perturbed precession

To calculate the perturbation of the precession angle we apply our  $\delta$  operator to Eq. (6.24)

$$\begin{aligned}\delta\dot{\Psi} &= \delta(g_{\mu\nu}e_3^\mu e_{1;\lambda}^\nu u^\lambda) \\ &= \frac{\dot{\Psi}}{2}(h_{00} + h_{33} - h_{11}) + c_{01}g_{\mu\nu}\bar{e}_3^\mu\bar{e}_1^\lambda\bar{e}_{1;\lambda}^\nu + c_{03}g_{\mu\nu}\bar{e}_3^\mu\bar{e}_3^\lambda\bar{e}_{1;\lambda}^\nu + \frac{dc_{13}}{d\tau} + \delta\Gamma_{310}\end{aligned}\tag{6.67}$$

where  $\delta\Gamma_{310} = \delta\Gamma_{\nu\alpha}^\mu e_{3\mu}e_1^\nu u^\alpha$ . The expression Eq. (6.67) contains the ambiguous term  $\frac{dc_{13}}{d\tau}$ . On integrating over one radial period this term disappears since we enforce  $c_{13}(0) = c_{13}(\mathcal{T})$ . Terms like  $c_{01}g_{\mu\nu}\bar{e}_3^\mu\bar{e}_1^\lambda\bar{e}_{1;\lambda}^\nu$  require us to interpret the tetrad as a field rather than only being defined at points on the worldline. The tetrad (6.27, 6.29) is defined everywhere within the region between  $r = p/(1 \pm e)$ , by definition is always orthonormal and  $\bar{e}_0^\mu = \bar{u}^\mu$  is always a tangent vector to a geodesic. We can therefore interpret the tetrad as a field with the region  $r = p/(1 \pm e)$ .

We now have a well-defined method for calculating  $\Delta\psi$ :

- Given a metric perturbation  $h_{\mu\nu}$  and the conservative self force  $F_\mu^{\text{cons}}$  construct the perturbed tetrad (6.64).
- Then construct  $\delta\dot{\Psi}$  via Eq. (6.67).
- Calculate the integral in Eq. (6.45) to find  $\delta\Psi$ .
- Calculate the quantity  $\Delta\Psi$  at fixed frequencies via Eq. (6.43).
- Finally use Eq. (6.48) to calculate the spin precession invariant  $\Delta\psi$ .

To calculate numerical results we require values for the metric perturbation and the conservative parts of the self force.

## 6.5 Results

We now explicitly calculate the spin precession invariant  $\Delta\psi$ . The method presented in this chapter provides a prescription for calculating  $\Delta\psi$  using the self force. We compare the results for self force with a post-Newtonian expansion. Agreement between the two independent methods provides confidence that our prescription and results are correct.

### 6.5.1 Numerical results

In Ref. [4] my co-authors and I computed the spin precession invariant  $\Delta\psi$  using the above prescription. The numerical code was developed by Akcay whose method is outlined in [130] and uses the method of extended homogeneous solutions from [141]. This code produces a set of  $l$  modes for the metric perturbation and self force, which when summed over need to be regularised. Regularisation parameters were provided by Wardell [142] using the methods of Refs. [28, 143, 144, 145].

The Lorenz gauge used in this numerical calculation is not asymptotically flat as  $\lim_{r \rightarrow \infty} h_{tt}^{R,l=0} = -2\alpha$ . The value of  $\alpha$  depends on  $p$  and  $e$ . The calculation of  $\alpha$  is found from analytical expressions for the monopole mode  $h_{tt}^{R,l=0}$  in the frequency domain as described in detail in Ref. [130]. We may remove this feature by transforming the time coordinate  $t \rightarrow t(1 + \alpha)$  which creates a shift in the orbital period  $T$  and therefore the frequencies  $\Omega_r, \Omega_\phi$ . We insert this into our formula (6.43), for  $\Psi$  rather than  $\psi$ ,

$$\Delta\Psi = \delta\Psi - (1 + \alpha) \frac{\partial\bar{\Psi}}{\partial T} \delta T - (1 - \alpha) \frac{\partial\bar{\Psi}}{\partial\Phi} \delta\Phi. \quad (6.68)$$

### 6.5.2 Post-Newtonian expansion

The post-Newtonian (PN) expansion for  $\psi$  to  $O(e^4 p^{-3})$  was calculated by Akcay and Dolan [4]. We summarise the key steps here. A post-Newtonian expansion is an expansion in powers of  $(v/c)^{2n}$  where the value of  $n$  corresponds

to the  $n^{\text{th}}$  order PN expansion.

We can equivalently track PN order by writing expansions in powers of  $1/p$ . This is because  $p$  is a dimensionless quantity related to radial distance at first order by  $r \sim \frac{GMp}{c^2}$ . At first order, the particle travels on a circular orbit with speed  $v \sim r\Omega \sim \sqrt{\frac{GM}{rc^2}}$ , where  $\Omega$  is the frequency of a particle on a circular orbit on Schwarzschild spacetime from Eq. (3.14). Therefore we have  $1/p \sim (v/c)^2$ . Writing a PN expansion in powers of  $1/p$  allows us to set  $G = M = c = 1$  as before.

The spin precession scalar is given by  $\psi = \bar{\psi} + \Delta\psi + O(\mu^2)$ , where

$$\bar{\psi} = \frac{3}{2}p^{-1} + \left(\frac{9}{8} + \frac{3}{2}e^2\right)p^{-2} + \left(\frac{27}{16} + \frac{33}{4}e^2 + \frac{3}{16}e^4\right)p^{-3} + O(p^{-4}), \quad (6.69)$$

and

$$\begin{aligned} \mu^{-1}\Delta\psi = & \underbrace{-p^{-1}}_{\Delta\psi^{LO}} + \underbrace{\left(\frac{9}{4} + e^2\right)p^{-2}}_{\Delta\psi^{NLO}} \\ & + \underbrace{\left[\frac{739}{16} - \frac{123\pi^2}{64} + \left(\frac{341}{16} - \frac{123\pi^2}{256}\right)e^2 - \frac{e^4}{2}\right]p^{-3}}_{\Delta\psi^{NNLO}} + O(p^{-4}). \end{aligned} \quad (6.70)$$

One may compare the PN series for  $\bar{\psi}$ , Eq. (6.69), with our previous series expansion given in Eq. (6.39) to verify agreement at the PN order presented here. The agreement of Eq. (6.39) and Eq. (6.69) provides confidence in the accuracy of the PN expansion.

The derivation of Eqs. (6.69-6.70) relied upon many previous works. The starting point for the post-Newtonian calculation was the spin-orbit Hamiltonian given in Ref. [146] to next-to-leading order NLO and Refs. [147, 148] given in Arnowitt-Deser-Misner (ADM) [149] coordinates. ADM coordinates describe the behaviour of two masses  $m_1, m_2$  with spins  $s_1, s_2$  in the centre-of-mass frame with coordinates  $r_1, r_2$  and momenta  $p_1, p_2$ . The Hamiltonian takes the form  $H = \mathbf{\Omega}_1 \cdot \mathbf{s}_1 + \mathbf{\Omega}_2 \cdot \mathbf{s}_2$ , where  $(\mathbf{\Omega}_1, \mathbf{\Omega}_2)$  are the spin precession

frequencies for each particle. To compare with an object of small mass in eccentric orbit around a Schwarzschild black hole, spin is restricted to just one object. We set  $m_1 = \mu$  and  $\boldsymbol{\Omega}_1 = \Omega \mathbf{k}$  where  $\mathbf{k}$  is normal to the equatorial plane. The spin precession scalar is defined as

$$\psi = \frac{\langle \Omega \rangle}{\langle \Omega_\phi \rangle}, \quad (6.71)$$

where  $\langle \rangle$  denotes the orbital average. The circular orbit results have been calculated in [116, 150].

The post-Newtonian calculation of  $\psi$  followed the approach of Ref. [139] using many of the quantities defined there. The first step is to expand the Hamiltonian to post-Newtonian orders in terms of  $c^{-2}$ . Then orbital averages are calculated using the quasi-Keplerian method of Ref. [150]. The orbital average calculation gives an expression valid to any mass ratio.

The expression for  $\psi$  is then expanded as a series in  $\mu$  to isolate the geodesic and linear-in-mass-ratio components of  $\psi$ . Finally expansions in  $c^{-2}$  are converted to expressions in terms of  $p, e$  to give the results of Eqs. (6.69-6.70).

### 6.5.3 Comparison of self force and post-Newtonian results

In Fig. 6.3 we compare our numerical results with the post-Newtonian expansion. We can compare numerical results with each post-Newtonian order from Eq. (6.70). The numerical results for  $\Delta\psi$  (purple circles) are compared with the expected leading order behaviour of  $1/p$  from the PN expansion (blue solid line) of Eq. (6.70). We then subtract the leading order PN behaviour away from the numerical results (orange triangles) and compare against next-to-leading-order PN expansion (yellow dashed line). We do the same for each subsequent PN order available from Eq. (6.70). The agreement at each PN order, between the numerical self force results and PN expansion, provide us with confidence that the prescription for calculating  $\Delta\psi$  outlined in this chapter is correct.

Comparison of numerical results  $\Delta\psi^{\text{num}}$  with the post-Newtonian expansion

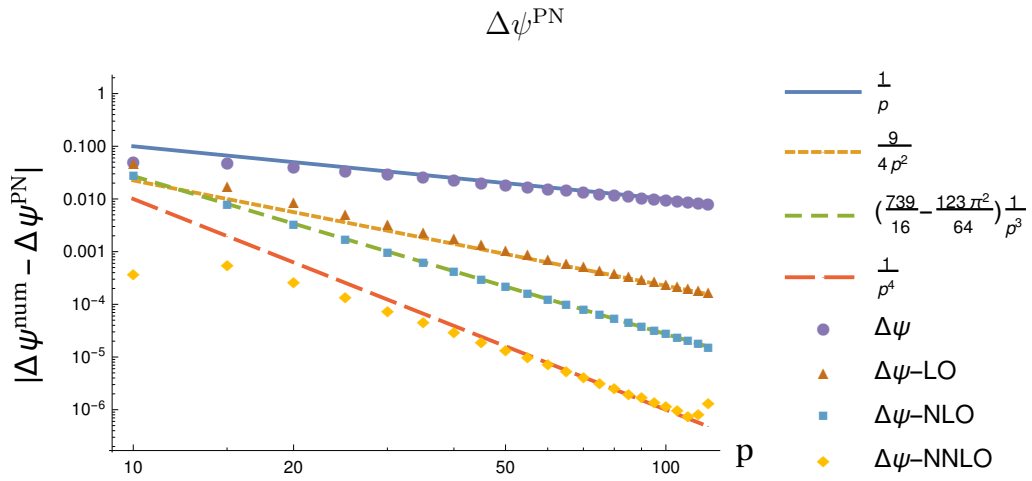


Figure 6.3: Graph of numerical  $\Delta\psi^{\text{num}}$  versus post-Newtonian expansion  $\Delta\psi^{\text{PN}}$  for  $e = 0.1$ . The plots show the difference between numerical results and different orders of the PN expansion from Eq. (6.70) as well as the expected large  $p$  behaviour of the next order term  $1/p^4$ . There is good agreement at each order.

## 6.6 Discussion

In this chapter we have presented the formulation of the spin precession scalar for eccentric orbits on Schwarzschild. This adds an additional invariant to the self force programme. Recent work by Kavanagh et al. [151] used the prescription for  $\Delta\psi$  presented in this chapter to calculate  $\Delta\psi$  analytically up to 5PN order. They report agreement with our numerical results up to expected errors from the numerical and analytical methods.

The next challenge is to compute the spin precession invariant on Kerr spacetime. The redshift invariant  $z$  of Eq. (6.9) has been calculated on Kerr spacetime for circular orbits [152, 153] and eccentric orbits [40, 154] both numerically using self force and as a PN expansion.

The Marck [138] tetrad discussed in Sec. 6.3.1 provides a way forward. On restricting the motion to the equatorial plane we again have symmetry between periapsides. Geodesic orbits are once again parametrised by frequencies  $\Omega_r, \Omega_\phi$  in a “gauge independent” way. Marck’s [138] tetrad for equatorial orbits depends only on  $r$  and  $\dot{r}$  and as such respects the symmetry condition (6.25). Ref. [138] gives the test body value

$$\dot{\Psi} = \frac{\sqrt{\mathcal{K}}}{r^2 + \mathcal{K}} \left( E + \frac{a}{L - aE} \right), \quad (6.72)$$

where  $\mathcal{K}$  is the Carter constant, which can be used to calculate the background value  $\bar{\psi}$  of the spin precession angle. Recently, in Ref. [155], Akcay outlined a prescription for calculating  $\Delta\psi$  for equatorial orbits in the Kerr spacetime. The procedure is essentially an extension of the methods presented in this chapter using the tetrad of Marck [138].

Generic geodesics in Kerr spacetime depend not only on  $r$  and  $\dot{r}$  but also  $\theta$  and  $\dot{\theta}$ , which contributes an additional frequency in the theta component  $\Omega_\theta$ . Due to this there is no obvious symmetry between periapsides. Therefore a new approach will be needed.

# Chapter 7

## Bound state solutions of the Dirac equation on Kerr spacetime

### 7.1 Introduction

This chapter investigates the behaviour of fermions on a Kerr black hole spacetime. We look for quasi-bound states of fermions by solving the Dirac equation in Kerr spacetime.

There are many interesting motivations for investigating fermionic spin-half fields on black hole spacetimes. For example, there is an analogue of the hydrogen atom. Essentially we are replacing the hydrogen nucleus with a black hole. Since the hydrogen atom has a discrete spectrum of energy states which electrons can populate, it is reasonable to investigate the existence of a similar spectrum for black holes. This analogy is not exact however, due to the nature of black holes. The states decay into the black hole and therefore have a finite lifetime though they may be long-lived. We call these states *quasi-bound*. The existence of such states has some bearing on the no-hair conjecture.

The no-hair conjecture [14, 15, 13] states that a black hole can be com-

pletely characterised by the three parameters: mass  $M$ , charge  $Q$  and angular momentum  $J$ . Any perturbation to a black hole will decay, changing only these three parameters. This motivates the study of fields on black hole space times.

In a certain low-frequency regime, bosonic fields experience superradiance [68, 156, 157, 158, 159]. In this region the mode frequency is  $\omega < \omega_c = m\Omega_h$ , with  $\Omega_h = a/(2Mr_h)$  the angular speed of the horizon at  $r = r_h$  and  $m$  the azimuthal number of the mode. Superradiance is a phenomenon by which the bosonic field can extract rotational energy from the black hole. The bosonic field is amplified due to superradiance and grows in time. If the mode is trapped in a bound state as we investigate here, this growth creates an instability referred to as the “black-hole bomb” [156, 157].

Interestingly, fermions do not experience superradiance [160, 161, 162, 163, 164]. This means that all quasi-bound states decay. We examine the behaviour of fermionic states around the critical frequency  $\omega_c$  to investigate the possibility that states may be long-lived.

Other authors have studied the Dirac equation on black hole spacetimes, in particular investigating the existence of bound states. For Schwarzschild spacetime, Lasenby *et.al.* [165] formulated the Dirac equation in Painlevé - Gullstrand coordinates and calculated the spectrum of bound states numerically. For the Kerr spacetime, there have been analytical approximations to the mode frequency  $\omega$  in the region  $M\mu \ll 1$  [166, 167] and small  $a \ll 1$  [168]. We compare our numerical results to these approximations in Sec. 7.4.

The Dirac equation may be split into two pairs of coupled differential equations for radial and angular functions. These are known as the Chandrasekhar-Page equations [169, 170]. We re-derive these in Sec. 7.2.3. The angular equations were considered in Ref. [171]. Dolan and Gair [171] presented solutions for angular eigenvalues  $\lambda$  in terms of a three-term recurrence relation which is solved using a continued fraction method. We outline this method in Sec. 7.3.2.

This chapter gives a solution to the radial equations in Sec. 7.3.3 in terms

of a matrix-valued recurrence relation. We combine the solutions of the radial and angular Chandrasekhar-Page equations to simultaneously solve for the angular eigenvalue  $\lambda$  and the mode frequency  $\omega$ .

## 7.2 Dirac equation on Kerr spacetime

In flat Minkowski spacetime the Dirac equation has the form

$$i\hat{\gamma}^a \partial_a \Psi = \mu \Psi. \quad (7.1)$$

where  $\mu$  is the field mass,  $\Psi$  is a Dirac four-spinor and  $\hat{\gamma}^a$  are constant  $4 \times 4$  matrices satisfying the relation

$$\{\hat{\gamma}^a, \hat{\gamma}^b\} = \hat{\gamma}^a \hat{\gamma}^b + \hat{\gamma}^b \hat{\gamma}^a = 2\eta^{ab} I_4, \quad (7.2)$$

where  $I_4$  is the  $4 \times 4$  identity matrix. Since we are dealing with spinors, upon extending the Dirac equation to curved spacetimes, the partial derivative does not simply become a covariant derivative. Instead we make use of spinor connection matrices over the affine connection  $\Gamma_{\alpha\beta}^\nu$ .

The Dirac equation on a curved spacetime takes the form [172]

$$(i\gamma^\nu \nabla_\nu - \mu) \Psi = 0, \quad (7.3)$$

where  $\nabla_\nu$  is a generalised covariant derivative which acts as usual on tensors, and acts on spinors as

$$\nabla_\nu \Psi = \partial_\nu \Psi - \Gamma_\nu \Psi, \quad (7.4)$$

where  $\Gamma_\nu$  are spinor connection matrices. The  $\gamma^\nu$  are now Dirac  $4 \times 4$  matrices satisfying the anticommutation relations

$$\{\gamma^\alpha, \gamma^\beta\} = 2g^{\alpha\beta} I_4. \quad (7.5)$$

Note that the  $\gamma^\alpha$  are not in general constant matrices, as opposed to the  $\hat{\gamma}^a$  matrices.

### 7.2.1 Spinors

Spinors themselves are not physical quantities. Instead we can form physical quantities by combining spinors and adjoint spinors. The adjoint spinor is defined as  $\bar{\Psi} = \Psi^\dagger \hat{\gamma}^0$ , where  $\Psi^\dagger$  is the conjugate transpose. For any two spinors  $\bar{\Phi}\Psi$  is always a scalar (see Ref. [173] for details). Similarly  $\bar{\Phi}\gamma^\mu\Psi$  always gives the  $\mu$  component of a vector.

Since  $\bar{\Phi}\Psi$  is a scalar we know that the covariant derivative of  $\bar{\Phi}\Psi$  takes the form

$$\nabla_\mu(\bar{\Phi}\Psi) = \partial_\mu(\bar{\Phi}\Psi), \quad (7.6)$$

and using the product rule gives

$$(\nabla_\mu\bar{\Phi})\Psi + \bar{\Phi}\nabla_\mu\Psi = (\partial_\mu\bar{\Phi})\Psi + \bar{\Phi}\partial_\mu\Psi. \quad (7.7)$$

Using the definition for the derivative of the spinor  $\nabla_\mu\Psi$  (7.4) and rearranging we find

$$\begin{aligned} (\nabla_\mu\bar{\Phi})\Psi &= (\partial_\mu\bar{\Phi})\Psi + \bar{\Phi}\partial_\mu\Psi - \bar{\Phi}(\partial_\mu\Psi - \Gamma_\mu\Psi), \\ (\nabla_\mu\bar{\Phi})\Psi &= (\partial_\mu\bar{\Phi} + \bar{\Phi}\Gamma_\mu)\Psi. \end{aligned} \quad (7.8)$$

Therefore the derivative of the adjoint spinor is defined by

$$\nabla_\mu\bar{\Phi} = \partial_\mu\bar{\Phi} + \bar{\Phi}\Gamma_\mu. \quad (7.9)$$

Similarly, we can find the derivative of the  $\gamma^\mu$  matrices by considering the covariant derivative of the vector given by  $\bar{\Phi}\gamma^\mu\Psi$ :

$$\begin{aligned} \nabla_\nu(\bar{\Phi}\gamma^\mu\Psi) &= \partial_\nu(\bar{\Phi}\gamma^\mu\Psi) + \Gamma_{\alpha\nu}^\mu\bar{\Phi}\gamma^\alpha\Psi \\ \bar{\Phi}(\nabla_\nu\gamma^\mu)\Psi &= \partial_\nu(\bar{\Phi}\gamma^\mu\Psi) + \Gamma_{\alpha\nu}^\mu\bar{\Phi}\gamma^\alpha\Psi - (\nabla_\nu\bar{\Phi})\gamma^\mu\Psi - \bar{\Phi}\gamma^\mu(\nabla_\nu\Psi) \\ \bar{\Phi}(\nabla_\nu\gamma^\mu)\Psi &= \bar{\Phi}(\partial_\nu\gamma^\mu)\Psi + \Gamma_{\alpha\nu}^\mu\bar{\Phi}\gamma^\alpha\Psi - \bar{\Phi}\Gamma_\nu\gamma^\mu\Psi + \bar{\Phi}\gamma^\mu\Gamma_\nu\Psi, \end{aligned} \quad (7.10)$$

therefore the derivative of the gamma matrices is given by

$$\nabla_\nu\gamma^\mu = \partial_\nu\gamma^\mu + \Gamma_{\alpha\nu}^\mu\gamma^\alpha - \Gamma_\nu\gamma^\mu + \gamma^\mu\Gamma_\nu. \quad (7.11)$$

### 7.2.2 Tetrad basis

To construct suitable  $\Gamma_\nu$  we make use of the fact that the  $\gamma^\alpha$  matrices may be constructed from the  $\hat{\gamma}^a$  matrices and an orthonormal tetrad  $e_a^\alpha$ . Orthonormal tetrads were first discussed in Sec. 6.3. The  $\gamma^\alpha$  and  $\hat{\gamma}^a$  may be related by

$$\gamma^\alpha = e_a^\alpha \hat{\gamma}^a, \quad (7.12)$$

since this satisfies Eq. (7.5) via Eq. (7.2) and the orthonormal relations for the tetrad (6.20). The generalised covariant derivative of the tetrad is

$$\nabla_\mu e_\alpha^a = \partial_\mu e_\alpha^a + \omega_\mu{}^a{}_b e_\alpha^b - \Gamma^\nu{}_{\alpha\mu} e_\nu^a, \quad (7.13)$$

where  $\omega_\mu{}^a{}_b$  is called the spin-connection. Imposing tetrad compatibility  $\nabla_\mu e_a^\alpha = 0$ , the spin-connection is defined as

$$\omega_\mu{}^a{}_b = e_\nu^a e_b^\lambda \Gamma^\nu{}_{\mu\lambda} - e_b^\lambda \partial_\mu e_\lambda^a. \quad (7.14)$$

The spin connection can be obtained directly from derivatives of the tetrad as described in Ref. [64] using

$$\omega_{\mu ab} = \frac{1}{2} e_\mu^c (\lambda_{abc} + \lambda_{cab} - \lambda_{bca}), \quad (7.15)$$

where

$$\lambda_{abc} = e_a^\mu (\partial_\nu e_{b\mu} - \partial_\mu e_{b\nu}) e_c^\nu. \quad (7.16)$$

Imposing compatibility on the gamma matrices  $\nabla_\nu \gamma^\alpha = 0$ , which follows from tetrad compatibility and Eq. (7.12), we find a condition for the spinor connection matrices

$$\partial_\nu \gamma^\mu + \Gamma_{\alpha\nu}^\mu \gamma^\alpha - \Gamma_\nu \gamma^\mu + \gamma^\mu \Gamma_\nu = 0. \quad (7.17)$$

We now find that on setting

$$\Gamma_\alpha = -\frac{1}{4} \omega_{\alpha bc} \hat{\gamma}^b \hat{\gamma}^c \quad (7.18)$$

we have a definition for  $\Gamma_\alpha$  which satisfies Eq. (7.17).

### 7.2.3 Separability: Chandrasekhar-Page equations

Chandrasekhar [169] showed how to separate variables for a massive Dirac field on the Kerr spacetime. Page [170] extended this to the Kerr-Newman spacetime. The solution of the Dirac equation then reduces to two radial and two angular equations coupled via an angular eigenvalue  $\lambda$  and a frequency  $\omega$ . These equations are known as the Chandrasekhar-Page equations. We re-derive these equations here.

#### Canonical tetrad

Chandrasekhar originally used the Newman-Penrose formalism and the Kinnersley tetrad. Here we make use of the ‘canonical’ tetrad defined by Carter [174] which allows us to express the Dirac equation in component form. This canonical tetrad is given in Eq. (4.14) of [175] in terms of inverse components

$$\begin{aligned} e_\mu^0 dx^\mu &= \frac{\sqrt{\Delta}}{\rho} (dt - a \sin^2 \theta d\phi), & e_\mu^1 dx^\mu &= \frac{\rho}{\sqrt{\Delta}} dr, \\ e_\mu^3 dx^\mu &= \frac{\sin \theta}{\rho} [-a dt + (r^2 + a^2) d\phi], & e_\mu^2 dx^\mu &= \rho d\theta. \end{aligned} \quad (7.19)$$

Inverting tetrad components via  $e_\alpha^a = \eta^{ab} g_{\alpha\beta} e_b^\beta$  gives

$$\begin{aligned} e_0^t &= \frac{r^2 + a^2}{\rho\sqrt{\Delta}}, & e_0^\phi &= \frac{a}{\rho\sqrt{\Delta}}, \\ e_1^r &= \sqrt{\Delta}/\rho, & e_2^\theta &= 1/\rho, \\ e_3^t &= \frac{a \sin \theta}{\rho}, & e_3^\phi &= \frac{1}{\rho \sin \theta}, \end{aligned} \quad (7.20)$$

and all other components of  $e_\alpha^a$  are zero. The  $\Delta$  and  $\rho$  were defined in Eq. (3.31) of our discussion of the Kerr spacetime metric, Sec. 3.3.

### Spin connection

The non-trivial components of the spin connection are

$$\begin{aligned}
 \omega_{t01} &= -\frac{M(r^2 - a^2 \cos^2 \theta)}{\rho^4}, & \omega_{t23} &= \frac{2aMr \cos \theta}{\rho^4}, \\
 \omega_{r03} &= \frac{ar \sin \theta}{\rho^2 \sqrt{\Delta}}, & \omega_{r12} &= -\frac{a^2 \sin \theta \cos \theta}{\rho^2 \sqrt{\Delta}}, \\
 \omega_{\theta03} &= -\frac{a\sqrt{\Delta} \cos \theta}{\rho^2}, & \omega_{\theta12} &= -\frac{r\sqrt{\Delta}}{\rho^2}, \\
 \omega_{\phi01} &= \frac{a \sin^2 \theta}{\rho^4} \mathcal{B}, & \omega_{\phi02} &= \frac{a\sqrt{\Delta} \sin \theta \cos \theta}{\rho^2}, \\
 \omega_{\phi13} &= -\frac{r\sqrt{\Delta} \sin \theta}{\rho^2}, & \omega_{\phi23} &= -\frac{\cos \theta}{\rho^4} \mathcal{A},
 \end{aligned} \tag{7.21}$$

where

$$\mathcal{A} = \rho^2 \Delta + 2Mr(r^2 + a^2) \tag{7.22}$$

and

$$\mathcal{B} = a^2 r \cos^2 \theta - a^2 M \cos^2 \theta + r^3 + Mr^2. \tag{7.23}$$

### Gamma matrices

For gamma matrices  $\hat{\gamma}^a$  which satisfy the relation of Eq. (7.2) we use the  $\hat{\gamma}^a$  of Ref. [176] given as

$$\begin{aligned}
 \hat{\gamma}^0 &= i \begin{pmatrix} O & I_2 \\ I_2 & O \end{pmatrix}, & \hat{\gamma}^1 &= i \begin{pmatrix} O & \sigma_3 \\ -\sigma_3 & O \end{pmatrix}, \\
 \hat{\gamma}^2 &= i \begin{pmatrix} O & \sigma_1 \\ -\sigma_1 & O \end{pmatrix}, & \hat{\gamma}^3 &= i \begin{pmatrix} O & \sigma_2 \\ -\sigma_2 & O \end{pmatrix},
 \end{aligned} \tag{7.24}$$

where  $\sigma_a$  are the standard Pauli matrices

$$\sigma_1 = \begin{pmatrix} 0 & 1 \\ 1 & 0 \end{pmatrix}, \quad \sigma_2 = \begin{pmatrix} 0 & -i \\ i & 0 \end{pmatrix}, \quad \sigma_3 = \begin{pmatrix} 1 & 0 \\ 0 & -1 \end{pmatrix}. \tag{7.25}$$

The  $\gamma^\mu$  matrices are now found by combining the  $\hat{\gamma}$  of Eq. (7.24) with the tetrad of Eq. (7.20) via Eq. (7.12).

### Spinor connection matrices

We introduce the complex quantity

$$\varrho = r + ia \cos \theta, \quad (7.26)$$

and its conjugate

$$\varrho^* = r - ia \cos \theta, \quad (7.27)$$

so that  $\rho^2 = \varrho\varrho^*$ . The spinor connection matrices  $\Gamma_\mu$  (7.18) take the form,

$$\begin{aligned} \Gamma_t &= \frac{M}{2} \begin{pmatrix} \varrho^{-2} \sigma_3 & O \\ O & -\varrho^{*-2} \sigma_3 \end{pmatrix}, \\ \Gamma_r &= -\frac{1}{2} \left( \frac{a \sin \theta}{\sqrt{\Delta}} \right) \begin{pmatrix} \varrho^{-1} \sigma_2 & O \\ O & -\varrho^{*-1} \sigma_2 \end{pmatrix}, \\ \Gamma_\theta &= -\frac{1}{2} (\sqrt{\Delta}) \begin{pmatrix} (i\varrho)^{-1} \sigma_2 & O \\ O & -(i\varrho)^{* -1} \sigma_2 \end{pmatrix}, \\ \Gamma_\phi &= \frac{1}{2} \sqrt{\Delta} \sin \theta \begin{pmatrix} (i\varrho)^{-1} \sigma_1 & O \\ O & -(i\varrho)^{* -1} \sigma_1 \end{pmatrix} + \frac{1}{2} \begin{pmatrix} \varpi \sigma_3 & O \\ O & -\varpi^* \sigma_3 \end{pmatrix}, \end{aligned} \quad (7.28)$$

where

$$\varpi = i \cos \theta - a\varrho^{-2}(\varrho + M) \sin^2 \theta. \quad (7.29)$$

### Separable ansatz

We introduce the ansatz

$$\Psi = \Delta^{-1/4} \begin{pmatrix} \varrho^{-1/2} \eta_-(r, \theta) \\ \varrho^{*-1/2} \eta_+(r, \theta) \end{pmatrix} e^{i(m\phi - \omega t)} \quad (7.30)$$

where  $\eta_\pm(r, \theta)$  are two-spinors. The azimuthal dependence is given by the half-integer  $m$  and dependence on time is encompassed in the mode frequency  $\omega$ .

Taking the Dirac equation (7.3) and multiplying by  $-i\Delta^{1/4}\rho \begin{pmatrix} \varrho^{*1/2} & O \\ O & -\varrho^{1/2} \end{pmatrix}$

now yields a pair of equations for the two spinors  $\eta_{\pm}$

$$0 = \left\{ \mp \frac{i}{\sqrt{\Delta}} [-(r^2 + a^2)\omega + am] + \sigma_3 \sqrt{\Delta} \partial_r \right\} \eta_{\mp} \mp i\mu r \eta_{\pm} \\ + \left\{ \sigma_1 \left( \partial_{\theta} + \frac{1}{2} \cot \theta \right) + i\sigma_2 (-a\omega \sin \theta + m \csc \theta) \right\} \eta_{\mp} + a\mu \cos \theta \eta_{\pm}. \quad (7.31)$$

Introducing the ansatz

$$\eta_{+} = \begin{pmatrix} R_1(r)S_1(\theta) \\ R_2(r)S_2(\theta) \end{pmatrix}, \quad \eta_{-} = - \begin{pmatrix} R_2(r)S_1(\theta) \\ R_1(r)S_2(\theta) \end{pmatrix}, \quad (7.32)$$

and multiplying Eq. (7.31) by  $\sigma_3$  leads to a pair of coupled first-order ordinary differential equations

$$\sqrt{\Delta} (\partial_r - iK/\Delta) R_1 = (\lambda + i\mu r) R_2, \\ \sqrt{\Delta} (\partial_r + iK/\Delta) R_2 = (\lambda - i\mu r) R_1, \quad (7.33)$$

and

$$\left( \partial_{\theta} + \frac{1}{2} \cot \theta - m \csc \theta + a\omega \sin \theta \right) S_1 = (+\lambda + a\mu \cos \theta) S_2, \\ \left( \partial_{\theta} + \frac{1}{2} \cot \theta + m \csc \theta - a\omega \sin \theta \right) S_2 = (-\lambda + a\mu \cos \theta) S_1, \quad (7.34)$$

where

$$K = (r^2 + a^2)\omega - am, \quad (7.35)$$

and  $\lambda$  is a separation constant.

### 7.2.4 Mode frequency

Each bound state's mode frequency  $\omega$  contains much of the key information about that state. The frequency is split into real and imaginary parts  $\omega = \omega_R + i\omega_I$ . The imaginary part corresponds to a decay rate. As we are dealing with fermions, which do not experience superradiance [160, 161, 162, 163, 164],

we expect that the modes will decay, corresponding to negative imaginary part  $\omega_I < 0$ .

To first order in the mass ratio, the spectrum of states is hydrogenic [166]. The real part of the frequency is [166]

$$\omega_R/\mu \approx 1 - \frac{(M\mu)^2}{2n^2}, \quad (7.36)$$

where  $n = \ell + \hat{n} + 1$  is the principal quantum number,  $\ell$  is the orbital angular momentum and  $\hat{n} = 0, 1, 2, \dots$

### 7.3 Recurrence relation method

In this section we outline how to find solutions to both the radial (7.33) and angular (7.34) equations satisfying a pair of boundary conditions using recurrence relations. This is based on the work of Leaver [177] who developed a method for calculating the quasi-normal modes of massless fields. Leaver [177] showed that quasinormal mode solutions of the wave equation for bosonic massless fields on Kerr spacetime could be formulated as a three-term recurrence relation which can be solved as a continued fraction. In Ref. [159] this method was adapted to calculate bound states of the massive bosonic field on Kerr spacetime. Ref. [178] made use of a *matrix-valued* recurrence relation and a continued fraction method to find bound states and quasinormal modes for the massive vector fields on Schwarzschild spacetime.

The angular equations were considered in [171, 179, 180] where three term recurrence relations for the angular eigenvalues are presented. Here we apply these methods to the radial equations so that we can find full solutions for bound states.

### 7.3.1 Formulation details

In general, three-term recurrence relations of the form

$$\alpha_n x_{n+1} + \beta_n x_n + \gamma_n x_{n-1} = 0, \quad n = 1, 2, \dots \quad (7.37)$$

have two independent solutions  $f_n$  and  $g_n$ . If in the limit

$$\lim_{n \rightarrow \infty} \frac{f_n}{g_n} = 0, \quad (7.38)$$

then  $f_n$  is known as the minimal solution and  $g_n$  the dominant solution [55]. Note that a minimal solution does not necessarily exist.

To find the minimal solution, providing it exists, we can rewrite the recurrence relation (7.37) as

$$\frac{x_k}{x_{k-1}} = - \frac{\gamma_k}{\beta_k + \alpha_k \left( \frac{x_{k+1}}{x_k} \right)} \quad (7.39)$$

which can be written as a continued fraction

$$\frac{x_k}{x_{k-1}} = - \frac{c_k}{b_k - \frac{a_k c_{k+1}}{b_{k+1} - \dots}} = - \frac{c_k}{b_k} \frac{a_k c_{k+1}}{b_{k+1} - \dots} \dots \quad (7.40)$$

Pincherle's theorem [55] says that the continued fraction (7.40) converges if and only if the recurrence relation has a minimal solution. In this case the continued fraction converges to  $\frac{f_k}{f_{k-1}}$ .

In our case  $x_n$  are coefficients of a convergent infinite sum and therefore we require

$$\lim_{n \rightarrow \infty} x_n = 0, \quad (7.41)$$

and  $x_n/x_{n-1}$  must converge. Leaver's method [177] relied on the fact that for a convergent sum the coefficients must be a minimal solution to the recurrence relation. We are therefore looking for minimal solutions.

### 7.3.2 Angular equations

Solutions to the angular equations (7.34)  $\{S_1, S_2\}$  are known as mass-dependent spin-weighted spheroidal harmonics [171]

$$S_{\{1,2\}} = {}_{s=\pm 1/2}S_{jm\mathcal{P}}^{(a\omega)(a\mu)}. \quad (7.42)$$

Each eigenstate may be labelled by three numbers:  $j$  the angular momentum,  $m$  the azimuthal component of the angular momentum and  $\mathcal{P}$  the parity which takes values  $\mathcal{P} = \pm 1$ . The angular momentum  $j$  is a positive half integer whilst  $m$  may take values  $m = -j, -j + 1, \dots, j$ .

The spheroidal harmonics (7.42) can be decomposed using spin-weighted spherical harmonics  ${}_sY_{km\mathcal{P}}(\theta)$ , defined in [171], by writing

$${}_sS_{jm\mathcal{P}}^{(a\omega)(a\mu)} = \sum_{k=|m|}^{\infty} {}_sC_{km\mathcal{P}j}^{(a\omega)(a\mu)} {}_sY_{km\mathcal{P}}(\theta). \quad (7.43)$$

There is a relationship between coefficients which allows us to define a single quantity

$$b_k = (-1)^{j-k} {}_{1/2}C_{km\mathcal{P}j}^{(a\omega)(a\mu)} = {}_{-1/2}C_{km\mathcal{P}j}^{(a\omega)(a\mu)} \quad (7.44)$$

where there are implicit hidden indices on  $b_k$ .

Using the ansatz (7.43) in the angular equations (7.34) we can obtain a three-term recurrence relation for  $b_k$

$$\begin{aligned} \alpha_k b_{k+1} + \beta_k b_k &= 0, & k &= |m|, \\ \alpha_k b_{k+1} + \beta_k b_k + \gamma_k b_{k-1} &= 0, & k &= |m| + 1, |m| + 2, \dots \end{aligned} \quad (7.45)$$

where [171]

$$\begin{aligned} \alpha_k &= (a\mu + (-1)^{j-k} \mathcal{P} a\omega) \frac{\sqrt{(k+1)^2 - m^2}}{2(k+1)}, \\ \beta_k &= (-1)^{j-k} \mathcal{P} (k+1/2) \left( 1 - \frac{am\omega}{k(k+1)} \right) + \frac{a\mu m}{2k(k+1)} - \lambda, \\ \gamma_k &= (a\mu - (-1)^{j-k} \mathcal{P} a\omega) \frac{\sqrt{k^2 - m^2}}{2k}. \end{aligned} \quad (7.46)$$

Solutions to the three-term recurrence relation (7.45) are found using continued fractions. If we write the relations (7.45) as

$$\frac{b_k}{b_{k-1}} = -\frac{\gamma_k}{\beta_k + \alpha_k \left(\frac{b_{k+1}}{b_k}\right)} \quad (7.47)$$

and use the initial relation (7.45), we may write the recurrence relation as a continued fraction

$$\beta_{|m|} - \frac{\alpha_{|m|}\beta_{|m|+1}}{\beta_{|m|+1}-} \frac{\alpha_{|m|+1}\gamma_{|m|+2}}{\beta_{|m|+2}-} \dots = 0. \quad (7.48)$$

The sum (7.43) converges if and only if  $b_k$  is a minimal solution of the recurrence relation (7.45). Therefore the continued fraction (7.48) converges to 0 if and only if the sum (7.43), with coefficients  $b_k$ , gives solutions to the angular equations. This gives rise to a discrete set of eigenvalues for  $\lambda$ .

We look for roots of the equation (7.48) using a numerical root-finding algorithm. This requires an initial estimate for  $\lambda$ .

As an initial estimate, we make use of the series expansion given in Ref. [171]. The angular eigenvalues are expanded in terms of small  $a\mu$  and  $a\omega$  as a Taylor series

$$\lambda = \sum_{p=0}^{\infty} \sum_{q=0}^{\infty} \Lambda_{pq} (a\mu)^p (a\omega)^q, \quad (7.49)$$

presented here up to second order powers in  $a^2$  [171],

$$\begin{aligned} \lambda = & (j + 0.5)\mathcal{P} \\ & + (a\mu) \left( 0.5 \left( \frac{1}{j} - \frac{1}{j+1} \right) m \right) \\ & - (a\omega) \left( 0.5 \left( \frac{1}{j} + \frac{1}{j+1} \right) m\mathcal{P} \right) \\ & + ((a\omega)^2 + (a\mu)^2)\mathcal{P} \left[ \frac{j^2 - m^2}{8j^3} + \frac{(j+1)^2 - m^2}{8(j+1)^3} \right] \\ & + 2(a\mu)(a\omega) \left[ -\frac{j^2 - m^2}{8j^3} + \frac{(j+1)^2 - m^2}{8(j+1)^3} \right] + O(a^3). \end{aligned} \quad (7.50)$$

### 7.3.3 Radial equations

#### Boundary conditions

It is clear from the form of the radial equations (7.33) that there are singular points at  $r = \{0, r_-, r_+, \infty\}$ . We consider solutions in the region outside the outer horizon therefore do not need to consider  $r = \{0, r_-\}$ . Boundary conditions for bound states are that solutions are ingoing at the horizon and decay at infinity. We can use these boundary conditions to find series solutions for  $\{R_1, R_2\}$  which match the boundary conditions at both the horizon and infinity. These series will only be valid for certain values of  $\omega$  (and  $\lambda$ ) which gives rise to a discrete set of values for  $\omega$ .

On seeking to formulate the radial equations in a recurrence relation form, we find it useful to rescale the radial functions to remove half-powers of  $\Delta$ . Let  $R_2 = \sqrt{\Delta}R_+$  and  $R_1 = R_-$  in terms of which the radial equations (7.33) become

$$\begin{aligned} \left(\frac{d}{dr} - \frac{iK}{\Delta}\right) R_- &= (\lambda + i\mu r)R_+, \\ \left(\frac{d}{dr} + \frac{iK - M + r}{\Delta}\right) R_+ &= \frac{\lambda - i\mu r}{\Delta}R_-. \end{aligned} \quad (7.51)$$

#### Near horizon solutions

At the horizon, on multiplying by  $(r - r_+)$ , all terms in Eqs. (7.51) remain finite as  $r \rightarrow r_+$ . This is due to the fact that

$$\frac{r - r_+}{\Delta} = \frac{1}{(r - r_-)}, \quad (7.52)$$

which implies that the singular point at  $r = r_+$  is a regular singular point. Hence close to the horizon, solutions of Eqs. (7.51) have leading order behaviour

$$\begin{aligned} R_+ &\sim (r - r_+)^{\sigma-1}, \\ R_- &\sim (r - r_+)^{\sigma}, \end{aligned} \quad (7.53)$$

CHAPTER 7. BOUND STATE SOLUTIONS OF THE DIRAC EQUATION ON KERR SPACETIME

---

where  $\sigma$  is some complex constant to be determined by the boundary conditions and Eqs. (7.51). We have chosen different powers for  $(R_+, R_-)$  in Eq. (7.53) since we find that this leads to a three-term recurrence relation.

We can write the two solutions near the horizon in the form

$$\mathbf{R} = \begin{pmatrix} R_+ \\ R_- \end{pmatrix} = \begin{pmatrix} (r - r_+)^{\sigma-1} \\ (r - r_+)^{\sigma} \end{pmatrix} \sum_{k=0}^{\infty} \zeta_k (r - r_+)^k, \quad (7.54)$$

where  $\zeta_k$  are vector coefficients. Substituting (7.54) into Eqs. (7.51) and matching leading order powers of  $(r - r_+)$  gives

$$\begin{pmatrix} \sigma - \frac{1}{2} + \frac{2Mi(\omega - \frac{ma}{2Mr_+})r_+}{r_+ - r_-} & 0 \\ 0 & 0 \end{pmatrix} \zeta_0 = 0. \quad (7.55)$$

Equation (7.55) has two possible solutions. The first solution is that all components of the matrix are zero in which case we have a value of  $\sigma$  given by

$$\sigma_1 = \frac{1}{2} - \frac{2Mi(\omega - \frac{ma}{2Mr_+})r_+}{r_+ - r_-}. \quad (7.56)$$

We could in principle then calculate the value of  $\zeta_0$  from the next to leading order equation. We identify the term  $\omega_c = \frac{ma}{2Mr_+}$  as the critical superradiant frequency [68]. Alternatively the second solution is found by choosing the vector  $\zeta_0$  to be a scalar multiple of

$$\zeta_0 = \begin{pmatrix} 0 \\ 1 \end{pmatrix}. \quad (7.57)$$

In the case where  $\zeta_0$  is given by Eq. (7.57) we must look to the next to leading order equation, given by

$$\begin{pmatrix} 0 & \frac{\lambda - ir_+ \mu}{r_+ - r_-} \\ \lambda + ir_+ \mu & \sigma - \frac{2Mi(\omega - \frac{ma}{2Mr_+})r_+}{r_+ - r_-} \end{pmatrix} \zeta_0 = \begin{pmatrix} \sigma - \frac{1}{2} + \frac{2Mi(\omega - \frac{ma}{2Mr_+})r_+}{r_+ - r_-} & 0 \\ 0 & 0 \end{pmatrix} \zeta_1. \quad (7.58)$$

The lower component of Eq. (7.58) leads to a second value of  $\sigma$ , namely

$$\sigma_2 = \frac{2Mi(\omega - \frac{ma}{2Mr_+})r_+}{r_+ - r_-}. \quad (7.59)$$

The ingoing solution is given by  $\sigma = \sigma_1$  from Eq. (7.56). To see this we can look to the Dirac current given in ingoing coordinates by Eq. (60) Ref. [5], namely

$$\begin{aligned} \tilde{j}^t = \frac{1}{\rho^2} & \left[ \left( |\tilde{R}_2|^2 + (r^2 + 2Mr + a^2) |\Delta^{-1/2} \tilde{R}_1|^2 \right) (|S_1|^2 + |S_2|^2) \right. \\ & \left. + 4a \sin \theta \operatorname{Im}(\Delta^{-1/2} \tilde{R}_1^* \tilde{R}_2) \operatorname{Re}(S_1^* S_2) \right]. \end{aligned} \quad (7.60)$$

The ingoing condition requires the Dirac current to be finite on the horizon. The only term which may diverge in Eq. (7.60) is  $|\Delta^{-1/2} \tilde{R}_1|^2$ . Note that  $\tilde{R}_1$  is given by our  $R_-$  in Eq. (7.54) up to some constant factor. Thus we require the real part from  $\sigma_1$  of  $1/2$  to ensure that the Dirac current remains finite whilst  $\sigma_2$  would cause the Dirac current to diverge.

### Near infinity solutions

At infinity we have an irregular singular point of rank 1. This can be seen by considering the term  $\frac{\lambda}{\Delta}$  in Eqs. (7.51) at large  $r \gg 1$

$$\frac{\lambda}{\Delta} \approx \frac{\lambda}{r^2}. \quad (7.61)$$

We therefore seek solutions with leading order behavior at infinity of

$$\begin{aligned} R_+ & \sim r^{\nu-1} e^{rq}, \\ R_- & \sim r^\nu e^{rq}, \end{aligned} \quad (7.62)$$

where  $\nu$  and  $q$  are to be determined by the boundary conditions and Eqs. (7.51). The value of  $q$  is chosen by enforcing the condition  $\operatorname{Re}(q) < 0$  since we are looking for bound state solutions. We seek values of  $\nu$  and  $q$  by writing the

solutions for large  $r$  in the form

$$\mathbf{R} = \begin{pmatrix} R_+ \\ R_- \end{pmatrix} = \begin{pmatrix} r^{\nu-1} e^{rq} \\ r^\nu e^{rq} \end{pmatrix} \sum_{k=0}^{\infty} \boldsymbol{\nu}_k r^{-k}, \quad (7.63)$$

and matching powers of  $r$ . At leading order we have

$$\begin{pmatrix} q - i\omega & -i\mu \\ i\mu & q + i\omega \end{pmatrix} \boldsymbol{\nu}_0 = 0, \quad (7.64)$$

which has non trivial solutions for  $\boldsymbol{\nu}_0$  if the determinant of the matrix is zero. This gives

$$q = \pm \sqrt{\mu^2 - \omega^2}, \quad (7.65)$$

from which we take the negative root.

Solving for  $\boldsymbol{\nu}_0$  gives any scalar multiple of

$$\boldsymbol{\nu}_0 = \begin{pmatrix} i\mu \\ q - i\omega \end{pmatrix}. \quad (7.66)$$

At next to leading order

$$\begin{pmatrix} \nu - 2iM\omega & -\lambda \\ 2iM\mu - \lambda & \nu + 2iM\omega \end{pmatrix} \boldsymbol{\nu}_0 = - \begin{pmatrix} q - i\omega & -i\mu \\ i\mu & q + i\omega \end{pmatrix} \boldsymbol{\nu}_1. \quad (7.67)$$

Using  $q$  from Eq. (7.65) and  $\boldsymbol{\nu}_0$  from Eq. (7.66) we can solve Eq. (7.67) simultaneously for  $\nu$  and  $\boldsymbol{\nu}_1$ . We find that  $\nu$  is given by

$$\nu = M \frac{\mu^2 - 2\omega^2}{q}, \quad (7.68)$$

with  $\boldsymbol{\nu}_1$  determined up to a scalar multiple. The value of  $\boldsymbol{\nu}_1$  is not presented here since we no longer make use of it.

### Full solution

We now know the form of the solutions near the horizon through Eq. (7.54) and knowledge of  $\sigma$  (7.56). The form of the solutions near infinity is given by

Eq. (7.62) with  $q$  and  $\nu$  given by (7.65) and (7.68) respectively. Combining these solutions, we can now seek a solution valid at both boundaries. Following Leaver's method [177] we look for a solution of the form

$$\mathbf{R} = \begin{pmatrix} R_+ \\ R_- \end{pmatrix} = \begin{pmatrix} (r - r_+)^{\sigma-1} (r - r_-)^{-\sigma+\nu} e^{rq} \\ (r - r_+)^{\sigma} (r - r_-)^{-\sigma+\nu} e^{rq} \end{pmatrix} \sum_{k=0}^{\infty} \boldsymbol{\xi}_k \left( \frac{r - r_+}{r - r_-} \right)^k. \quad (7.69)$$

The form of Eq. (7.69) always satisfies the ingoing boundary conditions at the horizon. The boundary condition at infinity will only be satisfied for certain values of  $\omega$  for which the series (7.69) converges [177].

Inserting the series (7.69) into the radial Eqs. (7.51) we obtain a three-term matrix-valued recurrence relation

$$\begin{aligned} \boldsymbol{\alpha}_0 \boldsymbol{\xi}_1 + \boldsymbol{\beta}_0 \boldsymbol{\xi}_0 &= 0, \\ \boldsymbol{\alpha}_k \boldsymbol{\xi}_{k+1} + \boldsymbol{\beta}_k \boldsymbol{\xi}_k + \boldsymbol{\gamma}_k \boldsymbol{\xi}_{k-1} &= 0 \quad k > 0. \end{aligned} \quad (7.70)$$

The matrices are of the form

$$\boldsymbol{\alpha}_k = \begin{pmatrix} \alpha_{k1} & \alpha_{k2} \\ 0 & \alpha_{k4} \end{pmatrix}, \quad \boldsymbol{\beta}_k = \begin{pmatrix} \beta_{k1} & \beta_{k2} \\ \beta_{k3} & \beta_{k4} \end{pmatrix}, \quad \boldsymbol{\gamma}_k = \begin{pmatrix} \gamma_{k1} & 0 \\ \gamma_{k3} & \gamma_{k4} \end{pmatrix}, \quad (7.71)$$

CHAPTER 7. BOUND STATE SOLUTIONS OF THE DIRAC EQUATION ON KERR SPACETIME

---

with entries

$$\begin{aligned}
\alpha_{k1} &= (k + \sigma + 1)(r_+ - r_-) - i(2M\omega r_+ - am), \\
\alpha_{k2} &= -(\lambda + i\mu r_+)(r_+ - r_-), \\
\alpha_{k4} &= (k + \sigma + \frac{1}{2})(r_+ - r_-) + i(2M\omega r_+ - am), \\
\beta_{k1} &= (r_+ - r_-) [q(r_+ - r_-) - 2(k + \sigma) + \nu] + 2i(2a^2\omega - am), \\
\beta_{k2} &= (\lambda + i\mu r_-)(r_+ - r_-), \\
\beta_{k3} &= -(\lambda - i\mu r_+)(r_+ - r_-), \\
\beta_{k4} &= (r_+ - r_-) [q(r_+ - r_-) - 2(k + \sigma) + \nu + 1] - 2i(2a^2\omega - am), \\
\gamma_{k1} &= (k + \sigma - 1 - \nu)(r_+ - r_-) - i(2M\omega r_- - am), \\
\gamma_{k3} &= (\lambda - i\mu r_-)(r_+ - r_-), \\
\gamma_{k4} &= (k + \sigma - \frac{3}{2} - \nu)(r_+ - r_-) + i(2M\omega r_- - am). \tag{7.72}
\end{aligned}$$

Now that we have a matrix-valued three-term recurrence relation (7.70), we may solve using a matrix-valued continued fraction [178, 181]. Setting  $\boldsymbol{\xi}_{n+1} = \mathbf{A}_n \boldsymbol{\xi}_n$  we seek the non-trivial solutions of  $\mathbf{M} \boldsymbol{\xi}_0 = \mathbf{0}$ , where

$$\mathbf{M} \equiv \beta_0 - \alpha_0 [\beta_1 - \alpha_1 (\beta_2 + \alpha_2 \mathbf{A}_2) \gamma_2]^{-1} \gamma_1. \tag{7.73}$$

and

$$\mathbf{A}_n = -(\beta_{n+1} + \alpha_{n+1} \mathbf{A}_{n+1})^{-1} \gamma_{n+1}, \tag{7.74}$$

with  $^{-1}$  denoting the matrix inverse. Equation (7.73) is the matrix analogue of Eq. (7.48). Non-trivial solutions  $\boldsymbol{\xi}_0$  exist if

$$\det |\mathbf{M}| = 0. \tag{7.75}$$

We are now able to solve both continued fractions, Eq. (7.48) and Eq. (7.75), for pairs of  $\{\lambda, \omega\}$ . As initial estimates for  $\omega$  we use the hydrogenic approximation Eq. (7.36).

## 7.4 Results

### 7.4.1 Fine and hyperfine structure

The spectrum of bound states has been considered by a number of authors [166, 167, 168]. At leading order in  $M\mu$  the spectrum is hydrogenic (7.36) [166]. The next terms appear at  $O((M\mu)^4)$  and  $O((M\mu)^5(\frac{am}{M}))$ . In analogy to the hydrogen spectrum, we refer to these as the fine structure and hyperfine structure terms. Thus the real part of the mode frequency may be written as a power series

$$\frac{\omega_R}{\mu} = \mathcal{E}^{(0)} + \mathcal{E}^{(1)} + \mathcal{E}^{(2)} + O((M\mu)^6), \quad (7.76)$$

where  $\mathcal{E}^{(0)} = 1 - \frac{(M\mu)^2}{2n^2}$  is the hydrogenic first order spectrum and  $\mathcal{E}^{(1)}, \mathcal{E}^{(2)}$  are the fine structure and hyperfine structure coefficients which depend on  $\{n, j, \ell\}$  and are  $O((M\mu)^4)$  and  $O((M\mu)^5(\frac{am}{M}))$  respectively. We identify  $\ell = j + \frac{1}{2}\mathcal{P}$  as the orbital angular momentum, and use this now as an index instead of  $\mathcal{P}$ .

The calculation of the fine structure term was carried out in Chap. 5 of Ref. [166]. The fine structure calculation uses Painlevé-Gullstrand coordinates to write the Dirac equation (7.3) in Hamiltonian form  $i\partial_t\Psi = \hat{H}\Psi$  and applies a Foldy-Wouthesen transformation [182] to write the Hamiltonian as an expansion in powers of  $(M\mu)$ . The first order equation has hydrogenic solutions, whilst the expectation value of the second order Hamiltonian when closed with the first order wavefunctions gives the fine structure coefficients. A key correction to the calculation of the fine structure term in Ref. [166] was found in Ref. [5], involving a missing factor of two, giving

$$\mathcal{E}^{(1)} = \frac{(M\mu)^4}{n^4} \left( \frac{15}{8} - \frac{3n}{2j+1} - \frac{3n}{2\ell+1} \right). \quad (7.77)$$

In Fig. 7.1 we extract the fine structure term by plotting numerical data for the difference between  $\omega_R/\mu$  and the hydrogenic approximation  $\mathcal{E}^{(0)}$ , and rescaling by  $(M\mu)^4$ . We also plot the expected result for  $\mathcal{E}^{(1)}$  from Eq. (7.77) making it clear that in the limit  $M\mu \rightarrow 0$  the numeric and analytic results agree.

A fine structure term  $\mathcal{E}^{(1)}$  was also identified by Ternov and Gaina [167]. However while they agree with the scaling at  $O((M\mu)^4)$ , they present different coefficients. Since our numerical results agree with (7.77) as shown in Fig. 7.1 we are confident in the accuracy of Eq. (7.77).

In Ref. [167] they also present a calculation of the hyperfine structure term  $\mathcal{E}^{(2)}$ . The scaling of this term is at  $O((M\mu)^5 (\frac{am}{M}))$ . However, as for the fine structure term, we find our numerical data does not agree with the coefficients presented in Ref. [167]. Since corotating ( $m = +j$ ) and counterrotating modes ( $m = -j$ ) modes have the same fine structure coefficient (7.77) we can extract the hyperfine structure term  $\mathcal{E}^{(2)}$  by taking the difference between the two. In Fig. 7.2 we investigate the hyperfine splitting by plotting the difference between co and counterrotating modes for two different values of  $a = \{0.01, 0.02\}$ . The approximate values of the hyperfine coefficients can be read off from the data in Fig. 7.2 in the limit as  $M\mu \rightarrow 0$ .

We show that the splitting scales with  $(am/M)(M\mu)^5$  which agrees with the scaling of Ref. [167]. However the coefficients do not agree with Ref. [167].

## 7.4.2 Decay rates

The imaginary part of the mode frequency was considered in Ref. [168]. The leading order behaviour of  $\omega_I/\mu$  in  $M\mu \ll 1$ ,  $am/M \ll 1$  takes the form

$$\omega_I/\mu \sim -\alpha_{j\ell n} (M\mu)^{4+2\ell+2S}, \quad (7.78)$$

where  $S = \pm 1/2$  and

$$\begin{aligned} \alpha_{j\ell n} = & \left( \frac{r_+ - r_-}{r_+ + r_-} \right)^{1+2\ell} \left( \frac{r_+ - r_-}{(2\ell + 1)(r_+ + r_-)} \right)^{2S} \frac{(n + \ell)!}{n^{4+2\ell} (2\ell)! (2\ell + 1)! (n - \ell - 1)!} \\ & \times \prod_{p=1}^{j+1/2} \left[ 1 + \frac{4(2Mr_+ \mu - am)^2}{(p - 1/2)^2 (r_+ - r_-)^2} \right]. \end{aligned} \quad (7.79)$$

Fine structure: comparison of analytic and numerical results

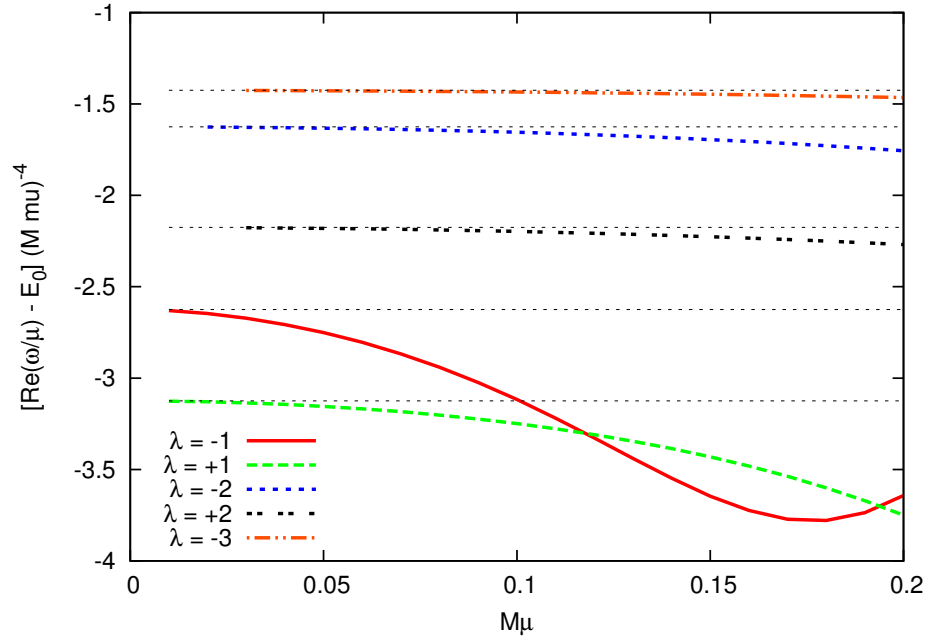


Figure 7.1: Comparison of numerical data (coloured curves) with the analytic approximation (black dotted lines) given in Eq. (7.77) for Schwarzschild space-time. The numerical data shows  $\text{Re}(\omega/\mu) - \mathcal{E}^{(0)}$  multiplied by  $(M\mu)^{-4}$ . The plot shows the modes with  $\lambda = -1$  ( $j = 1/2, \ell = 0$ ),  $\lambda = +1$  ( $j = 1/2, \ell = 1$ ),  $\lambda = -2$  ( $j = 3/2, \ell = 1$ ),  $\lambda = +2$  ( $j = 3/2, \ell = 2$ ),  $\lambda = -3$  ( $j = 5/2, \ell = 2$ ). Analytical predictions of  $\mathcal{E}^{(1)}$  are shown in dotted lines, given by Eq. (7.77), as  $-21/8, -25/8, -13/8, -87/40$  and  $-57/40$  respectively.

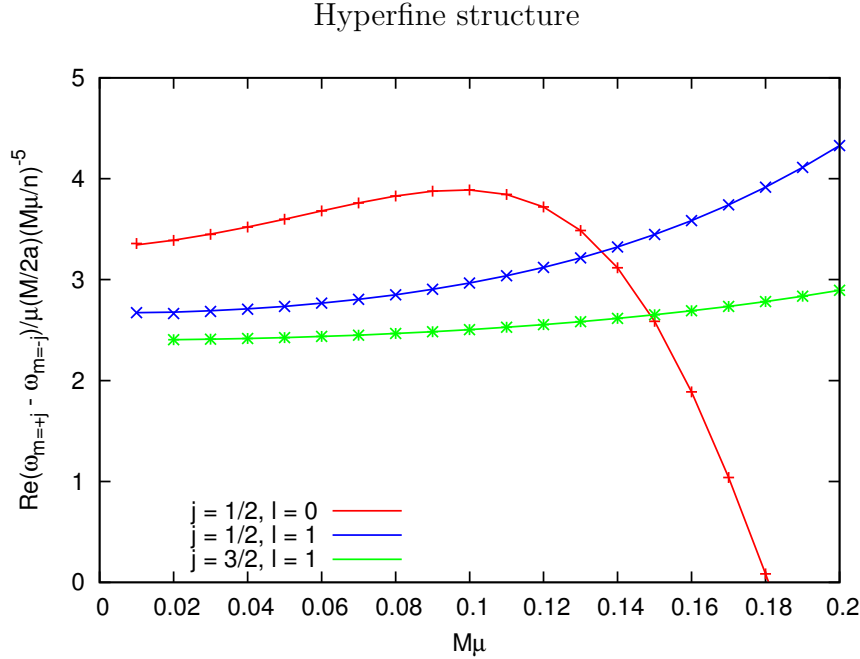


Figure 7.2: Extraction of hyperfine structure by plotting the difference between corotating ( $m = +j$ ) and counterrotating modes ( $m = -j$ ), and rescaling by  $\frac{1}{2}(M/a)n^5(M\mu)^{-5}$ . We plot two data sets  $a = 0.01$  (solid lines) and  $a = 0.02M$  (points). The agreement between the two sets provides evidence that the hyperfine splitting scales with  $(am/M)(M\mu)^5$  at leading order as given in Ref. [167].

In Fig. 7.3 we compare the approximation of Eq. (7.78) with our numerical results for the  $a = 0$  (Schwarzschild case). We find excellent agreement in the  $M\mu \rightarrow 0$  limit.

In Fig. 7.4 we investigate the decay rate of the bound states for high values of  $a$  in Kerr. We again observe a power-law behaviour for low values of  $(M\mu) \ll 1$  as expected from Eq. (7.78). We cannot however expect numerical results to match the values presented in Eq. (7.78) since we are now considering values of  $a \sim M$ . For co-rotating modes ( $m > 0$ ) at high  $a$  values there appears to be a local minimum in the decay rate as a function of  $M\mu$  for rapidly rotating black holes.

Fig. 7.5 highlights that this local minimum occurs at  $Re(\omega) = \omega_c$ , the critical superradiant frequency. The damping rate is suppressed below the critical frequency and increases rapidly above it. We may infer that states with frequencies  $Re(\omega) \leq \omega_c$  have long lifetimes. Note that whilst we plot a continuous spectrum of  $\omega$  for values of  $M\mu$  the values of  $\omega$  are discrete for each specific value of  $M\mu$ .

### 7.4.3 Kerr spectrum

In Fig. 7.6 we plot the spectrum of states for Kerr. The plots show a range of modes with  $\ell = 0$  and  $\ell = 1$  for all  $m$ . Corotating modes ( $m > 0$ ) are shown in blue/pink whilst counterrotating ( $m < 0$ ) modes are shown in red. We present three plots highlighting different features of the mode frequency.

The top plot shows the real part of the mode frequency. The middle plot reveals the fine structure by showing  $Re(\omega/\mu) - 1$  multiplied by  $(M\mu)^{-2}$ . We observe that for small  $M\mu$  the states are ordered in terms of their value of  $\omega_R$  first according to their values of  $j$ , then  $\ell$  followed by  $m$ , with the  $j = 1/2, \ell = 0, m = -1/2$  having the smallest values of  $\omega_R$ . For larger values of  $\omega_R$  this ordering changes.

The bottom plot shows the decay rate plotted as  $-\omega_I/\mu$ . The ordering

Decay rates: Schwarzschild

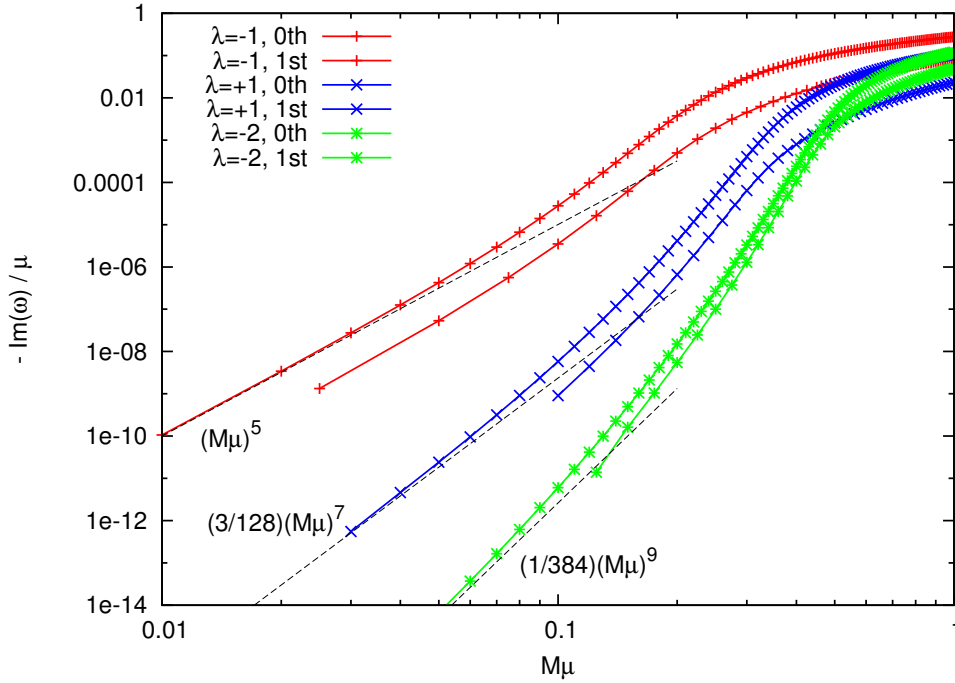


Figure 7.3: Comparison of numerical results with the analytical expression of Eq. (7.78). We use a log-log plot to examine the power-law scaling of the decay rate. The points and solid lines show numerical data for  $-\text{Im}(\omega/\mu)$  for the first two modes with  $\lambda = -1$  ( $j = 1/2, \ell = 0$ ),  $\lambda = +1$  ( $j = 1/2, \ell = 1$ ) and  $\lambda = -2$  ( $j = 3/2, \ell = 1$ ). The dotted lines show the analytical results  $(M\mu)^5$ ,  $\frac{3}{128}(M\mu)^7$  and  $\frac{1}{384}(M\mu)^9$  (see Eq. (7.78)).

## Decay rate for Dirac bound states on Kerr spacetime

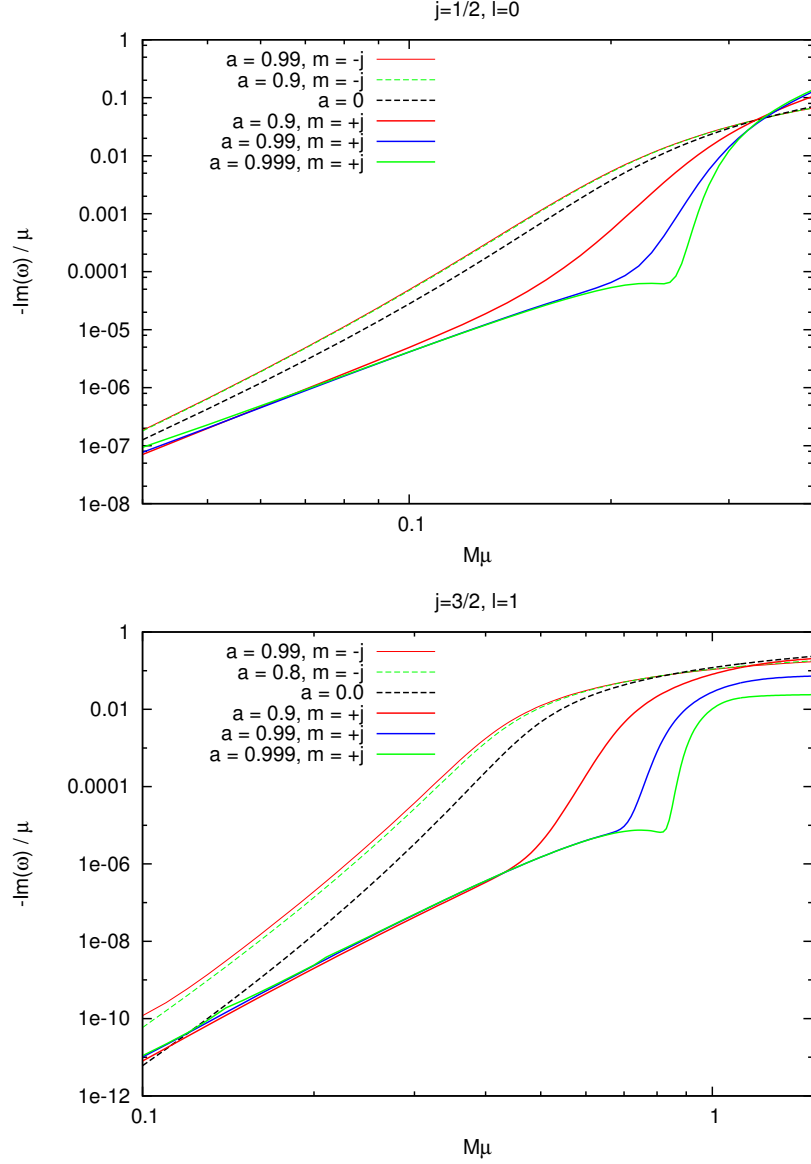


Figure 7.4: Decay rate of bound states on Kerr spacetime. The plots show both corotating ( $m = +j$ ) and counter-rotating ( $m = -j$ ) modes for different values of  $a$ . We plot  $-\frac{\omega_I}{\mu}$  using logarithmic axes to emphasise the power law relationships.

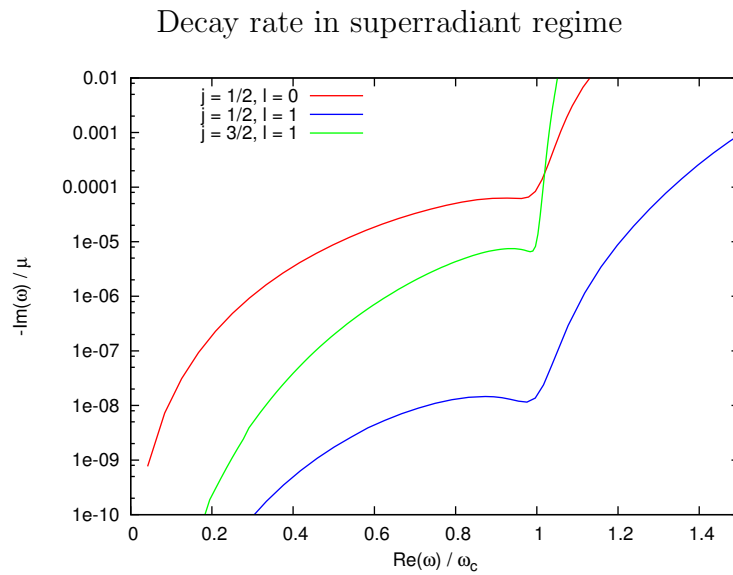


Figure 7.5: Plot of the decay rate for co-rotating modes  $m = +j$  at  $a = 0.999M$  as a function of  $\text{Re}(\omega)/\omega_c$ , where  $\omega_c = m\Omega_H$  is the critical superradiant frequency. The plot shows that decay is suppressed for  $\text{Re}(\omega) < \omega_c$ , and that a local minimum arises at  $\text{Re}(\omega) = \omega_c$ .

observed in the previous plots persists for small values of  $M\mu$ . We again observe a suppression in the decay rate for the maximally corotating  $m = j$  modes seen as a “kink” in the spectrum.

## 7.5 Discussion

In this chapter, we find bound states of the Dirac equation on Kerr spacetime via a recurrence relation in Sec. 7.3. We find a spectrum of bound states given by values of the mode frequency.

In Fig. 7.1 and Fig. 7.2 we extracted the fine and hyperfine structure of the spectrum in analogy with the hydrogen atom. We compared the fine structure with predictions in the literature [5, 166, 167]. The predictions for the hyperfine structure from Ref. [168] were found not to agree with our numerical results. An interesting future project would be to attempt to find an accurate analytic result for the hyperfine structure term as a further confirmation of the accuracy of our numerical results.

We investigated the existence of bound states of the Dirac equation with frequencies at and below the critical superradiant frequency  $\omega_c$ . In Fig. 7.5 we showed that there is a local minimum in the decay rate as a function of  $M\mu$  at the critical superradiant frequency. Around the critical frequency we find small values for the decay rate which suggests that such modes, if excited, would be long lived.

The work of this chapter provides evidence that a spectrum of bound states for the Dirac equation can exist. The question remains however as to whether such a spectrum can be excited by some realistic initial data. A time domain solution of the Dirac equation on the Kerr spacetime would be an interesting project to carry out. We would like, in future, to investigate in particular whether long-lived states can be excited.

In recent works by Barranco *et al.* [183, 184, 185], it was shown that scalar bound states can be excited by arbitrary initial data. They present a time-

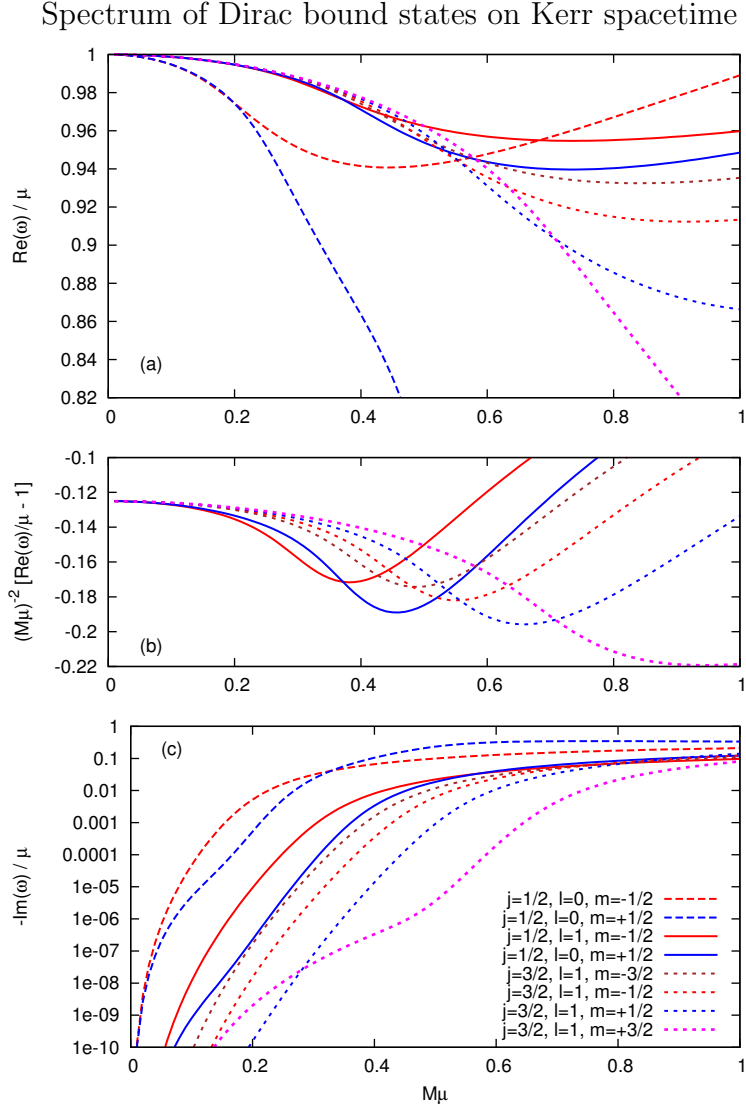


Figure 7.6: The spectrum of Dirac bound states for Kerr black hole with  $a = 0.9M$ . The top plot shows the real part of the frequency,  $\omega_R/\mu$  for  $j = 1/2$ ,  $\ell = 0$  (dashed),  $j = 1/2$ ,  $\ell = 1$  (solid) and  $j = 3/2$ ,  $\ell = 1$  (dotted) modes with colour corresponding to corotating (blue/pink) and counterrotating. The second (middle) plot extracts the fine structure behaviour for the  $\ell = 1$  states by plotting  $[\text{Re}(\omega)/\mu - 1]/(M\mu)^2$ . We observe the ordering of modes according to  $\ell, j$  and  $m$ . The bottom plot shows the decay rates  $-\omega_I/\mu$ .

domain evolution of a massive scalar field on Schwarzschild spacetime and find that quasi-bound states can be excited. These solutions, coined “scalar wigs,” were shown to exist with lifetimes in excess of the age of the universe [186].

Future work could also adapt the method presented in this chapter to calculate quasinormal modes. In Leaver’s original paper [177] the quasinormal modes for the massless Dirac field on Schwarzschild were calculated. Quasinormal modes have since been calculated for Kerr spacetime by Jing and Pan in Ref. [187], however, this is again for the massless Dirac field. To adapt our method to calculate quasinormal modes for the massive Dirac field we would need to change the ansatz of Eq. (7.69). Quasinormal modes are characterised by purely outgoing waves at infinity, hence, we would need to choose the positive sign for  $q$  in Eq. (7.65). This would lead to different values for the matrices in our continued fraction (7.70). The continued fraction’s minimal solution would then correspond to values of  $\omega$  which satisfy the outgoing boundary conditions at infinity and therefore give the quasinormal mode frequencies.

# Chapter 8

## Conclusions

In this thesis we have investigated how different fields interact with black holes. In Chap. 2 we investigated an analogue black hole described by the draining bathtub vortex. Using the eikonal approximation and a numeric solution of the scalar wave equation we showed that the propagation of a pulse-like disturbance maps out the lightcone of the effective spacetime. Our investigations present interesting possible experiments for the real draining bathtub vortex.

In Chap. 3 we introduced our black hole spacetimes. We again solved the scalar wave equation and investigated the difference in the evolution of a Gaussian pulse between the analogue and black hole spacetimes.

The next three chapters, 4, 5 and 6 considered the self force. In these three chapters we considered the scalar, electromagnetic and gravitational self force respectively. Chapter 4 calculated scalar self force using the worldline integration method. We presented the first results of this method in the Kerr spacetime and highlight where challenges remain.

We used the mode sum method to calculate electromagnetic self force in Chap. 5. The electromagnetic self force was calculated for a particle held static outside a Schwarzschild black hole and sourcing an electromagnetic field. We calculated the self force using both analytical and numerical techniques giving evidence as to the effectiveness of the discontinuous differential equation

---

solving method of Markakis and Barack [105].

Chapter 6 considered the gauge dependence of the gravitational self force. We constructed the spin precession invariant for eccentric orbits on the Schwarzschild spacetime. We compared the self force prescription for the spin precession invariant with a post-Newtonian calculation. The agreement between the two provides confidence in the formulation of Chap. 6.

Finally, in Chap. 7, we considered the Dirac field on Kerr spacetime. Using a three-term recurrence relation and continued-fraction methods we find a spectrum of bound states for the Dirac field. We compared with analytical results in the literature. A particularly interesting feature was observed at the critical superradiant frequency whereby bound state modes can have long lifetimes.

We have investigated the black hole spacetimes described by the Schwarzschild and Kerr metrics through a number of different avenues. In particular the self force investigations help contribute to the ongoing work towards using self force to examine possible sources for LISA. With the recent announcement that LISA will go ahead [18], following the three detections at LIGO [6, 9, 10] the future of gravitational wave astronomy looks bright. The limits of general relativity will be probed ever deeper. Will general relativity survive these ever more stringent tests on the theory? Only time will tell.

# Appendices



# Appendix A

## Dirac delta distribution

The Dirac delta function  $\delta(r - r_0)$  is a distribution only defined by its action on a test function  $g(r)$  via the integral [188]

$$\int_{-\infty}^{\infty} \delta(r - r_0)g(r)dr = g(r_0). \quad (\text{A.1})$$

Similarly we can define the derivative of the delta function using integration by parts

$$\int_{-\infty}^{\infty} \delta'(r - r_0)g(r)dr = \int_{-\infty}^{\infty} -\delta(r - r_0)g'(r)dr = -g'(r_0). \quad (\text{A.2})$$

We can derive how the Dirac delta distribution and its derivative transform under coordinate transformations  $r \rightarrow r^*$  from their definitions for a general function  $g(r) = g(r(r^*)) = \tilde{g}(r^*)$ . Consider

$$\begin{aligned} g(r_0) &= \tilde{g}(r_0^*) \\ \int_{-\infty}^{\infty} \delta(r - r_0)g(r)dr &= \int_{-\infty}^{\infty} \delta(r^* - r_0^*)\tilde{g}(r^*)dr^* \\ \int_{-\infty}^{\infty} \delta(r - r_0)g(r)\frac{dr}{dr^*}dr^* &= \int_{-\infty}^{\infty} \delta(r^* - r_0^*)\tilde{g}(r^*)dr^* \end{aligned} \quad (\text{A.3})$$

which gives

$$\delta(r - r_0) = \frac{dr}{dr^*}\delta(r^* - r_0^*). \quad (\text{A.4})$$

---

By a similar argument

$$-\frac{dg}{dr}(r_0) = -\frac{dr^*}{dr}\Big|_{r_0} \frac{d\tilde{g}}{dr^*}(r_0^*),$$

$$\int_{-\infty}^{\infty} \delta'(r - r_0)g(r)dr = \frac{dr^*}{dr}\Big|_{r_0} \int_{-\infty}^{\infty} \delta'(r^* - r_0^*)\tilde{g}(r^*)dr^* \quad (\text{A.5})$$

$$\int_{-\infty}^{\infty} \delta'(r - r_0)g(r)\frac{dr}{dr^*}dr^* = \frac{dr^*}{dr}\Big|_{r_0} \int_{-\infty}^{\infty} \delta'(r^* - r_0^*)\tilde{g}(r^*)dr^*, \quad (\text{A.6})$$

giving

$$\delta'(r - r_0)\frac{dr}{dr^*} = \frac{dr^*}{dr}\Big|_{r_0} \delta'(r^* - r_0^*), \quad (\text{A.7})$$

where  $\frac{dr^*}{dr}\Big|_{r_0}$  denotes  $\frac{dr^*}{dr}$  evaluated at  $r_0$ .

We also use the Heaviside step function  $\Theta(x)$ , defined as [188],

$$\Theta(x) = \begin{cases} 1, & x > 0, \\ 0, & x < 0, \end{cases} \quad (\text{A.8})$$

The derivative of the Heaviside function is the delta function.

# Bibliography

- [1] D. Dempsey and S. R. Dolan. Waves and null congruences in a draining bathtub. *Int. J. Mod. Phys.*, **D25**:1641004, 2016.
- [2] B. Wardell, C. R. Galley, A. Zenginoğlu, M. Casals, S. R. Dolan, and A. C. Ottewill. Self-force via Green functions and worldline integration. *Phys. Rev.*, **D89**:084021, 2014.
- [3] A. G. Smith and C. M. Will. Force on a static charge outside a Schwarzschild black hole. *Phys. Rev.*, **D22**:1276–1284, 1980.
- [4] S. Akcay, D. Dempsey, and S. R. Dolan. Spin–orbit precession for eccentric black hole binaries at first order in the mass ratio. *Class. Quant. Grav.*, **34**:084001, 2017.
- [5] S. R. Dolan and D. Dempsey. Bound states of the Dirac equation on Kerr spacetime. *Class. Quant. Grav.*, **32**:184001, 2015.
- [6] B. P. Abbott et al. Observation of Gravitational Waves from a Binary Black Hole Merger. *Phys. Rev. Lett.*, **116**:061102, 2016.
- [7] J. A. Wheeler and K. Ford. *Geons, black holes, and quantum foam: A life in physics*. 1998.
- [8] J. Casares. Observational evidence for stellar-mass black holes. *IAU Symp.*, **238**:3–12, 2007.

- [9] B. P. Abbott et al. GW151226: Observation of gravitational waves from a 22-solar-mass binary black hole coalescence. *Phys. Rev. Lett.*, **116**:241103, 2016.
- [10] B. P. Abbott et al. GW170104: Observation of a 50-solar-mass binary black hole coalescence at redshift 0.2. *Phys. Rev. Lett.*, **118**:221101, 2017.
- [11] S. Doeleman et al. Event-horizon-scale structure in the supermassive black hole candidate at the Galactic Centre. *Nature*, **455**:78, 2008.
- [12] <http://www.eventhorizontelescope.org/science/index.html>.
- [13] R. Ruffini and J. A. Wheeler. Introducing the black hole. *Phys. Today*, **24**:30, 1971.
- [14] W. Israel. Event horizons in static electrovac space-times. *Commun. Math. Phys.*, **8**:245–260, 1968.
- [15] B. Carter. Axisymmetric black hole has only two degrees of freedom. *Phys. Rev. Lett.*, **26**:331–333, 1971.
- [16] B. P. Abbott et al. Tests of general relativity with GW150914. *Phys. Rev. Lett.*, **116**:221101, 2016.
- [17] P. Amaro-Seoane et al. Low-frequency gravitational-wave science with eLISA/NGO. *Class. Quant. Grav.*, **29**:124016, 2012.
- [18] <https://www.elisascience.org/news/top-news/gravitational-wave-mission-selected>.
- [19] L. Barack. Gravitational self force in extreme mass-ratio inspirals. *Class. Quant. Grav.*, **26**:213001, 2009.
- [20] S. A. Hughes. Gravitational-wave physics. *Nucl. Phys. Proc. Suppl.*, **138**:429–432, 2005. [,429(2005)].

## BIBLIOGRAPHY

---

- [21] W. G. Unruh. Experimental black hole evaporation. *Phys. Rev. Lett.*, **46**:1351–1353, 1981.
- [22] M. Abraham. *Theorie der Elektrizitat, V. 2: Elektromagnetische, Theorie der Strahlung*. Leipzig: Teubner, 1905.
- [23] H. A. Lorentz. *The theory of electrons*. Leipzig: Teubner, 1909.
- [24] Y. Mino, M. Sasaki, and T. Tanaka. Gravitational radiation reaction to a particle motion. *Phys. Rev.*, **D55**:3457–3476, 1997.
- [25] T. C. Quinn and R. M. Wald. An axiomatic approach to electromagnetic and gravitational radiation reaction of particles in curved space-time. *Phys. Rev.*, **D56**:3381–3394, 1997.
- [26] S. E. Gralla and R. M. Wald. A rigorous derivation of gravitational self-force. *Class. Quant. Grav.*, **25**:205009, 2008.
- [27] S. E. Gralla and R. M. Wald. Derivation of gravitational self-force. *Fundam. Theor. Phys.*, **162**:263–270, 2011.
- [28] L. Barack and A. Ori. Mode sum regularization approach for the self force in black hole space-time. *Phys. Rev.*, **D61**:061502, 2000.
- [29] S. L. Detweiler. Radiation reaction and the self force for a point mass in general relativity. *Phys. Rev. Lett.*, **86**:1931–1934, 2001.
- [30] S. L. Detweiler and B. F. Whiting. Self force via a Green’s function decomposition. *Phys. Rev.*, **D67**:024025, 2003.
- [31] E. Poisson, A. Pound, and I. Vega. The motion of point particles in curved spacetime. *Living Rev. Rel.*, **14**:7, 2011.
- [32] S. L. Detweiler. A consequence of the gravitational self-force for circular orbits of the Schwarzschild geometry. *Phys. Rev.*, **D77**:124026, 2008.

- [33] A. Le Tiec. The overlap of numerical relativity, perturbation theory and post-newtonian theory in the binary black hole problem. *Int. J. Mod. Phys.*, **D23**:1430022, 2014.
- [34] A. Pound. Second-order gravitational self-force. *Phys. Rev. Lett.*, **109**:051101, 2012.
- [35] S. E. Gralla. Second order gravitational self force. *Phys. Rev.*, **D85**:124011, 2012.
- [36] S. Detweiler. Gravitational radiation reaction and second order perturbation theory. *Phys. Rev.*, **D85**:044048, 2012.
- [37] A. Pound and J. Miller. Practical, covariant puncture for second-order self-force calculations. *Phys. Rev.*, **D89**:104020, 2014.
- [38] A. Pound. Conservative effect of the second-order gravitational self-force on quasicircular orbits in Schwarzschild spacetime. *Phys. Rev.*, **D90**:084039, 2014.
- [39] A. Pound. Second-order perturbation theory: problems on large scales. *Phys. Rev.*, **D92**:104047, 2015.
- [40] M. van de Meent and A. G. Shah. Metric perturbations produced by eccentric equatorial orbits around a Kerr black hole. *Phys. Rev.*, **D92**:064025, 2015.
- [41] M. van de Meent. Gravitational self-force on eccentric equatorial orbits around a Kerr black hole. *Phys. Rev.*, **D94**:044034, 2016.
- [42] S. Weinfurtner, E. W. Tedford, M. C. J. Penrice, W. G. Unruh, and G. A. Lawrence. Measurement of stimulated Hawking emission in an analogue system. *Phys. Rev. Lett.*, **106**:021302, 2011.

## BIBLIOGRAPHY

---

- [43] S. Weinfurtner, E. W. Tedford, M. C. J. Penrice, W. G. Unruh, and G. A. Lawrence. Classical aspects of Hawking radiation verified in analogue gravity experiment. *Lect. Notes Phys.*, **870**:167–180, 2013.
- [44] M. Visser. Acoustic black holes: Horizons, ergospheres, and Hawking radiation. *Class. Quant. Grav.*, **15**:1767–1791, 1998.
- [45] M. Novello, M. Visser, and G. Volovik. *Artificial black holes*. River Edge, USA: World Scientific, 2002.
- [46] C. Barcelo, S. Liberati, and M. Visser. Analogue gravity. *Living Rev. Rel.*, **8**:12, 2005.
- [47] G. Rousseaux, P. Maissa, C. Mathis, P. Couillet, T. G. Philbin, and U. Leonhardt. Horizon effects with surface waves on moving water. *New J. Phys.*, **12**:095018, 2010.
- [48] R. Schutzhold and W. G. Unruh. Gravity wave analogs of black holes. *Phys. Rev.*, **D66**:044019, 2002.
- [49] T. Torres, S. Patrick, A. Coutant, M. Richartz, E. W. Tedford, and S. Weinfurtner. Observation of superradiance in a vortex flow. *Preprint arXiv:1612.06180*, 2016.
- [50] R. S. Hanni. Wave fronts near a black hole. *Phys. Rev.*, **D16**:933–936, 1977.
- [51] T. J. Hollowood and G. M. Shore. The causal structure of QED in curved spacetime: analyticity and the refractive index. *JHEP*, **12**:091, 2008.
- [52] E. Poisson. *A relativist's toolkit*. Cambridge University Press, 2004.
- [53] M. Visser. van Vleck determinants: Geodesic focusing and defocusing in Lorentzian space-times. *Phys. Rev.*, **D47**:2395–2402, 1993.

- [54] W. E. Schiesser. *The numerical method of lines integration of partial differential equations*. Academic, San Diego, CA, 1991.
- [55] W. H. Press, S. A. Teukolsky, W. T. Vetterling, and B. P. Flannery. *Numerical recipes in C: The art of scientific computing*. Cambridge University Press, 1992.
- [56] K. Schwarzschild. On the gravitational field of a mass point according to Einstein's theory. *Abh. Konigl. Preuss. Akad. Wissenschaften Jahre 1906,92, Berlin,1907*, pages 189–196, 1916.
- [57] G. D. Birkhoff and R. E. Langer. *Relativity and modern physics*. Harvard University Press, 1923.
- [58] C. W. Misner, K. S. Thorne, and J. A. Wheeler. *Gravitation*. W. H. Freeman, San Francisco, 1973.
- [59] *NIST Digital Library of Mathematical Functions*. <http://dlmf.nist.gov/>, Release 1.0.13 of 2016-09-16. F. W. J. Olver, A. B. Olde Daalhuis, D. W. Lozier, B. I. Schneider, R. F. Boisvert, C. W. Clark, B. R. Miller and B. V. Saunders, eds.
- [60] M. Casals, S. Dolan, A. C. Ottewill, and B. Wardell. Self-force and Green function in Schwarzschild spacetime via quasinormal modes and branch cut. *Phys. Rev.*, **D88**:044022, 2013.
- [61] A. Ori. On the structure of the Green's function beyond the caustics theoretical findings and experimental verification. <http://physics.technion.ac.il/amos/acoustic.pdf>.
- [62] S. R. Dolan and A. C. Ottewill. Wave propagation and quasinormal mode excitation on Schwarzschild spacetime. *Phys. Rev.*, **D84**:104002, 2011.

## BIBLIOGRAPHY

---

- [63] R. P. Kerr. Gravitational field of a spinning mass as an example of algebraically special metrics. *Phys. Rev. Lett.*, **11**:237–238, 1963.
- [64] S. Chandrasekhar. *The mathematical theory of black holes*. Oxford Univ. Press, 1985.
- [65] S. A. Teukolsky. The Kerr metric. *Class. Quant. Grav.*, **32**:124006, 2015.
- [66] B. Carter. Global structure of the Kerr family of gravitational fields. *Phys. Rev.*, **174**:1559–1571, 1968.
- [67] R. Penrose. Naked singularities. *Annals N. Y. Acad. Sci.*, **224**:125–134, 1973.
- [68] S. R. Dolan. Superradiant instabilities of rotating black holes in the time domain. *Phys. Rev.*, **D87**:124026, 2013.
- [69] S. A. Hughes. The evolution of circular, nonequatorial orbits of Kerr black holes due to gravitational wave emission. *Phys. Rev.*, **D61**:084004, 2000.
- [70] M. Abramowitz and I. Stegun. *Handbook of mathematical functions with formulas, graphs, and mathematical tables*. Dover Publications, 1964.
- [71] T. C. Quinn. Axiomatic approach to radiation reaction of scalar point particles in curved space-time. *Phys. Rev.*, **D62**:064029, 2000.
- [72] J. Hadamard. *Lectures on Cauchy’s problem in linear partial differential equations*. Yale University Press, New Haven, 1923.
- [73] A. Zenginoglu and C. R. Galley. Caustic echoes from a Schwarzschild black hole. *Phys. Rev.*, **D86**:064030, 2012.
- [74] M. Casals and B. Wardell. Self-force via worldline integration of the Green function. 17th Capra Meeting on Radiation Reac-

- tion in General Relativity, <http://www.tapir.caltech.edu/capra17/cgi-bin/abstract.cgi?id=cd6fd7365091903b9748c2ff48b477a3>.
- [75] N. Warburton. personal communication, July 2016.
- [76] N. Warburton and L. Barack. Self force on a scalar charge in Kerr spacetime: circular equatorial orbits. *Phys. Rev.*, **D81**:084039, 2010.
- [77] M. Casals, S. Dolan, A. C. Ottewill, and B. Wardell. Pade approximants of the Green function in spherically symmetric spacetimes. *Phys. Rev.*, **D79**:124044, 2009.
- [78] M. Casals and A. C. Ottewill. Spectroscopy of the Schwarzschild black hole at arbitrary frequencies. *Phys. Rev. Lett.*, **109**:111101, 2012.
- [79] M. Casals and B. C. Nolan. A Kirchhoff integral approach to the calculation of Green’s functions beyond the normal neighbourhood. *Phys. Rev.*, **D86**:024038, 2012.
- [80] P. R. Anderson and B. L. Hu. Radiation reaction in Schwarzschild spacetime: Retarded Green’s function via Hadamard WKB expansion. *Phys. Rev.*, **D69**:064039, 2004.
- [81] W. G. Anderson, E. E. Flanagan, and A. C. Ottewill. Quasi-local contribution to the gravitational self-force. *Phys. Rev.*, **D71**:024036, 2005.
- [82] P. R. Anderson, A. Eftekharzadeh, and B. L. Hu. Self-force on a scalar charge in radial infall from rest using the Hadamard-WKB expansion. *Phys. Rev.*, **D73**:064023, 2006.
- [83] A. C. Ottewill and B. Wardell. Quasilocal contribution to the scalar self-force: Geodesic motion. *Phys. Rev.*, **D77**:104002, 2008.
- [84] A. C. Ottewill and B. Wardell. Quasi-local contribution to the scalar self-force: Non-geodesic Motion. *Phys. Rev.*, **D79**:024031, 2009.

## BIBLIOGRAPHY

---

- [85] B. Wardell. personal communication, June 2016.
- [86] R. H. Price. Nonspherical perturbations of relativistic gravitational collapse. 1. Scalar and gravitational perturbations. *Phys. Rev.*, **D5**:2419–2438, 1972.
- [87] R. H. Price. Nonspherical perturbations of relativistic gravitational collapse. ii. integer-spin, zero-rest-mass fields. *Phys. Rev.*, **D5**:2439–2454, 1972.
- [88] M. Casals and A. C. Ottewill. High-order tail in Schwarzschild spacetime. *Phys. Rev.*, **D92**:124055, 2015.
- [89] M. Casals, C. Kavanagh, and A. C. Ottewill. High-order late-time tail in a Kerr spacetime. *Phys. Rev.*, **D94**:124053, 2016.
- [90] B. Wardell. <http://www.barrywardell.net/Research/Code/Hadamard-WKB>.
- [91] R. Haas and E. Poisson. Mode-sum regularization of the scalar self-force: Formulation in terms of a tetrad decomposition of the singular field. *Phys. Rev.*, **D74**:044009, 2006.
- [92] N. Warburton and L. Barack. Self force on a scalar charge in Kerr spacetime: eccentric equatorial orbits. *Phys. Rev.*, **D83**:124038, 2011.
- [93] N. Warburton. Self force on a scalar charge in Kerr spacetime: inclined circular orbits. *Phys. Rev.*, **D91**:024045, 2015.
- [94] J. Thornburg and B. Wardell. Scalar self-force for highly eccentric equatorial orbits in Kerr spacetime. *Phys. Rev.*, **D95**:084043, 2017.
- [95] P. A. M. Dirac. Classical theory of radiating electrons. *Proc. Roy. Soc.*, **A167**:148–169, 1938.

- [96] B. S. DeWitt and R. W. Brehme. Radiation damping in a gravitational field. *Annals of Physics*, **9**:220–259, 1960.
- [97] S. E. Gralla, A. I. Harte, and R. M. Wald. A rigorous derivation of electromagnetic self-force. *Phys. Rev.*, **D80**:024031, 2009.
- [98] J. Kuchar, E. Poisson, and I. Vega. Electromagnetic self-force on a static charge in Schwarzschild–de Sitter spacetimes. *Class. Quant. Grav.*, **30**:235033, 2013.
- [99] A. G. Wiseman. The self-force on a static scalar test charge outside a Schwarzschild black hole. *Phys. Rev.*, **D61**:084014, 2000.
- [100] L. M. Burko. Self-force on static charges in Schwarzschild space-time. *Class. Quant. Grav.*, **17**:227–250, 2000.
- [101] M. J. Pfenning and E. Poisson. Scalar, electromagnetic, and gravitational self forces in weakly curved space-times. *Phys. Rev.*, **D65**:084001, 2002.
- [102] T. D. Drivas and S. E. Gralla. Dependence of self-force on central object. *Class. Quant. Grav.*, **28**:145025, 2011.
- [103] R. Haas. Time domain calculation of the electromagnetic self-force on eccentric geodesics in Schwarzschild spacetime. 2011. *Preprint* arXiv:1112.3707.
- [104] M. Casals, E. Poisson, and I. Vega. Regularization of static self-forces. *Phys. Rev.*, **D86**:064033, 2012.
- [105] C. Markakis and L. Barack. High-order difference and pseudospectral methods for discontinuous problems. 2014. *Preprint* arXiv:1406.4865.
- [106] K. Martel and E. Poisson. A one parameter family of time symmetric initial data for the radial infall of a particle into a Schwarzschild black hole. *Phys. Rev.*, **D66**:084001, 2002.

## BIBLIOGRAPHY

---

- [107] R. H. Price and L. M. Burko. Late time tails from momentarily stationary, compact initial data in Schwarzschild spacetimes. *Phys. Rev.*, **D70**:084039, 2004.
- [108] M. Campanelli and C. O. Lousto. The imposition of initial data in the Teukolsky equation. 1. The nonrotating case. *Phys. Rev.*, **D58**:024015, 1998.
- [109] M. Campanelli, W. Krivan, and C. O. Lousto. The imposition of Cauchy data to the Teukolsky equation. 2. Numerical comparison with the Zerilli-Moncrief approach to black hole perturbations. *Phys. Rev.*, **D58**:024016, 1998.
- [110] S. E. Field, J. S. Hesthaven, and S. R. Lau. Persistent junk solutions in time-domain modeling of extreme mass ratio binaries. *Phys. Rev.*, **D81**:124030, 2010.
- [111] L. Barack and A. Ori. Gravitational self force and gauge transformations. *Phys. Rev.*, **D64**:124003, 2001.
- [112] S. A. Teukolsky. Rotating black holes - separable wave equations for gravitational and electromagnetic perturbations. *Phys. Rev. Lett.*, **29**:1114–1118, 1972.
- [113] N. K. Johnson-McDaniel. Taming the post-Newtonian expansion: Simplifying the modes of the gravitational wave energy flux at infinity for a point particle in a circular orbit around a Schwarzschild black hole. *Phys. Rev.*, **D90**:024043, 2014.
- [114] A. G. Shah. Gravitational-wave flux for a particle orbiting a Kerr black hole to 20th post-Newtonian order: a numerical approach. *Phys. Rev.*, **D90**:044025, 2014.

- [115] N. Sago, R. Fujita, and H. Nakano. Accuracy of the post-Newtonian approximation for extreme-mass ratio inspirals from black-hole perturbation approach. *Phys. Rev.*, **D93**:104023, 2016.
- [116] S. R. Dolan, N. Warburton, A. I. Harte, A. Le Tiec, B. Wardell, and L. Barack. Gravitational self-torque and spin precession in compact binaries. *Phys. Rev.*, **D89**:064011, 2014.
- [117] A. I. Harte. Mechanics of extended masses in general relativity. *Class. Quant. Grav.*, **29**:055012, 2012.
- [118] D. Bini and T. Damour. Two-body gravitational spin-orbit interaction at linear order in the mass ratio. *Phys. Rev.*, **D90**:024039, 2014.
- [119] A. G. Shah and A. Pound. Linear-in-mass-ratio contribution to spin precession and tidal invariants in Schwarzschild spacetime at very high post-Newtonian order. *Phys. Rev.*, **D91**:124022, 2015.
- [120] D. Bini and T. Damour. Analytic determination of high-order post-Newtonian self-force contributions to gravitational spin precession. *Phys. Rev.*, **D91**:064064, 2015.
- [121] L. Barack and N. Sago. Gravitational self-force correction to the innermost stable circular orbit of a Schwarzschild black hole. *Phys. Rev. Lett.*, **102**:191101, 2009.
- [122] L. Barack and N. Sago. Beyond the geodesic approximation: conservative effects of the gravitational self-force in eccentric orbits around a Schwarzschild black hole. *Phys. Rev.*, **D83**:084023, 2011.
- [123] A. Le Tiec, A. H. Mroue, L. Barack, A. Buonanno, H. P. Pfeiffer, N. Sago, and A. Taracchini. Periastron advance in black hole binaries. *Phys. Rev. Lett.*, **107**:141101, 2011.

## BIBLIOGRAPHY

---

- [124] T. Damour. Gravitational self force in a Schwarzschild background and the effective one body formalism. *Phys. Rev.*, **D81**:024017, 2010.
- [125] L. Barack, T. Damour, and N. Sago. Precession effect of the gravitational self-force in a Schwarzschild spacetime and the effective one-body formalism. *Phys. Rev.*, **D82**:084036, 2010.
- [126] S. R. Dolan, P. Nolan, A. C. Ottewill, N. Warburton, and B. Wardell. Tidal invariants for compact binaries on quasicircular orbits. *Phys. Rev.*, **D91**:023009, 2015.
- [127] D. Bini and T. Damour. Gravitational self-force corrections to two-body tidal interactions and the effective one-body formalism. *Phys. Rev.*, **D90**:124037, 2014.
- [128] D. Bini and A. Geralico. Tidal invariants along the worldline of an extended body in Kerr spacetime. *Phys. Rev.*, **D91**:084012, 2015.
- [129] P. Nolan, C. Kavanagh, S. R. Dolan, A. C. Ottewill, N. Warburton, and B. Wardell. Octupolar invariants for compact binaries on quasicircular orbits. *Phys. Rev.*, **D92**:123008, 2015.
- [130] S. Akcay, N. Warburton, and L. Barack. Frequency-domain algorithm for the Lorenz-gauge gravitational self-force. *Phys. Rev.*, **D88**:104009, 2013.
- [131] W. de Sitter. Einstein's theory of gravitation and its astronomical consequences. *Mon. Not. Roy. Astron. Soc.*, **77**:155–184, 1916.
- [132] I. I. Shapiro, R. D. Reasenberg, J. F. Chandler, and R. W. Babcock. Measurement of the de Sitter precession of the Moon: A relativistic three-body effect. *Phys. Rev. Lett.*, **61**:2643–2646, 1988.
- [133] C. W. F. Everitt et al. Gravity Probe B: Final results of a space experiment to test general relativity. *Phys. Rev. Lett.*, **106**:221101, 2011.

- [134] R. P. Breton, V. M. Kaspi, M. Kramer, M. A. McLaughlin, M. Lyutikov, S. M. Ransom, I. H. Stairs, R. D. Ferdman, F. Camilo, and A. Possenti. Relativistic spin precession in the double pulsar. *Science*, **321**:104–107, 2008.
- [135] J. Lense and H. Thirring. Ueber den Einfluss der Eigenrotation der Zentralkörper auf die Bewegung der Planeten und Monde nach der Einsteinschen Gravitationstheorie. *Phys. Z.*, **19**:156–163, 1918.
- [136] M. Mathisson. Neue mechanik materieller systemes. *Acta Phys. Polon.*, **6**:163–2900, 1937.
- [137] A. Papapetrou. Spinning test particles in general relativity. 1. *Proc. Roy. Soc. Lond.*, **A209**:248–258, 1951.
- [138] J. A. Marck. Solution to the equations of parallel transport in Kerr geometry; tidal tensor. *Proc. Roy. Soc.*, **A385**:431–438, 1983.
- [139] S. Akcay, A. Le Tiec, L. Barack, N. Sago, and N. Warburton. Comparison between self-force and post-Newtonian dynamics: Beyond circular orbits. *Phys. Rev.*, **D91**:124014, 2015.
- [140] C. Cutler, D. Kennefick, and E. Poisson. Gravitational radiation reaction for bound motion around a Schwarzschild black hole. *Phys. Rev.*, **D50**:3816–3835, 1994.
- [141] L. Barack, A. Ori, and N. Sago. Frequency-domain calculation of the self force: The high-frequency problem and its resolution. *Phys. Rev.*, **D78**:084021, 2008.
- [142] B. Wardell. personal communication, June 2016.
- [143] A. Heffernan, A. Ottewill, and B. Wardell. High-order expansions of the Detweiler-Whiting singular field in Schwarzschild spacetime. *Phys. Rev.*, **D86**:104023, 2012.

## BIBLIOGRAPHY

---

- [144] B. Wardell. *Green functions and radiation reaction from a spacetime perspective*. PhD thesis, University Coll., Dublin, 2009.
- [145] B. Wardell and N. Warburton. Applying the effective-source approach to frequency-domain self-force calculations: Lorenz-gauge gravitational perturbations. *Phys. Rev.*, **D92**:084019, 2015.
- [146] T. Damour, P. Jaranowski, and G. Schaefer. Hamiltonian of two spinning compact bodies with next-to-leading order gravitational spin-orbit coupling. *Phys. Rev.*, **D77**:064032, 2008.
- [147] J. Hartung, J. Steinhoff, and G. Schafer. Next-to-next-to-leading order post-Newtonian linear-in-spin binary Hamiltonians. *Annalen Phys.*, **525**:359–394, 2013.
- [148] J. Hartung and J. Steinhoff. Next-to-next-to-leading order post-Newtonian spin-orbit Hamiltonian for self-gravitating binaries. *Annalen Phys.*, **523**:783–790, 2011.
- [149] R. L. Arnowitt, S. Deser, and C. W. Misner. The dynamics of general relativity. *Gen. Rel. Grav.*, **40**:1997–2027, 2008.
- [150] A. Bohe, S. Marsat, G. Faye, and L. Blanchet. Next-to-next-to-leading order spin-orbit effects in the near-zone metric and precession equations of compact binaries. *Class. Quant. Grav.*, **30**:075017, 2013.
- [151] C. Kavanagh, D. Bini, T. Damour, S. Hopper, A. C. Ottewill, and B. Wardell. Spin-orbit precession along eccentric orbits for extreme mass ratio black hole binaries and its effective-one-body transcription. 2017. *Preprint* arXiv:1706.00459.
- [152] A. G. Shah, J. L. Friedman, and T. S. Keidl. EMRI corrections to the angular velocity and redshift factor of a mass in circular orbit about a Kerr black hole. *Phys. Rev.*, **D86**:084059, 2012.

- [153] C. Kavanagh, A. C. Ottewill, and B. Wardell. Analytical high-order post-Newtonian expansions for spinning extreme mass ratio binaries. *Phys. Rev.*, **D93**:124038, 2016.
- [154] D. Bini, T. Damour, and A. Geralico. High post-Newtonian order gravitational self-force analytical results for eccentric equatorial orbits around a Kerr black hole. *Phys. Rev.*, **D93**:124058, 2016.
- [155] S. Akcay. Self-force correction to geodetic spin precession in Kerr space-time. 2017. *Preprint* arXiv:1705.03282.
- [156] W. H. Press and S. A. Teukolsky. Floating orbits, superradiant scattering and the black-hole bomb. *Nature*, **238**:211–212, 1972.
- [157] T. Damour, N. Deruelle, and R. Ruffini. On quantum resonances in stationary geometries. *Lett. Nuovo Cim.*, **15**:257–262, 1976.
- [158] V. Cardoso, O. J. C. Dias, J. P. S. Lemos, and S. Yoshida. The black hole bomb and superradiant instabilities. *Phys. Rev.*, **D70**:044039, 2004.
- [159] S. R. Dolan. Instability of the massive Klein-Gordon field on the Kerr spacetime. *Phys. Rev.*, **D76**:084001, 2007.
- [160] M. Martellini and A. Treves. Absence of superradiance of a Dirac field in a Kerr background. *Phys. Rev.*, **D15**:3060–3061, 1977.
- [161] B. R. Iyer and A. Kumar. Dirac equation in Kerr space-time. *Pramana*, **8**:500–511, 1977.
- [162] B. R. Iyer and A. Kumar. Note on the absence of massive fermion superradiance from a Kerr black hole. *Phys. Rev.*, **D18**:4799–4801, 1978.
- [163] R. Gueven. Wave mechanics of electrons in Kerr geometry. *Phys. Rev.*, **D16**:1706–1711, 1977.

## BIBLIOGRAPHY

---

- [164] S. M. Wagh and N. Dadhich. Absence of superradiance of the Dirac particles in the Kerr-Newman geometry and the weak positive energy condition. *Phys. Rev.*, **D32**:1863–1865, 1985.
- [165] A. Lasenby, C. Doran, J. Pritchard, A. Caceres, and S. Dolan. Bound states and decay times of fermions in a Schwarzschild black hole background. *Phys. Rev.*, **D72**:105014, 2005.
- [166] S. R. Dolan. *Scattering, absorption and emission by black holes*. PhD thesis, University of Cambridge, 2007.
- [167] I. M. Ternov and A. B. Gaina. Energy spectrum of the Dirac equation for the Schwarzschild and Kerr fields. *Sov. Phys. J.*, **31**:157–163, 1988.
- [168] I. M. Ternov, A. B. Gaina, and G. A. Chizhov. Finite motion of electrons in the field of microscopically small black holes. *Sov. Phys. J.*, **23**:695–700, 1980.
- [169] S. Chandrasekhar. The solution of Dirac’s equation in Kerr geometry. *Proc. Roy. Soc.*, **A349**:571–575, 1976.
- [170] D. N. Page. Dirac equation around a charged, rotating black hole. *Phys. Rev.*, **D14**:1509–1510, 1976.
- [171] S. Dolan and J. Gair. The massive Dirac field on a rotating black hole spacetime: Angular solutions. *Class. Quant. Grav.*, **26**:175020, 2009.
- [172] D. R. Brill and J. A. Wheeler. Interaction of neutrinos and gravitational fields. *Rev. Mod. Phys.*, **29**:465–479, 1957.
- [173] M. Nakahara. *Geometry, Topology and Physics*. Graduate student series in physics. Taylor & Francis, 2003.
- [174] B. Carter. Hamilton–Jacobi and Schrodinger separable solutions of Einstein’s equations. *Commun. Math. Phys.*, **10**:280, 1968.

- [175] D. L. Wiltshire, M. Visser, and S. M. Scott. *The Kerr spacetime: rotating black holes in general relativity*. Cambridge University Press, 2009.
- [176] M. Casals, S. R. Dolan, B. C. Nolan, A. C. Ottewill, and E. Winstanley. Quantization of fermions on Kerr space-time. *Phys. Rev.*, **D87**:064027, 2013.
- [177] E. W. Leaver. An analytic representation for the quasi normal modes of Kerr black holes. *Proc. Roy. Soc. Lond.*, **A402**:285–298, 1985.
- [178] J. G. Rosa and S. R. Dolan. Massive vector fields on the Schwarzschild spacetime: quasi-normal modes and bound states. *Phys. Rev.*, **D85**:044043, 2012.
- [179] K. G. Sufferin, E. D. Fackerell, and C. M. Cosgrove. Eigenvalues of the Chandrasekhar–Page angular functions. *J. Math. Phys.*, **24**:1350–1358, 1983.
- [180] E. G. Kalnins and W. Miller. Series solutions for the Dirac equation in Kerr-Newman space-time. *J. Math. Phys.*, **33**:286–296, 1992.
- [181] C. Simmendinger, A. Wunderlin, and A. Pelster. Analytical approach for the Floquet theory of delay differential equations. *Phys. Rev.*, **E59**:5344–5353, 1999.
- [182] L. L. Foldy and S. A. Wouthuysen. On the Dirac theory of spin 1/2 particle and its nonrelativistic limit. *Phys. Rev.*, **78**:29–36, 1950.
- [183] J. Barranco, A. Bernal, J. C. Degollado, A. Diez-Tejedor, M. Megevand, M. Alcubierre, D. Nunez, and O. Sarbach. Are black holes a serious threat to scalar field dark matter models? *Phys. Rev.*, **D84**:083008, 2011.

## BIBLIOGRAPHY

---

- [184] J. Barranco, A. Bernal, J. C. Degollado, A. Diez-Tejedor, M. Megevand, M. Alcubierre, D. Nunez, and O. Sarbach. Schwarzschild black holes can wear scalar wigs. *Phys. Rev. Lett.*, **109**:081102, 2012.
- [185] J. Barranco, A. Bernal, J. C. Degollado, A. Diez-Tejedor, M. Megevand, M. Alcubierre, D. Núñez, and O. Sarbach. Schwarzschild scalar wigs: spectral analysis and late time behavior. *Phys. Rev.*, **D89**:083006, 2014.
- [186] J. Barranco, A. Bernal, J. C. Degollado, A. Diez-Tejedor, M. Megevand, D. Nunez, and O. Sarbach. Self-gravitating black hole scalar wigs. 2017. *Preprint* arXiv:1704.03450.
- [187] J.-l. Jing and Q.-y. Pan. Dirac quasinormal frequencies of the Kerr-Newman black hole. *Nucl. Phys.*, **B728**:109–120, 2005.
- [188] G. B. Arfken and H. J. Weber. *Mathematical methods for physicists*. Academic Press, San Diego, CA, 1995.